LASER MICROTEXTURING OF SURFACES AND APPLICATIONS

A Ph.D. thesis Dissertation

Presented to the faculty advisory committee of the Graduate School

At the School of Engineering and Applied Science

Of the University of Virginia

In partial fulfillment of the Requirements for the degree of

Doctor of Philosophy

Charles L. Brown Department of Electrical and Computer Engineering

by

Anustup Chakraborty

December 2023

APPROVAL SHEET

This Ph.D. dissertation is submitted in partial fulfillment of the requirements

for the degree of

Doctor of Philosophy (Electrical and Computer Engineering)

_____

Anustup Chakraborty

This Ph.D. dissertation has been read and approved by the Examining Committee:

_____

Professor Mool C. Gupta, Advisor (ECE)

_____

Professor Andreas Beling, Committee Chair (ECE)

_____

Professor Gary Koenig (ChE)

_____

Professor Kyusang Lee (ECE & MSE)

_____

Professor Arthur Lichtenberger (ECE)

Accepted for the School of Engineering and Applied Science:

_____

Professor Jennifer L. West, Dean, School of Engineering and Applied Science

December 2023

To my parents and my late grandparents

ACKNOWLEDGEMENTS

I am thankful to my advisor, Professor Mool C. Gupta, who has guided me at every step to achieve my research goals and helped me to become a better researcher. Through his support, I had the opportunity to pursue valuable and interesting research and learned to address complicated research problems. The skills I've gained during my Ph.D. will serve as a lasting compass for my entire career.

I extend my sincere appreciation to my committee members: Professor Andreas Beling, who chaired my committee and provided invaluable insights and guidance on laser systems, photonics, and physics; Professor Kyusang Lee, who provided valuable feedback on the optical characteristics of laser microtextured materials and scientific scope on laser applications; Professor Gary Koenig for his expertise and insights on surface chemistry and battery materials; Professor Arthur Lichtenberger for his suggestions on enhancing adhesion strength between metals and thermally sprayed coatings through laser microtexturing, along with his insights into the advantages of laser processes. Their mentorship and expertise have played a pivotal role in shaping the trajectory of my research.

I acknowledge the support and funding of the NASA Langley Professor Program, NSF I/UCRC grant No. 1338917, NSF ECCS Grant No. ECCS-2005098, and the UVA-CCAM program. I would also like to thank my inter-university collaborators and colleagues: Benjamin Chalfant, John Sions at Commonwealth Center of Advanced Manufacturing (CCAM), Tyler Daspit of UVA Mechanical Engineering, Dr. Berhanu Bulcha, and Dr. Tilak Hewagama at NASA Goddard Space Flight Center.

I would like to extend thanks to the staff and administrators who answered my questions, supported me, and made my graduate experience even more cherished: Richard White, Dr. Cathy Dukes, Joe Thompson of the NMCF, and Natalie Dworak of the AMF. I would like to give a special thanks to Beth and Crystal of the UVA ECE Dept., who were always there for moral support and help. Thank you for your guidance and helping me navigate the academic landscape.

I would also like to express gratitude for the assistance and cooperation of my friends, fellow researchers, and colleagues, namely, Pawan, Arpan, Mahantesh, Anil, Raju, Sadik, and numerous other colleagues for their emotional support, and fruitful discussions throughout my time at UVA. Your contributions and shared insights greatly enriched my academic experience.

Finally, I am grateful for the unwavering support and love of my family. Their motivation, patience, and belief in my abilities have been a constant source of strength and made this journey possible.

Abstract

Surface properties play an essential role in many applications and allow the control of adhesion, wettability, and durability, etc. Surface microtexturing is a well-established method to enhance the surface properties of materials, including fatigue strength, corrosion resistance, anti-biofouling, adhesion, and hydrophobicity. Standard surface microtexturing techniques, such as chemical etching, electrical discharge, sandblasting, micro-milling, ion beam texturing, and lithography, often involve toxic chemicals, lack controllability, require multiple steps, use of elevated temperatures, or heavy equipment. In this thesis, we investigated the laser microtexturing process and its application in two key areas: enhancing the adhesion strength of thermal spray coatings on metallic surfaces and creating superhydrophobic and superhydrophilic surfaces. Laser microtexturing allows the generation of high-quality surfaces in a single, contactless step, addressing the limitations of traditional methods. Surfaces of materials like aluminum, steel, and glass were laser microtextured. A full-area laser microtexturing method was developed based on the thermomechanical rearrangement of surface features with minimal ablation.

The laser-microtextured surface was subjected to a thermal spray process, resulting in the accumulation of metallic particles. Compared to grit-blasted samples, surfaces with a 5 μm deep microtexture exhibited an adhesive tensile strength surpassing grit-blasted samples by over 17%, offering improved durability, resilience, and reduced maintenance costs for metal components.

The laser microtexturing method was also used to demonstrate the fabrication of superhydrophobic and superhydrophilic properties. Furthermore, the controlled transition between superhydrophobicity and superhydrophilicity was explored and a cost-effective laser microtexturing technique for inducing superhydrophilicity was introduced. A thin

polydimethylsiloxane (PDMS) coating can transform the laser-microtextured surface into a superhydrophobic state, and this thin layer can be easily removed through laser ablation, enabling a reversible shift between superhydrophilicity and superhydrophobicity. Additionally, the superhydrophobic surfaces created using laser ablation of PDMS achieved water contact angles exceeding 150°, roll-off angles less than 3°, and optical transmission values of over 90% on transparent glass surfaces.

The study of laser microtextured superhydrophilic and superhydrophobic surfaces will impact numerous applications, including self-cleaning surfaces, corrosion protection, anti-icing coatings, microfluidic systems, water collection, and efficient thermal management.

TABLE OF CONTENTS

LIST OF FIGURES

LIST OF TABLES

CHAPTER 1: Introduction and Motivation

Surface modifications have been shown to improve the surface properties of materials. Some of the commonly used surface microtexturing techniques are chemical etching, electrical discharge, electrochemical machining, micro-milling, ion-beam etching, hot embossing, lithography, and sandblasting. Micro- and nanoscale patterns created on the surfaces of metals, polymers, ceramics, and glass materials find wide-ranging applications across various domains, including engineering, medicine, and biology. For example, the fabrication of microtexture effectively enhances the load-bearing capacity, wear resistance, and friction coefficient of silicon carbide mechanical seals. Hydrodynamic lubrication in steel can also be improved by creating dimples on the surface. One of the alternative techniques for surface microtexturing is using a laser. In comparison with other surface microtexturing methods, laser microtexturing stands out by generating high-quality surfaces economically through a single, contactless step. This highly scalable process eliminates the need for hazardous chemicals and offers additional benefits such as easy automation, localized treatment, and the facile creation of three-dimensional profiles. Laser microtexturing opens the door to a range of functionalities, including but not limited to the enhancement of coating adhesion, the augmentation of frictional properties, the facilitation of self-cleaning mechanisms, and the precise control of wetting characteristics. Depending on the laser microtexturing parameters employed, various microtexture patterns and sizes can be produced. The impact of these microtexture patterns on surface functionalities can be described in terms of the feature geometry and/or the underlying surface chemistry. The geometric characteristics of features exert influence over the wetting properties of a surface by influencing the contact angle (CA) between a liquid droplet and the material surface. Moreover, these features play a pivotal role in enhancing surface

adhesion properties as the surface microtexture effectively increases the available surface area for coatings[1,2,3].

Nanosecond, picosecond, and femtosecond lasers represent the three primary categories of lasers commonly employed for surface microtexturing, and their key distinguishing feature lies in the duration of the optical pulses they emit[3].

In the case of nanosecond lasers, the process generally involves the initial absorption of light energy, leading to localized heating at the targeted site, followed by material melting and eventual vaporization. Nanosecond laser pulses provide ample time for the thermal wave to propagate into the metallic substrate, resulting in the formation of a relatively thicker molten layer. This situation generates a recoil pressure that expels substrate material in the form of liquid and vapor due to vaporization. Despite numerous reports on surface microtexturing using nanosecond lasers, a common challenge associated with this technique is the tendency for microtextured patterns to acquire an oval shape in square microtexturing and suffer from distortion in other patterns due to material melting and evaporation from the targeted surface. Nanosecond laser microtexturing is better suited for thicker substrates due to the extended duration of laser pulses. However, it can lead to the formation of a heat-affected zone around the microtexturing hole, which is susceptible to oxide layer formation. This can impact the surface morphology, leading to cracking and the formation of pores on the microtextured surface[3].

In the context of picosecond laser surface microtexturing, the laser pulses initially interact with the free electrons on the substrate surface. Following electron excitation, heat energy is transferred to the lattice of the targeted substrate through heat conduction, and the material is removed by melting and ablation once the lattice temperature exceeds the thermodynamic critical temperature of the surface. Importantly, this process results in material removal within the pulse focus area, leaving

other areas of the surface unaffected. Picosecond pulse ablation is used for patterning thin films by scanning the laser beam in a grid pattern, as depicted in the SEM image in Figure 1[3].

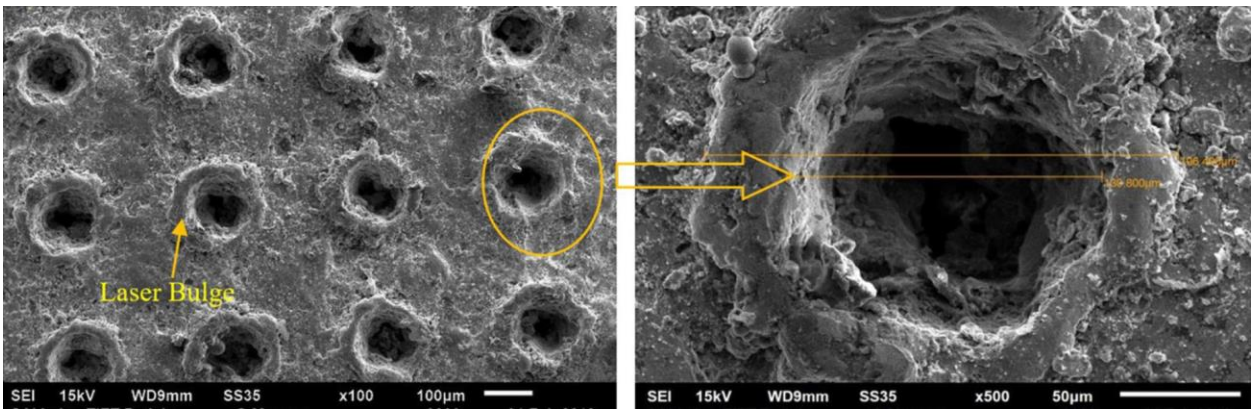

Fig. 1: SEM image of (a) picosecond laser microtextured steel substrate; (b) magnified laser microtextured hole. *This figure is reprinted from Materials Today Communications, Vijay Kumar, Rajeev Verma, Saurabh Kango, Vishal S Sharma, Recent progresses and applications in laser-based surface texturing systems, 26 101736-101754, copyright 2020, with permission from Elsevier.*

Femtosecond lasers find widespread application in delicate and precise surface modification tasks (Figure 2), particularly in fields such as optics, microelectronics, and various surface modification processes. Ultra-short pulse lasers, like femtosecond lasers, are characterized by high peak power and very short (~10^{-15} sec) pulse duration. This high peak power, along with the extremely short time scales involved, leads to complex energy exchange processes between the laser and the material. Consequently, surface damage, shockwave formation, and the generation of surface debris are typical outcomes associated with femtosecond lasers[3,4].

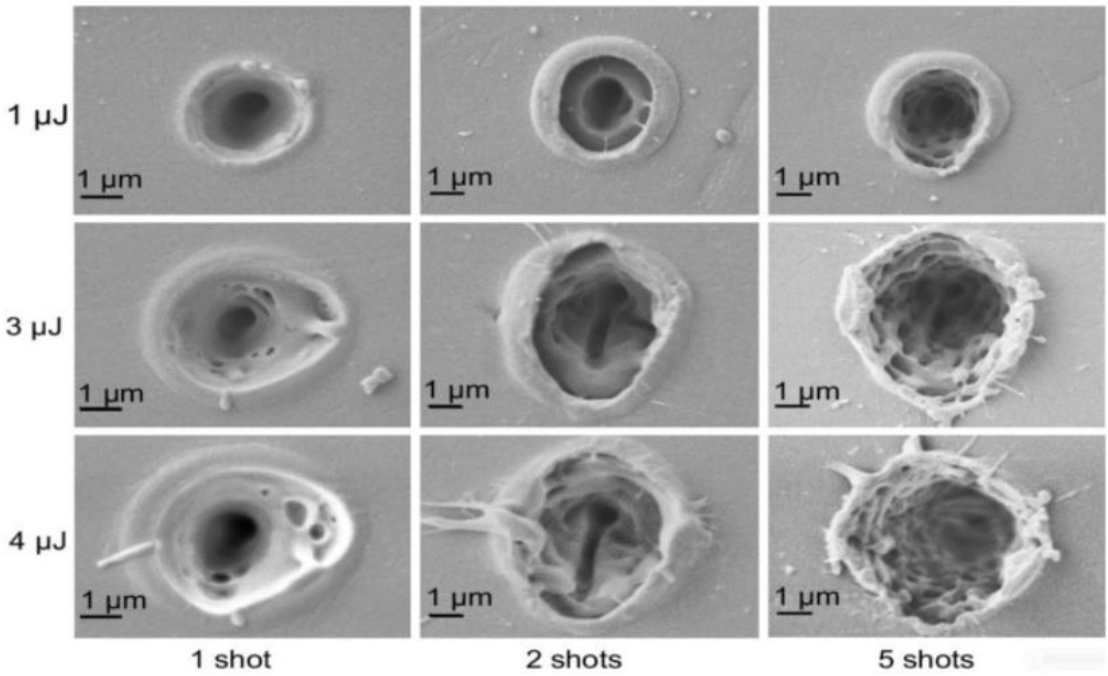

Fig. 2: SEM images of femtosecond laser ablated structures in PMMA showing the evolution of porosity for 1,2 and 5 shots. *This figure is reprinted from the Materials Today Communications, Vijay Kumar, Rajeev Verma, Saurabh Kango, Vishal S Sharma, Recent progresses and applications in laser-based surface texturing systems, 26 101736-101754, copyright 2020, with permission from Elsevier.*

The research presented in this thesis addresses critical needs in materials science and surface engineering, offering innovative solutions to longstanding challenges in various industries. The primary focus on enhancing the adhesion strength of coatings on metallic surfaces is of paramount importance in fields like automotive, power generation, and aerospace. The superior adhesion strength achieved through full-area laser microtexturing has the potential to significantly enhance the durability and resilience of metal components, ultimately reducing maintenance costs and improving the overall performance and safety of critical machinery and structures. This innovation meets the ever-growing demand for more reliable and long-lasting materials in industries where safety and efficiency are top priorities.

Furthermore, the development of a rapid, cost-effective, and large-scale superhydrophobic surface creation method has extensive implications for a wide range of applications. Industries such as solar panel manufacturing, greenhouse construction, and the production of water-resistant glass and plastic materials stand to benefit from the efficiency and cost-effectiveness of this approach. The ability to apply superhydrophobic coatings to various surfaces with high throughput opens up new possibilities for achieving water-repellent properties, which are increasingly sought after in today's environmentally conscious and technology-driven world. Additionally, the novel method for creating extreme superhydrophilic and reversible superhydrophobic surfaces on transparent substrates like glass holds promise for optical devices, microfluidics, and beyond. This research addresses the growing demand for versatile, sustainable, and high-performance surface engineering techniques in a variety of industries.

The primary focus of this thesis is to demonstrate the potential of laser microtexturing in two key areas: enhancing the adhesion strength of coatings on metallic surfaces and creating superhydrophobic and superhydrophilic surfaces. While prior research has explored these fields, this study achieved the highest adhesion strength for metallic coatings through a full-area laser microtexturing approach. This study also introduces an innovative method for achieving superhydrophobic surfaces through pulsed laser ablation of PDMS, notably without the requirement of substrate microtexturing. The ablated PDMS particles form a microtextured layer over the substrate, thus rendering the surface superhydrophobic. Further, an innovative approach for attaining extreme superhydrophobic surfaces with contact angles exceeding 170°, along with superhydrophilic surfaces featuring contact angles of less than 1°, and the ability to combine superhydrophobic and superhydrophilic properties, also known as reversible wettability, is presented.

Traditionally, laser microtexturing has primarily relied on the ablation process. However, the full-area laser microtexturing method presented in this thesis differs significantly by predominantly relying on the thermomechanical rearrangement of molten material with minimal ablation. The key innovation lies in carefully selecting the laser power to induce melting while minimizing ablation, followed by scanning the laser beam across the entire surface. This process results in the formation of closely spaced peaks and valleys on the surface, significantly enhancing the surface area and thereby improving the grip for thermally sprayed coating powders. The enhancement in coating adhesion strength has substantial implications, as it can lead to increased durability, resilience, and reduced maintenance costs for metal components. These advancements hold promise for various industries, including automotive, power generation, and aerospace[1].

In the realm of superhydrophobic surface creation, this thesis introduces a one-step method that is rapid, acid-free, and cost-effective. This method involves pulsed laser deposition of laser-ablated PDMS micro/nanoparticles onto a substrate, eliminating the need for surface microtexturing of the substrate. This feature makes it ideal for large-scale applications with high throughput. Moreover, the deposited PDMS micro/nanoparticle film is only a few micrometers thick and can be precisely controlled. This versatile technique can be applied to a wide range of materials and has diverse applications, including superhydrophobic coatings for solar panels, greenhouses, and water-resistant glass or plastic applications[5].

On the other hand, extreme surface superhydrophilicity with a water contact angle (WCA) of less than 1° is achieved by creating densely packed, pillar-like micro/nanostructures on the surface. This unique surface microtexture facilitates rapid water entry and spreading, making it exceptionally wettable. The superhydrophilic properties remain stable over extended periods, with no significant changes in contact angle observed for up to two months. Additionally, when a thin

layer of polydimethylsiloxane (PDMS) is applied to these superhydrophilic surfaces, they exhibit superhydrophobic behavior, characterized by a water contact angle (WCA) of approximately 169° and a roll-off angle (ROA) of less than 2°. This hierarchical surface microtexture, combined with the low surface energy of PDMS, imparts superhydrophobicity to the surface. Notably, the PDMS coating can be easily removed using laser ablation, restoring the surface to its original superhydrophilic state. This innovative method for achieving reversible wettable surfaces offers numerous advantages. It eliminates the need for high temperatures, hazardous chemicals, and complex fabrication steps, making it a quick and versatile process applicable to a wide range of materials. The contact angle achieved in this study represents one of the highest reported values for superhydrophobicity. Moreover, this method enables the fabrication of selective micron-scale areas with superhydrophilic and superhydrophobic properties. It also demonstrates the reversible transition of wettability on optically transparent substrates, such as glass.

CHAPTER 2: Literature Review

This chapter serves as a comprehensive examination of the existing body of knowledge that forms the foundation of this research thesis. Within this chapter, three key subsections provide an in-depth exploration of critical topics related to the research objectives. In the first subsection, the focus is on the latest advancements and research findings concerning laser-based surface modification techniques. This section delves into various methodologies, parameters, and outcomes associated with laser microtexturing. The second subsection discusses the current state of the art in creating surfaces with extreme wetting properties, providing an overview of techniques, materials, and potential applications, along with an exploration of how laser surface microtexturing can enhance both superhydrophilic and superhydrophobic properties. Finally, the third subsection scrutinizes the influence of laser surface microtexturing on adhesion strength, covering relevant studies, experimental results, and their implications. Together, these subsections provide a holistic understanding of the contextual landscape surrounding the research topics, paving the way for the subsequent chapters' investigations and findings.

2.1 Laser microtexturing

The process of laser microtexturing involves directing a profiled laser beam onto various material surfaces, resulting in localized and short-term thermal or photochemical effects that result in the melting, heating, removal, or alteration of the material in a controlled fashion[6]. The laser pulse energy density, pulse width, scanning speed, and laser frequency influence the shape and height of the surface features considerably. Generally, increasing the laser fluence results in the expulsion of more molten materials, which leads to wider grooves and increased height of the resolidified

surface microtexture, thereby increasing the surface roughness[1,7] Figure 3 gives an idea of increasing surface roughness with increasing laser fluence on aluminm[7] .

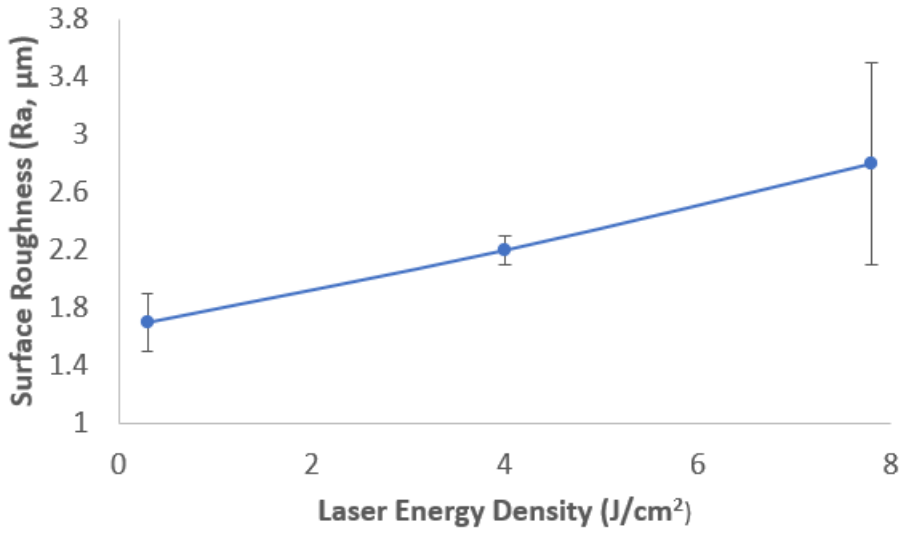

Fig. 3: Surface roughness values (Ra) of laser microtextured aluminum alloy at different laser energy densities [7]. *This figure is adapted from the Journal of Manufacturing Process, Seung Jai Won, Hong Seok Kim, Effetc of laser parameters on morphological change and surface properties of aluminum alloy in masked laser surface texturing, Recent progresses and applications in laser-based surface texturing systems,* 48 *260-269, copyright 2019, with permission from Elsevier.*

The number of laser pulses is also a significant factor that affects the surface roughness. Figure 4 shows the microtextural roughness variation of a hole region that was irradiated by a laser. The surface roughness decreased as the number of laser pulses increased due to the planarization effect caused by repeated laser irradiations. When the laser pulse was irradiated 5 times, the surface roughness of the hole region was 0.15 µm (48.7% lower than that of the single laser irradiation). In addition, the surface roughness when the laser was irradiated 10 times was further reduced to 0.07 µm (77% lower than that of single laser irradiation). In the case of 20 laser irradiations, the surface roughness was 0.07 µm, which was similar to the 10 laser irradiation case. After 10 laser irradiations, no further improvement in surface roughness (obtained from the planarization effect) was observed[7].

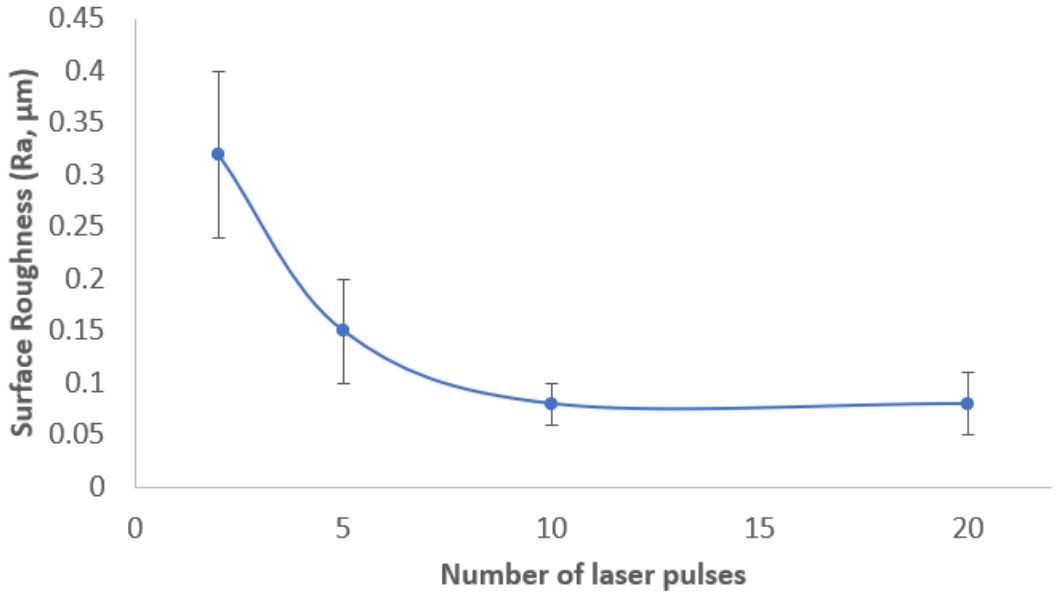

Fig. 4: Surface roughness (Ra) of hole region as a function of number of laser pulses on aluminum at a constant laser energy density[7]. *This figure is adapted from the Journal of Manufacturing Process, Seung Jai Won, Hong Seok Kim, Effetc of laser parameters on morphological change and surface properties of aluminum alloy in masked laser surface texturing,* 48 *260-269, copyright 2019, with permission from Elsevier.*

Furthermore, it's important to note that surface roughness plays a pivotal role in determining the wettability of metallic substrate surfaces. Wettability, in turn, has a significant impact on the corrosion resistance of these surfaces. Research on laser surface microtexturing of Ti-6Al-4V[7], for instance, has shown that the laser process enhances the surface roughness of the substrate when compared to its as-received state. Additionally, it has been reported that as surface roughness decreases, wettability also decreases[8]. This decrease in wettability results in a more hydrophobic substrate surface, ultimately improving corrosion resistance. Hence, further analysis of the wettability of laser microtextured surfaces would provide valuable insights into the influence of laser surface microtexturing parameters on hydrophobicity and corrosion resistance[7, 8,9].

One of the critical factors influencing the morphology of material surfaces is the scanning speed of the laser. Figure 5 presents the depths of the microtexture achieved at different scanning speeds, revealing a pronounced decrease in depth as scanning speed increased. This decline in

microtexture depth can be attributed to the fact that the average power and repetition frequency remained constant, resulting in consistent pulse energy. As the scanning speed increased, there was a decrease in the number of laser pulses applied per unit length, leading to reduced material removal due to a decrease in pulse overlap. Laser pulse overlap refers to the temporal alignment of multiple laser pulses during a specific time interval[9]. Furthermore, Figure 6 also illustrates the surface morphology at various scanning speeds, highlighting the significant impact of scanning speed on both microtexture morphology and melt accumulation. Notably, at a scanning speed of 10 mm/s, the depth of the microtexture was the highest among the tested speeds, but the degree of melt accumulation was the lowest. As the scanning speed continued to rise, the reduced overlap of surface pulses resulted in a decreased material removal rate. Consequently, the shallowest microtexture depth was observed at a scanning speed of 40 mm/s, accompanied by a significant accumulation of melted material within the texture, which adversely affected the quality of the processing. In summary, the optimal range for scanning speed of the laser beam, falling between 10-20 mm/s, appeared to yield the best processing quality, striking a fine balance between microtexture depth and melt accumulation[9].

The relation between the depth of microtexture and repetition rate has been indicated in Figure 6. It can be seen that the depth of the microtexture increased with the repetition rate. Elevated laser repetition rate can have a notable impact on material removal rates, potentially resulting in a coarser surface finish if not adequately managed. This phenomenon arises from the higher number of laser pulses delivered within a given timeframe, leading to increased material removal and the formation of surface irregularities. Increased laser frequencies can also introduce greater thermal energy into the material. This excess heat can induce material melting, recrystallization, or even vaporization, thereby increasing the likelihood of surface roughness due to the creation of recast

layers, microcracks, and other surface imperfections. The extent of overlap between successive laser pulses plays a pivotal role in this context. When laser frequency is excessively high, and pulses substantially overlap, it can result in excessive material removal and subsequent surface roughening. Conversely, sparse pulse distribution may lead to an uneven surface microtexture. In essence, the influence of laser frequency on surface roughness is multifaceted, encompassing material removal rates, heat effects, and pulse overlap considerations. Effective control and optimization of laser frequency, in conjunction with other pertinent parameters, are essential to achieve the desired surface quality in laser material processing applications[9].

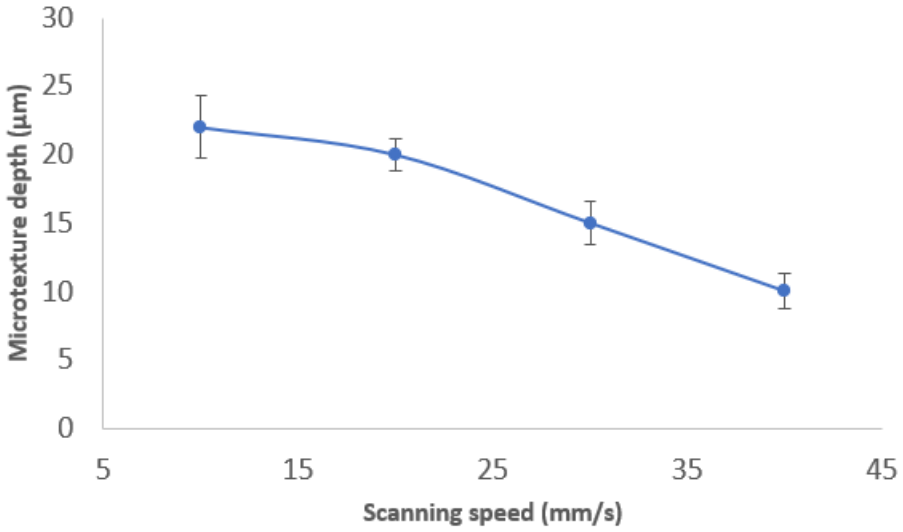

Fig. 5: Relationship between microtexture depth and laser scanning speed on Ti-Al alloy surface[9]. *This figure is adapted from the IOP Conference Series: Materials Science and Engineering, Xiaoying Xi, Yongzhi Pan, Pengcheng Wang, Xiuli Fu, Effect of laser processing parameters on surface texture of Ti6Al4V alloy,* 563 *022052-022059, copyright 2019, with permission from IOP Publishing.*

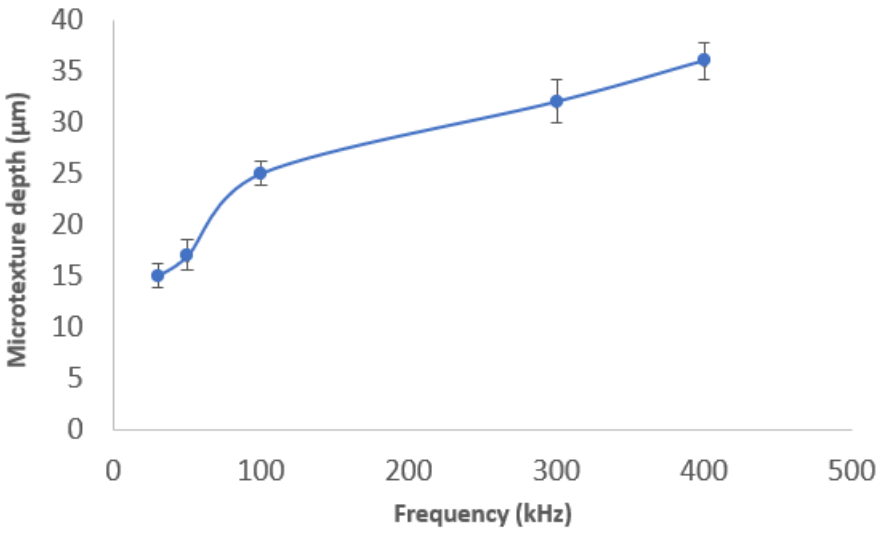

Fig. 6. Relationship between microtexture depth and repetition rate of the laser on Ti-Al alloy surface[9]. *This figure is adapted from the IOP Conference Series: Materials Science and Engineering, Xiaoying Xi, Yongzhi Pan, Pengcheng Wang, Xiuli Fu, Effect of laser processing parameters on surface texture of Ti6Al4V alloy,* 563 *022052-022059, copyright 2019, with permission from IOP Publishing.*

2.2 Superhyrophilic and Superhydrophobic Surfaces

The term "superhydrophilicity" was first coined by Fujishima *et al.*[10]. According to Drelich and Chibowski[11], it refers to textured or structured materials with a surface roughness factor (r) (defined in the Wenzel equation) greater than one, denoted as $r > 1$. On such surfaces, water spreads completely, forming a continuous layer rather than droplets. This super-spreading water layer allows for the easy removal of dirt and stains from the surface. The wettability of such surfaces depends on both surface free energy and geometric structure. Specifically, superhydrophilic surfaces are materials whose surfaces exhibit water contact angles (WCAs) lower than 5°[12].

Since its introduction, numerous techniques have been developed to create superhydrophilic surfaces by combining surface chemistry with rough structures. Due to their wide range of applications, superhydrophilic surfaces have been fabricated on various substrate materials,

including silicon, textiles, glass, aluminum, steel, and other metals. In the following section, we describe the methods used to create superhydrophilic surfaces[12].

The primary objective of surface modification is to enhance surface performance by altering various characteristics, including roughness, surface energy, surface charge, hydrophilicity, biocompatibility, and functionality. Numerous techniques have been developed to create superhydrophilic surfaces, such as vapor deposition, phase inversion, ultrasonic spray pyrolysis, calcination, hydrothermal treatment, layer-by-layer assembly, sol-gel self-assembly, electrochemical anodization, etching, electrospinning, interfacial polymerization, and solution coating. Each fabrication method offers distinct advantages and may have limitations, depending on the specific components used and intended applications. Nevertheless, these methods have demonstrated the potential to significantly enhance surface properties, leading to improved performance[12].

Plasma processing serves as an efficient method for anchoring functional graft chains onto material or film surfaces, offering the advantage of altering only the physical and chemical properties of the surface while preserving bulk properties. However, it requires a vacuum environment, which can increase operational costs. Plasma treatment allows precise control of the modified layer thickness down to the angstrom level. Various gases, including hydrogen, argon, helium, oxygen, nitrogen, and fluorine-containing plasmas, are commonly used to modify surfaces. Plasma treatment generates charged and neutral species, such as electrons, positive ions, negative ions, radicals, atoms, and molecules, depending on the gas used. These methods eliminate the need for hazardous chemicals while inducing surface modifications with minimal degradation and roughness compared to wet chemical techniques. Additionally, the deposited film's properties can be adjusted by manipulating the deposition rate, energy range, and surface topography. Plasma

treatment has been extensively employed to introduce hydrophilic groups to material or film surfaces, resulting in reduced water contact angles. For instance, superhydrophilic vertically aligned carbon nanotube (VACNT) films grown on titania (Ti) were produced using microwave plasma-enhanced chemical vapor deposition with Fe catalyst[13,14]. The contact angle was significantly reduced from 154° to nearly 0° by subsequent oxygen plasma treatment for 2 minutes at 400 V and 80 mTorr[12].

Ultraviolet (UV) irradiation represents another method for generating superhydrophilic surfaces without altering bulk properties. It involves the chemical bonding between a substrate and an active layer. Recent studies have highlighted the role of surface topography and roughness in fine-tuning superhydrophilicity. One approach is to create surfaces with photocatalytic particles, exemplified by the pioneering work on titania-based superhydrophilic surfaces dating back to 1997[12]. Building upon this approach, metal oxide photocatalysts like TiO_2, ZnO, SiO_2, SnO_2, WO3, and V_2O_5 have been developed to induce superhydrophilic behavior when exposed to UV light radiation. Commonly used materials include titanium dioxide (TiO_2), SiO_2, ZnO, and tungsten trioxide (WO_3). For instance, Lai et al.[15] transformed a superhydrophobic TiO_2 nanotube film into a superhydrophilic film by selectively photocatalyzing the organic monolayer on the TiO_2 nanotube surface with UV light through a photomask. This resulted in a decrease in the water contact angle from 156° to 5°. This change was attributed to altered surface composition and enhanced wettability due to the rough TiO_2 nanotube structure. Similarly, Ashkarran and Mohammadizadeh[16] achieved superhydrophilicity by exposing TiO_2 thin films to UV illumination for approximately 10 minutes, resulting in a near-zero contact angle.

Some of the other methods used to make superhydrophilic surfaces are etching, calcination, hydrothermal treatment, and electrospinning[12].

Etching is a process in which a film or foil is exposed to high-energy particle radiation, typically metal ions directed perpendicular to the material, followed by immersion in an acid or alkaline bath. This procedure alters surface topography and can influence surface wettability, potentially leading to superhydrophilicity. Etching can also be employed as a preliminary step before coating a material to ensure proper adhesion. It can yield cylindrical pores with uniform size distributions and intricate pattern structures[12]. For instance, an artificial superhydrophilic surface was created, inspired by fish scales, to gain insights into wetting behavior[17].

Calcination is a process involving the application of heat to a substance without fusion, causing changes in its physical or chemical constitution. The objectives of calcination typically include removing absorbed moisture or other volatile constituents, as well as oxidizing a part or the entire substance. This process often occurs at or above the thermal decomposition temperature or transition temperature. Studies have shown that superhydrophilic surfaces can be produced through calcination[12]. For example, Cu_2O and CuO membranes with superhydrophilic properties were prepared by calcinating $Cu(OH)_2$ parent films at 130°C for 5 hours and reducing the $Cu(OH)_2$ membrane in a hydrazine solution for 3-5 hours. The resulting membranes exhibited water contact angles lower than 1°, indicating superhydrophilic behavior[18].

Hydrothermal treatment is a method that combines heat and water as a medium to convert various resources into uniform products, particularly producing porous and chemically homogeneous particles. It involves autoclaves and sealed steel cylinders capable of withstanding high temperatures and pressures. Researchers have demonstrated that hydrothermal treatment can lead to the formation of superhydrophilic surfaces[12]. For instance, in a study[19], TiO_2 thin films were prepared using a hydrothermal dip-coating process, and their superhydrophilic durability was

investigated through repetitive cycles of water soaking and drying. The TiO_2 film exhibited superhydrophilic properties, with a contact angle of less than 5° within 5 seconds.

Electrospinning, on the other hand, is a technique that produces nanofibers from a charged solution or melt by applying a high electric field. These nanofibers possess unique properties due to their nanoscale diameters and high aspect ratios, making them suitable for various applications. Electrospinning has been considered effective for creating superhydrophilic surfaces[12]. For example, α-Fe_2O_3 nanofibers were generated via electrospinning poly(vinyl alcohol)/ferrous acetate composite nanofiber precursors and subsequent calcination. A water contact angle of 0° was exhibited by the resulting α-Fe_2O_3 nanofibers[20].

Laser-induced surface modifications have proven to be highly effective in creating superhydrophilic surfaces. The wetting properties of these surfaces are significantly influenced by laser parameters, including pulse width, scanning speed, and frequency. In a study conducted by Lavieja et al.[21], a nanosecond laser was employed to induce superhydrophilicity on a polymer surface by adjusting the focal point. This process resulted in the formation of minute surface ripples due to the intense localized heating initiated by the laser. The reported contact angle achieved in this study was just slightly below 1°. In another investigation, Pan et al.[22] explored the effects of laser-generated surface microstructures on steel surfaces and their resulting superhydrophilic properties. By varying laser processing parameters, they successfully introduced groove-like textures onto the surface. The measured contact angle exhibited fluctuations around 0°. However, there is a need for further research to achieve even lower contact angles while simultaneously improving the durability of these superhydrophilic surfaces.

The combination of a low surface free energy solid and a low interfacial contact area between water and solid is needed to produce water-repellant or superhydrophobic surfaces. Slight tilting

of the surface should make the water easily roll off the surface while cleaning the surface by carrying all the contaminant particles away without leaving any residue. When considering the methods to produce a superhydrophobic surface, two major techniques are investigated in research and used in industry: chemical coatings and surface microtexture. Chemical coatings demonstrate an ease of fabrication, low-cost application, and high scalability. However, chemical coatings face durability challenges and can be application-limited. Meanwhile, surface microtexture is often more difficult to fabricate and does not easily scale to large-area applications. The advantages of surface microtexture include superior durability, longevity, and fine control over the resultant wetting properties. It is worthwhile to mention that controlled and reversible conversion between superhydrophobic and superhydrophilic wetting states can be used for targeted drug delivery, water-harvesting, and antireflective, water-proofing, and liquid self-transportation coatings[23].

To produce a superhydrophobic surface, the presence of microtexture alone is not sufficient. This is due to the interactions between water and the surface. These interactions can be manipulated by the presence of surface microtexture. However, the surface free energy of the material is an integral facet of the wetting dynamics. Table 1 lists the highest reported water contact angles (CAs) for a few surfaces with their corresponding surface free energy. It is interesting to note that certain surfaces need to be microtextured and then coated with something with a lower surface free energy, like poly(dimethylsiloxane) (PDMS) to make them superhydrophobic[23].

Table 1. Surface free energy of different polymers[24]. *This figure is reprinted from "Superhydrophobic Properties of Replicated Laser Microtextured Surfaces," Ph.D. Thesis, with permission from the author.*

Surface	**Surface Free Energy (mJ/m^2)**	**CA (°)**
Polytetrafluoroethylene (PTFE Teflon)	18	168
Fluorinated Ethylene Propylene (FEP Teflon)	19	160
Poly(dimethylsiloxane) (PDMS)	21	163
Polypropylene (PP)	29	160
Poly(vinylidene fluoride) (PDVF)	30	171
Polyethylene (PE)	31	173
Polystyrene (PS)	36	158

The surface free energyis the amount of excess energy at the surface of a material compared to its bulk.. A high surface energy material interacts different with a liquid than low surface energy. These interactions manifest primarily in the form of van der Waals forces and electrostatic attraction[23]. The surface energy formulation for solid surfaces was presented by Vanoss et al.[25] , and the surface energy can be written as:

$$\gamma = \gamma^L + \gamma^P \quad (1)$$

where γ^L is the apolar component due to Lifshitz-van der Waals intermolecular interactions, and γ^P is due to electron-acceptor and electron-donor intermolecular interactions. The apolar component γ^P , owing to electron-acceptor and electron-donor intermolecular interactions, could be expressed as:

$$\gamma^P = 2\sqrt{\gamma^+ . \gamma^-} \quad (2)$$

where γ^+ and γ^- are the electron acceptor and electron donor parameters of the acid-base component of the solid and liquid surface free energy, respectively. The interfacial free energy for a solid–liquid system could be written as

$$\gamma_{SL} = \gamma_S + \gamma_L - 2\sqrt{\gamma_L^S . \gamma_L^L} - 2\sqrt{\gamma_S^+ . \gamma_L^-} - 2\sqrt{\gamma_S^- . \gamma_L^+} \quad (3)$$

where subscripts *S* and *L* represent solid and liquid phases, respectively. Therefore, the Young's equation for the surface free energy of a solid becomes:

$$\gamma_L cos\theta = \gamma_S - \gamma_{SL} - Pe_L \quad (4)$$

where γ_S is the solid surface free energy, γ_{SL} is the interfacial solid-liquid free energy, γ_L is the liquid surface tension, θ is the contact angle, and Pe_L is the pressure of the liquid film, which is negligibly small and considered to be zero.

In contrast, surface tension in a liquid describes the inward force exerted by the liquid's surface due to the uneven forces at play within the liquid itself. This phenomenon results from the interplay between the liquid's surface tension and the surface free energy of a solid. It plays a critical role in determining how a liquid behaves when placed on a solid surface, a phenomenon known as wetting. More precisely, when a low surface free energy solid interacts with a high surface tension liquid, the resulting interfacial contact area tends to be relatively small. The interfacial area plays a major role in controlling the wetting behavior[23].

As a result of this delicate balance of forces, a water droplet assumes a consistent shape when it rests on a surface. This equilibrium contact angle (θ_E), also known as the static contact angle, represents the angle formed between the solid surface and the tangent line at the point where the droplet makes contact with the surface, as illustrated in Figure 1. The static contact angle can be computed using Young's equation, as shown in Equation 5, where θ_E denotes the static contact angle in degrees, γ_{LV} is the surface tension at the liquid-vapor interface in millinewtons per meter (mN/m), γ_{LS} is the interfacial tension at the liquid-solid interface in mN/m, and γ_{SV} is the surface tension at the solid-vapor interface in mN/m[23].

$$\cos\theta_E = \frac{(\gamma_{SV} - \gamma_{LS})}{\gamma_{LV}} \quad (5)$$

A surface is classified as hydrophilic if the static contact angle (CA) of a 10 µL drop of deionized water measures less than 90º. When the static CA is 90º or greater, the surface is considered hydrophobic. Furthermore, if the static CA reaches 150º or higher, the surface is referred to as superhydrophobic. Superhydrophobic surfaces are typically achieved through a combination of materials with low surface energy and surface texture. An excellent example of a naturally occurring superhydrophobic surface can be found on the leaves of a lotus plant. When a raindrop lands on a lotus leaf, it tends to either bounce off upon impact or roll off the leaf's surface, carrying away any dirt particles it encounters[23].

While the contact angle (CA) is a commonly reported metric for assessing superhydrophobic surfaces, other parameters are also essential for a comprehensive evaluation. One such parameter is the roll-off angle (ROA), which signifies the angle at which a 10 µL droplet of deionized water, resting on the surface, initiates motion, often referred to as the sliding angle. During surface tilt measurements, before movement begins, the water droplet experiences some deformation, leading to changes in static CA measurements. The droplet inclines toward the lower side of the tilted surface, indicating the direction of subsequent sliding motion. The static CA measured on the lower side of the tilted surface is greater than that on a flat surface and is termed the advancing contact angle (ACA). Conversely, the static CA measured on the opposite side of the droplet from the ACA is lower than that on a flat surface and is known as the receding contact angle (RCA). The difference between ACA and RCA is referred to as contact angle hysteresis (CAH). Figure 7 illustrates these concepts, including the deformation of a water droplet due to surface tilt[23].

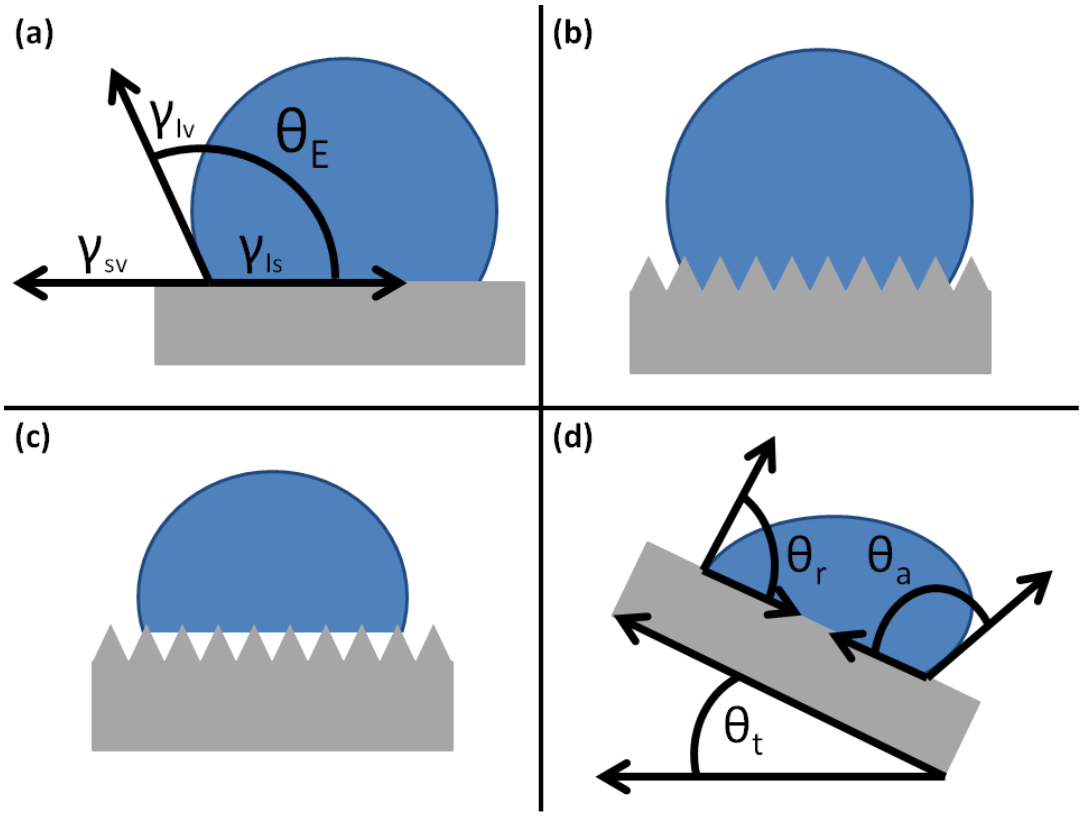

Fig. 7: The various parameters and wetting modes for a droplet of liquid on a surface: (a) Static contact angle (θ_E), (b) Wenzel wetting, (c) Cassie-Baxter wetting, (d) Advancing contact angle (θ_a) and receding contact angle (θ_r), with roll-off angle (θ_t) of the surface. The different surface and interfacial tensions (mN/m) are liquid-vapor γ_{LV}, liquid-solid γ_{LS}, and solid-vapor γ_{SV}[26]. *This figure is reprinted from "Anti-ice and Condensation Properties of Microtextured Superhydrophobic Surfaces," Ph.D. thesis, with permission from the author.*

Two clear examples illustrate how surface microtexture plays a crucial role in decreasing the wettability of a material with low surface-free energy. Yeong and Gupta[27] demonstrated that microtexturing Fluorinated ethylene propylene (FEP) Teflon sheet increased the CA from 112º to 160º, while the ROA decreased from 45º to 4º. Similarly, Chun et al.[28] demonstrated that microtexturing polystyrene increased the CA from 103º to 158º.

Wetting properties are not limited to water alone; they extend to other liquids as well. The contact angles (CAs) of various liquids on microtextured PDMS were measured. As anticipated, as shown

in Table 2, liquids with surface tensions lower than that of water exhibited correspondingly lower CAs.[23].

Table 2: Contact angles and sliding angles of different liquids on textured PDMS

Sample	Advancing CA (°)	Receding CA (°)	Sliding Angle (°)
Water (distilled)	161.3	157	4
Kerosene	wets	wets	—
Gasoline	wets	wets	—
Ethyl Alcohol	84.5	68.9	25
Isopropyl Alcohol	wets	wets	—
Oil (10W30)	81.4	50	25
Naptha	wets	wets	—
Ethylene Glycol 50%	144.2	134.3	25

Laser processing techniques offer the possibility of creating surface roughness to achieve superhydrophobic surfaces. Ta et al.[29] conducted a study where they investigated various direct laser processing conditions and parameters for enhancing the superhydrophobic properties of metals, successfully achieving contact angles exceeding 150°. Mulroney et al.[30] employed a different approach, microtexturing aluminum using a nanosecond laser, followed by replicating the surface features onto polycarbonate through hot embossing. Subsequently, they thermally cured PDMS on the microtextured polycarbonate sheet and removed it, resulting in a superhydrophobic surface with a contact angle above 150° and an impressively low roll-off angle (ROA) of less than 2°. In another research effort by Chakraborty et al.[5], superhydrophobic surfaces were created by depositing laser-ablated polymer micro/nano particles on ceramic and metallic surfaces, achieving contact angles exceeding 150° without modifying the substrate's surface. Despite the notable advancements demonstrated by these methods in attaining superhydrophobic surfaces with elevated contact angles, there is potential for achieving even greater contact angles.

Numerous methods are commonly employed to create superhydrophobic surfaces, including techniques such as spin-coating, surface etching[31], vapor-liquid sol-gel[32], electroless replacement deposition[33], chemical etching, solution-immersion processes, spray coating[34], and the laser textured mold approach[35,36,37]. Su et al.[32] introduced a highly efficient vapor-liquid sol-gel method for robust superhydrophobic surfaces on polyester textiles, utilizing tetraethyl orthosilicates and dihydroxyl-terminated polydimethylsiloxane with hydrochloric acid as a catalyst. Another method by Su et al.[33] involved depositing steel plates in a CuSO4 solution, immersing them in a V-PDMS solution, and treating them with UV light to achieve superhydrophobic steel surfaces. Esmaeilirad et al.[38] developed physically and thermally stable superhydrophobic aluminum alloy surfaces using chemical etching, creating micro-nano structures through treatments with HCl, CH_3COOH, and silanes, resulting in a maximum water contact angle of 165°. Similar techniques were applied by Chu and Wu[39] to achieve superhydrophobic surfaces on aluminum and copper. Xu et al.[40] utilized a solution-immersion process with ethanolic stearic acid to immerse copper foams, yielding progressively denser clusters and increased water contact angles over time. Zhao et al.[41] adopted a chemical approach involving SiO_2-coated SiC nanowires immersed in an ethanol solution of fluoro alkylsilane to create superhydrophobic surfaces. Gong et al.[42] presented a spray coating method with SiO_2 nanoparticles blended with PDMS, while Wu et al.[43] demonstrated a process replicating macro/nano-scale aluminum structures into PDMS to achieve superhydrophobic surfaces. Mulroney et al.[30] employed laser microtexturing on aluminum followed by replication on polycarbonate and thermal curing of PDMS, resulting in superhydrophobic surfaces with a contact angle above 150° and a roll-off angle below 2°. Notably, these methods, unlike laser-based approaches, involve multiple steps, and various chemicals, including acids, and may require extensive surface modifications.

The concept of achieving reversible wettability transitions is intriguing and can be realized through various external stimuli, including ultraviolet (UV) irradiation, pH fluctuations, electric fields, and heat treatments[44,45]. In an investigation carried out by Zhou et al.[46], an exceptionally responsive superhydrophobic TiO film was developed through anodic oxidation. When exposed to UV irradiation, this film demonstrated a swift shift from superhydrophobic to superhydrophilic in just 13 minutes. However, reversing this transition, from superhydrophilic to superhydrophobic, required a considerably longer duration of 100 hours when subjected to heating at 60°C without UV irradiation. Wang et al.[47] introduced a method for achieving a rapid and reversible wettability transition by creating a hierarchical micro/nanostructure on brass through alternate current (AC) etching. The initial superhydrophilic state of the etched brass (EB) surface transformed into a superhydrophobic state after a 1-minute modification with stearic acid. Subsequently, when the modified EB surface was annealed at 350°C for 5 minutes, it reverted to a superhydrophilic state. However, a notable drawback of this approach is its reliance on elevated temperatures and the use of potentially hazardous chemicals. In another investigation by Zhu et al.[48], a superhydrophobic coating composed of carbon nanotubes (CNTs) and polyethylene was fabricated through a hot-pressing process, followed by silver (Ag) deposition and surface fluorination. The surface chemical composition and wettability of the coating were finely tuned through air-plasma treatment and surface fluorination. These techniques offered precise control over surface properties, enabling the reversible transition between superhydrophobicity and superhydrophilicity. Reversible wettability transitions using plasma were also demonstrated by Wang et al.[49] and Majhy et al.[50]. Nonetheless, it's worth noting that this process is relatively complex, involving multiple steps and the utilization of various chemicals.

In recent research, there has been a growing focus on achieving superhydrophilicity and reversible wettability using laser-based surface modification techniques. For instance, Li et al.[51] developed a micro/nanoscale hierarchical structure with superhydrophobic properties on brass surfaces through laser ablation and subsequent heat treatment, showcasing the ability to transition between superhydrophobic and superhydrophilic states within a relatively short timeframe of 4 hours, involving a series of heating and reheating cycles. Similarly, Yalishev et al.[52] and Long et al.[53] found that superhydrophilic metal samples created via laser microtexturing could be transformed into superhydrophobic surfaces by subjecting them to vacuum or organic compound environments and subsequently reversed through a 300 °C heating process. However, these methods are somewhat time-consuming and may require specific storage conditions or elevated temperatures. Notably, although these studies reported the attainment of superhydrophilic surfaces following laser microtexturing, the precise quantification of superhydrophilic contact angles showed gradual increases over several days, and the reported contact angles for superhydrophobicity remained below 165°.

2.3 Effect of Surface Microtexturing on Adhesion

Enhancing the adhesion strength between thermally sprayed metallic coatings and substrates is crucial for improving the performance of these coatings. The preparation of substrates before thermal spraying typically involves two key steps: cleaning and roughening. Surface cleaning, often involving the use of chemicals to remove contaminants and grease, is followed by a roughening process achieved through grit blasting or laser treatment.

Laser treatment offers precise control over surface microtexturing and can be optimized by adjusting parameters such as laser wavelength, spot size, scanning rate, pulse duration, and pulse

frequency to enhance adhesion. However, achieving strong adhesion is critical, as low adhesion strength can pose significant challenges for thermally sprayed coatings.

The formation of nanosecond laser-induced microtextures on surfaces can be attributed to localized surface melting, ablation, and the generation of superheated droplets over the solid surface. Importantly, laser pulse energy density and frequency play a significant role in determining the shape and height of these surface features. Increasing laser fluence and frequency leads to the expulsion of more molten material, resulting in wider grooves and increased height of the resolidified microtextures. Fine-tuning laser parameters allows for control over microtexture formation, which in turn influences the bonding strength of thermal spray coatings. Laser surface microtexturing enhances the bond strength of thermally sprayed coatings by creating a mechanically interlocked bond between the substrate and the coating. Metallic powder particles from the thermal spray process effectively fill the pores on the laser-microtextured surface, establishing a robust bond between the surface and the coating. The nature of this bond falls into five categories: embedding, anchoring, holding-on, spreading, and a mixture of these styles, depending on the material. Both mechanical and physicochemical bonds may exist, with the bonding mechanism influenced by factors such as particle-substrate contact time, contact temperature, and contact area upon impact. It's important to note that adhesion strength not only depends on the contact area ratio and feature density but also varies with microtexture shape and pattern.

Among the commonly used metals for thermal spray processes, aluminum, and its alloys are notable for their high surface energy and resistance to corrosion, making them ideal for various industries. Aluminum alloys are favored for their formability and high strength-to-weight ratio.

The focus of this thesis, in part, is on laser microtexturing of the aluminum alloy Al-7075 and Inconel steel to improve the adhesion strength of thermal spray coatings[1].

Extensive research has been conducted on enhancing the adhesion strength of thermally sprayed coatings on aluminum alloys with surface microtextures. Notable studies in this field include the work of Wong et al.[54] and Sharma et al.[55], who investigated the improvement of adhesive bonding in aluminum alloys through surface microtexturing. In their experiments, substrates were prepared by employing three different grit-blasting techniques, followed by the deposition of coatings using the thermal spray process. Notably, the grit-blasted samples exhibited significantly higher adhesion strength when compared to untextured samples. Kromer et al.[56] conducted research focused on measuring the tensile adhesion strength of NiAl powder coatings on Al 2017 substrates, which find widespread use in aircraft structural applications. In this study, NiAl powder with a mean particle size of 67 µm was thermally sprayed onto laser-textured aluminum alloy substrates. The adhesion test results indicated that a decrease in the density of holes on the metal surface led to a reduction in the adhesion strength of the thermally sprayed coating. The maximum reported adhesion strength achieved in this study was 52 MPa. Kromer et al.[57] also explored the adhesion strength of thermal spray coatings, this time on grit-blasted and laser-microtextured aluminum alloy surfaces. Additionally, Kromer et al.[58] conducted a separate study in which aluminum 2017 alloy samples were both laser microtextured and grit-blasted and subsequently coated with NiAl powder (Amdry 956) using thermal spray. These samples underwent microtexturing via a pulsed laser. Kromer et al.[58] also investigated the bond strength of bond coats on a laser microtextured superalloy substrate. The maximum reported adhesive bond strength in these studies was 33 Mpa. In a recent study by Zhang et al.[59], a nanosecond pulsed laser was employed to induce microtextures on the surface of aluminum alloy. This laser-induced microtexture effectively

improved the bond strength of an Al-Cu aluminum alloy coating applied via the cold-spray process. The maximum reported bond strength achieved in this study was approximately 48 Mpa. Nevertheless, there remains a need for further advancements in enhancing the adhesion strength of thermal spray coatings on aluminum alloys to ensure their durability and reliable performance, especially for extended operational periods.

Inconel 718 is another commonly used metal alloy in thermal spray processes, known for its excellent corrosion resistance and high tensile and creep-rupture properties. It contains nickel, chromium, and molybdenum, and the addition of niobium allows for age hardening, annealing, and welding without spontaneous hardening during heating and cooling cycles. This alloy finds extensive applications in various industries, including aerospace, chemical and marine engineering, and nuclear reactors. Despite its exceptional thermal properties and corrosion resistance, there is room for further improvement of its surface properties, particularly for tribological applications. Laser surface treatment is a viable method for enhancing these properties, offering advantages such as precision, short processing times, localized heating, and cost-effectiveness. However, it's crucial to address the challenges associated with high-temperature thermal processing during laser treatment, as it can lead to issues like thermal erosion and surface imperfections such as micro-cracks and cavities. Proper process optimization and selection of laser parameters can mitigate these defects and yield high-quality end products with the desired surface characteristics[60].

Considerable research efforts have been dedicated to exploring the laser microtexturing of Inconel alloy surfaces, with a primary focus on assessing microstructural changes and their impact on mechanical properties. Zhu et al.[61] examined the influence of processing parameters on the microstructure of laser-solid-formed Inconel 718 superalloy, finding that the selection of laser

power and beam diameter dictated whether fine or coarse columnar dendritic microstructures formed in the IN718 superalloy. In a separate study, Kulka et al.[62] scrutinized the microstructure and properties of laser-treated Inconel alloy, identifying three distinct regions within the re-melted zone. These regions included a compact borides zone rich in nickel, chromium, and iron borides (located near the surface), a zone exhibiting an elevated percentage of Ni-Cr-Fe matrix (situated farther from the surface), and a zone where the Ni-Cr-Fe matrix dominated (found at the layer's end). Notably, their investigation revealed that the obtained hardness was comparable to that achieved through diffusion boriding. Lastly, Xu et al.[63] delved into the creep behavior of laser-processed Inconel 718, unveiling significant improvements in microstructure and creep resistance resulting from laser treatment. Enhancements in mechanical properties and the formation of an improved microstructure due to laser treatment contribute to enhanced bonding of the thermally sprayed micro powder.

CHAPTER 3: Mechanism of Laser Microtexture Formation and its Influence on Adhesion and Wetting Properties

The formation of surface features through the melting, ablation, and resolidification of materials is directly affected by various laser parameters, including fluence, pulse width, speed, and frequency. Higher laser frequencies result in a greater number of pulses per unit surface area, leading to the creation of deeper surface features, increased surface area, and, consequently, enhanced coating adhesion. The depth and density of these features can be precisely controlled by adjusting the laser fluence and frequency, while higher laser power levels result in more material ablation, leading to the generation of additional particles. These particles can settle and resolidify on the surface, augmenting nanoscale roughness and further improving coating adhesion. It is crucial to select an optimal feature height to ensure the stability of the microtexture during atmospheric plasma spray (APS) processing, which is a widely used process to coat surfaces.

The formation mechanism of pulsed laser-induced micropillars can be attributed to the initial development of ripple-like structures. This formation process is influenced by several factors, including interference between incident and scattered laser light at the surface, heat-mass transfer, and hydrodynamic and plasmonic effects. As the microstructure evolves, these ripples gradually break down, giving rise to the formation of micropillars. The breakdown of ripples is primarily driven by the expansion and sputtering of molten material due to the recoil pressure resulting from the laser-material interaction. Once expelled, the molten material rapidly cools upon leaving the laser-irradiated area. As the surface temperature drops below the vaporization point at the end of the laser pulse, the effect of recoil pressure diminishes. Ultimately, gravitational forces and surface tension guide the molten material back to settle on the surface[1].

In the interaction between a pulsed laser and solid metal, a portion of laser energy is reflected from the top surface, while some is absorbed within a shallow penetration depth in the metal. Two mechanisms govern laser energy absorption: the resonance absorption mechanism and the inverse Bremsstrahlung (IB) absorption mechanism, with the latter dominating interactions between nanosecond lasers and metals. Metals, rich in free electrons, absorb photon energy through the IB mechanism, transferred to lattices and free electrons via collisions. If absorbed electron energy surpasses the Fermi energy, electrons can escape, forming a plasma and electromagnetic field. The electron–photon relaxation time is much shorter than the nanosecond laser heating pulse width, achieving heat equilibrium between electrons and lattice[64].

During laser–metal interactions, electromagnetic waves are generated on the target surface. These waves, described by Maxwell's equations, propagate through metals in the laser–metal interaction area. Laser energy penetrates the metal surface in proportion to (1-R), where R is the reflectivity. Absorbed energy decays within the material based on the absorption coefficient α. According to the Beer–Lambert law, intensity (I) exponentially decays with depth (z),

$$I(z) = (1 - R)I_0 e^{\alpha z} \tag{6}$$

where I_0 is the surface intensity, $\alpha = 4\pi k/\lambda_0$ is the absorption coefficient, k is the extinction coefficient, and λ_0 is the wavelength[64].

The process of metal melting and resolidification occurs when the fluence of laser light surpasses the melting threshold of long laser pulses (figure 8). In the interaction between nanosecond lasers and target materials, the laser pulse duration exceeds the electron cooling rate, which is approximately 1 ps. Excited electrons, with sufficient collision time, transfer their energy to the lattices. The absorbed laser energy initially raises the target surface to the metal fusion point and

subsequently to the vaporization temperature. It's noteworthy that metals require more energy for vaporization than for melting. The material vapor emanates from the target approximately 3 to 5 ns after laser interaction, exhibiting planar expansion until 10–15 ns. Between 100 and 200 ns, the vapor plume visibly separates from the target surface, indicating an upper limit for the maximum evaporation time. Throughout the interaction, the primary source of energy loss is the melting and evaporation of metal materials[64].

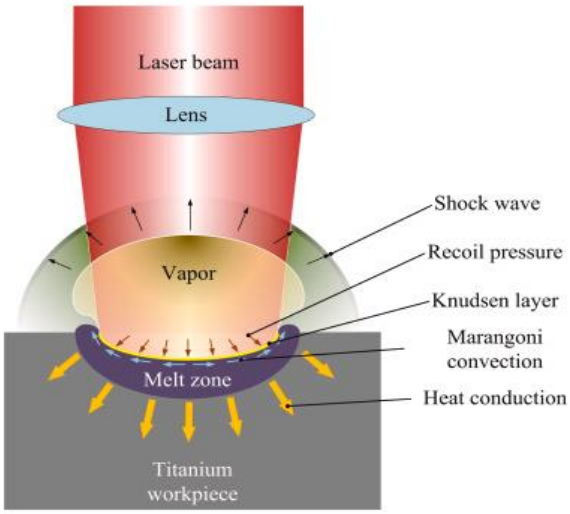

Fig. 8. Physical phenomena under nanosecond pulsed laser irradiation.

It's important to emphasize that across various laser microtextured and even grit-blasted surfaces, the adhesion strength of commonly used protective metallic powders, such as Amdry 9951 (CoNiCrAlY) powder, consistently exceeds that of Amdry 995C (CoNiCrAlY) powder. This superiority can be attributed to the significantly smaller mean particle size of Amdry 9951 powder in comparison to Amdry 995C powder. This size difference facilitates enhanced infiltration of molten particles into the laser-generated microtexture, resulting in increased tensile adhesive strength. Achieving optimal coating-substrate adhesion necessitates aligning the powder size with the surface topography to attain a superior surface-filling ratio.

In contrast to grit-blasting, which primarily offers macroscale roughness, a fully laser microtextured approach, where the entire substrate surface is microtextured, provides superior control over the depth, uniformity, and precise location of the microscale features.. At the same time, the maximum adhesion strength reported in scientific literature for thermally sprayed Amdry 9951 (CoNiCrAlY) bond coats on laser microtextured surfaces is approximately 52 MPa, on par with measured grit-blasted samples at around 55 MPa. The utilization of the fully microtextured laser method has generated an impressive adhesion strength of 65 MPa for bond coats on laser microtextured samples. This represents a notable increase of approximately 17%[1].

In polymers, energy absorption follows a non-linear pattern compared to metals. The ablation process hinges on how laser beam's energy is absorbed by a material's top layer or substrate. Ablation encompasses both vaporization and melt ejection from the focal area. When the laser beam's energy is below the ionization potential of polymer-bound valence electrons, vaporization doesn't occur. However, impurities or inclusions, acting as sources of free electrons, can facilitate energy absorption through inverse bremsstrahlung when exposed to energetic photons in the laser beam. This process breaks chemical bonds, generating heat, particularly with long laser pulses. This energy absorption aligns with the Beer-Lambert law, where absorbed energy depends on laser light intensity and material thickness[2].

Photoionization initiates laser-induced material breakdown. Valence electrons absorb sufficient energy from laser photons during photoionization, moving to the conduction band and generating free electrons through multiphoton or impact ionization. Subsequent collisions of energized free electrons lead to the emission of secondary electrons via inverse bremsstrahlung absorption, causing an avalanche increase in free electron numbers. This cascade eventually results in material removal through melting or vaporization, especially with infrared (IR) radiation. In contrast,

ultraviolet (UV) radiation can ionize and decompose polymers with minimal melting, making it a preferred option for ablation with laser surface treatment[2].

Laser surface microtexturing represents an effective technique for altering the contact angle properties of material surfaces. The contact angle, a crucial parameter for assessing surface wettability, holds significant importance across various engineering and industrial domains. Surfaces exhibiting hydrophilic characteristics with small contact angles are favored for applications aiming to enhance anti-fogging and adhesive properties. Conversely, hydrophobic or superhydrophobic surfaces, boasting contact angles exceeding 150° find utility in enhancing self-cleaning, corrosion resistance, and bacterial repellence[7].

Figure 9 illustrates the change in the contact angle of the microtextured surface in relation to laser energy intensity on the aluminum substrate. Initially, the contact angle of the specimen prior to laser microtexturing was 63°. Consequently, it is evident that at an intensity of 0.39 GW/cm^2, the contact angle increased by approximately 30% to reach 86.4°. This shift in contact angle aligns with the Cassie-Baxter model, which can be expressed as follows:

$$\cos\theta_{CB} = f_1 cos\theta_r - f_2 \quad (7)$$

where θ_r is the contact angle of the reference surface, f_1 is the area fraction of the water-solid surface, f_2 is the area fraction of the water-air surface, and θ_{CB} is the contact angle of the Cassie-Baxter model[7].

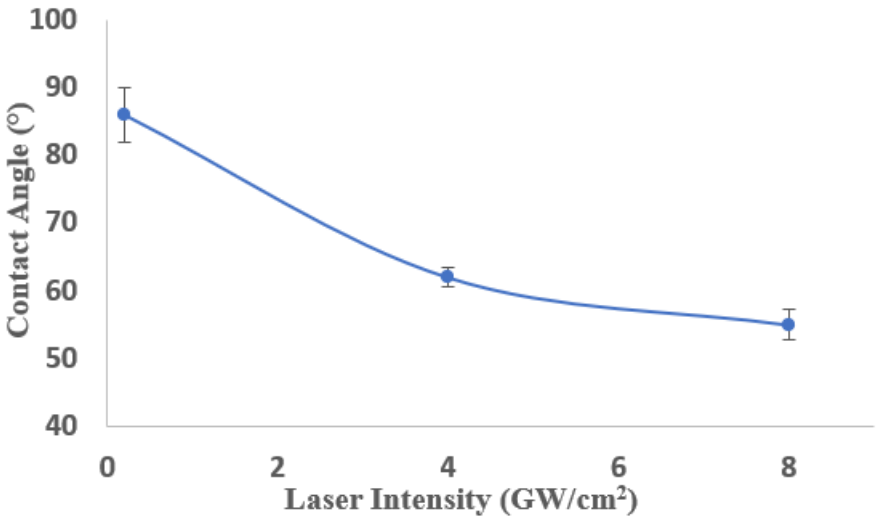

Fig. 9: Variation of contact angle with laser intensity[7]. *This figure is reprinted from the Journal of Manufacturing Process, Seung Jai Won, Hong Seok Kim, Effetc of laser parameters on morphological change and surface properties of aluminum alloy in masked laser surface texturing, Recent progresses and applications in laser-based surface texturing systems,* 48 *260-269, copyright 2019, with permission from Elsevier.*

In accordance with eq. (8), the contact angle is determined by the ratio of f_1 to f_2. In the context of this study, the surface irregularity increased following laser microtexturing. Consequently, it can be inferred that the contact angle increases due to a reduction in the contact area f_1 between the surface and water, coupled with an increase in the contact area f_2 between air and water. The decrease in the contact angle with higher laser intensity was associated with heightened surface heterogeneity. As surface heterogeneity increased, it became more challenging to maintain water droplets in the Cassie-Baxter state, causing them to flow into the surface valleys. This, in turn, reduced the contact between water and air, resulting in a decreased contact angle. Notably, at a laser intensity of 7.8 GW/cm^2, the surface state can be explained using Wenzel's theory because the contact angle was more hydrophilic than the contact angle of the specimen before microtexturing. Wenzel's contact angle theory can be expressed using the following equation:

$$\cos\theta_W = f\cos\theta_r \tag{8}$$

where θ_r is the contact angle of the flat reference surface, f is the ratio between the actual area and the apparent area, and θ_W is the contact angle from the Wenzel model. Equation 9 illustrates that as the value of *f* increases, the hydrophilic surface exhibits a heightened level of hydrophilicity. The observed change in the contact angle in Figure 9 may also be attributed to alterations in surface roughness. Specifically, as surface roughness increased, the contact angle tended to decrease[7].

Figure 10 illustrates the variation in the contact angle resulting from repetitive laser irradiation. As the number of laser irradiations increased, there was a tendency for the contact angle to decrease. This is because the surface roughness increases with laser pulses. Consequently, this diminished the contact between water and air, leading to a decrease in the contact angle, in accordance with the Cassie-Baxter theory[7].

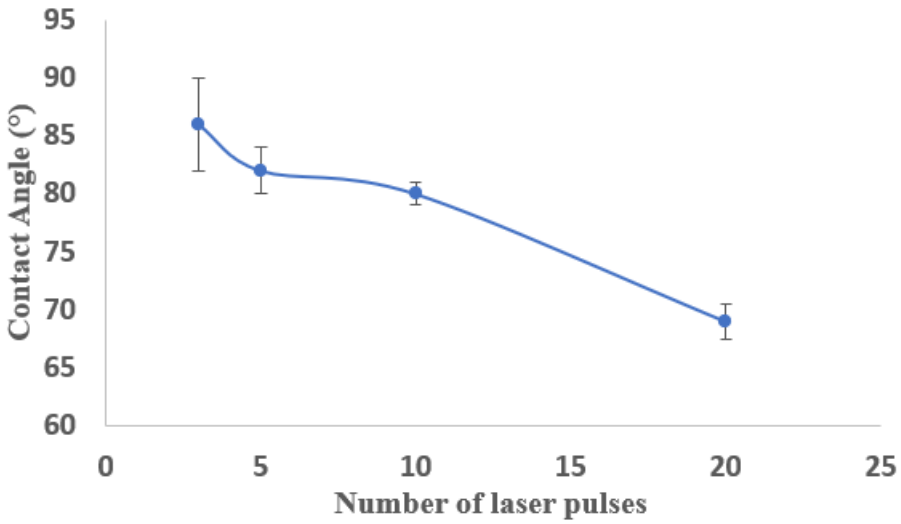

Fig. 10: Variation of contact angle with number of pulses[7]. *This figure is reprinted from the Journal of Manufacturing Process, Seung Jai Won, Hong Seok Kim, Effetc of laser parameters on morphological change and surface properties of aluminum alloy in masked laser surface texturing, Recent progresses and applications in laser-based surface texturing systems,* 48 *260-269, copyright 2019, with permission from Elsevier.*

In conclusion, the contact angle of the surface-treated specimen appears to be strongly influenced by both surface roughness and the geometric characteristics of the pattern. For instance, Kam et al.[65] demonstrated that by creating a conical surface structure using a laser, the contact angle could

be adjusted within a wide range, from super-hydrophilic (0°) to hydrophobic (113°), depending on the processing conditions. It is anticipated that by finely tuning the shape of micro-patterns, a diverse range of wettable surfaces can be effectively generated. The tightly packed and evenly distributed surface features, coupled with the addition of nanoscale roughness, have a vital role in controlling the surface's wettability characteristics. The hierarchical surface structures created through laser microtexturing substantially enhance surface wettability, leading to a notable reduction in the contact angle (CA) within the Wenzel region[66]. On the contrary, when the surface is coated with a low-surface energy material such as PDMS, these micro/nano hierarchical surface structures contribute to achieving an exceptionally high degree of water repellency[67,68,69].

Factors such as nanopillar height, pillar spacing, intrinsic contact angle, and water nanodroplet impingement velocity have a significant influence on the transition of a water droplet from the Wenzel to the Cassie-Baxter wetting state. There exists a critical pillar height that determines whether a water droplet on the pillared surface is in the Wenzel or Cassie-Baxter wetting state. The free-energy barrier between the Wenzel and Cassie-Baxter states can be computed using statistical mechanics and simulations of rain impacting the surface. This barrier varies, ranging from a few tenths of kBT_0 (where kB is the Boltzmann constant, and T_0 is the ambient temperature) for a rough surface at the critical pillar height to nearly 8 kBT_0 for surfaces with pillar heights greater than the length scale of water droplets. Importantly, the barrier for transitioning from the Wenzel to Cassie-Baxter state is much higher than that from the Cassie-Baxter to Wenzel state, particularly for very rough surface[70].

Ambrosia conducted a study that examined how the static contact angle (CA) of a water droplet on a graphite surface is influenced by factors such as surface fraction and pillar heights[71]. The study found that the static contact angle (CA) increased with increasing pillar height up to a certain

threshold. Beyond this threshold, further increases in pillar height had diminishing effects on the static CA. The influence of pillar height on the static CA was more pronounced when the pillars were shorter or when they covered a smaller fraction of the surface. When the pillar surface fraction dropped below 36%, simulations revealed that the static CA did not align with the predictions of the Cassie-Baxter model. This discrepancy was attributed to the deformation of a portion of the water droplet between the tops of the pillars[71].

CHAPTER 4: Laser Fabrication Method of Microtextured Surfaces and Morphology/Composition Characterization

4.1 Introduction

This chapter offers a comprehensive exploration of the laser systems employed for conducting various experiments within this thesis.These laser systems are instrumental in the generation of laser-induced microtextured surfaces. An extensive overview of the various laser setups employed, encompassing a range of laser types, each distinguished by its unique characteristics, has been presented in this chapter. Subsequently, this chapter delves into the characterization techniques that have been applied. These techniques serve as instrumental tools, guiding our exploration of surface morphology and offering insights into the fine details of laser microtextured features. Additionally, the characterization of the compositional alterations and optical properties that manifest during the laser microtexturing process have also been addressed in this chapter. This comprehensive comprehension of both the equipment and methodologies is fundamental in unlocking the full potential of laser microtexturing, expanding its utility across diverse scientific domains.

4.2 Laser Fabrication Method

For the adhesion improvement of thermally sprayed coatings on laser microtextured aluminum, a ytterbium fiber laser (YLP-G-10, IPG Photonics) of 532 nm wavelength, 10 W average power pulse width of 1.3 ns, pulse energy of 20.2 μJ, and Gaussian beam profile was used. The galvanometer scan head used was a SCANcube 14, SCANLAB, with a scan pattern designed in EZCad (Beijing JCZ Technology Co. Ltd). The laser repetition rate varied from 400 kHz to 600 kHz, and a focused laser beam with a full width at a half-maximum (FWHM) size of 20 μm was

used. The laser fluence used for the experiments was 0.76 J/cm^2, 0.92 J/cm^2, and 0.8 J/cm^2. These values were selected considering the necessity for laser energy to be adequate for surface melting with minimal ablation. This approach ensures that thermomechanical formation of surface features can occur, and the determined fluence values closely align with this criterion. The laser beam scan speed was maintained at 60 mm/s. For each laser fluence, the side-to-side overlap between the lines was 50%. A galvanometer (SCANLAB SCANcube 14) controlled by a custom LabVIEW program was used to perform the raster scan of the aluminum surface. This enabled us to achieve consistent microtexture patterns on the sample. A nitrogen gas atmosphere was used during laser microtexturing to prevent oxidation. The pressure of the gas was maintained at 5 MPa. The different laser parameters used in the microtexturing process are shown in Table 3.

In the case of adhesion improvement of thermally sprayed coating on laser microtextured Inconel steel, a 355 nm wavelength nanosecond pulsed laser was used to microtexture. The UV nanosecond laser was a Coherent Matrix 355-8-50, operated at 50 kHz pulse repetition rate, 8 W average power, and 4 ns pulse width. It is a diode-pumped solid-state, Q-switched laser. The focused laser beam had a full-width half-maximum (FWHM) size of 25 μm. The laser fluence used for the experiments were 1.71 J/cm^2, 2.02 J/cm^2, and 2.32 J/cm^2. These values were selected considering the necessity for laser energy to be adequate for surface melting with minimal ablation. This approach ensures that thermomechanical formation of surface features can occur, and the determined fluence values closely align with this criterion. The laser beam scan speed was maintained at 60 mm/s. For each of the laser fluences, the side-to-side overlap between the lines was 50%. Two scans were done orthogonally to each other at each of the parameter settings. Orthogonal laser scans play a pivotal role in achieving a denser surface microtexture. By employing laser scanning in orthogonal directions, the laser beam covers a given area more

comprehensively and uniformly. This meticulous and overlapping scanning strategy ensures that each point on the surface receives two passes of laser treatment from different directions. As a result, any irregularities or gaps in the microtexture are significantly minimized or eliminated, leading to a denser and more homogenous microtexture. The precision and control offered by orthogonal laser scans enhance the surface's functional properties, making it particularly beneficial in applications where a uniform and finely microtextured surface is crucial, such as in the development of superhydrophobic or superhydrophilic surfaces, advanced coatings, or microtextured materials used in various industries. The different laser parameters used in the microtexturing process are shown in Table 4.

The schematic of the laser setup is shown in figure 11.

Table 3: Laser processing parameters (laser wavelength = 532 nm, scan speed = 60 mm/s, No. of scans =1); Line #1, Line #2, and Line #3 indicate the use of different process parameters.

Pattern Index	**Frequency (kHz)**	**Fluence (J/cm^2)**
Line #1	400	0.76
Line #2	400	0.92
Line #3	600	0.80

Table 4: Laser processing parameters for Inconel (laser wavelength = 355 nm, scan speed = 60 mm/s); Line A, Line B, and Line C indicate the use of different process parameters.

Pattern Index	**Frequency (kHz)**	**Fluence (J/cm^2)**	**Line spacing (μm)**	**No. of scans**
Line A	50	1.71	10	2 (0° and 90°)
Line B	50	2.02	10	2 (0° and 90°)
Line C	50	2.32	10	2 (0° and 90°)

In the experiments involving the creation of superhydrophobic surfaces through laser ablation, a 355 nm wavelength nanosecond pulsed laser was used to ablate the PDMS coating made on a glass slide. The 355 nm wavelength 20 nanoseconds pulsed width laser from Coherent Matrix 355-8-50, operated at 50 kHz pulse repetition rate, at 8 W average power, was used in this study as shown

in figure S1. High Dynamics PIMag linear *XY* stages were used for mounting the samples, and the laser beam was scanned using the Sino-Galvo SG7210 system.

For the experiments involving superhydrophilic surfaces and integrated superhydrophilic-superhydrophobic surfaces, a 355 nm wavelength picosecond pulsed laser from Spectra-Physics IceFyre 355-30, operating at 1 MHz, at 30 W average power and pulse energy of 20 μJ was used. The pulse width of the picosecond laser was 10 ps. A focused laser beam of full width at a half-maximum (FWHM) size of 50 μm was used. The laser beam was scanned using the Sino-Galvo SG7210 system. High Dynamics PIMag linear *XY* stage was used for mounting the samples.

The schematic of the laser setup is shown in figure 10.

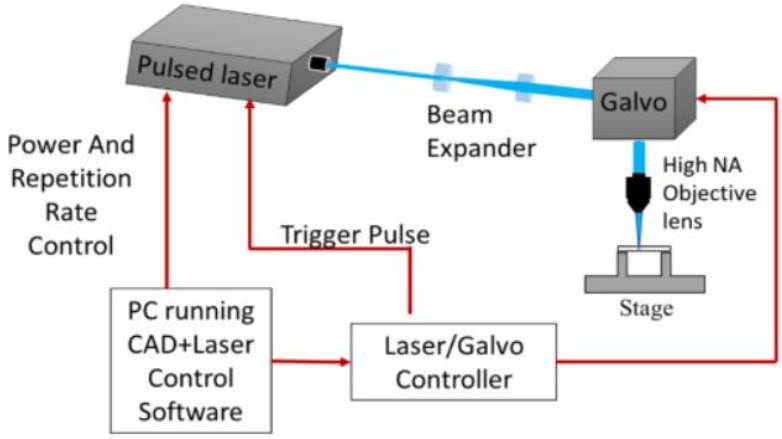

Fig. 11: Schematic of the laser fabrication method setup

4.3 Microtexture Characterization

The surface morphology, cross-sectional characterization, and elemental analysis were done using FEI Quanta 650 Field Emission SEM. 3D optical profile measurements were done using Olympus LEXT OLS4000 3D Laser Microscope to understand the variation in the microtexture heights, the peak-to-valley spacing, and the density and uniformity of the features. Chemical composition analysis was done by XPS (PHI Versaprobe III). Optical transmission measurements were

obtained using a UV-VIS-NIR spectrophotometer (Agilent CARY 5000) with a tungsten halogen visible and deuterium arc UV light source and a silicon photodiode receiver. The water contact angle measurements were done using the Ramé-Hart Model 250 Goniometer. 10 μL water droplets were used for all measurements. Optical images of the superhydrophilic patterned surface were taken using Hirox RH-8800 Light Microscope.

The optical characterization of the laser microtextured glass surface covered with PDMS was performed by transmitting light across the solar spectrum range (350-2500nm) and detecting the transmitted light using a power measurement meter (Thorlabs S302C thermal power sensor).

CHAPTER 5: Laser Microtexturing for Adhesion Improvement

5.1 Introduction

This section explores surface microtexturing techniques aimed at enhancing coating adhesion strength, with a focus on comparing two commonly used methods: grit blasting and laser processing. In particular, the study involves the application of a nanosecond pulsed laser for microtexturing Al 7075 alloy and Inconel substrates, resulting in a substantial increase in surface area. The laser-based microtexturing process encompasses melting, ablation, and resolidification of the entire substrate surface, yielding a distinctive morphology characterized by densely packed pillar-like surface features. Importantly, the morphology of this microtexture can be finely tuned by adjusting the laser processing parameters. Subsequently, the laser microtextured surface is coated with metallic particles through a thermal spray process. The tensile adhesive strength of these thermally sprayed metallic coatings is found to be remarkably higher, exceeding that of grit-blasted samples by over 17%, especially when a 5 μm deep microtexture is employed. Notably, this represents the highest reported adhesion strength achieved through laser-based microtexturing techniques for thermally sprayed bond coatings which has diverse applications in automotive, aerospace and power generation.

5.2 Experimental Approach

The substrates used were McMaster-Carr aluminum alloy (Al 7075) and Inconel alloy (INCONEL 718) micromachined samples (diameter = 1 inch; thickness – 0.5 inches) polished down to a roughness of less than 1 μm. The chemical composition by weight of Al 7075 and INCONEL 718 was supplied by the manufacturer and is given in table 5 and table 6, respectively. The coating powders used for the thermal spray process were Oerlikon Metco Amdry 995C (CoNiCrAlY) and

Oerlikon Metco Amdry 9951 (Co[Ni]CrAlY)). CoNiCrAlY is usually used for bond coats[72,73,74]. The mean particle sizes of the powders were 90 μm and 38 μm, respectively. The different particle sizes were chosen to demonstrate the effect of particle size on surface morphology.

Table 5: Al 7075 alloy composition (as obtained from the manufacturer)

Material Type	**Al 7075**
Al wt%	89.77
Zn wt%	5.4
Mg wt%	2.42
Cu wt%	1.42
Fe wt%	0.42
Cr wt%	0.21
Si wt%	0.13
Mn wt%	0.12

Table 6: INCONEL 718 alloy composition (as obtained from the manufacturer)

Material Type	**INCONEL 718**
Ni wt%	53
Cr wt%	18.2
Fe wt%	18.1
Mo wt%	2.8
Ti wt%	1.1
Co wt%	0.98
Ta wt%	0.85
Mn wt%	0.2
Si wt%	0.2

Some of the samples were prepared by grit-blasting method. In this procedure, we affixed the samples securely onto a plate using double-sided tape, ensuring their stability during the abrasive blasting process. The nozzle was systematically moved over the samples, following the specified parameters outlined in Table 7. We executed this raster scan through a dedicated LabVIEW program on a computer, controlling the nozzle's movement through a connected controller. Subsequently, compressed air was applied to clear away any remaining dust from the samples. Finally, thoroughly cleaned sample surfaces using ethanol were obtained.

Table 7: Grit-blasting parameters

Blast Media	Alumina (~50 μm particle size)
Pressure	0.28 MPa
Nozzle distance	~140 mm
Nozzle Angle	70 °
Nozzle traverse speed	1000 mm/sec
Passes	2 orthogonal passes

Both the grit-blasted and laser microtextured samples underwent a metal powder coating process using atmospheric plasma spray (APS). This procedure utilized an Oerlikon Metco F4MB-XL plasma gun affixed to a 6-axis robotic arm. The initial phase involved purging the grit-blasted and laser-microtextured samples with compressed air for cleaning purposes. Subsequently, these samples were secured onto vertical fixtures. The thermal spray gun was then activated and moved across the substrate in a defined rectangular raster pattern. Before introducing the powder, a pre-heat phase was initiated to raise the substrate's temperature to 100°C, and the powder feed was allowed to stabilize for 1-2 minutes before the deposition commenced. Table 8 outlines the various APS parameters employed throughout this study.

Table 8: Deposition parameters for a thermal spray for Amdry 9951 and 995C powders

APS Parameters	Amdry 9951	Amdry 995C
Carrier gas	Argon	Argon
Carrier gas flow rate (nlpm)	4.5	3.5
Powder feeding rate (g/min)	60.5	60.1
Spray distance (mm)	120	120
Number of passes	10	10
Surface speed (mm/s)	1250	1250
Plasma temperature (°C)	2922	2612
Particle velocity (m/s)	210	166
Gun current (A)	600	600
Primary gas type	Argon	Argon
Primary gas flow rate (nlpm)	56.8	56.9
Secondary gas type	Hydrogen	Hydrogen
Secondary gas flow rate (nlpm)	8.5	57
Injector standoff distance (mm)	6	6
Water flow rate (lpm)	15.6	15.7

5.3 Characterization

The coated samples were subjected to tensile adhesion testing, where the tensile pressure required to debond the coatings was measured. This was done following the ASTM C633 standard using an Instron C633 mechanical analyzer. As shown in figure 12, the cylindrical sample was glued between two cylindrical rods. The load was applied in the direction perpendicular to the interface between the coating and the substrate. The tensile load was gradually increased until the coating was ruptured or detached from the substrate. The glue used in the process was Polyamide-epoxy FM 1000 Adhesive Film. The adhesion strength was calculated from the load at sample failure divided by the coating area.

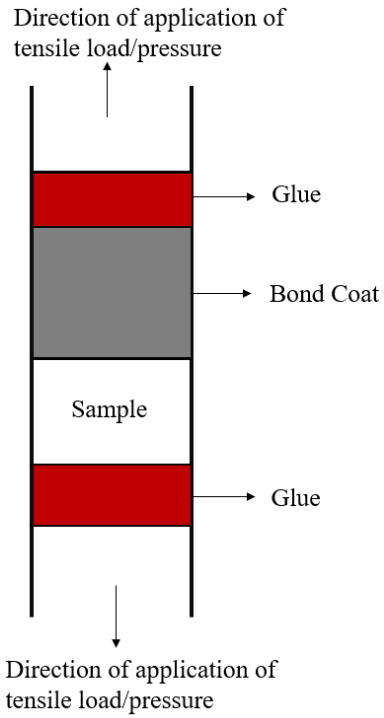

Fig. 12: Sample assembled for tensile adhesion testing; Bond Coat – Coating layer that is attached to the sample; Top Coat – Coating Layer that is attached to the glue[1].

5.4 Results and Discussion

Figure 13 serves as a reference, displaying the surface of a flat, untextured aluminum sample. In contrast, Figure 14 presents the surface of a sample that has undergone grit-blasting. In the grit-blasting process, alumina particles impact the aluminum surface with considerable velocity, resulting in plastic deformation. The extent of deformation is influenced by various factors, including the velocity, shape, size, and hardness of the alumina particles.

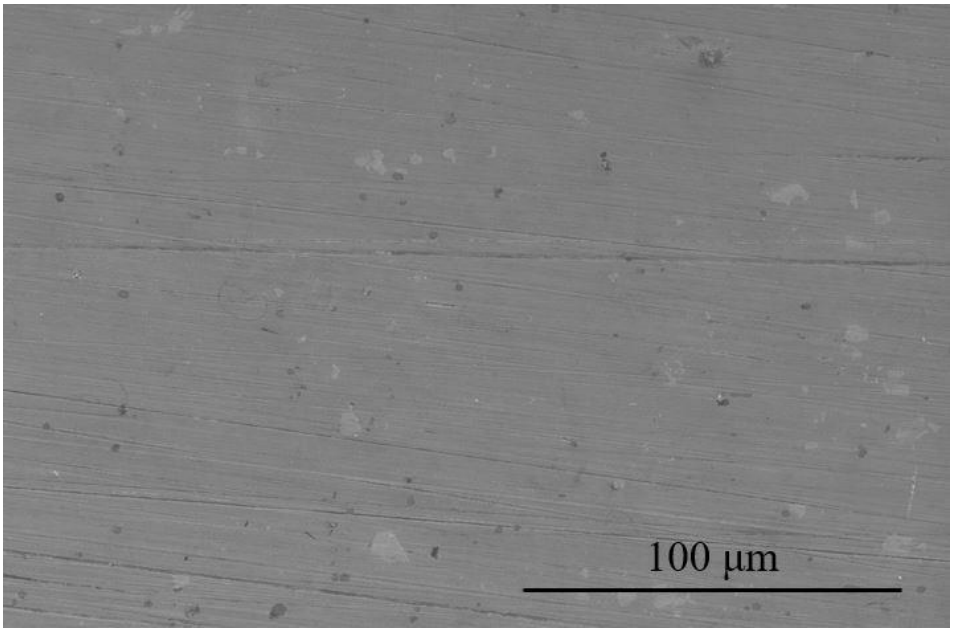

Fig. 13: SEM image of an untextured metal surface.

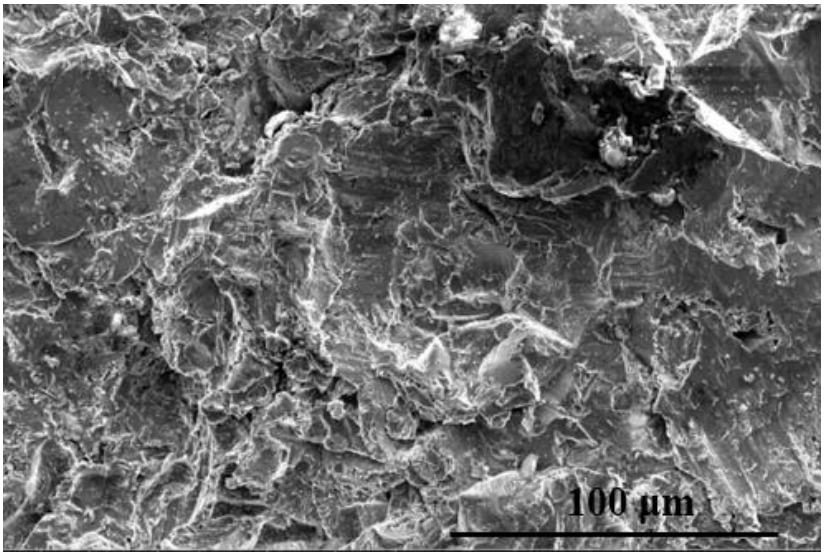

Fig. 14: SEM image of the surface of a grit-blasted sample

Figure 15 shows the variation of the surface morphology with changing laser fluences. It can be

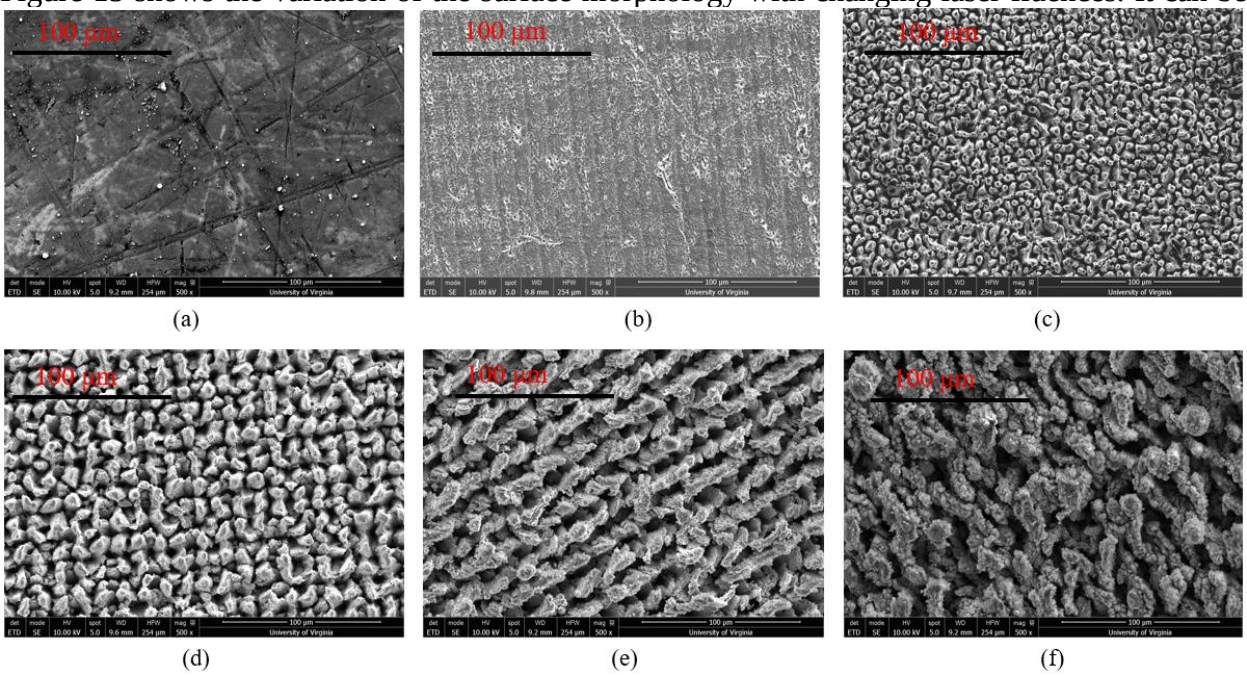

Fig. 15: (a) SEM image of untextured aluminum surface; SEM image of laser microtextured aluminum surface at a fluence of (b) 0.38 J/cm^2, (c) 0.45 J/cm^2, (d) 0.61 J/cm^2, (e) 0.76 J/cm^2, (f) 0.91 J/cm^2. The frequency and the scanning speed were kept constant at 400 kHz and 60 mm/s, respectively.

seen that at higher laser fluences, the ablation is much more significant than at lower ones. The fluence at which the laser starts to mark features on the surface is between 0.38 J/cm^2 and 0.45 J/cm^2.

Figure 16 illustrates how the surface morphology changes with varying laser repetition rates (frequencies). When maintaining a constant fluence, lower frequencies entail significantly fewer laser pulses striking the surface per second compared to higher frequencies.

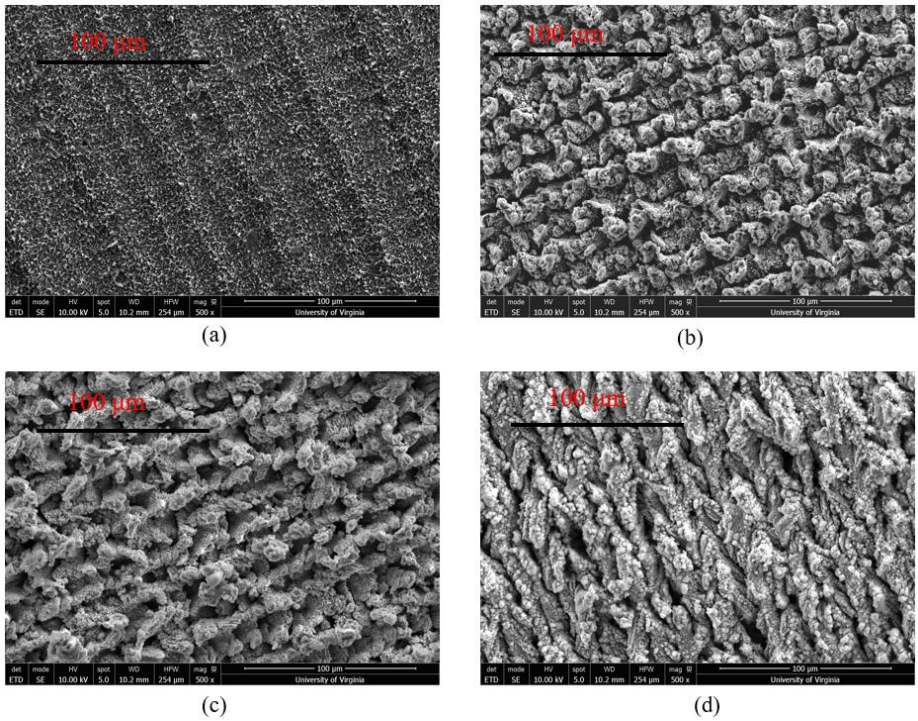

Fig. 16: SEM image of laser microtextured aluminum surface at (a) 20 kHz, (b) 200 kHz, (c) 300 kHz, (d) 600 kHz. The laser fluence and the scanning speed were kept constant at 0.916 J/cm^2 and 60 mm/s, respectively.

At higher laser frequency, consequently, there is less time for the molten surface material to cool down, leading to higher temperatures and, consequently, increased ablation. This causes the laser to rearrange the molten material differently at higher frequencies compared to lower ones. As evident, the surface exhibits more pronounced ablation and roughening at higher frequencies.

Figure 17 shows the different laser surface microtextured patterns. It can be seen that pillar-like structures have been formed on the surface with periodic grooves due to the thermomechanical process of melting and resolidification combined with some ablation. The thermally sprayed molten powders enter into the grooves and thus provide interlocking. The surface shown in figure 16(c) was obtained with the highest number of pulses per unit area compared to the other two surfaces. The three laser microtextured patterns were chosen in such a way that they provide a range of variations in feature height and spacing between the peaks. Looking at the morphology,

some resolidified droplet formation appears to occur, which further reinforces the process of melting, ablation, and resolidification of the material. On the other hand, the surface features reported by Kromer et al.[58,57,56] consist of a series of uniform holes drilled on the aluminum surface by laser ablation. Since the spacing between these holes was greater than 100 μm, the increase in the surface area was much less than that obtained by the full-area microtexturing method reported in this thesis.

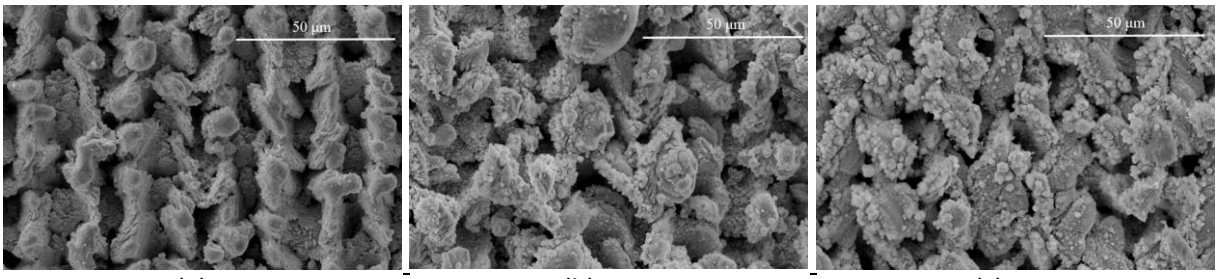

(a) (b) (c)

Fig. 17: (a) SEM image of laser microtextured (0.763 J/cm^2, 60 mm/s, 400 kHz) aluminum sample; (b) SEM image of laser textured (0.916 J/cm^2, 60 mm/s, 400 kHz) aluminum sample; (c) SEM image of laser microtextured (0.803 J/cm^2, 60 mm/s, 600 kHz) aluminum sample

Figure 18 quantifies the micropillar height variations. The average height for the laser microtextured features was around 5 μm, which is less than the average surface feature height of 6.5 μm for grit-blasted surfaces. There are considerable height variations on the laser microtextured and grit-blasted samples, with maximum heights reaching up to 27 μm, 28.2 μm, 41.6 μm, and 61.48 μm for line #1, line #2, line #3, and line #4 respectively. The average distance between the peaks in all the laser microtextured patterns was 5 μm. Compared to this, the depth of the laser-ablated holes on the aluminum surface reported by Kromer et al. [58,57,56] is 25-80 μm. Even though a larger hole depth results in a larger increase in surface area, it takes more time and does not necessarily imply full infiltration by the thermally sprayed coating.

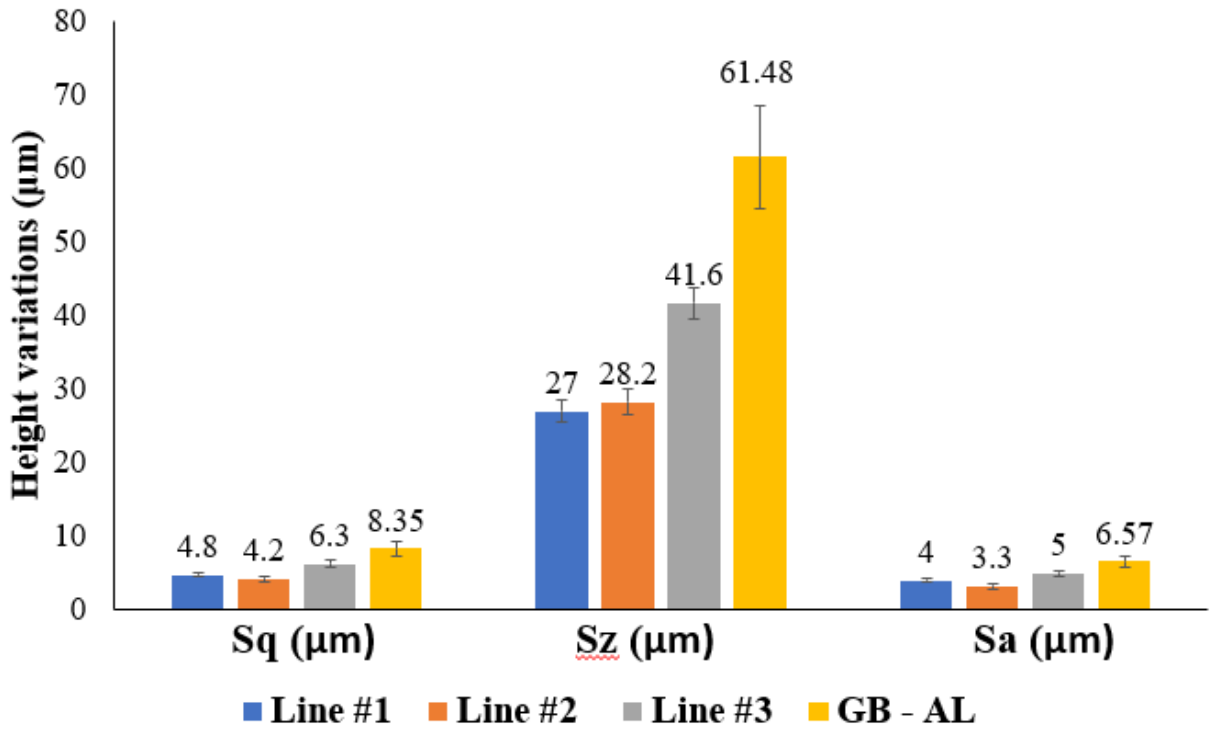

Fig. 18: Feature height variations on Aluminum substrate. Line #1 – 0.763 J/cm^2, 60 mm/s, 400 kHz; Line #2 – 0.916 J/cm^2, 60 mm/s, 400 kHz; Line #3 – 0.803 J/cm^2, 60 mm/s, 600 kHz; GB – Grit-blasted. Sq: RMS roughness; Sz: Max peak to Max valley distance; Sa: Average roughness; The line # denotes the different laser parameters used.

Figure 19 shows the surface morphology variation of a grit-blasted aluminum sample. It can be observed that there is no periodicity in the features formed on the surface as the grits impact the surface in a randomized manner. Figures 20, 21, and 22 offer a detailed surface profile analysis for the three laser microtexture patterns shown in figure 17. The 2D map visually highlights variations in feature height and density across the surface, while the 3D map provides a more comprehensive visualization of feature distribution. It's evident that Line #2 exhibits taller peaks compared to Line #1, and Line #3 surpasses both Line #1 and Line #2 in peak height. This discrepancy can be attributed to the fact that Line #3 received the highest number of laser pulses per unit area, while Line #2 had a higher laser fluence than Line #1. Given that the scan speed remained constant, both laser frequency and fluence emerged as pivotal factors governing peak

height on the surface. These two parameters are closely interrelated in controlling the micropillar height.

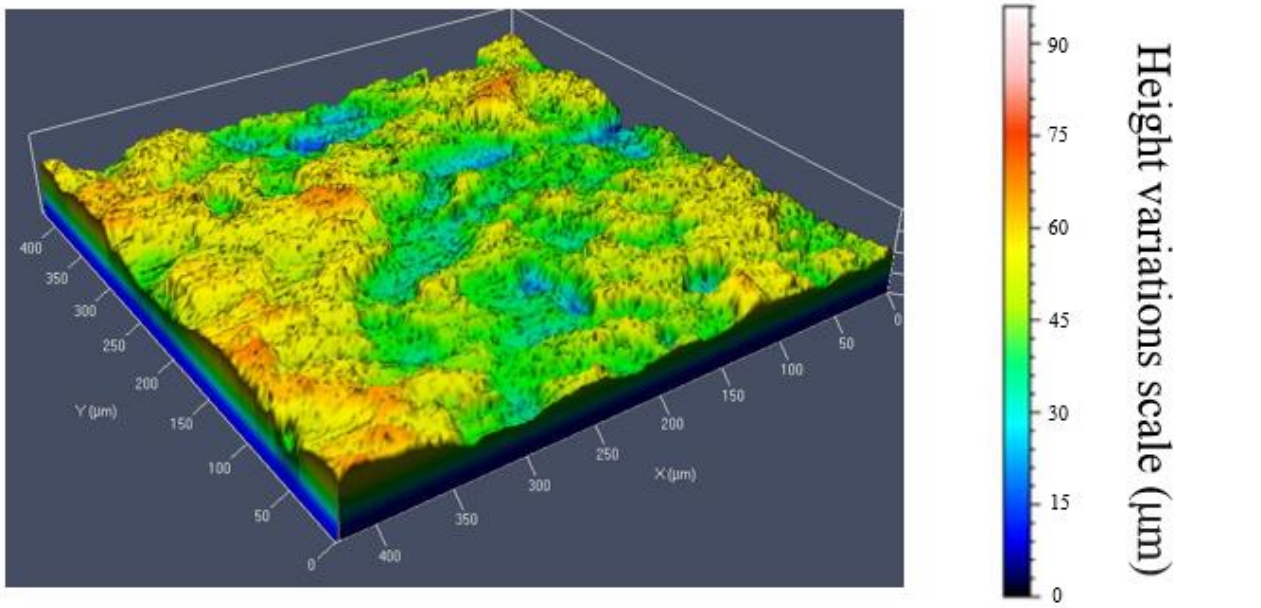

Fig. 19: 3D surface profile of a grit-blasted sample.

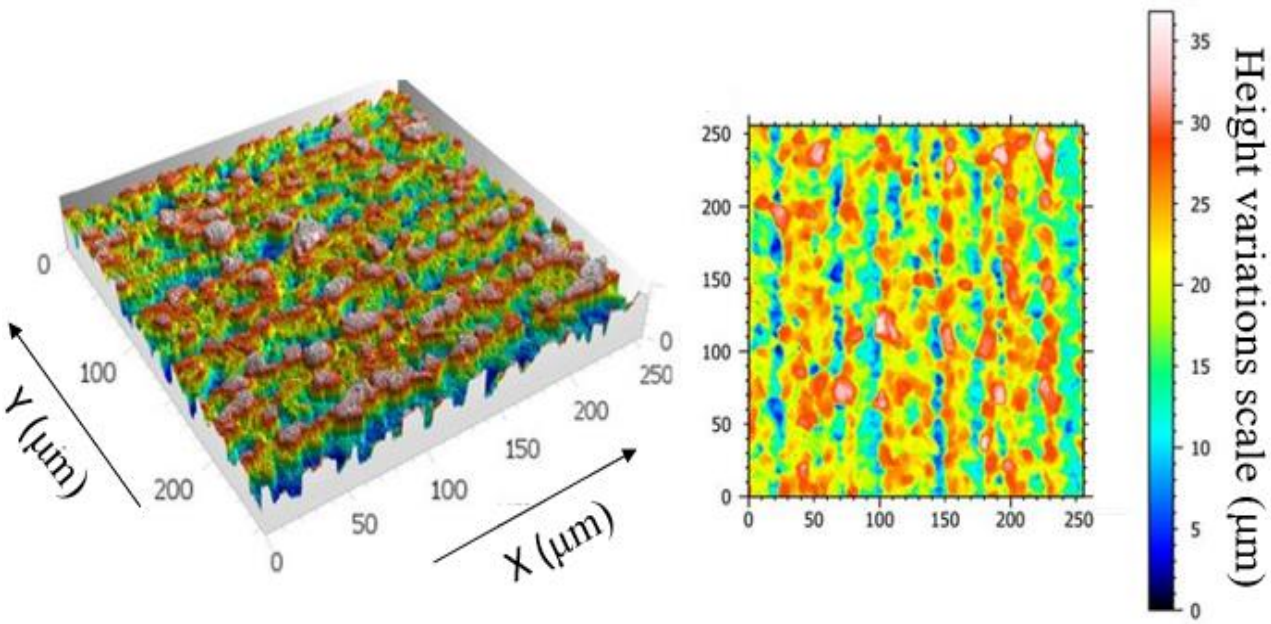

Fig. 20: (a) 3D surface profile of Line #1; (b) 2D surface profile of Line #1; Axes scales are in microns.

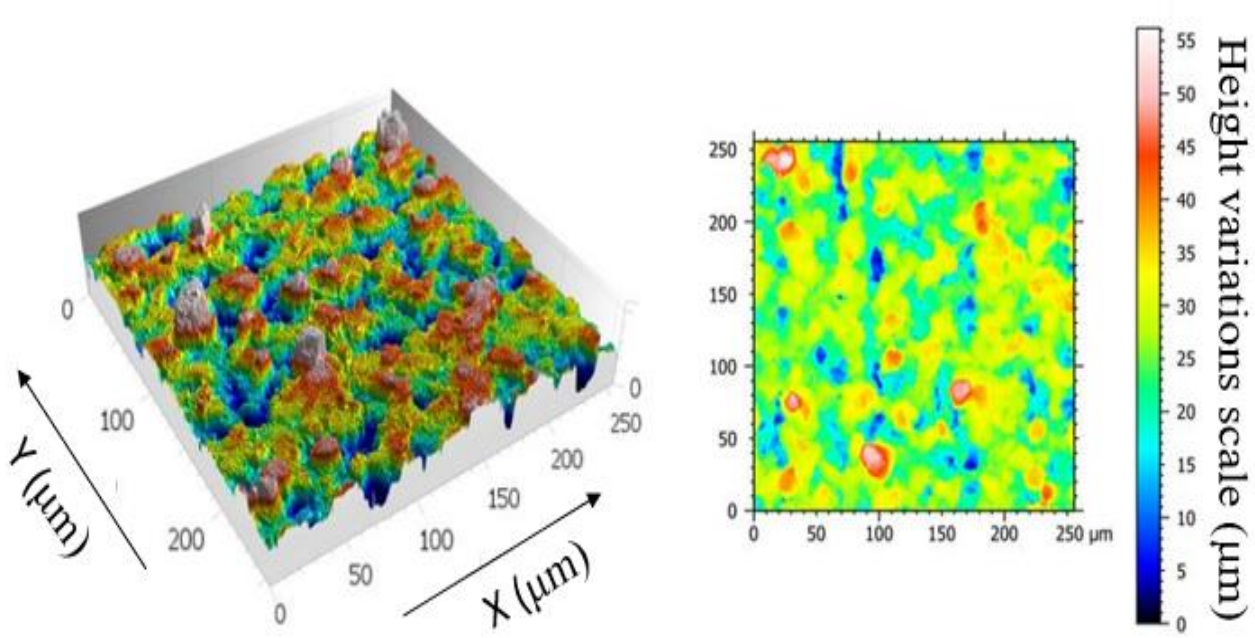

Fig. 21: (a) 3D surface profile of Line #2; (b) 2D surface profile of Line #2; Axes scales are in microns.

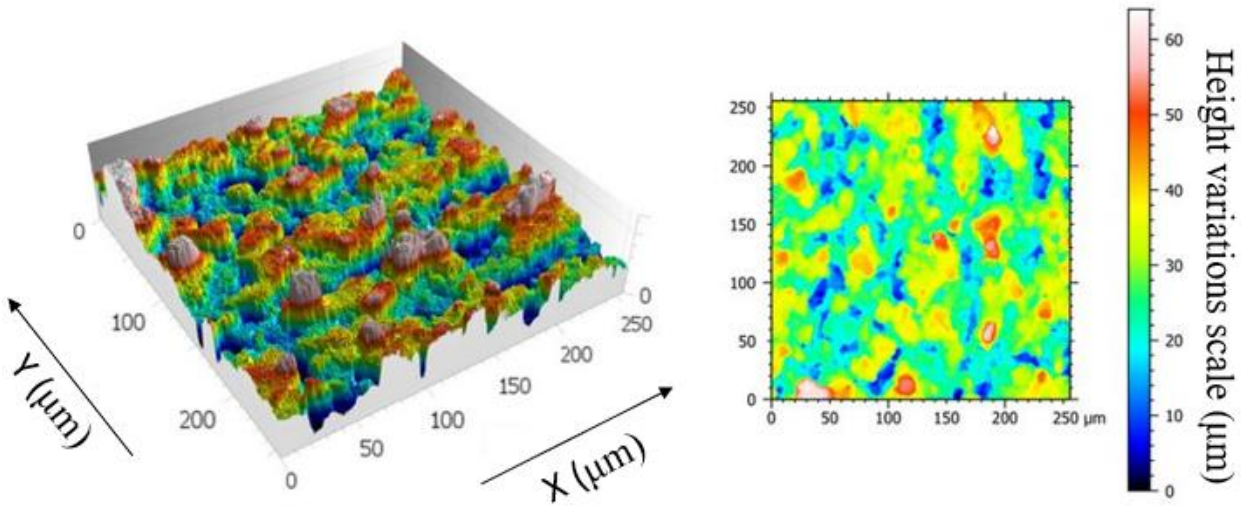

Fig. 22: (a) 3D surface profile of Line #3; (b) 2D surface profile of Line #3; Axes scales are in microns.

Figure 23 shows the surface of the laser microtextured Inconel. Line C had the highest average peak height compared to line B and line C as it was microtextured with the highest fluence. The three laser microtextured patterns for both metals were chosen in such a way that they capture a

range of variations in feature height and spacing between the peaks. It can be seen that pillar-like structures have been formed on the surface with periodic grooves due to the thermomechanical process of melting and resolidification combined with some ablation. The thermally sprayed molten powders enter into the grooves and thus provide interlocking. Looking at the morphology, some resolidified droplet formation appears to occur, which further reinforces the process of melting, ablation, and resolidification of the material.

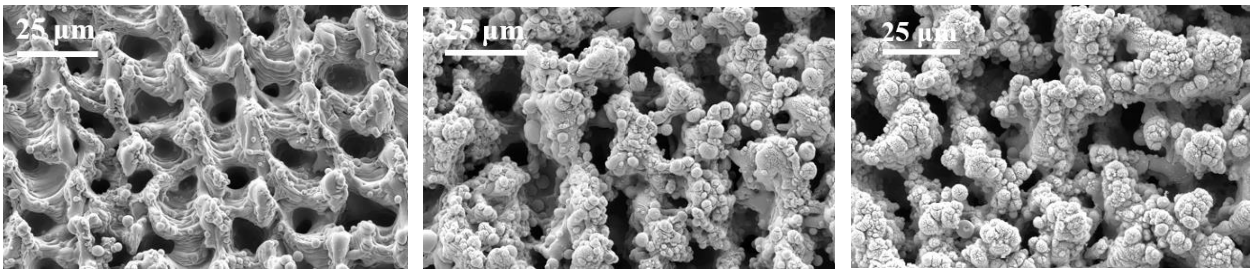

(a) (b) (c)

Fig. 23: SEM image of laser microtextured Inconel surface; (a) Lina A; (b) Line B; (c) Line C; Line A – 50 kHz, 1.71 J/cm^2, Line B – 50 kHz, 2.02 J/cm^2, Line C – 50 kHz, 2.32 J/cm^2.

Figures 24, 25, and 26 provide a detailed surface profile for the three laser microtexture patterns shown in figure 22. The 2D map shows the differences in height and density of the features across the surface, while the 3D map gives a more thorough visualization of the distribution of the features. It can also be observed that line B has higher peaks than that of line A, and line C has higher peaks than line A and line B. This can be attributed to the fact that line C had the highest fluence, and line B had more laser fluence than line A. Since the scan speed and frequency were kept constant, the fluence is the main factor controlling the height of the peaks on the surface.

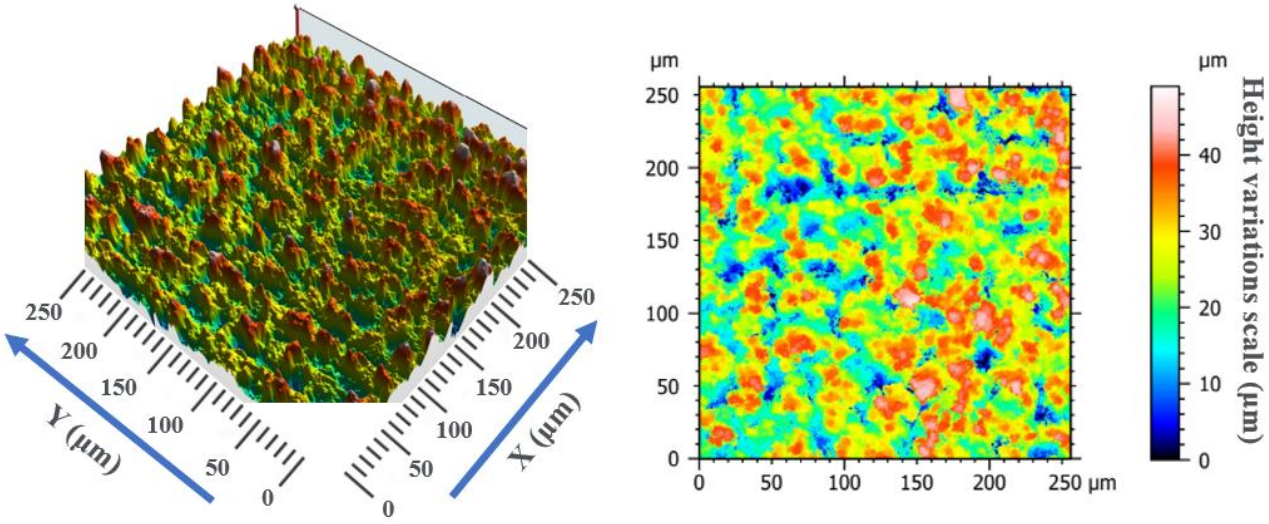

Fig. 24: (a) 3D surface profile of Line A; (b) 2D surface profile of Line A

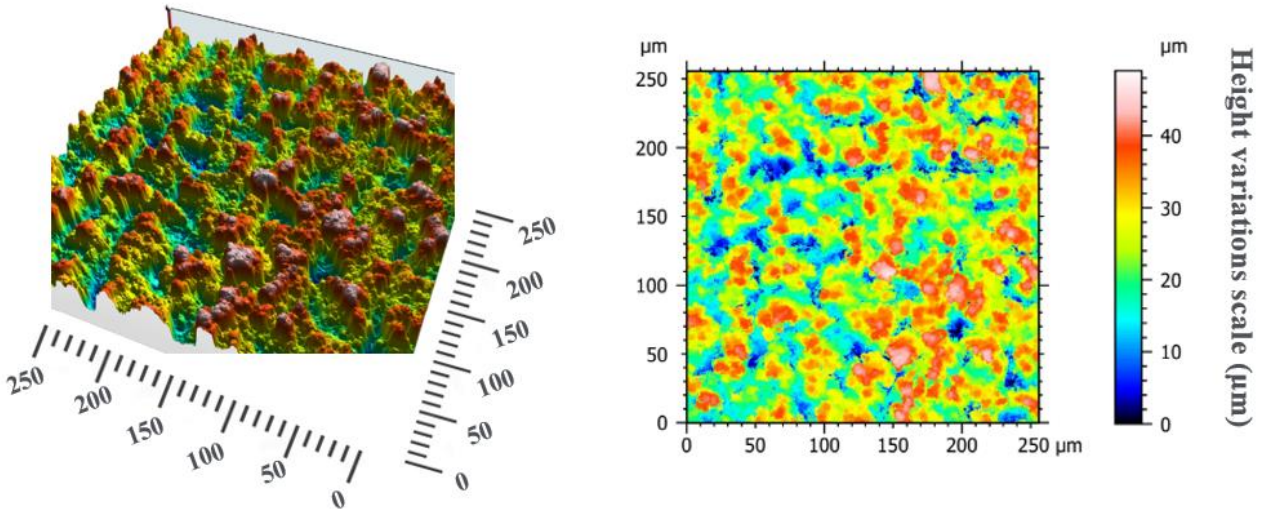

Fig. 25: (a) 3D surface profile of Line B; (b) 2D surface profile of Line B;

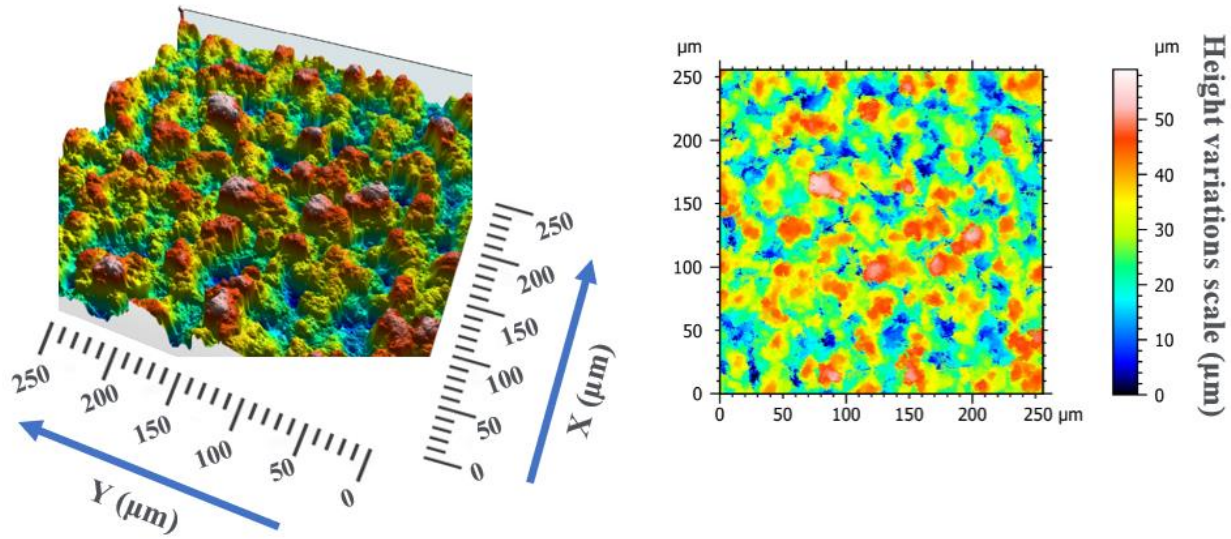

Fig. 26: (a) 3D surface profile of Line C; (b) 2D surface profile of Line C

In the case of Inconel, the average height for laser microtextured features was around 6 µm, which is less than the depth of 7.95 µm for grit-blasted Inconel surfaces. The maximum heights of the peaks for line A, line B, and line C were 35.99 µm, 49.33 µm, and 55.67 µm, respectively. Grit-blasted Inconel samples displayed a maximum height of 65.23 µm. Figure 27 quantifies the micropillar height variations.

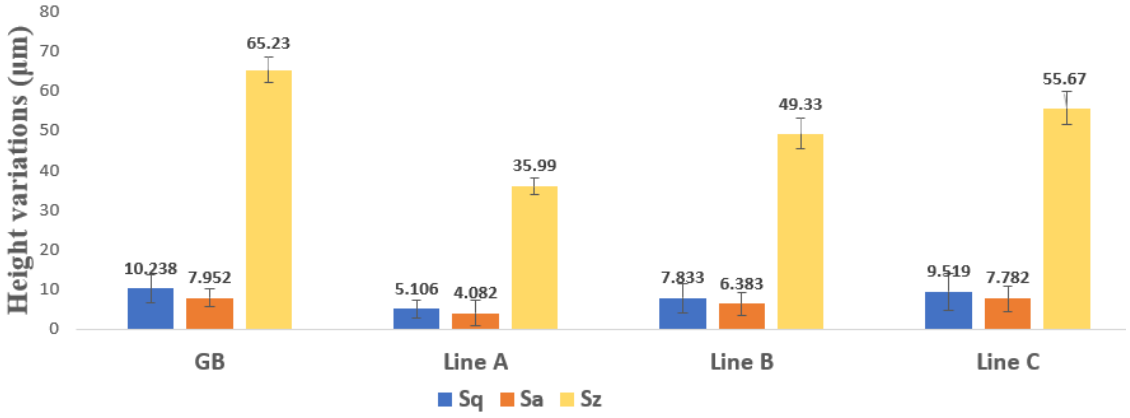

Fig. 27: Feature height variations on Inconel substrate. GB – Grit-blasted. Sq: RMS roughness; Sz: Max peak to Max valley distance; Sa: Average roughness; The line # denotes the different laser parameters used.

Significantly higher tensile adhesive strength for laser microtextured surfaces compared to those reported in previous laser microtexturing research studies[59,58,56,57,55] were obtained. Our results are shown in figures 28 and 29. Four samples were tested for each of the laser microtexturing and grit-blasting methods to obtain the adhesion data and the associated error bars. The laser microtextured patterns in our study were significantly denser and different in shape than those reported in previous literature, as the laser was used to scan the surface area of the samples in its entirety. Thus, it can be proven that densely packed features are beneficial in increasing bonding strength. The average laser-formed feature height in this work was around 5 μm compared to feature depths of 80-180 μm reported in previous laser studies[58,57]. Hence, the throughput of the full-area laser microtexturing method is higher, and the associated cost will be much lower. Maintaining consistent thermal spray parameters allows for a potential elevation of the microtexture height by a couple of microns, enhancing the possible penetration of the thermally sprayed coating. Nevertheless, to achieve greater microtexture height, an increase in laser power or frequency is necessary, which may lead to increased ablation. This adjustment has the potential to impact the microtexture morphology and subsequent surface area, crucial factors for enhancing adhesion strength.

The enhanced adhesion strength of thermally sprayed coatings, achieved through improved surface microtexturing, opens up a diverse array of potential applications. These applications encompass enhanced oxidation and hot corrosion resistance for components like airfoils, turbine buckets, ceramic clearance control coatings, and exhaust manifolds, as well as systems dealing with flue gas and fly ash. Consequently, the surface microtexturing method elucidated in this work holds the promise of finding broad-ranging utility in enhancing adhesion strength for thermally sprayed coatings on various metals and alloys.

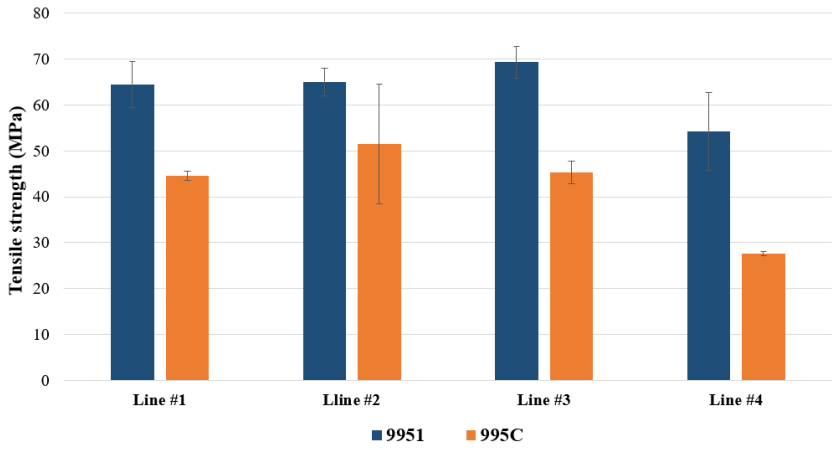

Fig. 28: Adhesion strength for grit-blasted and laser microtextured samples. Line #1 – 0.763 J/cm^2, 60 mm/s, 400 kHz; Line #2 – 0.916 J/cm^2, 60 mm/s, 400 kHz; Line #3 – 0.803 J/cm^2, 60 mm/s, 600 kHz; Line #4 – Grit-blasted. Lines #1, #2, and #3 denote the different laser parameters used.

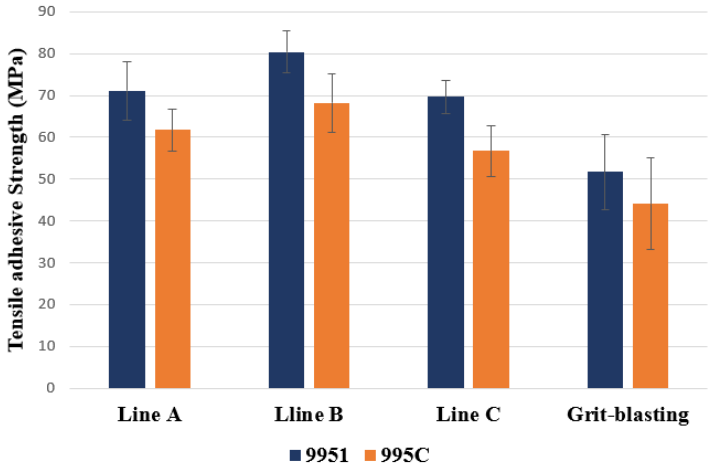

Fig. 29: Adhesion strength for grit-blasted and laser microtextured Inconel samples.

Figure 30 illustrates the surface coating achieved through thermal spraying on the aluminum sample that underwent grit-blasting following the tensile adhesion test. Notably, delamination is observable across the coating's surface in the case of the grit-blasted sample. The grit-blasted sample exhibited both cohesive failure at the epoxy-coating interface and adhesive failure. Conversely, the laser microtextured sample exclusively displayed adhesive failure at the epoxy-thermal spray coating interface during the sample pull-off pressure evaluation.

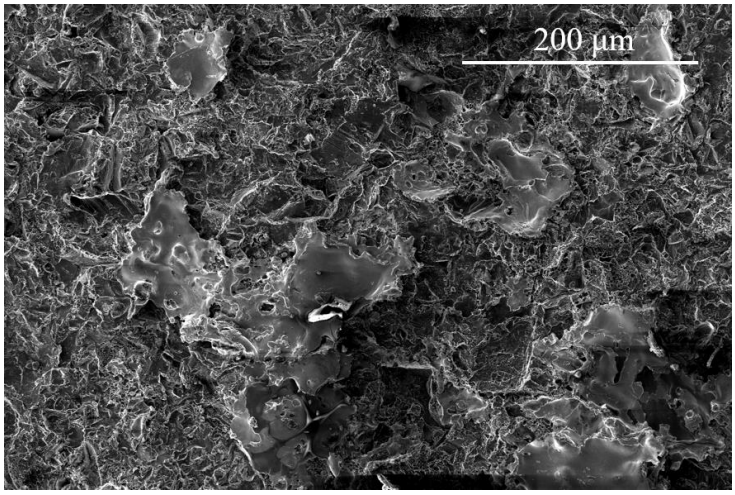

Fig. 30: SEM image of the surface of a grit-blasted sample.

The cross-sectional interface morphology of the laser microtextured aluminum samples (line #2) and the thermally sprayed coating are shown in figures 31 and 32. The EDS spectra in figures 31 and 32 show the oxygen concentration at the sample-Amdry 995C interface and sample-9951 interface. Even though nitrogen gas was constantly blown on the samples during the laser

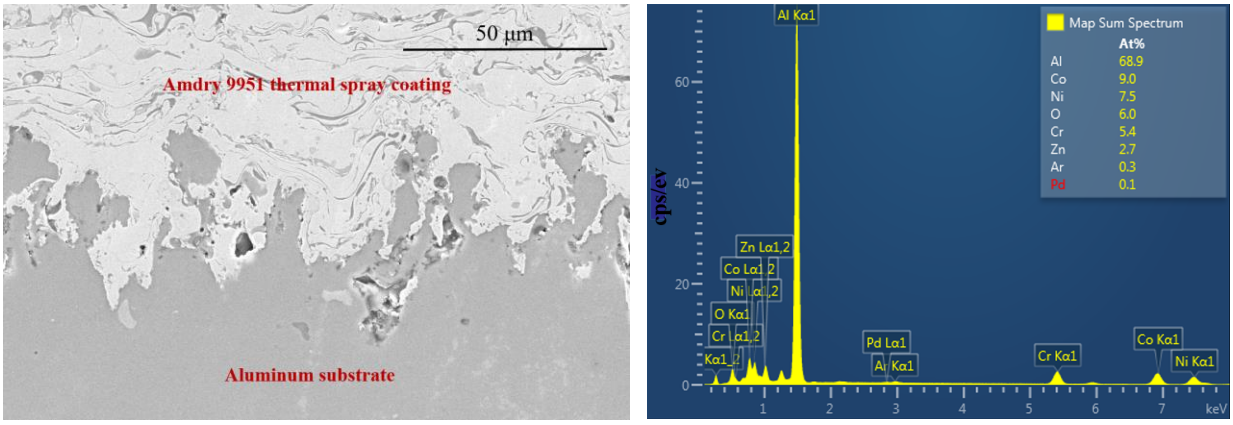

Fig. 31: (a) SEM cross-section image of the interface of line #3 and Amdry 9951; (b) EDS spectra showing the elemental composition of the interface of line #3 and Amdry 9951; Line #3 – 0.803 J/cm^2, 60 mm/s, 600 kHz[1].

microtexturing process to displace the oxygen in the air, the samples still showed some oxidation. The oxidation could be further reduced by increasing the gas flow rate on the surface of the sample. However, the samples would need to be in a vacuum to prevent oxidation entirely. Oxidation can

also happen during the thermal spray process, depending on the thermal spray parameters and the kind of coating powder used.

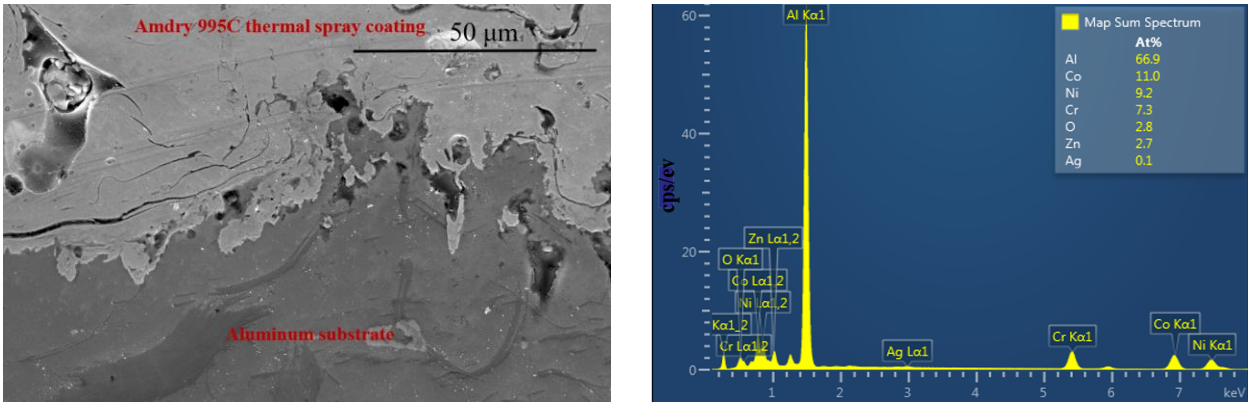

Fig. 32: (a) SEM cross-section image of the interface of line #3 and Amdry 995C; (b) EDS spectra showing the elemental composition of the interface of line #3 and Amdry 995C; Line #3 – 0.803 J/cm^2, 60 mm/s, 600 kHz[1].

Figure 33 provides insight into the cross-sectional interface morphology, comparing the grit-blasted sample with laser microtextured for thermally sprayed Amdry 995C particles. Notably, the coating on the grit-blasted sample exhibits significantly less infiltration than that on the laser microtextured surfaces. This disparity can be attributed to the absence of densely packed periodic grooves on the surface of the grit-blasted samples. Consequently, despite the grit-blasted surface having the maximum peak-to-valley distance, its surface features are non-periodic and more widely spaced when compared to the laser microtextured surfaces. The average coating thickness was determined to be approximately 275 µm.

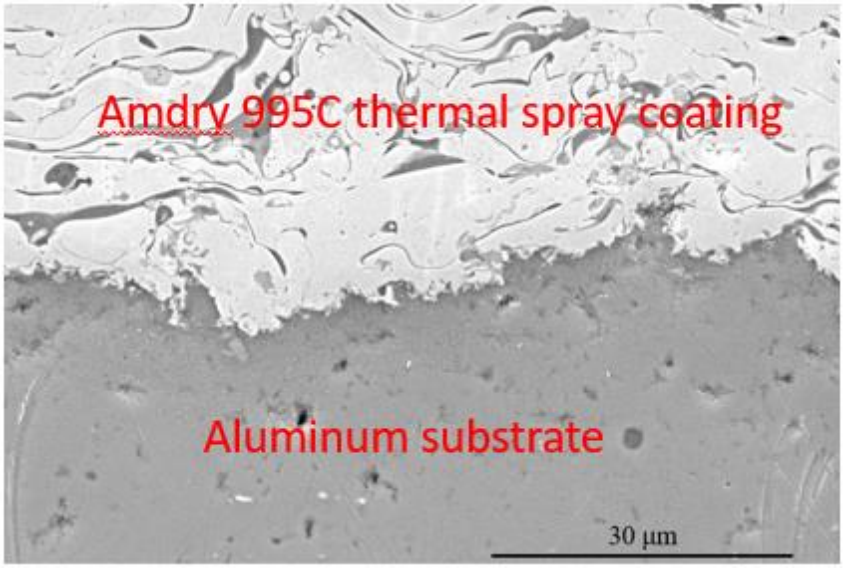

Fig. 33: (a) SEM cross-section image of the interface of grit-blasted (GB) surface and Amdry 995C.

The cross-sectional interface morphology of the laser microtextured inconel samples and the thermally sprayed coating (Amdry 9951) is shown in figure 34. Line C, which underwent microtexturing with the highest fluence, exhibited the deepest and denser textures, consequently allowing for the most substantial penetration by the thermally sprayed coating. Conversely, Line A, microtextured with the lowest fluence, displayed shallower textures with more spacing between the peaks, resulting in the least penetration by the thermally sprayed coating. It's worth noting that excessive microtexture depth doesn't always directly translate to increased penetration and improved adhesion.

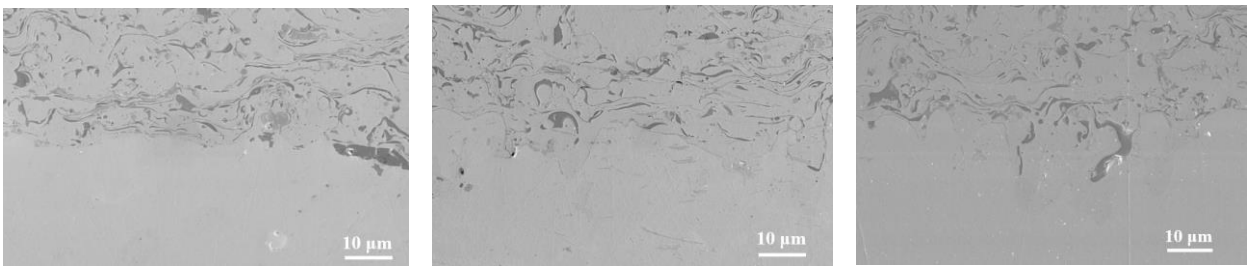

(a) (b) (c)

Fig. 34: SEM cross-section image of the interface of laser microtextured Inconel and thermally sprayed Amdry 9951; (a) Line A; (b) Line B; (c) Line C. Line A – 50 kHz, 1.71 J/cm^2, Line B – 50 kHz, 2.02 J/cm^2, Line C – 50 kHz, 2.32 J/cm^2.

The water wettability and the surface energy of the laser microtextured surfaces were investigated using contact angle measurements. The measurements were done using a Ramè-hart Goniometer model 250. The surface energy of the aluminum was measured to be 852.46 ± 0.95 mN/m. The untextured aluminum surface was found to be mildly hydrophilic with water contact angles (CA) of 81°± 6°. On the other hand, the laser microtextured aluminum surfaces were found to be highly hydrophilic, exhibiting water contact angles of 25°± 8°. This behavior can be explained by the fact that the water contact angle on a flat hydrophilic surface decreases with an increase in surface area, as expressed by Wenzel's equation[66,75]:

$$\cos\Theta_r = \mathrm{r}\cos\Theta_f \quad (1)$$

where Θ_f is the contact angle of water on an ideally smooth, flat surface, Θ_r is the contact angle of water on a rough surface with r as the roughness parameter. (r=1 for smooth surfaces and r >1 for rough surface)

5.5 Conclusion

In summary, the key points regarding laser microtexturing for improved adhesion are:

(i) Introduction of a novel method involving thermomechanical processes to create uniform micro "pillar" features, significantly enhancing coating adhesion strength by increasing the surface area.

(ii) Control of micropillar height through laser power and frequency adjustments, leading to improved adhesion compared to untextured surfaces.

(iii) Explanation of enhanced bond strength due to thermally sprayed particles filling gaps between the microtextured pillars and the study of surface morphology for better adhesion understanding.

CHAPTER 6. Superhydrophobic Surfaces by Laser Microtexturing

6.1 Introduction

Superhydrophobic surfaces serve crucial roles in various applications, including ice prevention, corrosion resistance, anti-biofouling properties, and microfluidic devices. Typically, polydimethylsiloxane (PDMS) is a commonly employed material for creating superhydrophobic surfaces. Numerous techniques, such as spin-coating, dip-coating, spray-coating, surface etching, and laser-textured molds[76,77,78], have been utilized to achieve superhydrophobicity. However, these methods often involve multiple steps, the use of various chemicals, or surface modifications. In this section, a one-stepapproach for inducing superhydrophobicity is introduced. This method involves the pulsed laser deposition of laser-ablated PDMS micro/nanoparticles and is applicable to a range of surfaces. The technique has been successfully demonstrated on three significant material classes: glass, PMMA, and aluminum, resulting in water contact angles exceeding 150° and roll-off angles below 3°. Moreover, on glass or PMMA coated with laser-ablated PDMS micro/nanoparticles, optical transmission values as high as 90% were achieved. Furthermore, this approach can be extended to create micron-scale patterned superhydrophobic PDMS surfaces, holding promise for applications in microfluidic microchannels and various optical devices.

6.2 Fabrication

The Polydimethylsiloxane (PDMS) SYLGARD 184 Silicon Elastomer was used for laser ablation studies. The substrates used were microscope glass slides of Length = 3 inches, Width = 1 inch, and Thickness = 0.04 inches purchased from Amscope. The aluminum alloy (McMaster-Carr Al 7075) samples of 1-inch length, 1-inch width, and 0.07-inch thickness were polished down to a roughness of less than 1 μm. The PMMA samples of 4 mm thickness, 1-inch width, and 1-inch

length were purchased from Ding&ng. The chemical composition of Al 7075 by weight was Al = 89.77%, Zn = 5.4%, Cu = 1.42%, Mn = 0.12%, Mg = 2.42 %, Fe = 0.42%, Cr = 0.21%, Ti = 0.11%, and Si = 0.13%.

The PDMS that was used in this experiment was a two-part solution mixture. Ten parts of the polymer and 1 part of the curing agent were mixed thoroughly and placed in a vacuum desiccator for 30 minutes to eliminate air pockets introduced during the mixing process. After eliminating the air bubbles, the PDMS solution was carefully poured and spread onto a microscope glass slide, as shown in figure 34a. The thickness of the PDMS layer was roughly 100-120 µm. As shown in the figure35a, this thickness was attained by placing cover glasses of 100-120 µm thickness around the edges of the top face of the glass slide and ensuring that the poured PDMS forms a smooth coverage by scraping off any excess PDMS off the top using a thin blade. Keeping a relatively low PDMS thickness makes it easier for the laser light to focus on the surface of the cured PDMS without undergoing significant absorption or scattering in the bulk of the PDMS layer. It also provides better control of the laser spot over the selected scan area. The poured PDMS on the glass slide was subjected to a temperature of 100°C for 25 min. on a hot plate to partially cure the PDMS. Two other glass slides with poured PDMS were prepared using the same process, and they were cured for 15 and 20 minutes, respectively. This was done to study the effect of different curing times on the laser ablation process. The thickness of the poured PDMS on these glass slides was also maintained at 100-120 µm. The glass slides and the aluminum on which the ablated PDMS micro/nanoparticles are to be deposited were treated with plasma (Jelight Company UVO-Cleaner Model 18) for 10 min.

The 355 nm wavelength laser was chosen for the ablation of the PDMS coating because the absorption of light by PDMS is higher in the UV spectrum. The UV nanosecond pulsed laser was used to ablate the deposited PDMS on glass, and the ablated material was transferred onto the target substrate through the ablated PDMS fragments. The experimental setup of this experiment is shown in figure 35b. Aluminum and glass were used as substrates. After the formation of the ablated PDMS micro/nanoparticles coating on the substrate, the substrates were heated for an additional 10 min. at 100°C to ensure good bonding and to fully cure the PDMS[76].

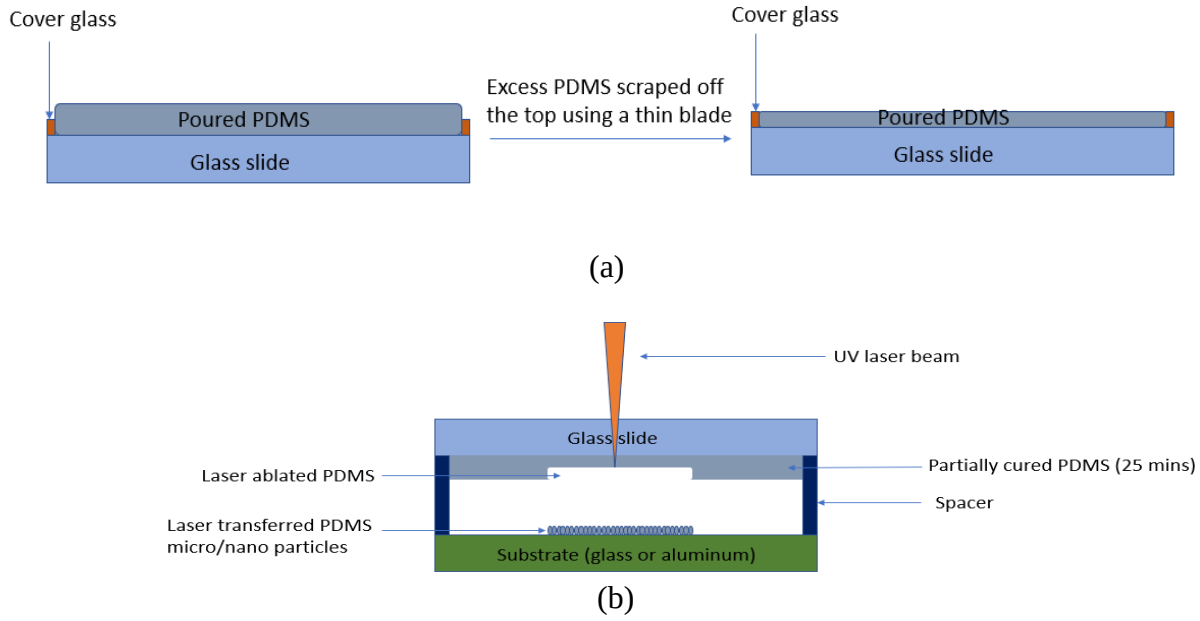

Fig. 35: (a) Schematic representation of the cross-section view of the PDMS deposition process on the glass; (b) Schematic representation of the pulsed laser ablated transferring process of PDMS onto different substrates.

6.3 Characterization

A shear (abrasion) test was performed using a micro tribometer (CETR Inc., CA, USA). Figure S2 shows a schematic of the shear test setup. A tool steel blade with a dimension of 3 x 2.4 x 7 mm was attached to a 1000 N load cell. The cell can record both normal and lateral forces. During the shear test, the glass substrate with the laser-ablated PDMS micro/nanoparticles coating was first

glued onto the sample stage of the micro tribometer. Then, the steel blade was brought into contact with the substrate under a 2 N normal force F_n, which keeps the blade in good contact with the substrate surface. The sample was moved laterally at a speed of 0.5 mm/s towards the steel blade. Once the steel blade came in contact with the coating, a shear force (F_s) was applied to the coating. The variation of the lateral shear force was recorded as a function of time until the coating was completely scraped off. The nominal ultimate shear strength τ_{Max} can be defined by equation 1:

$$\tau_{\text{Max}} = \frac{F_{S,Max}}{A_{Int}} \quad (1)$$

where $F_{S,Max}$ is the maximum shear force during the shear test, and A_{Int} is the interfacial contact area of the coating. An acoustic emission (AE) signal was also collected by the AE sensor attached to the substrate to monitor the process of scraping the coating off of the surface.

The wavelength range for the optical scan was from 200 nm to 1100 nm to ensure complete coverage of the UV and visible spectrum and some of the near IR spectrum as well. The measurements were done on different areas of a UV fused silica window (Thorlabs WG41010R), poured, and partially cured PDMS on silica and PDMS micro/nanoparticles deposited silica surface to ensure repeatability and minimize variability.

6.4 Results and Discussion

Different laser parameters were tested for the laser ablation process to determine the optimal condition to achieve superhydrophobic surfaces. It was found that scan speeds above 200 mm/s made the laser beam move too fast and did not ablate enough PDMS per unit area to create a superhydrophobic surface on the substrate. Hence, the laser scan speed was chosen to be 200 mm/s. The laser fluences were varied across a range of 1.1-2.3 J/cm^{2,} keeping the scan speed constant at 200 mm/s. Figure 36 shows the effect of varying laser fluence on the deposited PDMS

micro/nanoparticles on the glass substrate. It was observed that at higher fluences, more PDMS particles get ablated and deposited on the substrate. It is necessary to have a certain number of PDMS micro/nanoparticles on the substrate to achieve superhydrophobicity. The substrate surface starts to show superhydrophobicity above 2 J/cm^2. The side-to-side line spacing and the frequency of the laser were kept constant at 20 μm, and the laser was operated at 50 kHz, respectively. Nitrogen gas was blown on the PDMS during the laser ablation process to reduce oxidation. This enabled multiple uses of the same PDMS material for the laser ablation process. The contact angle of water on PDMS micro/nanoparticle deposited glass, PMMA, and aluminum substrate surfaces were 153.8° ± 1.7°, 157.3° ± 2.1°, and 156.8° ± 1.6° respectively, as shown in figure 37. The corresponding roll-off angles were 4.2°, 3.1°, and 3.8°, respectively. The separation between the PDMS-coated top glass and the substrate on which the laser-ablated PDMS micro/nanoparticles were deposited was 1 mm.

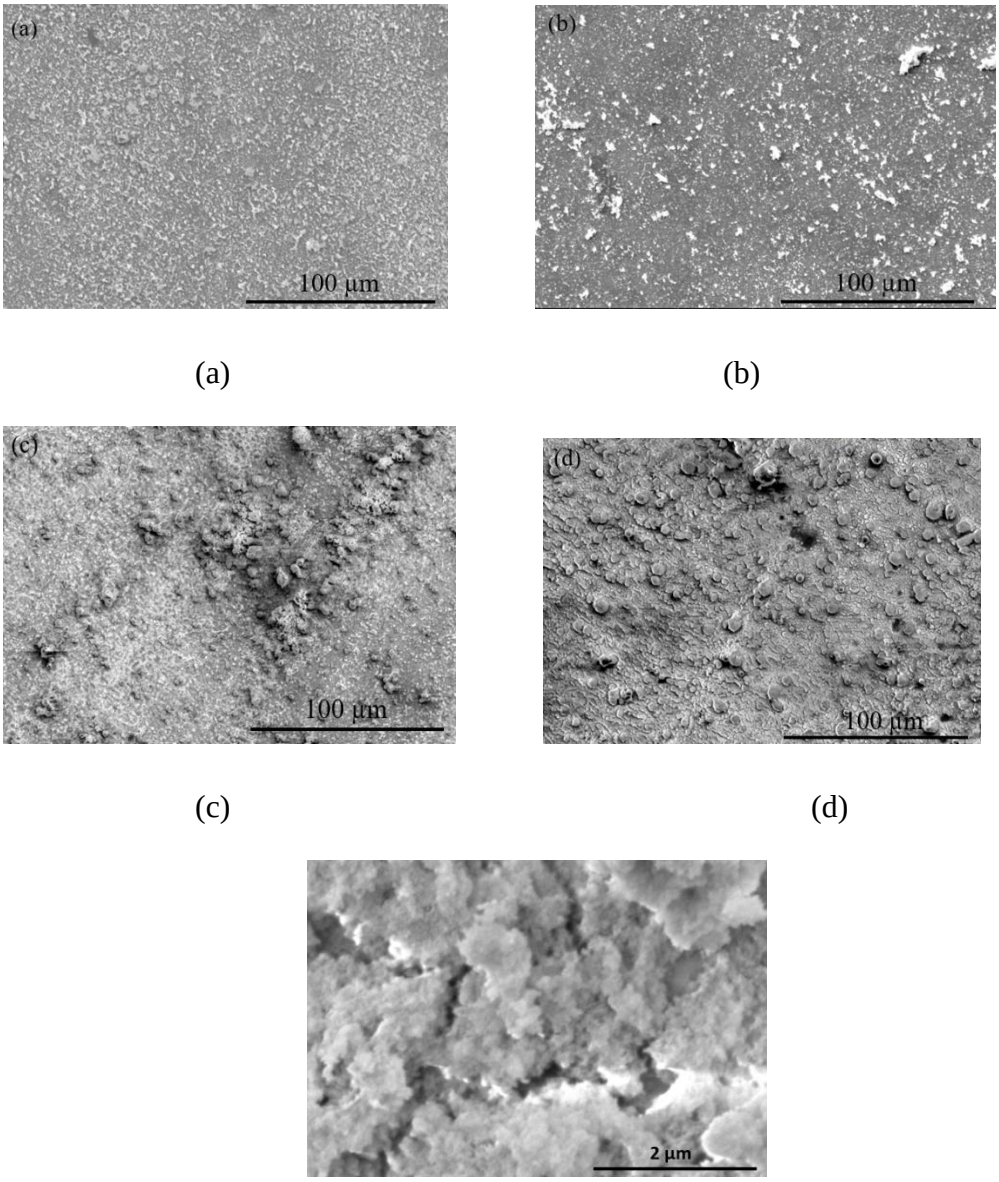

Fig. 36: Deposited PDMS micro/nanoparticles on glass at different UV laser fluences. The laser beam scan speed, frequency, and the line-spacing were kept constant at 200 mm/s, 50 kHz, and 20 µm, respectively. The laser energy density values used were (a) 1.12 J/cm^2; (b) 1.68 J/cm^2; (c) 1.98 J/cm^2; (d) 2.28 J/cm^2; (e) Magnified SEM image of PDMS micro/nanoparticles coating.

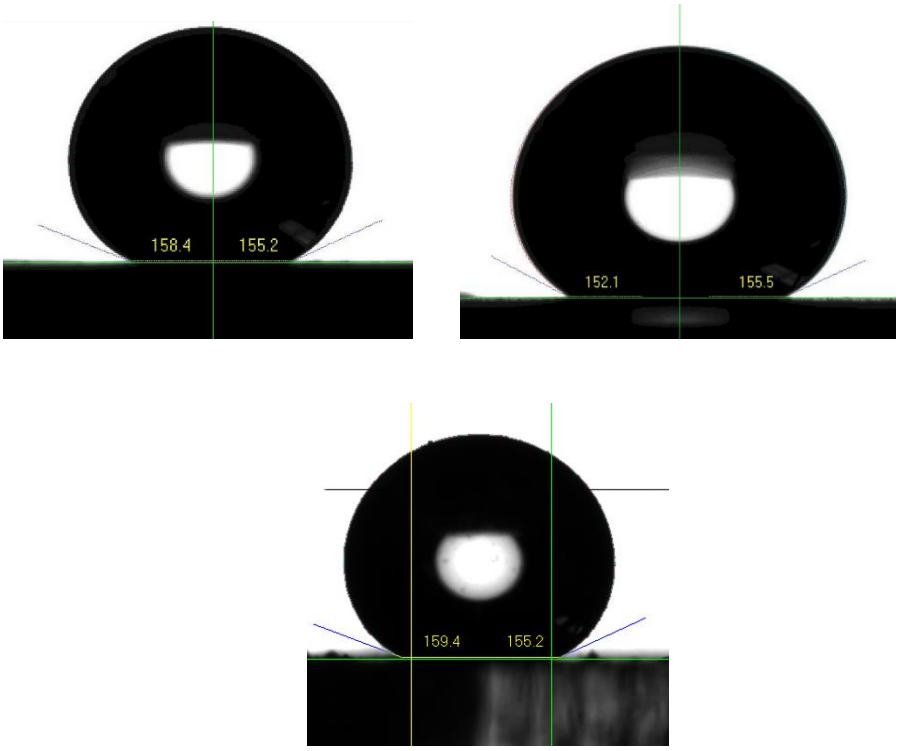

Fig. 37: The contact angle of water on PDMS micro/nanoparticles deposited film on aluminum (left), PMMA (bottom), and glass (right) surfaces.

The water contact angle (WCA) on a plane glass slide was found to be 43.4° ± 3.8°, and the WCA on a plasma-treated glass slide was found to be 23.3° ± 4.2°. Meanwhile, the aluminum surface was found to be mildly hydrophilic with water contact angles of 81.4 ± 5.8°, and the WCA on the plasma-treated aluminum sample was found to be 19.3 ± 3.6°. The decrease in the WCA can be attributed to an increase in the surface free energy due to the plasma treatment[77]. The plasma treatment of glass also allows for achieving an increased bond between the PDMS and glass[76,77,78]. As shown in figure 34b, there are two spacers, which are pieces of solid plastic separating the top glass coated with PDMS and the bottom substrate. Varying the thickness of the spacer varied the distance between the PDMS-coated top glass and the bottom substrate. This, in turn, affects the morphology of the laser-ablated PDMS micro/nanoparticles coating and its thickness.

Figure 38 shows the different morphologies of the PDMS micro/nanoparticles coated surface at different spacer thicknesses. The laser fluence used was 2 J/cm^2. It can be seen that at a smaller spacer thickness, more particles are present on the surface. The sizes of the particles also vary, ranging from a few nanometers to a few microns. The surface stopped being superhydrophobic with a spacer thickness of more than 8 mm as the film was not continuous and very thin.

Figure 39 shows the thickness variation of the PDMS micro/nanoparticles coated surface at different spacer thicknesses. The average coating thickness gradually decreases with an increase in the spacer thickness. This is because, with increasing spacer thickness, a lesser number of laser-ablated PDMS micro/nanoparticles reach the substrate. It can be seen that the laser-ablated PDMS micro/nanoparticles deposited at a spacer thickness of 1 mm had the highest average thickness of around 8 µm, while those deposited at spacer thicknesses of 5 mm and 8 mm had average thicknesses of around 4 µm and 2 µm, respectively. The coating is non-uniform with a lot of thickness variations, as can be seen in figures 37 (a), (b), and (c).

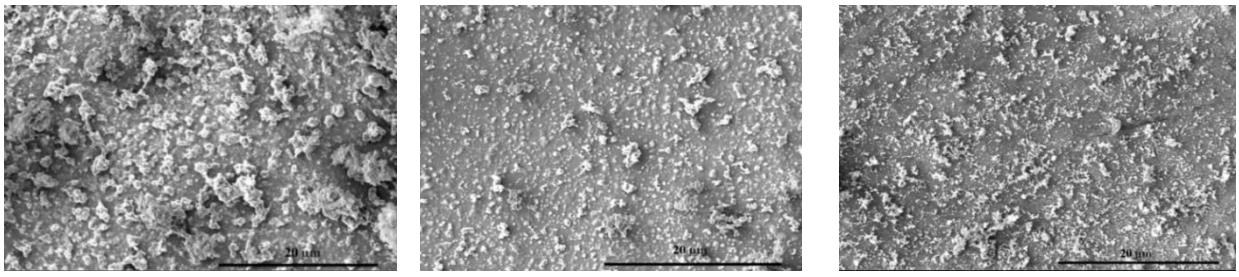

(a) (b) (c)

Fig. 38: PDMS micro/nanoparticles distribution at spacer thickness of (a) 1 mm, (b) 5 mm, and (c) 8 mm.

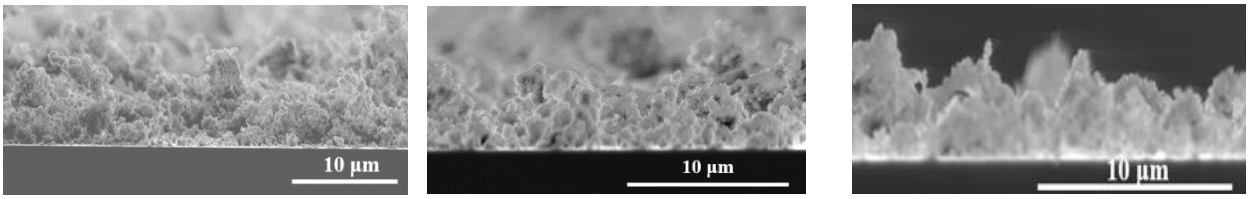

(a) (b) (c)

Fig. 39: SEM image of the cross-section of the laser-ablated PDMS micro/nanoparticles coating with spacer thicknesses of (a) 1 mm, (b) 5 mm, and (c) 8 mm.

Figure 40 shows the XPS spectrum of the different PDMS samples using a monochromatic X-ray source (1486.6 eV). Plane PDMS on glass refers to the poured and partially cured (25 min.). PDMS on glass and then laser treated refers to the poured and cured (25 min.) PDMS on glass that has been ablated by the laser to deposit the PDMS micro/nanoparticles on the substrate. There is no noticeable change in the position of the peaks, which indicates that there is no significant degradation of the PDMS[79].

The atomic percentage composition of the different elements is shown in table 9. The carbon content of all the samples under consideration was found to remain fairly constant. The silicon content of the laser-treated PDMS on glass increased by around 5%, while the oxygen content of both the laser-ablated PDMS micro/nanoparticles and the laser-treated PDMS on glass reduced considerably. This can be attributed to the breaking and forming of bonds between elements due to laser-matter interaction.

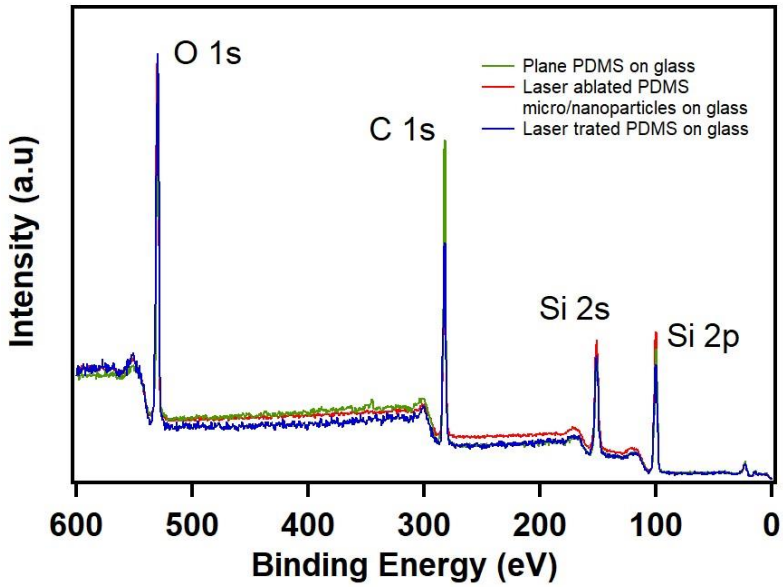

Fig. 40: XPS spectrum showing the peaks for the different elements (C, Si, and O). Spectra are shown only from 0 to 600 eV so that different colors can be seen easily.

Table 9: Elemental composition (at %) of the different samples of PDMS

	Elemental composition (%)		
Sample under consideration	O 1s	C 1s	Si 2p
Plane PDMS on glass	45.2	32.3	20.5
Laser-ablated PDMS micro/nano particles	39.7	33.2	21.4
Laser-treated PDMS on glass	33.4	33	26.6

Figure 41 displays the results of optical transmission measurements. On average, the optical transmission of cured PDMS on fused silica is approximately 6-7% lower than that of plain fused silica. In contrast, the optical transmission of laser-ablated PDMS micro/nanoparticle-coated fused silica is roughly 15% lower than that of plain glass on average. Similarly, the optical transmission of laser-ablated PDMS micro/nanoparticle-coated PMMA is about 10% lower than that of uncoated PMMA on average.

The reduced optical transmission observed in laser-ablated PDMS micro/nanoparticle-coated glass is primarily attributed to light scattering caused by the PDMS particles. Specifically, coatings deposited at shorter spacer lengths, resulting in higher PDMS micro/nanoparticle density and greater coating thickness, exhibit lower optical transmission values compared to coatings deposited with an 8 mm spacer thickness due to increased optical scattering. Notably, the optical transmission values experience a significant decrease in the shorter wavelength range due to amplified light scattering at shorter wavelengths.[80].

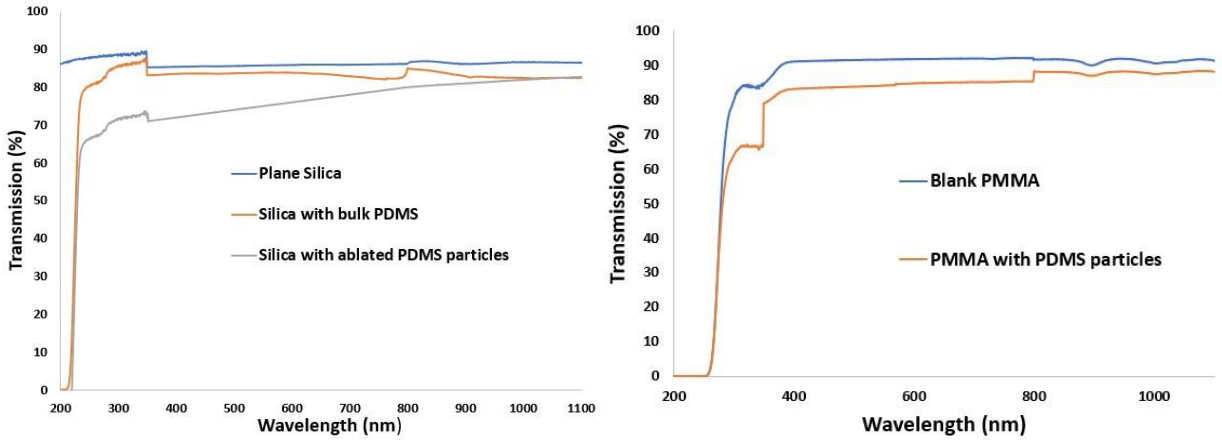

(a) (b)

Fig. 41: Optical transmission measurements on (a) silica and (b) PMMA

The laser-ablated PDMS micro/nanoparticles coated glass was placed on top of a solar cell, and the change in efficiency was measured. This was done to simulate a solar panel with laser-ablated PDMS micro/nanoparticles coated glass. The solar cell gave an efficiency of 4.45% with clear glass; meanwhile, the same solar cell gave an efficiency of 3.98% with the laser-ablated PDMS micro/nanoparticles coated glass. One sun illumination was used for the experiment. The solar cell used was a reference solar cell supplied by NREL with a rated efficiency of 4.49% under one sun illumination.

Figure 42 illustrates the shear strength of the laser-ablated PDMS micro/nanoparticle coating at various spacer thicknesses. The shear strength exhibits only a slight variation as the spacer thickness changes. Specifically, the shear strength achieved at a spacer thickness of 5 mm is marginally lower than that at 1 mm, with a difference of approximately 0.56 MPa. Furthermore, the shear strength at an 8 mm spacer thickness is slightly lower than that at 5 mm by approximately 0.32 MPa.

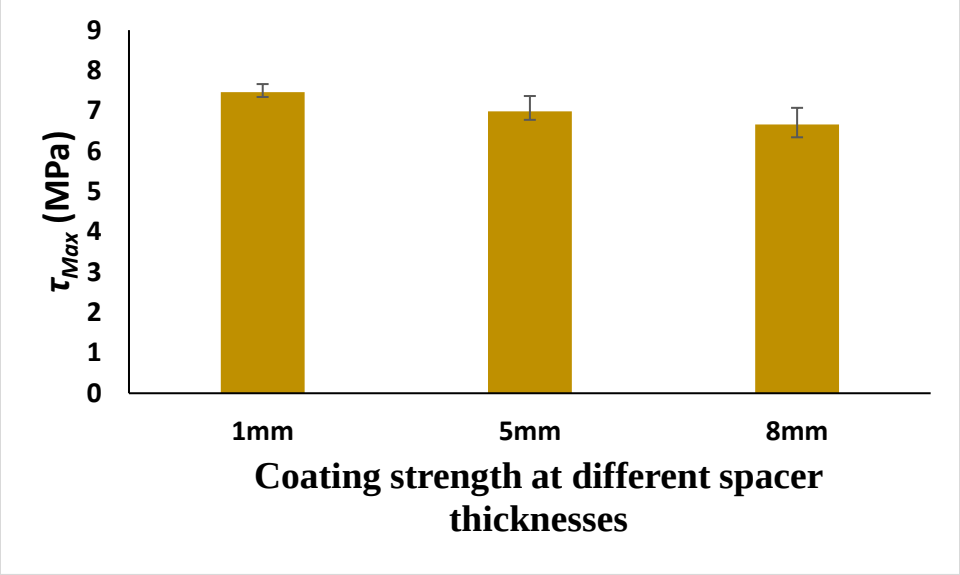

Fig. 42: Nominal ultimate shear strength (τ_{Max}) at different spacer thicknesses

This minor variation in shear strength can be attributed to differences in coating thickness associated with various spacer thicknesses. The coating deposited at a 1 mm spacer thickness requires more force to be removed than the coating deposited at a 5 mm spacer thickness. The reason behind this is that the coating at a 1 mm spacer thickness is thicker compared to the one at a 5 mm spacer thickness. The same rationale can be applied to the coating at an 8 mm spacer thickness, accounting for the observed decrease in shear strength.

The laser-ablated PDMS micro/nanoparticles deposition technique can also be used for patterned PDMS lines on different substrates, as shown in figure 43. A laser fluence of 2 J/cm^2 was used

for the laser ablation process. The spacer thickness was 1 mm. These PDMS lines are composed of laser-ablated PDMS micro/nanoparticles that bond to the substrate and form a continuous film, and their width and spacing can be varied.

To create PDMS line patterns on the substrate, two metal masks were employed. These masks

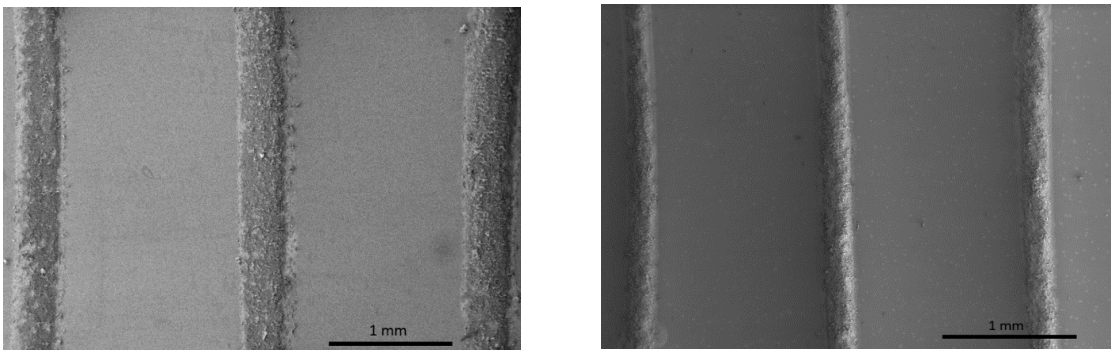

Fig. 43: SEM image of deposited PDMS lines on glass with a line width of 500 µm (left) and 200 µm (right).

featured finger-shaped openings with lengths of 2 mm and widths of 500 µm and 200 µm, respectively. The separation between these openings was 1.4 mm. Consequently, the resulting PDMS lines had widths of 500 µm and 200 µm, respectively, with an approximate spacing of 1.4 mm between the deposited lines. During the laser ablation process, these metal masks were positioned on the glass substrate, allowing the ablated PDMS micro/nanoparticles to be deposited through the open areas of the mask. Without the mask, the vaporized PDMS fragments generated by the laser ablation would disperse across the entire substrate surface, failing to form distinct line patterns.

Figure 44 demonstrates how the deposited PDMS micro/nanoparticles coating is influenced by different curing times of the poured PDMS on glass. With shorter curing times for the poured PDMS, the deposited PDMS lines exhibit breaks and irregularities due to uneven particle distribution. It's apparent that a curing time of 25 minutes results in a more consistent and uniform coating compared to curing times of 15 and 20 minutes. However, curing times exceeding 25

minutes do not yield significant differences in the deposited PDMS lines. Prolonged curing may even lead to decomposition without deposition. These experiments were conducted using a 1 mm spacer thickness on glass substrates.

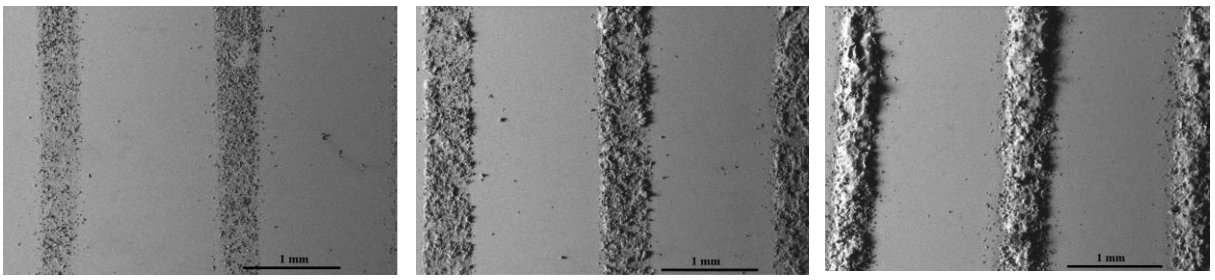

(a) (b) (c)

Fig. 44: SEM images showing the effect of the curing time of the poured PDMS on the laser-deposited PDMS micro/nanoparticles. The PDMS lines were deposited after curing the poured PDMS on glass for (a) 15 min, (b) 20 min, and (c) 25 min.

6.5 Applications

Superhydrophobic surfaces exhibit a diverse range of properties that find practical applications in both industrial and domestic settings. Below, we delve into some of these notable properties.

Antifogging -Preventing fog formation is vital for maintaining visibility. Superhydrophobic surfaces exhibit a unique behavior when moisture condenses. Although fog initially forms, these surfaces are adept at reducing fog persistence by promoting rapid evaporation, a phenomenon observed by Chen et al.[81]. The fog formed on a normal glass condensed to create a water film on the surface in a couple of minutes, whereas the fog formed on a superhydrophobic glass disappeared in 10 s and no water film was created thanks to the increased area. Chen et al.[81] fabricated a superhydrophobic surface using silica capsule particles with an apparent static CA of 152° and an ROA of less than 8° by the dip-coating method. This highly transparent surface could increase the evaporation rate of the fog and, therefore, cause the fog to disappear[82,83]. Laser ablated

PDMS micro/nanoparticles method can be used to coat glass surfaces to form a superhydrophobic surface with an even higher degree of transparency than the dip-coating method.

Self-cleaning - Surfaces that exhibit non-wettability have garnered significant attention for their remarkable ability to repel liquid droplets, preventing them from wetting the surface[84]. The exceptional water repellency of superhydrophobic surfaces is particularly advantageous for self-cleaning applications, as it facilitates the removal of dirt and contaminants when water droplets roll over the surface. This property is especially valuable in the context of solar panels, where transparent self-cleaning surfaces are essential. For instance, Park et al.[85] developed a microshell array made of PDMS with a static contact angle (CA) of 151° and a contact angle hysteresis (CAH) of 19°. Utilizing laser-ablated PDMS micro/nano particles for coating solar panels maintains their transparency without any discernible impact. This coating enables self-cleaning capabilities, effectively repelling dirt and contaminants. Notably, the transparency achieved surpasses that of the PDMS microshell array applied to solar panels to impart superhydrophobic properties. Nevertheless, a drawback of this method is that dirt particles have the potential to scratch the superhydrophobic PDMS particles, leading to their removal of the thin PDMS coating in certain areas and consequently, a loss of the superhydrophobic property.

Anti-icing - The accumulation of ice on aircraft wings is of utmost concern for safety, as it can lead to structural damage and disrupt aerodynamic performance[86]. These consequences necessitate the implementation of intricate anti-icing systems, resulting in increased aircraft preparation expenses and potential flight delays or cancellations. Likewise, ice accumulation can occur along the edges of wind turbine blades. Such ice buildup can disrupt the balance of the turbine blade, leading to decreased power generation efficiency, higher maintenance expenditures, and the risk of personal or property damage[87,88]. Aircraft wings and wind turbines are challenging to access

during operation, necessitating the integration of prevention or mitigation systems into their design. Auxiliary heating systems are frequently integrated into the leading edge of aircraft wings or turbine blades. Nevertheless, these systems consume energy, add complexity, and pose an increased risk of system failure[89,90,91,92,93]. The development of surfaces that can passively prevent or reduce ice buildup holds the potential to alleviate many of these concerns, and research into their fabrication is ongoing[94,95].

Superhydrophobic surfaces play a crucial role in preventing ice formation as water effortlessly rolls off, eliminating the chance for ice to develop. The application of laser-ablated PDMS micro/nanoparticles on extensive sections of aircraft engines and turbines offers a lightweight coating without any physical modification of the underlying surface. Due to its minimal thickness, this coating imposes no additional weight on the aircraft. Moreover, as aircraft primarily operate at high altitudes with fewer dirt particles, the PDMS coating is less prone to abrasion or damage.

Drag Reduction - The reduction of drag force is a significant challenge when it comes to solid objects moving through water, such as ships or submarines. To address this issue, various superhydrophobic coatings have been developed, drawing inspiration from the texture of shark skin. These coatings create air pockets between their microtextured features, following the Cassie-Baxter wetting model, which effectively reduces the contact between the solid surface and the liquid, resulting in reduced drag[83]. Drag diminishment by superhydrophobic surfaces was explored in different works, such as the study by Dong et al.[96], where they achieved the creation of a superhydrophobic coating on the curved surface of a model ship by utilizing the electroless deposition of gold aggregates. Since the laser ablated PDMS micro/nano particles coating has a lot of air pockets and microtextured features, it can be very effective in reducing drag. Yet, the relatively low durability of the coating, as evidenced by abrasion testing, could present a

significant challenge to its robustness in underwater environments. Factors such as continuous water brushing on a ship's body, interaction with aquatic animals and plants, among others, may affect the coating. However, the application of laser-ablated PDMS micro/nano particles coating can prove highly suitable for reducing drag in microfluidic devices dealing with much smaller water volumes. The degree of drag reduction is influenced by various factors, including the surface's wettability, Reynolds number, the size and direction of surface features, and the shear rate[97].

Anti-corrosion - Superhydrophobic surfaces, due to their ability to shed water and possess self-cleaning properties, generally exhibit a degree of resistance to chemical attacks in aqueous solutions, including acids, alkaline substances, or salt solutions. However, these surfaces often suffer from limited mechanical durability and can, depending on their material composition, be susceptible to chemical reactivity. In cases where they sustain damage, their hydrophobic properties may be compromised, leading to increased hydrophilicity. Therefore, enhancing the mechanical robustness of superhydrophobic surfaces has become a critical objective in the development of such surfaces for long-term corrosion resistance[98].

Xiu et al.[99] conducted research that highlighted the superior mechanical durability of a silica surface featuring hierarchical micro and nanoscale structures compared to a nanostructured superhydrophobic surface, as illustrated in figure 45. Following abrasion, only the nanostructures located at the peaks of the microstructures were removed, while those at the base remained mostly intact. This preservation of the nanostructures at the base was crucial for maintaining the surface's superhydrophobic properties[100].

The laser ablated PDMS micro/nano particles are susceptible to damagae and loss of hydrophobicity in extremely harsh environments due to their relatively low mechanical durability. Hence, their applications for corrosion protection is rather limited.

Solar - The inherent self-cleaning properties of superhydrophobic surfaces offer distinct advantages in the context of solar power generation. Contaminants like dust, dirt, and organic materials can obstruct sunlight, reducing its effectiveness in reaching the solar cells. Moreover, the presence of surface water and ice can amplify surface scattering and reflectivity, further impeding the solar panel's performance[89,101]. The conventional methods of removing water, ice, and contaminants from solar panels often rely on additional systems or physical access to the cells,

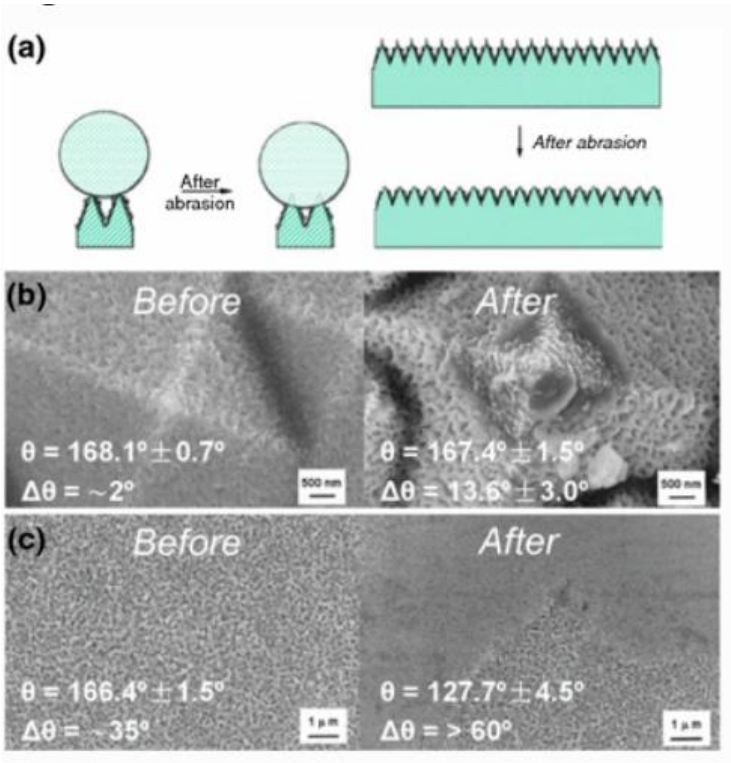

Fig. 45: (a) Illustration of water droplet on Si with two-scale structures before and after abrasion; (b) SEM morphology, static contact angle, and contact angle hysteresis of Si with two-scale structures before and after abrasion; (c) SEM morphology, static contact angle and contact angle hysteresis of Si with nanostructures before and after abrasion[100]. *This figure is reprinted from the Journal of Coatings Technology and Research 13, D. Zhang, L. Wang, H. Qian, Superhydrophobic*

surfaces for corrosion protection: a review of recent progresses and future directions, 11-29, copyright 2016, with permission from Springer Nature.

which may not always be feasible in various applications. Microtextured superhydrophobic surfaces, on the other hand, have proven to effectively eliminate these issues by preventing the accumulation of surface water and ice, along with the removal of contaminants[102,103,104] Laser-ablated PDMS micro/nano particles present an effetcive method for coating solar panels, providing surface roughness and superhydrophobic properties without the necessity of microtexturing the underlying solar panel itself. Moreover, the microtexture pattern on superhydrophobic surfaces can provide an additional advantage by serving as an anti-reflection coating[105], thereby aiding in the capture of more solar energy.

Water Repellant Textiles - Superhydrophobic coatings are typically applied to rigid substrates, but in applications involving textile fabrics, the substrate (fabric) is flexible. Wang et al.[106] modified cotton substrates with n-dodecanethiol and gold micro/nanostructures to create superhydrophobic surfaces on fabrics. These surfaces maintained a static contact angle (CA) of over 150° and retained superhydrophobicity even after the fabrics were folded multiple times[107]. Zimmermann et al.[108] also developed superhydrophobic textile fabrics using polymethyl silsesquioxane nanofilaments. To assess the wettability of these fabrics, a parameter called the water-shedding angle was introduced since the normal contact angle was not suitable for evaluating superhydrophobic textile properties. The water-shedding angle determined how effectively a water droplet rolled off the inclined fabric surface. Wang et al.[109] created fabrics modified with a fluorinated-decyl polyhedral oligomeric silsesquioxane and a fluorinated alkyl silane. These fabrics exhibited self-healing superhydrophobicity, superoleophobicity, and durability against acid exposure, ultraviolet rays, machine washing, and abrasion. Common methods for achieving superhydrophobic textiles involve the use of chemicals, potentially compromising clothing safety

or altering fabric quality. Laser-ablated PDMS micro/nano particles present a favorable alternative for coating fabric with a thin layer of microstructured PDMS to achieve superhydrophobicity. The flexibility of textiles is maintained, as the thin PDMS coating conforms to the textile's shape without impacting its wearability. However, it's crucial to consider the polar or non-polar nature of the fabric, which can influence the adhesion of PDMS particles to the substrate.Given the potential applications of superhydrophobic fabrics, they must withstand scratching, abrasion, and general wear. Specialized technical textiles are utilized in various industries, including automotive, aerospace, filtration, construction, and medicine[110].

6.6 Conclusions

To summarize the laser-based method for creating superhydrophobic surfaces:

(i) Deposition of pulsed laser-ablated PDMS nano/microparticles on various surfaces to generate superhydrophobic thin films was demonstrated. Versatility is demonstrated on glass, PMMA, and aluminum surfaces.

(ii) Comprehensive examination of surface morphology and optical properties of the laser-ablated PDMS micro/nanoparticle-deposited films, is reported. Factors like laser parameters, PDMS curing time, and spacer distance are considered.

(iii) Proof of concept for patterned superhydrophobic PDMS surfaces using a metal mask, offering potential applications in constructing superhydrophobic microchannels for microfluidic devices and other uses.

CHAPTER 7: Superhydrophilic Surfaces by Laser Microtexturing

7.1 Introduction

Laser surface microtexturing has become increasingly popular due to its low cost, scalability, automation, and lack of use of hazardous chemicals. Laser surface microtexturing can be used to control the wettability of various surfaces by varying surface roughness for a wide range of applications. In recent years, the reversible transition between superhydrophobicity and superhydrophilicity has gained significant attention due to a variety of applications, including self-cleaning, corrosion protection, anti-icing, microfluidics, water harvesting, and thermal management. The ability to manipulate liquid behavior facilitates processes like coalescence, rolling, and pinning. However, the current methods of making reversible superhydrophilic-superhydrophobic surfaces have several disadvantages, such as complex fabrication processes, use of high temperatures and chemicals, time-consuming, and high costs. This section presents a facile laser microtexturing method capable of inducing superhydrophilicity with a contact angle (CA) of less than 1° on surfaces. In contrast to earlier approaches, this method employs a higher number of scans to attain increased and uniformly distributed surface roughness, resulting in consistent superhydrophilicity.

7.2 Fabrication

The substrates used were microscope glass slides (Length = 3 inches; Width = 1 inch; Thickness = 0.04 inches) by Amscope, recrystallized silicon-carbide ceramic sheets (Length = 3 inches; Width = 3 inches; Thickness = 0.125 inches), and aluminum alloy (Al 7075) samples (Length = 1 inch; Width = 1 inch; Thickness = 0.07 inches) polished down to roughness of less than 1 µm. The chemical composition by weight of Al 7075 was Zn = 5.4%, Cu = 1.42%, Mn = 0.12%, Mg =

2.42 %, Fe = 0.42%, Cr = 0.21%, Ti = 0.11%, Si = 0.13%, and Al = 89.77%. The aluminum was purchased from McMaster-Carr. Polydimethylsiloxane (PDMS) SYLGARD 184 Silicon Elastomer was purchased from Dow Corning and used to coat the laser microtextured glass and aluminum samples.

The UV laser was chosen for this experiment because metals and ceramics reflect most of the laser energy from longer wavelength lasers. Additionally, shorter pulse width lasers are good candidates for laser microtexturing[111,112]. The laser fluence used for the experiments was 4.25 J/cm^2. The laser beam scan speed was maintained at 200 mm/s. For each laser fluence, the side-to-side overlap between the lines was 50%. The selected fluence value for this experiment was intended to permit a substantial degree of ablation. Alternative values can also be chosen, provided they remain above the ablation threshold value.The chosen scan speed facilitates a laser pulse overlap exceeding 50%, ensuring that the entire surface exposed to the laser undergoes ablation.

7.3 Characterization

After the laser treatment, each of the samples was inclined at an angle of 45°, and a drop of water (10μL) was dropped on one end of the microtextured area. Then, the movement of the water was observed as the water flowed across the length of the microtextured area. As a reference, a drop of water (10μL) was also dropped on a smooth, untextured area of each of the samples, and the water flow was observed. The time taken by the water to traverse/completely wet the length of the microtextured area was observed with a camera and recorded.

The optical characterization of the laser microtextured glass surface was performed by transmitting light across the solar spectrum range (350-2500nm) and detecting the transmitted light using a power measurement meter (Thorlabs S302C thermal power sensor).

7.4 Results and Discussion

Figures 46 and 47 show the variation of the surface morphology with a changing number of laser scans. It can be seen that at a higher number of scans, the ablation is much more significant. Increasing the number of scans also results in a more well-defined surface microtexture[112]. Moreover, scanning in different directions results in a more pronounced laser effect, resulting in increased depth and decreased spacing between the features.

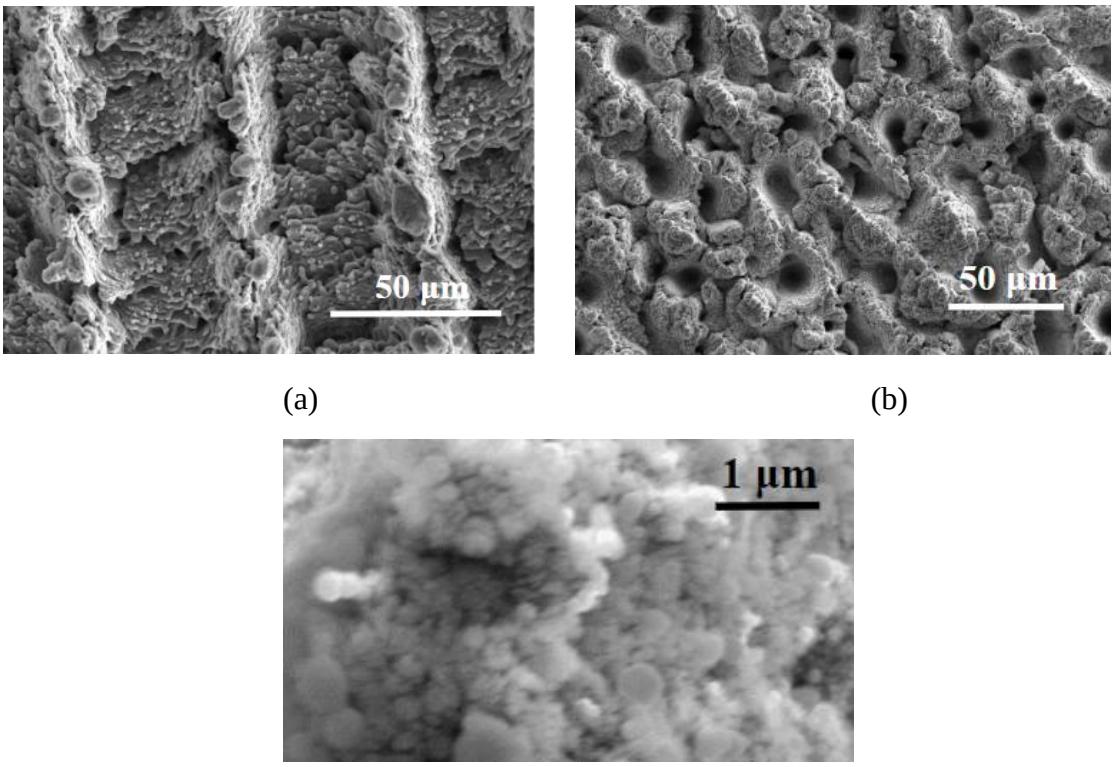

(a) (b)

(c)

Fig. 46: Laser micro/nanotextured aluminum sample at a fluence of 4.25 J/cm^2. (a) One scan (0°), (b) three scans (0°, 90°, and 45°), (c) Magnified image of the "three scans" surface showing nanostructures.

Figure 48 shows the superhydrophilic properties induced by laser surface microtexturing. The water contact angle (WCA) on glass and aluminum surfaces microtextured with one scan were found to be 17.2° ± 1.8° and 21.2° ± 1°, respectively. On the other hand, glass and aluminum

surfaces microtextured with three scans had a WCA of less than 1°. The contact angles of laser microtextured glass and aluminum are given in table 10. The greater wetting behavior observed at a higher number of scans can be attributed to more pronounced surface features and greater depth of the grooves, resulting in increased penetration and spreadability of the water droplet.

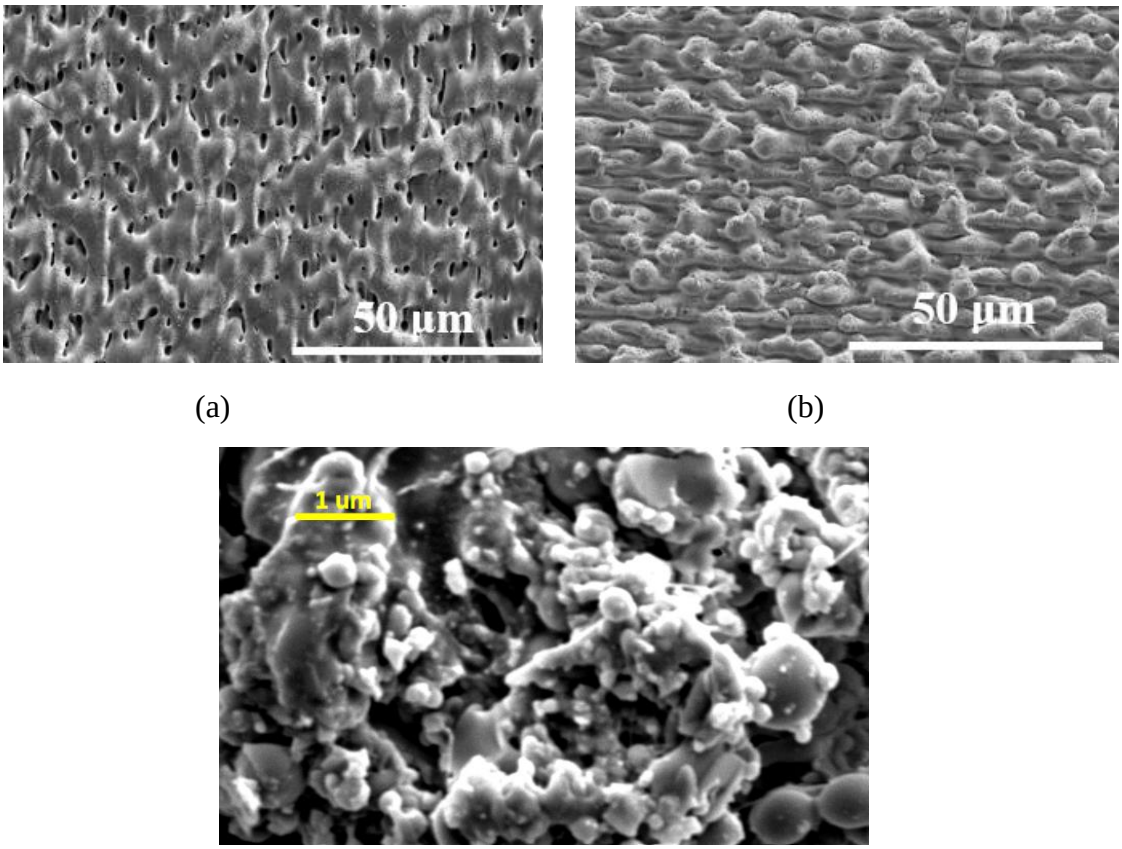

(a) (b)

(c)

Fig. 47: Laser micro/nanotextured glass sample at a fluence of 4.25 J/cm^2. (a) One scan (0°), (b) three scans (0°, 90°, and 45°), (c) Magnified image of the three scans surface showing nanostructures.

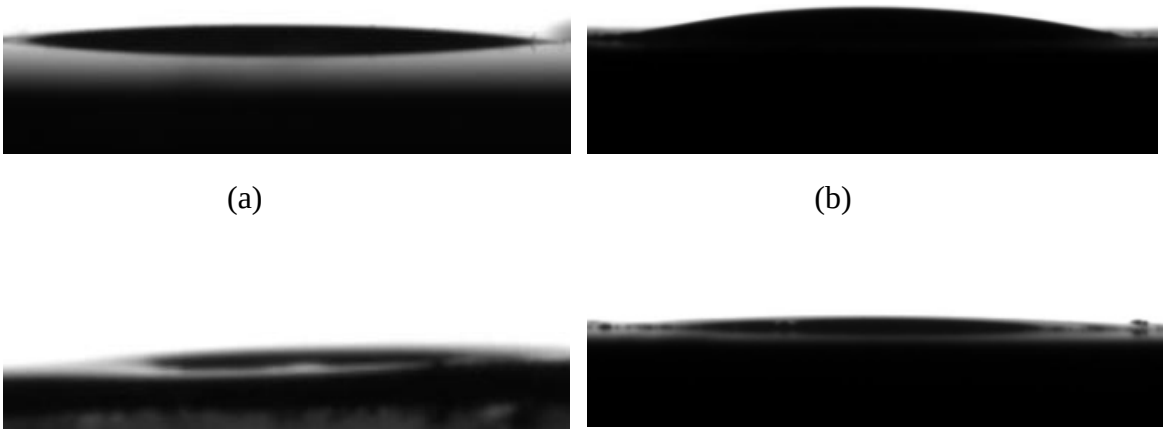

(a) (b)

(c) (d)

Fig. 48: Water drop sitting on the one scan surface of (a) glass and (b) aluminum. Water drop sitting on the three scans surface of (c) glass and (d) aluminum.

Table 10: Contact angle of superhydrophilic laser microtextured glass and aluminum

No. of scans	Material	Contact Angle (CA)
1	Aluminum	21.2° ± 1°
3 (0°, 45° and 90°)	Aluminum	<1°
1	Glass	17.2° ± 1.8°
3 (0°, 45° and 90°)	Glass	<1°

Modifying the surface microtexture has a direct impact on the spreading behavior of water, influencing the speed of water flow. It has been observed that increasing the average feature height leads to a higher rate of water flow compared to surfaces with a lower average feature height. The length and width of the microtextured surface that was considered for the water flow experiment are 3 cm and 1 cm, respectively, and the measurements of the time taken to traverse/wet were done in steps of 0.5 cm, 1 cm, 1.5 cm, 2 cm, 2.5 cm and 3 cm along the length for the surface with one and three scans. The same measurements were taken for the untextured surfaces as well. Thereafter, the velocities were calculated at each interval length. Compared to an untextured surface, there is a significant increase in the velocity for both glass and aluminum. The velocity of the water at different intervals of length for both glass and aluminum has been plotted in figure 49.

Figure 50 shows the position of the water drop with time on a microtextured (three scans) aluminum surface.

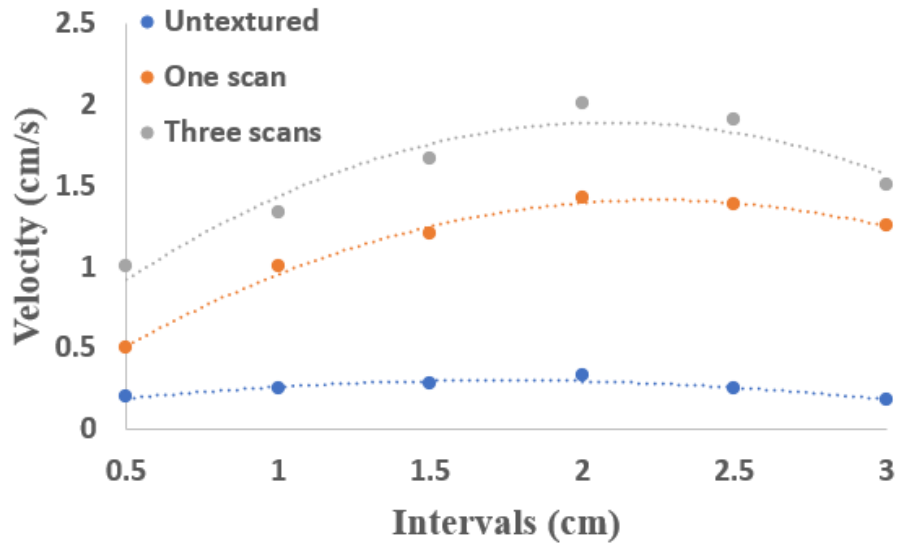

(a)

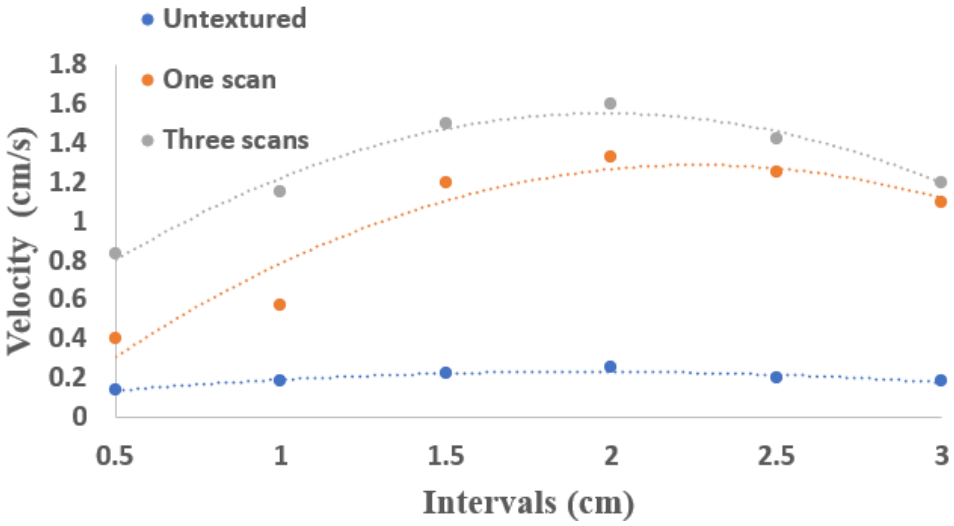

(b)

Fig. 49: Velocity of water at different distances on the laser microtextured surface of (a) aluminum and (b) glass.

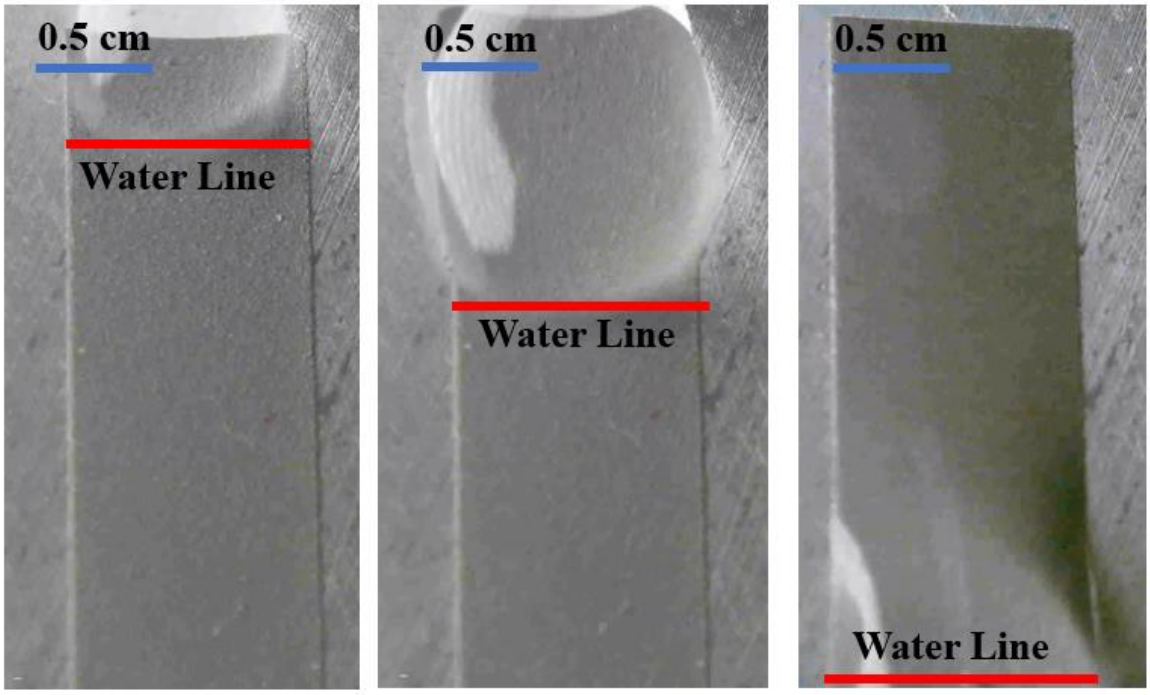

Fig. 50: Flow of water drop on microtextured (three scans) aluminum surface.

Figure 51 displays the optical profile of the laser microtextured aluminum surface obtained through three scans. It can be observed that the maximum peak height reaches approximately 70 µm, while the average feature height measures around 55 µm.

Figure 52 displays the optical profile of the laser microtextured glass surface obtained through three scans. It can be observed that the maximum peak height reaches approximately 60 µm, while the average feature height measures around 50 µm.

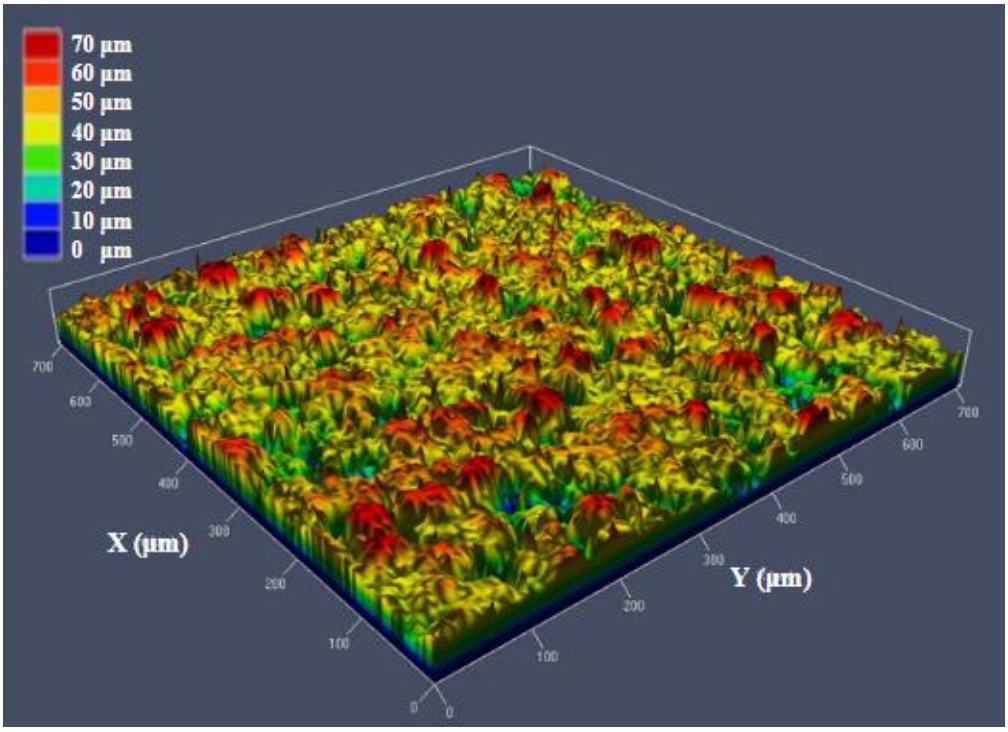

(a)

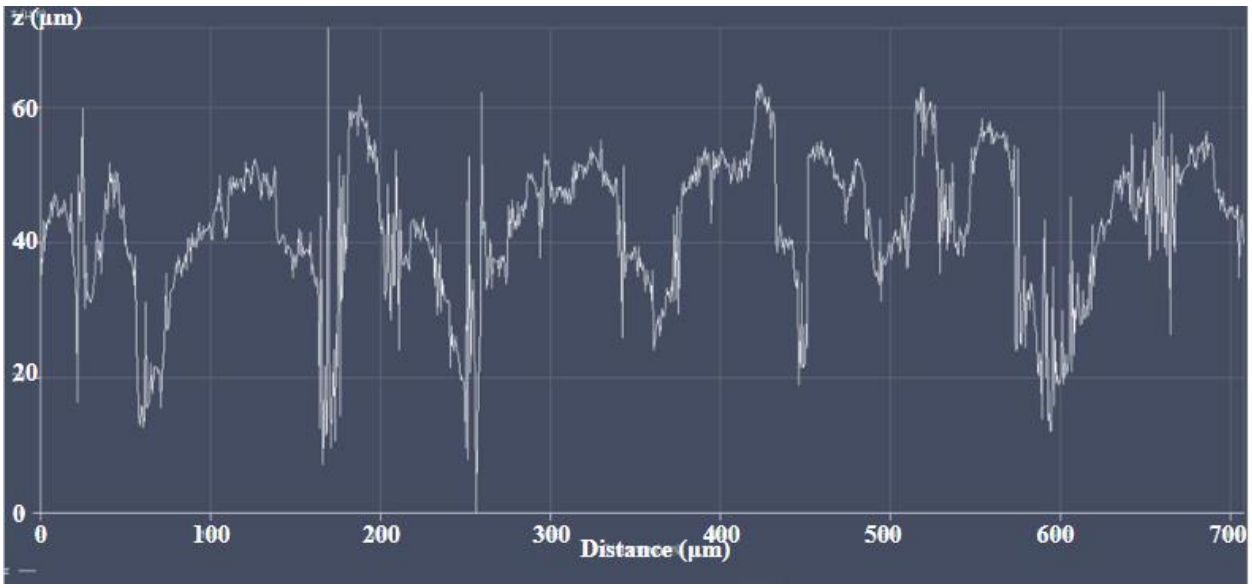

(b)

Fig. 51: (a) 3D surface profile of the laser microtextured aluminum three scans surface, (b) 1D surface graph showing the surface variations of the laser microtextured aluminum three scans surface.

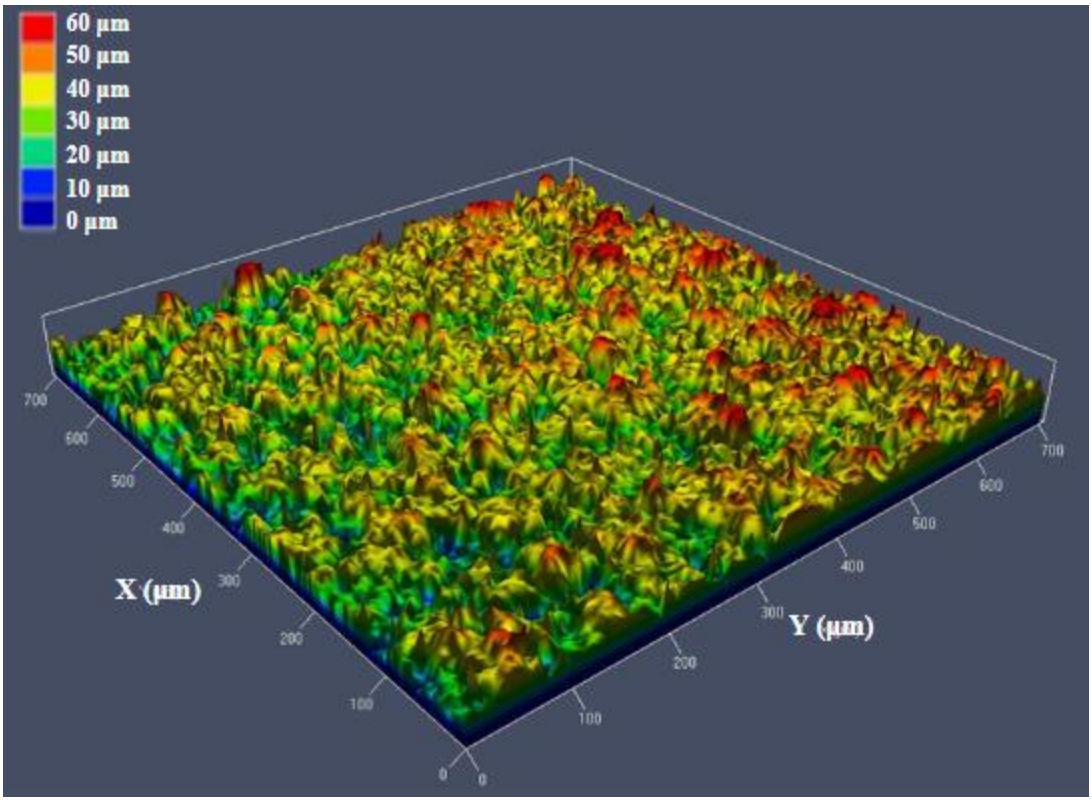

(a)

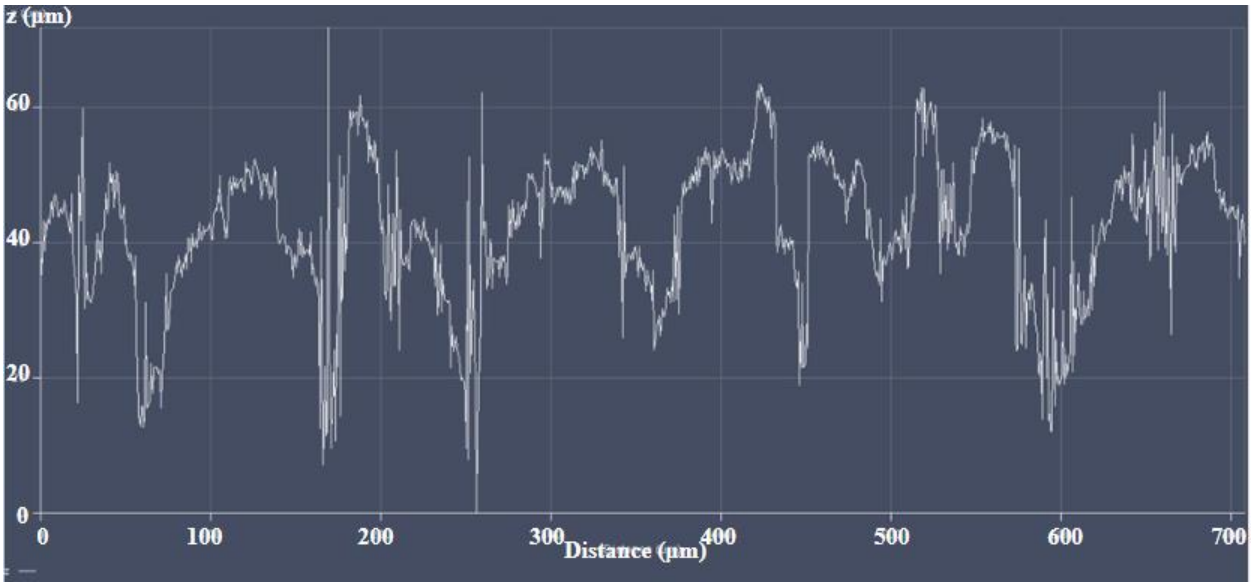

(b)

Fig. 52: (a) 3D surface profile of the laser microtextured glass three scans surface, (b) 1D surface graph showing the surface variations of the laser microtextured glass three scans surface.

7.5 Applications

The growing demand for functional materials with unique wetting properties has driven extensive research into the creation of superhydrophilic materials, which have a broad range of applications. Here, we discuss a few different applications of superhydrophilic surfaces.

Wastewater treatment - Superhydrophilic properties play a crucial role in enhancing the efficiency of oil-water separation processes, particularly in the context of wastewater treatment. These properties facilitate the creation of specialized membranes and materials designed to tackle the challenges of separating oil from water effectively. When discussing the separation of free-floating, dispersed, and dissolved oil in water filtration, superhydrophilic materials exhibit exceptional performance[113]. For instance, in a study[114] involving a superhydrophilic and underwater superoleophobic poly(acrylic acid)-grafted PVDF membrane, the material demonstrated remarkable capabilities. This membrane excelled in separating oil from water emulsions, even under low applied pressure or gravity-driven conditions. The high separation efficiency was evident through the achievement of water purity levels exceeding 99.99% in the filtrate after a single separation process, highlighting the effectiveness of superhydrophilic surfaces in removing oil contaminants from water. In another study[115] involving foam membranes, a similar trend was observed. The superhydrophilic properties of these membranes enabled them to efficiently separate heavy oil from water mixtures under gravity-driven conditions at elevated temperatures. The method proposed in this thesis for creating superhydrophilic surfaces can be applied to membranes to enhance oil-water separation effectiveness. This eliminates the need for membrane grafting with acids and is also applicable to foam membranes. Additionally, the proposed method achieves highly superhydrophilic surfaces, potentially increasing membrane separation efficiency.

Biomedical applications - Superhydrophilic materials have found extensive applications in biomedical research. For instance, researchers developed superhydrophilic vertically aligned carbon nanotube (VACNT) films designed for cell adhesion[13,116]. Rather than employing VACNT films, the method proposed in this thesis can be utilized to render the underlying substrate superhydrophilic, eliminating the necessity for external films. This approach also circumvents the use of relatively fragile films, potentially offering a more robust solution.

In another study[117], superhydrophilic and antibacterial zwitterionic polyamide thin film composite nanofiltration membranes (ZTFCMs) were reported. These membranes exhibited excellent water permeability and high selectivity for erythromycin (ERY) over sodium chloride (NaCl), making them well-suited for the separation of ERY/NaCl mixtures[118]. Enhancing the membranes' superhydrophilicity has the potential to further increase water permeability, thereby augmenting the rate of water passage through the membranes.

Pervaporation - Superhydrophilic materials have found applications in the separation of liquid mixtures. For instance, in an investigation done by Gong et al. [119], a superhydrophilic nanohybrid membrane was developed and evaluated for pervaporation performance in separating alcohol/water mixtures.

Wang et al. [120] introduced superhydrophilic and acid-resistant zeolite membranes, known as Ge-ZSM-5 membranes, which demonstrated exceptional pervaporation capabilities for dehydrating acetic acid and ethanol solutions.

In a study done by Shan et al. [121], a superhydrophilic water uptake membrane was employed for the pervaporation separation of ethanol/water mixtures. Initially, the base polyelectrolyte membrane exhibited a flux of 275 g/m^2 h and a permeate with 95.1% water content. However,

following the creation of a $CaCO_3$ multilayer on the polyelectrolyte membrane surface using a 0.4 mol/L calcium source, the flux dramatically increased to 1317 g/m^2 h, nearly five times that of the original membrane. Furthermore, the water content in the permeate rose from 5% to 98.8%. This enhanced performance was attributed to the water uptake function of the superhydrophilic $CaCO_3$ layer, which initially concentrated the feed, facilitating the penetration of water molecules into the permeate.

The proposed method in this thesis can enhance pervaporation membranes by imparting superior superhydrophilicity without using additional chemicals, resulting in improved robustness and consistent performance.

Other applications - Superhydrophilic surfaces have demonstrated impressive performance in various applications, including self-cleaning, anti-fogging, and anti-corrosion. For instance, Huang et. al.[122] made TiO_2 films with a multiscale porous structure were investigated for their anti-fog properties, and they showed promising results. In another study done by Wang et. al.[123], a PVDF-SMA/silica hybrid surface was created through a dip-coating process, exhibiting good anti-fogging properties.

Léonard et al. [124] introduced TiO_2 films containing multi-walled carbon nanotubes (MWCNTs) for anti-corrosion applications. The incorporation of MWCNTs enhanced the anti-corrosive properties of TiO_2, increasing the corrosion potential (anodic displacement) and reducing the corrosion current. In an investigation done by Sorcar et al. [125], superhydrophilic TiO_2 films were prepared using a NaOH-based alkaline electrolyte for self-cleaning applications. These superhydrophilic surfaces displayed effective self-cleaning and photocatalytic properties, facilitating the rapid reduction of oleic acid. Additionally, Choi et al. [126] presented the synthesis of multilayered films

composed of CHI/RHA nano silica. These films exhibited excellent anti-fogging and anti-frosting properties, even under challenging fogging and frosting conditions.

The method proposed in this thesis simplifies fabrication, eliminates the need for chemicals or electrolyte solutions, and reduces material usage compared to the aforementioned methods.

7.6 Conclusion

To summarize, the key points for laser microtexturing to make superhydrophilic surfaces include:

(i) Highly durable superhydrophilic surfaces with contact angles below 1° can be made by utilizing laser microtexturing with customizable micro/nanostructures by adjusting laser parameters. Prior research has typically employed a single laser scan to attempt to achieve superhydrophilic surfaces. In contrast, this study conducted three scans in normal, orthogonal, and 45° orientations. This approach imparted greater roughness and uniformity to the surface features, resulting in enhanced superhydrophilicity. The measured contact angle consistently remained below 1°, in contrast to contact angles reported in previous literature that, with just one scan, fluctuated to as high as 3-4°.

(ii) The technique has been demonstrated on glass and aluminum but can be extended to other materials classes.

(ii) A novel method of measuring superhydrophlicity by water flow measurement has been introduced.

CHAPTER 8: Integrated Superhydrophobic and Superhydrophilic Surfaces by Laser Microtexturing

8.1 Introduction

This chapter delves into the transition of superhydrophilic surfaces to their superhydrophobic state and, conversely, the restoration of superhydrophobic surfaces to the superhydrophilic state, achieving reversible wettability. This unique ability to control surface properties holds significant applications in the analysis of biological fluids and microfluidics. Unlike existing methods that rely on chemicals, specific storage conditions, and extended durations, the technique presented in this chapter eliminates the need for such additives and time-consuming processes. Reversibly wettable surfaces can be achieved within minutes, and these surfaces maintain their reversibility for extended periods, offering a more efficient and practical approach.

8.2 Fabrication

Following the laser microtexturing process on aluminum and glass, a thin layer of PDMS was applied to the samples. The PDMS utilized in this experiment consisted of a two-part solution mixture. Ten parts of the polymer were thoroughly mixed with one part of the curing agent to prepare the PDMS solution. Once prepared, the solution was poured into a circular glass petri dish measuring 90 mm X 15 mm. The dish was then placed on a hot plate heated to 115° C for 15 minutes. As a result of the heat, some of the PDMS evaporated and deposited onto the laser microtextured samples, which were positioned with the textured side facing downwards and resting on the edges of the petri dish. The thermal evaporation of PDMS occurs at a temperature

of 115° C and above[127]. Figure 53 depicts a schematic representation of the experimental setup. Following the PDMS deposition, the samples underwent laser treatment to remove the PDMS coating, leading to a reversible transition between superhydrophobic and superhydrophilic surface properties.

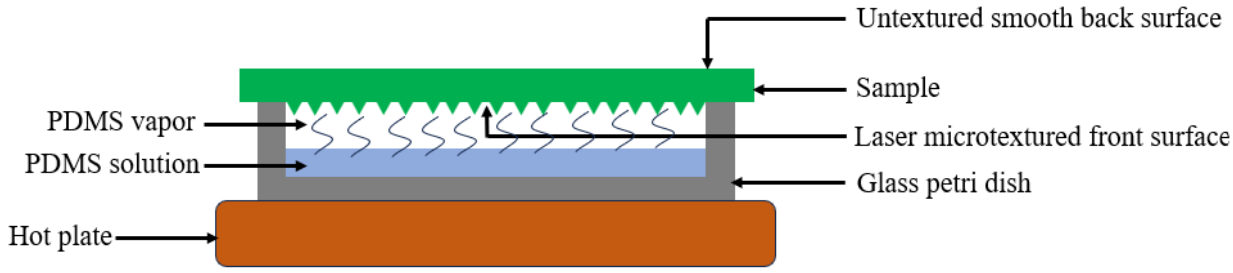

Fig. 53: Schematic of the PDMS deposition setup.

Figure 54 shows the superhydrophobic properties displayed by the one scan laser microtextured glass and aluminum surfaces after PDMS was deposited on them. The glass surface exhibited a WCA of 155.7° ± 2.6°, while the aluminum surface exhibited a WCA of 156.8° ± 2.6°. The glass and the aluminum surfaces exhibited roll-off angles (ROA) of 4.3° and 3.6°, respectively.

Figure 55 shows the superhydrophobic properties displayed by the three scans of laser microtextured glass and aluminum surfaces after PDMS was deposited on them. The glass surface exhibited a WCA of 166.7° ± 3.4°, while the aluminum surface exhibited a WCA of 168.2° ± 2.6°. Both surfaces exhibited roll-off angles (ROA) of 2°. The results are summarized in table 11.

Table 11: Contact and roll-off angle of PDMS deposited superhydrophobic laser microtextured glass and aluminum

No. of scans	Material	Contact Angle (CA)	Roll-off Angle (ROA)
1	Aluminum	156.8° ± 2.6°	~3.6°
3 (0°, 45° and 90°)	Aluminum	168.2° ± 2.6°	~4.3°
1	Glass	155.7° ± 2.6°	< 2°
3 (0°, 45° and 90°)	Glass	166.7° ± 3.4°	< 2°

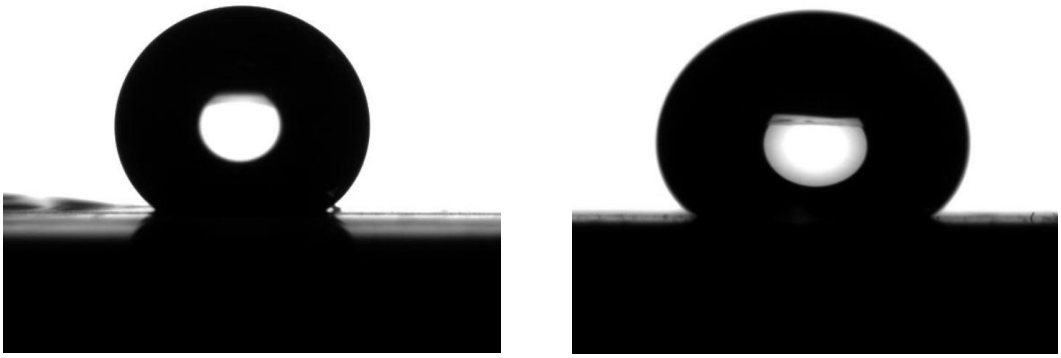

(a) **(b)**

Fig. 54: Water drop sitting on PDMS covered one scan surface of (a) glass and (b) aluminum.

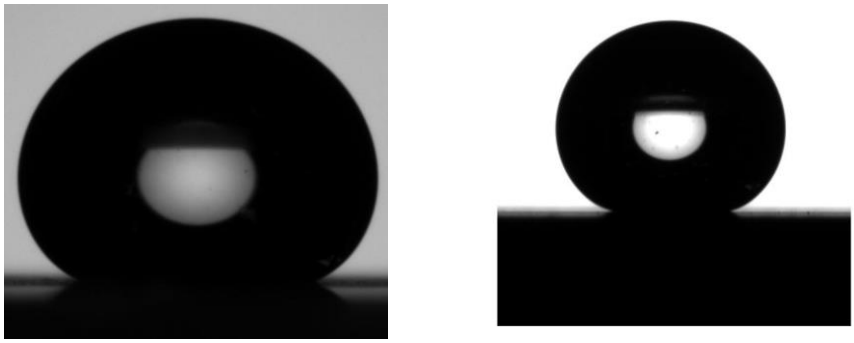

(a) **(b)**

Fig. 55: Water drop sitting on PDMS covered three scans surface of (a) glass and (b) aluminum.

The laser was used to remove the PDMS coating and make the surface superhydrophilic again. The power of the laser has to be carefully chosen so that the thin PDMS layer is ablated and removed from the top of the surface features without affecting the substrate. The energy density power required for this operation was found to be 1 J/cm^2.

8.3 Characterization

Figures 56 and 57 present the EDS analysis result for the surface following laser microtexturing and subsequent deposition of the PDMS coating on the laser microtextured surface, respectively. The introduction of the PDMS coating leads to an elevation in the silicon and carbon percentages,

attributable to the composition of PDMS as a polymer comprised of carbon and oxygen atom chains.

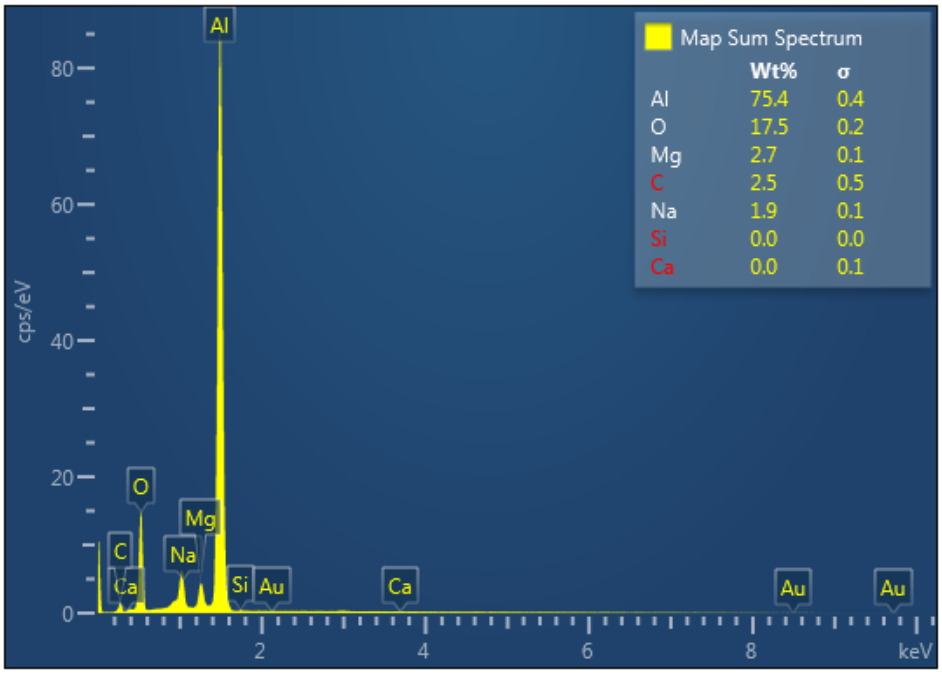

Fig. 56: EDS analysis showing an elemental composition of laser microtextured aluminum surface.

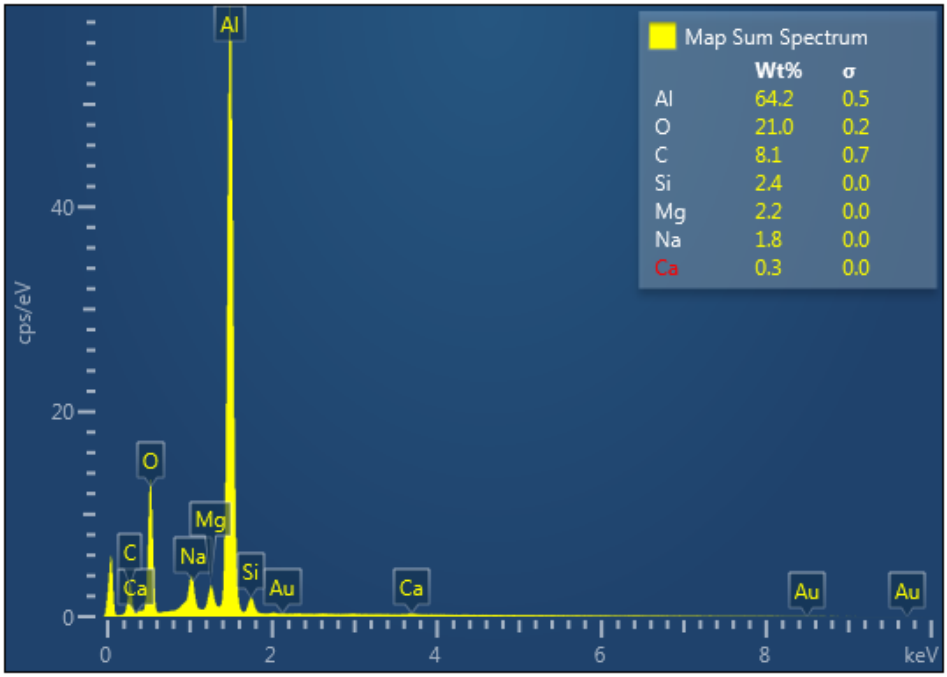

Fig. 57: EDS analysis showing the elemental composition of the PDMS-coated laser microtextured surface.

The optical transmission of the PDMS-covered laser microtextured glass was measured to be approximately 90% throughout the wavelength range from 400 nm to 2500 nm. This transparency was comparable to that of plain glass, which exhibited a transmission of 92% in the same wavelength range. These findings confirm that the PDMS-covered laser microtextured glass maintains its transparency and efficiently allows the passage of light. It is important to note that a minor portion of the light is lost due to scattering induced by the surface features resulting from laser microtexturing, which is not collected by the spectrometer detector.

8.4 Selective Superhydrophilicity and Superhydrophobicity

A superhydrophilic-superhydrophobic patterned surface is a cohesive system that integrates both the characteristics of extreme water repellency and water attractiveness on a single substrate. These surfaces possess the high-precision and high-resolution gradient wettability to finely control and manipulate solid-liquid interactions. These surfaces find various applications, such as droplet

microfluidics, which allows precise handling of minute reagent quantities by isolating fluids in distinct droplets within cell arrays. Another application utilizes the wettability contrast between superhydrophilic and superhydrophobic patterns to control the spreading of droplets, enabling effective concentration of solutes without loss on the hydrophilic spots during surface-enhanced Raman spectroscopy of highly diluted samples. Additionally, the wettability contrast between superhydrophilic and superhydrophobic regions can be utilized to confine fluids to specific areas, offering an energy-efficient means to manipulate fluids on open surfaces, making them suitable for microfluidic devices and water harvesting[128,129].

Figure 58 illustrates superhydrophilic surfaces represented as “squares” achieved by selectively removing PDMS from a superhydrophobic PDMS-coated aluminum surface. The dimensions of the squares shown are 500 μm and 200 μm; however, the laser removal process allows for even smaller sizes and different shapes, offering high controllability tailored to specific applications. This level of precision sets it apart from other methods like printing and chemical modification for creating patterned superhydrophobic-superhydrophilic surfaces.

In figure 58 (c), a magnified view of one such superhydrophilic “square” reveals a micro and nanopillar arrangement that induces superhydrophilicty. Meanwhile, figure 59 demonstrates how water drops of varying sizes are pinned on four selectively chosen superhydrophobic “squares”. This property enables accommodating and containing fluids of different volumes, which is crucial for analyzing biological fluids as described in nanoparticle arrays[128].

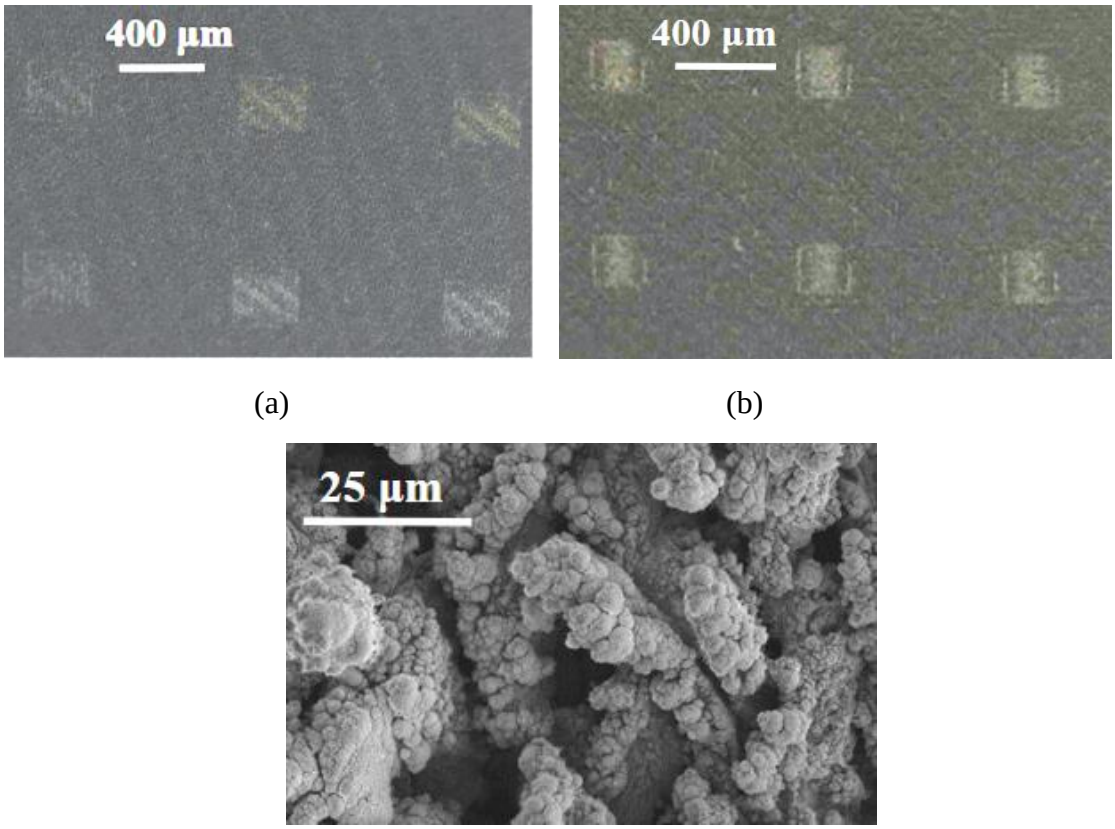

Fig. 58: Optical microscope image of superhydrophilic squares of sizes (a) 500 µm and (b) 200 µm surrounded by superhydrophobic surface. (c) Magnified SEM image of the superhydrophilic square.

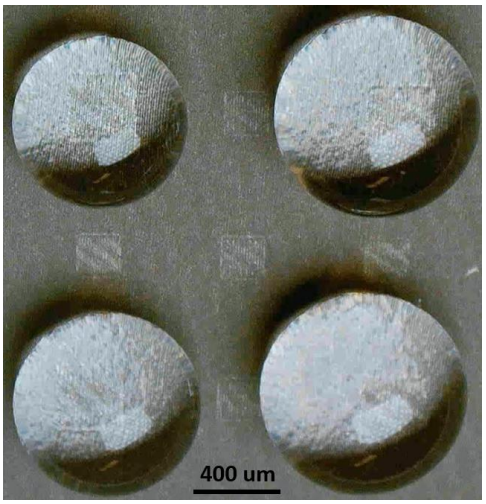

Fig. 59: Water drops of different sizes sitting on superhydrophilic squares of size 200 µm. The volume of water drop is 10 µl (top right), 15 µl (bottom left), 25 µl (bottom right) and 35 µl (top left).

7.4 Conclusion

The key points presented in this section are as follows:

(i) Laser microtextured superhydrophilic surfaces can be coated with a low surface free energy material like PDMS, applied through solution evaporation, to achieve contact angles exceeding 168° and a low roll-off angle of 2°.

(ii) Reversible wettability, which is transitioning between superhydrophobic and superhydrophilic states, can be achieved by laser PDMS removal from the superhydrophobic surface. Alternate superhydrophobic -superhydrophilic surfaces can be created using this method. Selective wettability is suitable for corrosion protection, self-cleaning, transparent surfaces, and microfluidic devices.

CHAPTER 9: Conclusion and Future Work

9.1 Conclusion

In the section on laser microtexturing for adhesion improvement, the research has introduced an innovative and highly effective method for laser microtexturing, achieved through a thermomechanical process, leading to the creation of dense, uniform pillar-like features. The significant increase in coating adhesion strength, resulting from a substantial enlargement in the total surface area, is a major outcome of this study. The micro "pillar" shape, amplifying the contact area ratio, plays a pivotal role in enhancing the adhesion strength of atmospheric plasma sprayed metallic coatings. Furthermore, the ability to control micropillar height exceeding 40 μm has demonstrated superior adhesion performance compared to various textured and non-textured surfaces outlined in the literature. The explanation for the amplified bond strength lies in the effective filling of gaps between the pillars by thermally sprayed particles. This comprehensive analysis of the laser microtexturing process's parameters and the study of cross-sections have contributed significantly to understanding and improving adhesion strength. As a result, the research outcomes offer substantial promise for a wide range of applications in surface engineering and materials science, potentially impacting coating technologies and their industrial use.

The research on laser microtexturing for creating superhydrophobic surfaces has introduced a laser-based technique for the creation of superhydrophobic surfaces, utilizing pulsed laser-ablated PDMS nano/microparticles deposition on diverse substrates to generate superhydrophobic thin films. The study successfully demonstrated the achievement of superhydrophobic properties on surfaces like glass, PMMA, and aluminum, with broader applicability across various materials. It involved the generation of PDMS micro/nanoparticles through laser ablation of partially cured

PDMS, providing a deep understanding of the science behind the thin film formation, considering factors such as laser ablation parameters, PDMS curing time, and spacer distance. Furthermore, the research uncovered the potential for creating patterned superhydrophobic PDMS surfaces using a metal mask, paving the way for applications in fields like microfluidics. The major outcome of this work is the development of a laser-based superhydrophobic surface creation method with wide-reaching implications, promising advancements in liquid-repelling technologies, anti-fouling, microfluidics, and beyond, thereby advancing scientific and technological frontiers.

Further, this thesis has put forward a laser microtexturing technique that enables the creation of durable superhydrophilic surfaces with contact angles measuring less than 1°. This achievement is made possible through the creation of thermal energy in the material by precise control of laser parameters, such as the number of scans, fluence, scan overlap, and scan speed, which tailor the shape and morphology of micro/nanostructures on the surface. Additionally, the study demonstrates the versatility of this technique by showing how these laser-generated surface microtexture can be easily coated with a low surface free energy material like PDMS, transforming them into superhydrophobic surfaces with high contact angles exceeding 170° and an exceptionally low roll-off angle of 2°. What sets this research apart is the ability to achieve reversible wettability, as the PDMS coating can be removed by a laser, restoring the surface to its superhydrophilic state. This breakthrough has potential for applications in corrosion protection, self-cleaning, microfluidics, and water harvesting. Moreover, the creation of alternating superhydrophilic and superhydrophobic surfaces offers an innovative approach with multifaceted utility, particularly in microfluidic devices.

9.2 Future work

Continued research into the primary and secondary effects of microtextured superhydrophobic surfaces could reveal opportunities to improve the current designs and fabrication techniques. In addition, future research efforts should focus on how these surfaces can affect application areas more broadly, such as wind power generation and refrigeration. So, concurrent research should occur in the future on the design, applications, and novel consequences of these surfaces.

In many applications, such as anti-icing surfaces or solar cells discussed earlier, the applications are the centerpiece of the research. The addition of a microtextured surface may reduce the ice adhesion strength on wind turbine blades, and the combination of native low surface free energy materials and surface microtexture can prevent ice buildup. In addition, the natural anti-reflection properties of microtextured surfaces would be useful for solar power generation applications. A commercialization opportunity exists for cold storage applications, solar power generation, and wind power generation.

To further advance the adhesion strength of thermally sprayed coatings through laser microtexturing, a multifaceted scientific exploration is imperative. A comprehensive understanding of the intricate physics underlying the laser microtexturing process, the complex mechanics governing thermal spray adhesion, and the varied parameters affecting coatings is crucial for optimizing adhesion strength. Further research should focus on refining the geometry and dimensions of the micropillar structures generated via laser microtexturing, shedding light on how thermally sprayed coatings infiltrate these structures and subsequently enhance adhesion. Detailed investigations into the chemical and mechanical bonds formed at the interface between thermally sprayed coatings and laser-microtextured surfaces will provide a holistic perspective on the laser microtexturing process, thus facilitating improvements in coating adhesion. Moreover,

the influence of oxidation induced by laser microtexturing on the interaction between surface microtextures and thermally sprayed coatings requires meticulous analysis to gauge its impact on adhesion. Additionally, exploring the morphology of the deposited thermal bond coat offers the potential for establishing a more robust and enduring coating structure, elevating its durability and reliability. These research avenues hold promise for enhancing adhesion in various industrial applications. It is worthwhile to note that the potential for improving adhesion through laser microtexturing extends beyond glass and aluminum and can encompass a broader spectrum of materials. The laser microtexturing method for adhesion improvement would be applicable to various other types of coating methods and is not limited to plasma-sprayed coatings.

To enhance the superhydrophobic surface generation process involving laser ablation of PDMS and subsequent PDMS micro/nanoparticle deposition, several avenues for refinement and optimization merit scientific exploration. Achieving an even thinner deposited coating represents a key facet of improvement, as this would significantly enhance the transparency of surfaces like glass. One viable approach to achieve this is by further increasing the spacer thickness during the deposition process, allowing for greater control over the thickness. Moreover, a thinner coating not only enhances transparency but also conserves materials and reduces costs. A deeper understanding of the intricate interactions between the laser and PDMS is pivotal in gaining precise control over the spread of ablated PDMS particles and, consequently, the entire deposition process. Such insights into the laser-PDMS interaction can facilitate fine-tuning the thickness of the deposited coating. Additionally, potential refinements can be made in depositing patterned superhydrophobic lines, particularly for applications in the realm of nanofluidics. This may involve using lasers with even smaller spot sizes and finer metal masks to achieve more intricate and precise patterns, opening up new possibilities for advanced applications in this domain.

Exploration into optimizing integrated superhydrophilic-superhydrophobic surfaces presents multifaceted research opportunities to enhance their stability, consistency, and durability. A promising avenue for advancement lies in investigating various laser scanning patterns to achieve more robust and enduring surface features, resulting in improved superhydrophilic characteristics. Delving deeper into the physics underlying water flow velocity and the interplay of surface forces in response to distinct laser microtexturing parameters promises a more comprehensive understanding. The intensity of the laser, a pivotal factor in determining microtexture height, profoundly influences water velocity. Molecular-level interactions at the interface between the substrate and PDMS coating, when PDMS is evaporated onto the superhydrophilic surface to confer superhydrophobicity, warrant further exploration. Controlled manipulation of the PDMS evaporation rate onto the superhydrophilic surface holds the potential to optimize material usage. Additionally, expediting the removal of PDMS to revert the surface to its superhydrophilic state can be achieved through precise control of laser speed, frequency, and spot overlap. Fine-tuning the requisite laser power for PDMS removal represents another intriguing research avenue, contributing to advancements in this field. It is also worth mentioning that achieving reversible and selective wettability via laser microtexturing is not limited to glass and aluminum; it can be applied to a diverse range of materials.

Optimizing some of the laser parameters used in the experiments could lead to reduced processing times and increased throughput. Investigating the scalability of these techniques for large-area applications and industrial settings is another avenue for future work. Overall, there is ample room for further exploration and refinement in these areas, offering exciting possibilities for advancements in surface engineering and materials science.

Appendix A: Additional Research

This work was done in collaboration with Prof. Gary Koening (Department of Chemical Engineering, UVA) and his students.

A.1 Lithium extraction from end-of-life cycle lithium batteries using laser processing

Since the 1990s, lithium-ion batteries (LIBs) have dominated the rechargeable battery market, particularly in portable electronic devices[130,131]. These batteries typically consist of a mix of valuable metals (such as cobalt, lithium, nickel, and manganese), metal oxides, organic chemicals, metal casings, and plastics[132,133]. The exact composition can vary depending on the manufacturer and type of battery. LIBs have found widespread use in mobile electronic gadgets like smartphones, laptops, and computers and have also seen applications in military, aerospace, navigation, electric vehicles, and medical equipment. In recent times, there has been explosive growth in the LIB industry, with China emerging as a key player in the production, consumption, and exportation of these batteries[134,135]. Environmental concerns and the global energy crisis have pushed for alternative energy sources for vehicles, resulting in a surge in LIB production and usage[136,137,138,139]. Consequently, this surge will inevitably lead to a significant volume of spent LIBs. Therefore, it is imperative to prioritize research into environmentally friendly and efficient recycling processes for these spent batteries[140,141,142].

Presently, the primary research approaches for extracting valuable metals from spent LIBs involve pyrometallurgy, hydrometallurgy, and biohydrometallurgy[143]. Pyrometallurgy, although capable of recovering metals, has limitations due to its high energy consumption and the emission of harmful gases, making it less favorable for plications[144,145]. On the other hand,

biohydrometallurgy, a relatively new technology in materials recycling, has gained significant attention and shows considerable potential. However, it is less efficient when dealing with spent LIBs that have a high metal content[146]. Hydrometallurgy involves the use of an organic acid and a reducing agent. Although this process is simpler than pyrometallurgy and hydrometallurgy, this process can pose risks in terms of safety concerns or scalability[147].

In this section, the primary goal is to develop a comprehensive, cost-effective, and convenient method for extracting Li from end-of-life cycle LCO electrodes. The process involves immersing LCO pellets (Thickness ~ 2 mm; Diameter = 4 mm) in water and disintegrating them by subjecting them to a nanosecond UV laser while submerged in water. This treatment disperses the LCO particles into the water. Subsequently, the UV nanosecond laser was used to treat the LCO particles dispersed in water. This creates a localized and controlled heat to generate Li^+ ions from the LCO within the aqueous solution. Additionally, the laser breaks down the LCO particles into even smaller particles.

A.2 Generating silicon nanoparticles from recycled silicon solar cells using laser to fabricate Li-ion battery electrodes

Silicon has emerged as a promising anode material for the next generation of Li-ion batteries, with certain commercial applications already utilizing it. This appeal stems from its impressive theoretical capacity of 3572 $mAhg^{-1}$, primarily attributed to its ability to form a $Li_{15}Si_4$ phase at room temperature. However, the utilization of silicon in Li-ion batteries is not without its challenges. One significant drawback is the substantial volume expansion, which can reach up to 300% during lithiation. This expansion frequently leads to mechanical stress within the silicon structures, causing breakage. This, in turn, results in pulverization and the loss of active material. Even when silicon structures are reduced below this critical dimension, the substantial volume

changes detrimentally affect the solid electrolyte interphase (SEI). The expansion upon lithiation and contraction upon delithiation prompts the creation of a new SEI, leading to a permanent capacity loss that cannot be rectified. Researchers have dedicated substantial efforts to addressing these challenges, such as developing various silicon nanoparticles[148,149].

This research explores a novel and cost-effective method for producing silicon nanoparticles using end-of-life cycle silicon. The process involves immersing silicon wafers obtained from silicon solar cells in water and subjecting them to pulsed UV laser ablation within the water medium to generate silicon nanoparticles. Subsequently, these nanoparticles are utilized to fabricate electrodes, which are subjected to multiple cycles of charging and discharging.

References

(1) Chakraborty, A.; Chalfant, B.; Sions, J.; Zimmerman, B.; Gupta, M. C. Improvement of thermal plasma sprayed coating adhesion strength by laser microtexturing of aluminum. *The International Journal of Advanced Manufacturing Technology* **2023**, *125* (5), 2629-2642.
(2) Obilor, A. F.; Pacella, M.; Wilson, A.; Silberschmidt, V. V. Micro-texturing of polymer surfaces using lasers: a review. *The International Journal of Advanced Manufacturing Technology* **2022**, *120* (1), 103-135.
(3) Kumar, V.; Verma, R.; Kango, S.; Sharma, V. S. Recent progresses and applications in laser-based surface texturing systems. *Materials Today Communications* **2021**, *26*, 101736.
(4) Orlandini, A.; Baraldo, S.; Porta, M.; Valente, A. Ablation threshold estimation for femtosecond pulsed laser machining of AISI 316L. *Procedia CIRP* **2022**, *107*, 617-622.
(5) Chakraborty, A.; Gottumukkala, N. R.; Gupta, M. C. Superhydrophobic Surface by Laser Ablation of PDMS. *Langmuir* **2023**, *39* (32), 11259-11267. DOI: 10.1021/acs.langmuir.3c00818.
(6) Pakuła, D.; Staszuk, M.; Dziekońska, M.; Kožmín, P.; Čermák, A. Laser Micro-Texturing of Sintered Tool Materials Surface. *Materials (Basel)* **2019**, *12* (19).
(7) Won, S. J.; Kim, H. S. Effects of laser parameters on morphological change and surface properties of aluminum alloy in masked laser surface texturing. *Journal of Manufacturing Processes* **2019**, *48*, 260-269.
(8) Ganesa Balamurugan, K. Effect of Laser Surface Texturing parameters on the texture formation in pure magnesium substrate. *Materials Today: Proceedings* **2023**, *72*, 2096-2101.
(9) Xi, X.; Pan, Y.; Wang, P.; Fu, X. Effect of Laser Processing Parameters on Surface Texture of Ti6Al4V Alloy. *IOP Conference Series: Materials Science and Engineering* **2019**, *563* (2), 022052.
(10) Fujishima, A.; Rao, T. N.; Tryk, D. A. Titanium dioxide photocatalysis. *Journal of Photochemistry and Photobiology C: Photochemistry Reviews* **2000**, *1* (1), 1-21.
(11) Drelich, J.; Chibowski, E. Superhydrophilic and superwetting surfaces: definition and mechanisms of control. *Langmuir* **2010**, *26* (24), 18621-18623.
(12) Otitoju, T. A.; Ahmad, A. L.; Ooi, B. S. Superhydrophilic (superwetting) surfaces: A review on fabrication and application. *Journal of Industrial and Engineering Chemistry* **2017**, *47*, 19-40.
(13) Lobo, A. O.; Marciano, F. R.; Ramos, S. C.; Machado, M. M.; Corat, E. J.; Corat, M. A. F. Increasing mouse embryonic fibroblast cells adhesion on superhydrophilic vertically aligned carbon nanotube films. *Materials Science and Engineering: C* **2011**, *31* (7), 1505-1511.
(14) Machado, M. M.; Lobo, A. O.; Marciano, F. R.; Corat, E. J.; Corat, M. A. F. Analysis of cellular adhesion on superhydrophobic and superhydrophilic vertically aligned carbon nanotube scaffolds. *Materials Science and Engineering: C* **2015**, *48*, 365-371.
(15) Lai, Y.; Lin, C.; Wang, H.; Huang, J.; Zhuang, H.; Sun, L. Superhydrophilic–superhydrophobic micropattern on TiO2 nanotube films by photocatalytic lithography. *Electrochemistry Communications* **2008**, *10* (3), 387-391.
(16) Ashkarran, A. A.; Mohammadizadeh, M. R. Superhydrophilicity of TiO2 thin films using TiCl4 as a precursor. *Materials Research Bulletin* **2008**, *43* (3), 522-530.
(17) Liu, M.; Wang, S.; Wei, Z.; Song, Y.; Jiang, L. Bioinspired Design of a Superoleophobic and Low Adhesive Water/Solid Interface. *Advanced Materials* **2009**, *21* (6), 665-669.
(18) Tang, K.; Wang, X.; Yan, W.; Yu, J.; Xu, R. Fabrication of superhydrophilic Cu2O and CuO membranes. *Journal of Membrane Science* **2006**, *286* (1), 279-284.

(19) Law, W. S.; Lam, S. W.; Gan, W. Y.; Scott, J.; Amal, R. Effect of film thickness and agglomerate size on the superwetting and fog-free characteristics of TiO2 films. *Thin Solid Films* **2009**, *517* (18), 5425-5430.
(20) Zhu, Y.; Zhang, J. C.; Zhai, J.; Jiang, L. Preparation of superhydrophilic α-Fe2O3 nanofibers with tunable magnetic properties. *Thin Solid Films* **2006**, *510* (1), 271-274.
(21) Lavieja, C.; Oriol, L.; Peña, J. I. Creation of Superhydrophobic and Superhydrophilic Surfaces on ABS Employing a Nanosecond Laser. *Materials (Basel)* **2018**, *11* (12).
(22) Pan, R.; Cai, M.; Liu, W.; Luo, X.; Chen, C.; Zhang, H.; Zhong, M. Extremely high Cassie–Baxter state stability of superhydrophobic surfaces via precisely tunable dual-scale and triple-scale micro–nano structures. *Journal of Materials Chemistry A* **2019**, *7* (30), 18050-18062.
(23) Mittal, K. L. Superhydrophobic Surfaces by Microtexturing: A Critical Review. John Wiley & Sons, Ltd, 2021.
(24) Caffrey, P. Superhydrophobic Properties of Replicated Laser Microtextured Surfaces. University of Virginia, Electrical Engineering - School of Engineering and Applied Science, Ph. D. (Doctor of Philosophy), 2015, Charlottesville, VA, 2015.
(25) Vanoss, C. J.; Good, R.; Busscher, H. J. Estimation of the polar surface-tension parameters of glycerol and formamide, for use in contact-angle measurements on polar solids. *Journal of Dispersion Science and Technology* **1990**, *11*, 75-81.
(26) Mulroney, A. Anti-Ice and Condensation Properties of Microtextured Superhydrophobic Surfaces. University of Virginia, Electrical Engineering - School of Engineering and Applied Science, Ph.D. (Doctor of Philosophy), 2019, Charlottesville, VA, 2019.
(27) Yeong, Y. H.; Gupta, M. C. Hot embossed micro-textured thin superhydrophobic Teflon FEP sheets for low ice adhesion. *Surface and Coatings Technology* **2017**, *313*, 17-23.
(28) Chun, D.-M.; Davaasuren, G.; Ngo, C. V.; Kim, C.-S.; Lee, G.-Y.; Ahn, S.-H. Fabrication of transparent superhydrophobic surface on thermoplastic polymer using laser beam machining and compression molding for mass production. *CIRP Annals - Manufacturing Technology* **2014**, *63*.
(29) Ta, V. D.; Dunn, A.; Wasley, T. J.; Li, J.; Kay, R. W.; Stringer, J.; Smith, P. J.; Esenturk, E.; Connaughton, C.; Shephard, J. D. Laser textured superhydrophobic surfaces and their applications for homogeneous spot deposition. *Applied Surface Science* **2016**, *365*, 153-159.
(30) Mulroney, A. T.; Gupta, M. C. Optically transparent superhydrophobic polydimethylsiloxane by periodic surface microtexture. *Surface and Coatings Technology* **2017**, *325*, 308-317.
(31) Park, S.; Huo, J.; Shin, J.; Heo, K. J.; Kalmoni, J. J.; Sathasivam, S.; Hwang, G. B.; Carmalt, C. J. Production of an EP/PDMS/SA/AlZnO Coated Superhydrophobic Surface through an Aerosol-Assisted Chemical Vapor Deposition Process. *Langmuir* **2022**, *38* (25), 7825-7832.
(32) Su, X.; Li, H.; Lai, X.; Zhang, L.; Wang, J.; Liao, X.; Zeng, X. Vapor–Liquid Sol–Gel Approach to Fabricating Highly Durable and Robust Superhydrophobic Polydimethylsiloxane@Silica Surface on Polyester Textile for Oil–Water Separation. *ACS Applied Materials & Interfaces* **2017**, *9* (33), 28089-28099.
(33) Su, X.; Li, H.; Lai, X.; Zhang, L.; Liang, T.; Feng, Y.; Zeng, X. Polydimethylsiloxane-Based Superhydrophobic Surfaces on Steel Substrate: Fabrication, Reversibly Extreme Wettability and Oil-Water Separation. *ACS Appl Mater Interfaces* **2017**, *9* (3), 3131-3141.
(34) Hafiz Muhammad, A.; Muhammad Arslan, Q.; Sullahuddin, M.; Ghulam, M. Techniques for the Fabrication of Super-Hydrophobic Surfaces and Their Heat Transfer Applications. In *Heat Transfer*, Konstantin, V. Ed.; IntechOpen, 2018; p Ch. 14.

(35) Liu, B.; Jiang, G.; Mei, X.; Wang, Z.; Wang, K.; Cui, J. Study on hierarchical structured PDMS for surface super-hydrophobicity using imprinting with ultrafast laser structured models. *Applied Surface Science* **2015**, *364*.
(36) Jiang, T.; Koch, J.; Unger, C.; Fadeeva, E.; Koroleva, A.; Zhao, Q.; Chichkov, B. Ultrashort picosecond laser processing of micro-molds for fabricating plastic parts with superhydrophobic surfaces. *Applied Physics A* **2012**, *108*-115.
(37) Sarbada, S.; Shin, Y. C. Superhydrophobic contoured surfaces created on metal and polymer using a femtosecond laser. *Applied Surface Science* **2017**, *405*, 465-475.
(38) Esmaeilirad, A.; Rukosuyev, M.; Jun, M.; Veggel, F. A cost-effective method to create physically and thermally stable and storable super-hydrophobic aluminum alloy surfaces. *Surface and Coatings Technology* **2015**, *285*.
(39) Chu, F.; Wu, X. Fabrication and condensation characteristics of metallic superhydrophobic surface with hierarchical micro-nano structures. *Applied Surface Science* **2016**, *371*, 322-328.
(40) Xu, J.; Cao, Y.; Ji, X.; Yan, Y. Fabrication of non-flaking, superhydrophobic surfaces using a one-step solution-immersion process on copper foams. *Applied Surface Science* **2013**, *286*, 220-227.
(41) Zhao, J.; Li, Z.; Zhang, M.; Meng, A. Super-hydrophobic surfaces of SiO2-coated SiC nanowires: Fabrication, mechanism and ultraviolet-durable super-hydrophobicity. *Journal of Colloid and Interface Science* **2015**, *444*, 33-37.
(42) Gong, X.; He, S. Highly Durable Superhydrophobic Polydimethylsiloxane/Silica Nanocomposite Surfaces with Good Self-Cleaning Ability. *ACS Omega* **2020**, *5* (8), 4100-4108.
(43) Wu, Y.; Wang, J.; Zhang, D.; Li, L.; Zhu, Y. Preparation and characterization of superhydrophobic surface based on polydimethylsiloxane (PDMS). *Journal of Adhesion Science and Technology* **2019**, *33* (17), 1870-1881.
(44) Li, H.; Chen, T.; Lu, Y.; Fu, X.; Chu, X.; Liu, Q.; Zhang, J. Reversible Superwetting Transition Between Superhydrophilicity and Superhydrophobicity on a Copper Sheet, and Its Corrosion Performance. *Frontiers in Materials* **2021**, *8*.
(45) Ye, X.; Hou, J.; Cai, D. Novel reversibly switchable wettability of superhydrophobic-superhydrophilic surfaces induced by charge injection and heating. *Beilstein J Nanotechnol* **2019**, *10*, 840-847.
(46) Zhou, X.; Yu, S.; Zang, J.; Lv, Z.; Liu, E.; Zhao, Y. Colorful nanostructured TiO2 film with superhydrophobic–superhydrophilic switchable wettability and anti-fouling property. *Journal of Alloys and Compounds* **2019**, *798*, 257-266.
(47) Wang, Z.; Zhu, L.; Li, W.; Liu, H. Rapid Reversible Superhydrophobicity-to-Superhydrophilicity Transition on Alternating Current Etched Brass. *ACS Applied Materials & Interfaces* **2013**, *5* (11), 4808-4814.
(48) Zhu, X.; Zhang, Z.; Wang, K.; Yang, J.; Xu, X.; Men, X.; Zhou, X. A facile route to mechanically durable responsive surfaces with reversible wettability switching. *New Journal of Chemistry* **2012**, *36* (5), 1280-1284, 10.1039/C2NJ00014H.
(49) Wang, J.-N.; Liu, Y.-Q.; Zhang, Y.-L.; Feng, J.; Sun, H.-B. Pneumatic smart surfaces with rapidly switchable dominant and latent superhydrophobicity. *NPG Asia Materials* **2018**, *10*, 470-477.
(50) Majhy, B.; Iqbal, R.; Sen, A. K. Facile fabrication and mechanistic understanding of a transparent reversible superhydrophobic - superhydrophilic surface. *Sci Rep* **2018**, *8* (1), 18018.

(51) Li, X.; Jiang, Y.; Jiang, Z.; Li, Y.; Wen, C.; Lian, J. Reversible wettability transition between superhydrophilicity and superhydrophobicity through alternate heating-reheating cycle on laser-ablated brass surface. *Applied Surface Science* **2019**, *492*.
(52) Yalishev, V. S.; Iqbal, M.; Kim, V. V.; Khan, S. A.; Ganeev, R. A.; Alnaser, A. S. Reversible wettability transition of laser-textured metals after vacuum storing and low-temperature annealing. *Applied Physics A* **2021**, *127* (5), 393.
(53) Long, J.; Zhong, M.; Zhang, H.; Fan, P. Superhydrophilicity to superhydrophobicity transition of picosecond laser microstructured aluminum in ambient air. *J Colloid Interface Sci* **2015**, *441*, 1-9.
(54) Wong, R. C. P.; Hoult, A. P.; Kim, J. K.; Yu, T. X. Improvement of adhesive bonding in aluminium alloys using a laser surface texturing process. *Journal of Materials Processing Technology* **1997**, *63* (1-3), 579-584.
(55) Sharma, M.; Eden, T.; Golesich, B. Effect of Surface Preparation on the Microstructure, Adhesion, and Tensile Properties of Cold-Sprayed Aluminum Coatings on AA2024 Substrates. *Journal of Thermal Spray Technology* **2014**, *24*, 410-422.
(56) Kromer, R.; Costil, S.; Cormier, J.; Berthe, L.; Peyre, P.; Courapied, D. Laser Patterning Pretreatment before Thermal Spraying: A Technique to Adapt and Control the Surface Topography to Thermomechanical Loading and Materials. *Journal of Thermal Spray Technology* **2016**, *25* (3), 401-410.
(57) Kromer, R.; Costil, S.; Verdy, C.; Gojon, S.; Liao, H. Laser surface texturing to enhance adhesion bond strength of spray coatings – Cold spraying, wire-arc spraying, and atmospheric plasma spraying. *Surface and Coatings Technology* **2018**, *352*, 642-653.
(58) Kromer, R.; Costil, S.; Cormier, J.; Courapied, D.; Berthe, L.; Peyre, P.; Boustie, M. Laser surface patterning to enhance adhesion of plasma sprayed coatings. *Surface and Coatings Technology* **2015**, *278*, 171-182.
(59) Zhang, C.; Zhang, D.; Luo, C.; Peng, W.; Zang, X. Nanosecond-Pulse Laser Assisted Cold Spraying of Al–Cu Aluminum Alloy. In *Coatings*, 2021; Vol. 11.
(60) Yilbas, B. S.; Ali, H.; Karatas, C.; Al-Sharafi, A. Laser texturing of Inconel 718 alloy surface: Influence of environmental dust in humid air ambient. *Optics & Laser Technology* **2018**, *108*, 346-354.
(61) Zhu, L.; Xu, Z. F.; Liu, P.; Gu, Y. F. Effect of processing parameters on microstructure of laser solid forming Inconel 718 superalloy. *Optics & Laser Technology* **2018**, *98*, 409-415.
(62) Kulka, M.; Dziarski, P.; Makuch, N.; Piasecki, A.; Miklaszewski, A. Microstructure and properties of laser-borided Inconel 600-alloy. *Applied Surface Science* **2013**, *284*, 757-771.
(63) Xu, Z.; Hyde, C. J.; Tuck, C.; Clare, A. T. Creep behaviour of inconel 718 processed by laser powder bed fusion. *Journal of Materials Processing Technology* **2018**, *256*, 13-24.
(64) Li, X; Guan, Y. Theoretrical fundamentals of short pulse laser-material interaction: A review. *Nanotechnol. Precision Eng.* **2020**, 3, 105-125.
(65) Kam, D. H.; Bhattacharya, S.; Mazumder, J. Control of the wetting properties of an AISI 316L stainless steel surface by femtosecond laser-induced surface modification. *Journal of Micromechanics and Microengineering* **2012**, *22* (10), Article.
(66) Wenzel, R. N. RESISTANCE OF SOLID SURFACES TO WETTING BY WATER. *Industrial & Engineering Chemistry* **1936**, *28* (8), 988-994.
(67) Wang, Z.; Ren, B. Preparation of superhydrophobic titanium surface via the combined modification of hierarchical micro/nanopatterning and fluorination. *Journal of Coatings Technology and Research* **2022**, *19* (3), 967-975.

(68) Aguilar-Morales, A. I.; Alamri, S.; Voisiat, B.; Kunze, T.; Lasagni, A. F. The Role of the Surface Nano-Roughness on the Wettability Performance of Microstructured Metallic Surface Using Direct Laser Interference Patterning. *Materials* **2019**, *12*, 22-54.
(69) Dixit, D.; Ghoroi, C. Role of randomly distributed nanoscale roughness for designing highly hydrophobic particle surface without using low surface energy coating. *Journal of Colloid and Interface Science* **2020**, *564*, 8-18.
(70) Koishi, T.; Yasuoka, K.; Fujikawa, S.; Ebisuzaki, T.; Zeng, X. C. Coexistence and transition between Cassie and Wenzel state on pillared hydrophobic surface. *Proc Natl Acad Sci U S A* **2009**, *106* (21), 8435-8440.
(71) Ambrosia, M.; Ha, M.; Balachandar, S. The effect of pillar surface fraction and pillar height on contact angles using molecular dynamics. *Applied Surface Science* **2013**, *282*, 211-216.
(72) Lima, C. R. C.; Guilemany, J. M. Adhesion improvements of Thermal Barrier Coatings with HVOF thermally sprayed bond coats. *Surface and Coatings Technology* **2007**, *201* (8), 4694-4701.
(73) Crespo, V.; Cano, I. G.; Dosta, S.; Guilemany, J. M. The influence of feedstock powders on the CGS deposition efficiency of bond coats for TBCs. *Journal of Alloys and Compounds* **2015**, *622*, 394-401.
(74) Karaoglanli, A. C.; Dikici, H.; Kucuk, Y. Effects of heat treatment on adhesion strength of thermal barrier coating systems. *Engineering Failure Analysis* **2013**, *32*, 16-22.
(75) Mądry, K.; Nowicki, W. Wetting between Cassie-Baxter and Wenzel regimes: a cellular model approach. *Eur Phys J E Soft Matter* **2021**, *44* (11), 138.
(76) Xiong, L.; Chen, P.; Zhou, Q. Adhesion promotion between PDMS and glass by oxygen plasma pre-treatment. *Journal of Adhesion Science and Technology* **2014**, *28*.
(77) Chau, K.; Millare, B.; Lin, A.; Upadhyayula, S.; Nuñez, V.; Xu, H.; Vullev, V. I. Dependence of the quality of adhesion between poly(dimethylsiloxane) and glass surfaces on the composition of the oxidizing plasma. *Microfluidics and Nanofluidics* **2011**, *10* (4), 907-917.
(78) Lundevall, Å.; Sundberg, P.; Mattsson, L. Improved glass bonding with plasma treatment. *Applied Adhesion Science* **2018**, *6*.
(79) Greczynski, G.; Hultman, L. X-ray photoelectron spectroscopy: Towards reliable binding energy referencing. *Progress in Materials Science* **2020**, *107*, 100591.
(80) Lockwood, D. J. Rayleigh and Mie Scattering. In *Encyclopedia of Color Science and Technology*, Luo, M. R. Ed.; Springer New York, **2016**; 1097-1107.
(81) Chen, Y.; Zhang, Y.; Shi, L.; Jing, L.; Xin, Y.; Yang, T.; Guo, Z. Transparent superhydrophobic/superhydrophilic coatings for self-cleaning and anti-fogging. *Applied Physics Letters* **2012**, *101*, 382-392.
(82) Jayaraj, J. J.; Chandrasekaran, D. M.; Joseph, B.; R B, D.; Govindaraj, M. Superhydrophobic surfaces: a review on fundamentals, applications, and challenges. *Journal of Coatings Technology and Research* **2018**, *12*, 336 - 342.
(83) Khodaei, M. Introductory Chapter: Superhydrophobic Surfaces - Introduction and Applications, Superhydrophobic surfaces - Fabrications to practical applications. InTechOpen. **2020**, 1123 - 1134.
(84) Tyowua, T.; Targema, M.; Ubuo, E. Non-Wettable Surfaces – From Natural to Artificial and Applications: A Critical Review. **2020**; 195-231.
(85) Park, Y.-B.; Im, H.; Im, M.; Choi, Y.-K. Self-cleaning effect of highly water-repellent microshell structures for solar cell applications. *J. Mater. Chem.* **2010**, *21*, 633-636.
(86) Liu, Y.; Ma, L.; Wang, W.; Kota, A.; Hu, H. An Experimental Study on Soft PDMS Materials for Aircraft Icing Mitigation. *Applied Surface Science* **2018**, *447*, 599-609.

(87) Parent, O.; Ilinca, A. Anti-icing and de-icing techniques for wind turbines: Critical review. *Cold Regions Science and Technology* **2011**, *65* (1), 88-96.
(88) Dalili, N.; Edrisy, A.; Carriveau, R. A review of surface engineering issues critical to wind turbine performance. *Renewable and Sustainable Energy Reviews* **2009**, *13* (2), 428-438.
(89) Carriveau, R.; Edrisy, A.; Cadieux, P.; Mailloux, R. Ice Adhesion Issues in Renewable Energy Infrastructure. *Journal of Adhesion Science and Technology - J ADHES SCI TECHNOL* **2012**, *26*, 447-461.
(90) Fakorede, O.; Feger, Z.; Ibrahim, H.; Ilinca, A.; Perron, J.; Masson, C. Ice protection systems for wind turbines in cold climate: characteristics, comparisons and analysis. *Renewable and Sustainable Energy Reviews* **2016**, *65*, 662-675.
(91) Nosonovsky, M.; Bhushan, B. Superhydrophobic surfaces and emerging applications: Non-adhesion, energy, green engineering. *Current Opinion in Colloid & Interface Science* **2009**, *14* (4), 270-280.
(92) Shen, Y.; Wu, X.; Tao, J.; Zhu, C.; Lai, Y.; Chen, Z. Icephobic materials: Fundamentals, performance evaluation, and applications. *Progress in Materials Science* **2019**, *103*, 509-557.
(93) Huang, X.; Tepylo, N.; Pommier-Budinger, V.; Budinger, M.; Bonaccurso, E.; Villedieu, P.; Bennani, L. A survey of icephobic coatings and their potential use in a hybrid coating/active ice protection system for aerospace applications. *Progress in Aerospace Sciences* **2019**, *105*.
(94) Waugh, D.; Avdic, D.; K.J, W.; Lawrence, J. Laser Surface Engineering of Polymeric Materials and the Effects on Wettability Characteristics. 2014.
(95) Qin, C.; Mulroney, A.; Gupta, M. Anti-Icing Epoxy Resin Surface Modified by Spray Coating of PTFE Teflon Particles for Wind Turbine Blades. *Materials Today Communications* **2019**, *22*, 100770.
(96) Dong, H.; Cheng, M.; Zhang, Y.; Wei, H.; Shi, F. Extraordinary drag-reducing effect of a superhydrophobic coating on a macroscopic model ship at high speed. *J. Mater. Chem. A* **2013**, *1*, 5886-5891.
(97) Shahsavari, A.; Nejat, A.; Chini, F. The Potential of Surface Nano-Engineering and Superhydrophobic Surfaces in Drag Reduction. 2019; pp 239-265.
(98) Khorsand, S.; Raeissi, K.; Ashrafizadeh, F. Corrosion resistance and long-term durability of super-hydrophobic nickel film prepared by electrodeposition process. *Applied Surface Science* **2014**, *305*, 498-505.
(99) Xiu, Y.; Liu, Y.; Hess, D. W.; Wong, C. P. Mechanically robust superhydrophobicity on hierarchically structured Si surfaces. *Nanotechnology* **2010**, *21* (15), 155705.
(100) Zhang, D.; Wang, L.; Qian, H.; Li, X. Superhydrophobic surfaces for corrosion protection: a review of recent progresses and future directions. *Journal of Coatings Technology and Research* **2016**, *13* (1), 11-29.
(101) Cucchiella, F.; D'Adamo, I. Estimation of the energetic and environmental impacts of a roof-mounted building-integrated photovoltaic systems. *Renewable and Sustainable Energy Reviews* **2012**, *16* (7), 5245-5259.
(102) Farhadi, S.; Farzaneh, M.; Kulinich, S. A. Anti-icing performance of superhydrophobic surfaces. *Applied Surface Science* **2011**, *257* (14), 6264-6269.
(103) Shirtcliffe, N. J.; McHale, G.; Atherton, S.; Newton, M. I. An introduction to superhydrophobicity. *Advances in Colloid and Interface Science* **2010**, *161* (1), 124-138.
(104) Yeong, Y.; Milionis, A.; Loth, E.; Sokhey, J.; Lambourne, A. Atmospheric Ice Adhesion on Water Repellent Coatings: Wetting and Surface Topology Effects. *Langmuir* **2015**, *31*.

(105) Kronlund, D.; Lindén, M.; Smått, J.-H. A polydimethylsiloxane coating to minimize weathering effects on granite. *Construction and Building Materials* **2016**, *124*, 1051-1058.
(106) Wang, T.; Hu, X.; Dong, S. A general route to transform normal hydrophilic cloths into superhydrophobic surfaces. *Chemical Communications* **2007**, (18), 1849-1851.
(107) Avrămescu, R. E.; Ghica, M. V.; Dinu-Pîrvu, C.; Prisada, R.; Popa, L. Superhydrophobic Natural and Artificial Surfaces-A Structural Approach. *Materials (Basel)* **2018**, *11* (5), 551-564.
(108) Zimmermann, J.; Artus, G. R. J.; Seeger, S. Long term studies on the chemical stability of a superhydrophobic silicone nanofilament coating. *Applied Surface Science* **2007**, *253* (14), 5972-5979.
(109) Wang, H.; Xue, Y.; Ding, J.; Feng, L.; Wang, X.; Lin, T. Durable, self-healing superhydrophobic and superoleophobic surfaces from fluorinated-decyl polyhedral oligomeric silsesquioxane and hydrolyzed fluorinated alkyl silane. *Angew Chem Int Ed Engl* **2011**, *50* (48), 11433-11436. DOI: 10.1002/anie.201105069 From NLM.
(110) Bahners, T.; Gutmann, J. Procedures for the Characterization of Wettability and Surface Free Energy of Textiles - Use, Abuse, Misuse and Proper Use: A Critical Review. *Reviews of Adhesion and Adhesives* **2019**, *7*, 259-293.
(111) Zhang, D.; Guan, L. 4.06 - Laser Ablation. In *Comprehensive Materials Processing*, Hashmi, S., Batalha, G. F., Van Tyne, C. J., Yilbas, B. Eds.; Elsevier, 2014; pp 125-169.
(112) Wang, H.; Chen, Q.; Yao, Y.; Che, L.; Zhang, B.; Nie, H.; Wang, R. Influence of Surface Preprocessing on 4H-SiC Wafer Slicing by Using Ultrafast Laser. In *Crystals*, 2023; Vol. 13.
(113) Otitoju, T. A.; Ahmad, A. L.; Ooi, B. S. Polyvinylidene fluoride (PVDF) membrane for oil rejection from oily wastewater: A performance review. *Journal of Water Process Engineering* **2016**, *14*, 41-59.
(114) Zhang, W.; Zhu, Y.; Liu, X.; Wang, D.; Li, J.; Jiang, L.; Jin, J. Salt-Induced Fabrication of Superhydrophilic and Underwater Superoleophobic PAA-g-PVDF Membranes for Effective Separation of Oil-in-Water Emulsions. *Angewandte Chemie International Edition* **2014**, *53* (3), 856-860.
(115) Zhang, W.; Zhang, F.; Gao, S.; Zhu, Y.; Li, J.; Jin, J. Micro/nano hierarchical poly(acrylic acid)-grafted-poly(vinylidene fluoride) layer coated foam membrane for temperature-controlled separation of heavy oil/water. *Separation and Purification Technology* **2015**, *156*, 207-214.
(116) Antonioli, E.; Lobo, A. O.; Ferretti, M.; Cohen, M.; Marciano, F. R.; Corat, E. J.; Trava-Airoldi, V. J. An evaluation of chondrocyte morphology and gene expression on superhydrophilic vertically-aligned multi-walled carbon nanotube films. *Materials Science and Engineering: C* **2013**, *33* (2), 641-647.
(117) Weng, X.-D.; Ji, Y.-L.; Ma, R.; Zhao, F.-Y.; An, Q.-F.; Gao, C.-J. Superhydrophilic and antibacterial zwitterionic polyamide nanofiltration membranes for antibiotics separation. *Journal of Membrane Science* **2016**, *510*, 122-130.
(118) Lu, T.; Xu, X.; Liu, X.; Sun, T. Super hydrophilic PVDF based composite membrane for efficient separation of tetracycline. *Chemical Engineering Journal* **2017**, *308*, 151-159.
(119) Gong, L.; Zhang, L.; Wang, N.; Li, J.; Ji, S.; Guo, H.; Zhang, G.; Zhang, Z. In situ ultraviolet-light-induced TiO2 nanohybrid superhydrophilic membrane for pervaporation dehydration. *Separation and Purification Technology* **2014**, *122*, 32-40.
(120) Wang, X.; Deng, X.; Bai, Z.; Zhang, X.; Feng, X.; Huang, W. The synthesis of super-hydrophilic and acid-proof Ge–ZSM-5 membranes by simultaneous incorporation of Ge and Al into a Silicalite-1 framework. *Journal of Membrane Science* **2014**, *468*, 202-208.

(121) Shan, L.; Gong, L.; Fan, H.; Ji, S.; Zhang, G. Spray-assisted biomineralization of a superhydrophilic water uptake layer for enhanced pervaporation dehydration. *Journal of Membrane Science* **2017**, *522*, 183-191.
(122) Huang, W.; Chen, Y.; Yang, C.; Situ, Y.; Huang, H. pH-driven phase separation: Simple routes for fabricating porous TiO2 film with superhydrophilic and anti-fog properties. *Ceramics International* **2015**, *41* (6), 7573-7581.
(123) Wang, J.-H.; Zhu, L.-P.; Zhu, B.-K.; Xu, Y.-Y. Fabrication of superhydrophilic poly(styrene-alt-maleic anhydride)/silica hybrid surfaces on poly(vinylidene fluoride) membranes. *Journal of Colloid and Interface Science* **2011**, *363* (2), 676-681.
(124) Léonard, G. L. M.; Remy, S.; Heinrichs, B. Overview of Superhydrophilic, Photocatalytic and Anticorrosive Properties of TiO2 Thin Films Doped with Multi-walled Carbon Nanotubes and Deposited on 316L Stainless Steel. *Materials Today: Proceedings* **2016**, *3* (2), 434-438.
(125) Sorcar, S.; Razzaq, A.; Tian, H.; Grimes, C. A.; In, S.-I. Facile electrochemical synthesis of anatase nano-architectured titanium dioxide films with reversible superhydrophilic behavior. *Journal of Industrial and Engineering Chemistry* **2017**, *46*, 203-211.
(126) Choi, M.; Xiangde, L.; Park, J.; Choi, D.; Heo, J.; Chang, M.; Lee, C.; Hong, J. Superhydrophilic coatings with intricate nanostructure based on biotic materials for antifogging and antibiofouling applications. *Chemical Engineering Journal* **2017**, *309*, 463-470.
(127) Töpper, T.; Lörcher, S.; Weiss, F.; Müller, B. Tailoring the mass distribution and functional group density of dimethylsiloxane-based films by thermal evaporation. *APL Materials* **2016**, *4* (5).
(128) Chen, H.; Li, X.; Li, D. Superhydrophilic–superhydrophobic patterned surfaces: From simplified fabrication to emerging applications. *Nanotechnology and Precision Engineering (NPE)* **2022**, *5* (3).
(129) Bakhtiari, N.; Azizian, S.; Jaleh, B. Hybrid superhydrophobic/hydrophilic patterns deposited on glass by laser-induced forward transfer method for efficient water harvesting. *Journal of Colloid and Interface Science* **2022**, *625*, 383-396.
(130) Idrees, M.; Liu, L.; Batool, S.; Luo, H.; Liang, J.; Xu, B.; Wang, S.; Kong, J. Cobalt-doping enhancing electrochemical performance of silicon/carbon nanocomposite as highly efficient anode materials in lithium-ion batteries. *Engineered Science* **2019**, *6*, 64-76.
(131) Xiao, W.; Zheng, Y.; He, H. Cascade extraction of lithium in anode of waste lithium ion battery. *Chin J Rare Metals* **2020**, *44* (10), 1078.
(132) Zhang, X.; Xie, Y.; Lin, X.; Li, H.; Cao, H. An overview on the processes and technologies for recycling cathodic active materials from spent lithium-ion batteries. *Journal of Material Cycles and Waste Management* **2013**, *15*, 420-430.
(133) Zeng, X.; Li, J.; Shen, B. Novel approach to recover cobalt and lithium from spent lithium-ion battery using oxalic acid. *Journal of hazardous materials* **2015**, *295*, 112-118.
(134) Sattar, R.; Ilyas, S.; Bhatti, H. N.; Ghaffar, A. Resource recovery of critically-rare metals by hydrometallurgical recycling of spent lithium ion batteries. *Separation and Purification Technology* **2019**, *209*, 725-733.
(135) Li, Y.; Wang, X.; Wang, Z.; Chen, L. Facile synthesis of SnO2 nanorods for Na-ion batteries. *ES Energy & Environment* **2019**, *3* (3), 55-59.
(136) Wang, M.; Tan, Q.; Liu, L.; Li, J. A low-toxicity and high-efficiency deep eutectic solvent for the separation of aluminum foil and cathode materials from spent lithium-ion batteries. *Journal of hazardous materials* **2019**, *380*, 120846.
(137) Wang, H.; Huang, K.; Zhang, Y.; Chen, X.; Jin, W.; Zheng, S.; Zhang, Y.; Li, P. Recovery of lithium, nickel, and cobalt from spent lithium-ion battery powders by selective ammonia

leaching and an adsorption separation system. *ACS Sustainable Chemistry & Engineering* **2017**, *5* (12), 11489-11495.
(138) Cano, Z. P.; Banham, D.; Ye, S.; Hintennach, A.; Lu, J.; Fowler, M.; Chen, Z. Batteries and fuel cells for emerging electric vehicle markets. *Nature Energy* **2018**, *3* (4), 279-289.
(139) Zhang, X.; Li, L.; Fan, E.; Xue, Q.; Bian, Y.; Wu, F.; Chen, R. Toward sustainable and systematic recycling of spent rechargeable batteries. *Chemical Society Reviews* **2018**, *47* (19), 7239-7302.
(140) Zhao, X.-C.; Yang, P.; Yang, L.-J.; Cheng, Y.; Chen, H.-Y.; Liu, H.; Wang, G.; Murugadoss, V.; Angaiah, S.; Guo, Z. Enhanced electrochemical performance of Cu2+ doped TiO2 nanoparticles for lithium-ion battery. *ES Materials & Manufacturing* **2018**, *1* (5), 67-71.
(141) Fan, E.; Li, L.; Zhang, X.; Bian, Y.; Xue, Q.; Wu, J.; Wu, F.; Chen, R. Selective recovery of Li and Fe from spent lithium-ion batteries by an environmentally friendly mechanochemical approach. *ACS Sustainable Chemistry & Engineering* **2018**, *6* (8), 11029-11035.
(142) Tan, Q.; Li, J. Recycling metals from wastes: a novel application of mechanochemistry. *Environmental science & technology* **2015**, *49* (10), 5849-5861.
(143) Chen, X.; Chen, Y.; Zhou, T.; Liu, D.; Hu, H.; Fan, S. Hydrometallurgical recovery of metal values from sulfuric acid leaching liquor of spent lithium-ion batteries. *Waste Management* **2015**, *38*, 349-356.
(144) Yan, L.; Wang, H.; Huang, D.; Luo, H. Electrodes with high conductivities for high performance lithium/sodium ion batteries. *Engineered Science* **2018**, *1* (27), 4-20.
(145) Peng, C.; Liu, F.; Wang, Z.; Wilson, B. P.; Lundström, M. Selective extraction of lithium (Li) and preparation of battery grade lithium carbonate (Li2CO3) from spent Li-ion batteries in nitrate system. *Journal of Power Sources* **2019**, *415*, 179-188.
(146) Li, H.; Oraby, E.; Eksteen, J. Extraction of copper and the co-leaching behaviour of other metals from waste printed circuit boards using alkaline glycine solutions. *Resources, Conservation and Recycling* **2020**, *154*, 104624.
(147) Xu, M.; Kang, S.; Jiang, F.; Yan, X.; Zhu, Z.; Zhao, Q.; Teng, Y.; Wang, Y. A process of leaching recovery for cobalt and lithium from spent lithium-ion batteries by citric acid and salicylic acid. *RSC Adv* **2021**, *11* (44), 27689-27700. DOI: 10.1039/d1ra04979h From NLM.
(148) Daulay, A.; Marpongahtun, A.; Gea, S. Synthesis and application of silicon nanoparticles prepared from rice husk for lithium-ion batteries, *Case Studies in Chemical and Environmental Engineering*, **2022**, 6, 100256.
(149) Tzeng, Y.; Chen, R.; He, J.-L. Silicon-Based Anode of Lithium Ion Battery Made of Nano Silicon Flakes Partially Encapsulated by Silicon Dioxide. *Nanomaterials* **2020**, *10*, 2467.

List of Publications

- Chakraborty, A., Chalfant, B., Sions, J. *et al.* Improvement of thermal plasma sprayed coating adhesion strength by laser microtexturing of aluminum. *Int J Adv Manuf Technol* 125, 2629–2642 (2023). DOI:10.1007/s00170-023-10859-7

- Chakraborty, A.; Mulroney, A.; Gupta, M. C. Superhydrophobic surfaces by microtexturing: A critical review. *Prog. Adhes. Adhes*. 2021 6, 621-649. DOI:10.1002/9781119846703.ch14

- Chakraborty, A.; Gottumukkala, N. R.; Gupta, M. C. Superhydrophobic Surface by Laser Ablation of PDMS. *Langmuir* 32, 11259-11267 (2023). DOI: 10.1021/acslangmuir.3c00818

- Chakraborty, A.; Gupta, M.C. Reversible extreme wettability using laser microtexturing, to be submitted to Applied Surface Science journal (under preparation)

- Presented a paper on laser microtexturing technique to improve adhesion strength of metallic micro powder coatings at SLIMS conference/workshop in Venice, Italy.

List of Patents

- Gupta, M. C.; Gottumukkala, Chakraborty, A. Superhydrophobic surfaces by transfer of laser ablated PDMS nano/microparticles and related methods and systems. US Patent No:63/357237. UVA License and Ventures Group (filed for full patent)

- Gupta, M. C.; Chakraborty, A.; Chalfant, B. Improvement of thermal plasma sprayed coating adhesion strength by laser microtexturing of aluminum and related compositions. US Patent No: 63/357458. UVA License and Ventures Group (filed for full patent)

Collection of Published Works

Superhydrophilic and Superhydrophobic surfaces with reversible wettability using laser processing (under preparation)

Anustup Chakraborty, and Mool C. Gupta

Abstract – Laser surface microtexturing has become increasingly popular due to its low-cost, scalability, automation, and lack of use of hazardous chemicals. Laser surface microtexturing can be used to control the wettability of various surfaces by varying surface roughness for a wide range of applications. In recent years, the reversible transition between superhydrophobicity and superhydrophilicity has gained significant attention due to a variety of applications, including self-cleaning, corrosion protection, anti-icing, microfluidics, water harvesting, and thermal management. The ability to manipulate liquid behavior facilitates processes like coalescence, rolling, and pinning. However, the current methods of making reversible superhydrophilic-superhydrophobic surfaces have several disadvantages, such as complex fabrication processes, use of high temperatures and chemicals, time-consuming, and high costs. This paper presents a facile, low-cost laser microtexturing method capable of inducing superhydrophilicity with a contact angle (CA) of less than 1° on surfaces. Additionally, by applying a thin polydimethylsiloxane (PDMS) coating, the microtextured surface can be rendered superhydrophobic with a CA of 169°. Furthermore, the thin PDMS layer can be easily removed by laser ablation, thereby restoring the superhydrophilic behavior, thus allowing to achieve a reversible transition between superhydrophilicity and superhydrophobicity. As an example, the reversibility is shown for transparent surface glass and aluminum. The laser method also allows the fabrication of selective areas having superhydrophilic and superhydrophobic properties.

The International Journal of Advanced Manufacturing Technology
https://doi.org/10.1007/s00170-023-10859-7

ORIGINAL ARTICLE

Improvement of thermal plasma sprayed coating adhesion strength by laser microtexturing of aluminum

Anustup Chakraborty[1] · Benjamin Chalfant[2] · John Sions[2] · Ben Zimmerman[2] · Mool C. Gupta[1]

Received: 17 August 2022 / Accepted: 10 January 2023

Abstract
Grit blasting and laser processing are two common methods used for surface microtexturing to enhance coating adhesion strength. This paper reports a thermomechanical method of laser microtexturing of Al 7075 alloy using a nanosecond pulsed laser to generate a large increase in surface area. The entire surface area of the substrate was microtextured using laser melting, ablation, and resolidification. The laser microtextured surface morphology consisted of tightly packed pillar-like surface features. The morphology of the microtexture was varied by controlling the laser processing parameters. The laser microtextured surface was coated with metallic particles using a thermal spray process. The tensile adhesive strength of the thermally sprayed metallic coating was higher by over 17% for a 5-μm deep microtexture, compared to that of grit-blasted samples. Also, this is the highest reported adhesion strength for laser-based microtexturing methods for thermally sprayed bond coatings.

Keywords Laser microtexturing · Thermally sprayed coating · Adhesion strength · Coatings · Laser processing

1 Introduction

Surface microtexturing has been utilized to improve the surface properties of materials. Some of the widely used surface microtexturing techniques are chemical etching, electrical discharge, and sandblasting [1]. Among the different surface microtexturing techniques, grit-blasting or sandblasting is a widely used method, but it does not allow selective roughening or generation of repeated patterns. Grit-blasting also leads to grit particle entrapment [2]. One of the alternative techniques for surface microtexturing is using a laser. Laser microtexturing can provide several advantages, easy automation, localized treatment, and three-dimensional profiles [3]. Surface microtexturing by laser is a low-cost and scalable method and eliminates the use of hazardous chemicals [4].

The adhesion strength between thermally sprayed metallic coating and the substrate improves when the surface is microtextured. Preparation of the substrates before being coated by the thermal spray process involves two steps: cleaning and roughening. Chemicals can be used to clean (degrease) the surface [5], while the roughening process can be performed by grit blasting or laser [6]. An increased coating contact area is favorable for increased adhesion bond strength. The laser wavelength, spot size, scanning rate, pulse duration, and pulse frequency can be optimized for enhanced adhesion [3]. However, low adhesion strength poses a serious problem to thermally sprayed coatings [7].

The formation of nanosecond laser-induced microtexture can be explained by localized surface melting, ablation, and the formation of superheated droplets around the solid surface [8]. The laser pulse energy density and frequency influence the shape and height of the surface features considerably. Increasing laser fluence and frequency results in the expulsion of more molten materials, which could lead

✉ Mool C. Gupta
mgupta@virginia.edu

Anustup Chakraborty
ac3xa@virginia.edu

Benjamin Chalfant
benjamin.chalfant@ccam-va.com

John Sions
john.sions@ccam-va.com

Ben Zimmerman
ben.zimmermann@ccam-va.com

[1] Charles L. Brown Department of Electrical and Computer Engineering, University of Virginia, Thornton Hall, 351 McCormick Road, Charlottesville, VA 22904, USA

[2] Commonwealth Center for Advanced Manufacturing, Disputanta, VA 23842, USA

Published online: 24 January 2023

to wider grooves and increased height of the resolidified surface microtexture. The laser parameters can be used to control the microtexture that influences the bonding strength of the thermal spray coatings.

Laser surface microtexturing improves the bond strength of thermally sprayed coatings by creating a mechanically interlocked bond between the substrate and the coating. Thermally sprayed metallic powder particles fill the pores on the surface created by laser microtexturing, and this results in a strong bond between the surface and the coating [9]. The thermally sprayed coating that is adhered to the surface by a mechanical interlocking mechanism has been classified into five types — embedding, anchoring, holding-on, spreading, and a mixture of several styles [10]. Depending on the material, both mechanical and physicochemical bonds can exist, and the bonding mechanism is influenced by particle–substrate contact time, contact temperature, and contact area upon impact [11]. It should also be noted that the adhesion strength is not only dependent on the contact area ratio and the density of the features but also varies with the microtexture shape and pattern [10, 12]. The thermal spray process parameters can also be optimized to enhance the adhesion strength as well. Adhesion strength can be significantly increased by increasing the particle velocity and keeping the particle temperature constant or by increasing the particle temperature and keeping the particle velocity at a fairly high constant value [13]. Other thermal spray process parameters, like gas flow rate and spray distance may also be optimized to get a potentially superior adhesion strength.

Among the most commonly used metals for the thermal spray process, aluminum has high-surface energy and provides strong resistance to corrosion in aggressive environments. Aluminum alloys have had a long history of usage in the construction, automotive, aviation, and astronautic industries [14, 15]. It greatly benefits from the favorable properties offered by adhesive bonding due to its excellent formidability and the high strength-to-weight ratio [14]. So, the focus of this study is on laser microtexturing of Al alloy Al-7075 and the improvement of adhesion strength of thermal spray coatings.

Extensive studies have been done on the adhesion strength of thermally sprayed coatings on surface microtextured aluminum alloys. A study on the improvement of adhesive bonding in aluminum alloys using surface microtexturing was done by Wong et al. [16] and Sharma et al. [17]. The substrates were grit-blasted using three different grit-blasting techniques, and the coating was deposited using the thermal spray process. Grit-blasted samples had significantly higher adhesion strength, compared to untextured samples. Kromer et al. [18] measured the tensile adhesion strength of NiAl powder coating on the Al 2017 substrates, as they are widely used in aircraft structural applications. NiAl powder with a mean particle size of 67 μm was thermally sprayed onto the laser-textured aluminum alloy substrates. The adhesion test results showed that a decreasing density of holes on the metal surface causes a reduction in the adhesion strength of the thermally sprayed coating. The maximum reported adhesion strength was 52 MPa. Kromer et al. [7] also measured the adhesion strength of thermal spray coatings on grit-blasted and laser-microtextured aluminum alloy. A separate study was done by Kromer et al. [6], where laser microtextured and grit-blasted aluminum 2017 alloy samples were coated with NiAl powder (Amdry 956) using thermal spray. The samples were microtextured using a pulsed laser. Kromer et al. [6] also studied the strength of bond coats on a laser microtextured superalloy substrate. The maximum reported adhesive bond strength was 33 MPa. A recent study done by Zhang et al. [19] used a nanosecond pulsed laser to induce microtexture on the surface of aluminum alloy. This laser microtexture improved the bond strength of the Al-Cu aluminum alloy coating that was cold-sprayed on the aluminum alloy. The maximum reported bond strength was around 48 MPa. There is a need for further improvement of the adhesion strength of thermal spray coatings on Al alloys for long-duration operation.

In this paper, a full-area method of laser microtexturing is reported, and a superior coating adhesion strength of bond coats is demonstrated. The traditional laser microtexturing method is based primarily on the ablation process. The laser microtexturing process described in this paper is primarily based on the thermomechanical rearrangement of the molten material with very low ablation. The laser microtexturing is based on selecting the laser power in such a way that it offers melting combined with low ablation, and the laser beam is scanned over the entire surface area. Hence, a series of closely packed peaks and valleys are formed on the surface, which gives the thermally sprayed coating powder more grip due to enhanced surface area. The improvement in the coating adhesion strength would lead to increased longevity, robustness, and lower maintenance costs of metal parts and has potential applications in the automobile, power generation, and aerospace industries.

2 Experiment

2.1 Material

The substrates used were McMaster-Carr aluminum alloy (Al 7075) micromachined samples (diameter = 1 inch; thickness — 0.5 inches) polished down to a roughness of less than 1 μm. The chemical composition by weight of Al 7075 is supplied by the manufacturer and is given in Table 1. The coating powders used for the thermal spray process were Oerlikon Metco Amdry 995C (CoNiCrAlY) and Oerlikon Metco Amdry 9951 (Co[Ni]CrAlY)). CoNiCrAlY is usually

Table 1 Al 7075 alloy composition (as obtained from the manufacturer)

Material Type	Al 7075
Al wt%	89.77
Zn wt%	5.4
Mg wt%	2.42
Cu wt%	1.42
Fe wt%	0.42
Cr wt%	0.21
Si wt%	0.13
Mn wt%	0.12

used for bond coats [20–22]. The mean particle sizes of the powders were 90 µm and 38 µm, respectively. The different particle sizes were chosen to demonstrate the effect of particle size on surface morphology.

2.2 Laser microtexturing

A ytterbium fiber laser (YLP-G-10, IPG Photonics) of 532 nm wavelength, 10-W average power pulse width of 1.3 ns, pulse energy of 20.2 µJ, the repetition frequency of 600 kHz, and Gaussian beam profile was used in this study. The galvanometer scan head used was a SCANcube 14, SCANLAB, with a scan pattern designed in EZCad (Beijing JCZ Technology Co. Ltd). The laser repetition rate varied from 400 to 600 kHz, and a focused laser beam with a full width at a half-maximum (FWHM) size of 20 µm was used. The laser fluence used for the experiments was 0.76 J/cm^2, 0.92 J/cm^2, and 0.8 J/cm^2. The laser beam scan speed was maintained at 60 mm/s. For each laser fluence, the side-to-side overlap between the lines was 50%. The overlap between the laser spots along the direction of scanning was 99.25% and 99.5% at 400 kHz and 600 kHz, respectively. A galvanometer (SCANLAB SCANcube 14) controlled by a custom LabVIEW program was used to perform the raster scan of the aluminum surface. This enabled us to achieve consistent microtexture patterns on the sample. A nitrogen gas atmosphere was used during laser microtexturing to prevent oxidation. The pressure of the gas was maintained at 5 MPa. A schematic diagram of the experimental setup is shown in Fig. 1. The different laser parameters used in the microtexturing process are shown in Table 2.

Table 2 Laser processing parameters (laser wavelength = 532 nm, scan speed = 60 mm/s, No. of scans = 1); line #1, line #2, and line #3 indicate the use of different process parameters

Pattern index	Frequency (kHz)	Fluence (J/cm^2)
Line #1	400	0.76
Line #2	400	0.92
Line #3	600	0.80

Table 3 Grit-blasting parameters

Blast media	Alumina (~50-µm particle size)
Pressure	0.28 MPa
Nozzle distance	~140 mm
Nozzle angle	70°
Nozzle traverse speed	1000 mm/s
Passes	2 orthogonal passes

2.3 Grit blasting

The thermal spray coating samples were prepared on grit-blasted samples. For this process, the samples were secured to a plate using double-sided tape to ensure they remained stationary during abrasive blasting. The nozzle was rastered over the samples using the nominal parameters, as shown in Table 3. The raster scan was performed using a custom LabVIEW program on a computer using a controller that was connected to the nozzle. Thereafter, compressed air was

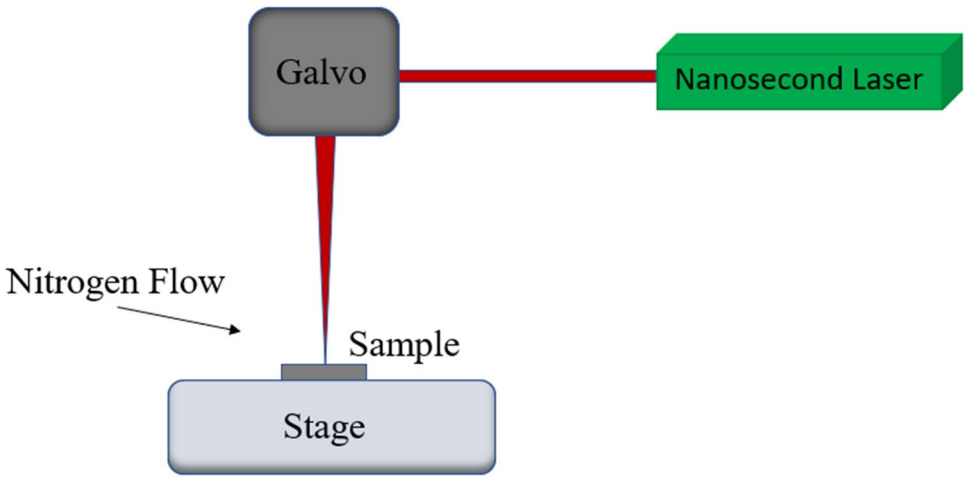

Fig. 1 Laser experimental setup with a galvanometer that can control laser scanning in 2D directions for laser processing of aluminum substrates

used on the samples to remove any residual dust. Then, the sample surface was cleaned with ethanol.

2.4 Thermal spray process

The grit-blasted and the laser microtextured samples were coated with metal powders by atmospheric plasma spray (APS) using an Oerlikon Metco F4MB-XL plasma gun attached to a 6-axis robotic arm. The first step of this process involved cleaning the grit-blasted and laser microtextured samples with compressed air. This was followed by attaching the samples to vertical fixtures. Thereafter, the thermal spray gun was turned on and passed over the substrate in a rectangular raster pattern. Before applying the powder, a pre-heat was executed to elevate the substrate temperature to 100 °C, and the powder feed was allowed to stabilize for 1–2 min before the deposition. Table 4 provides the different APS parameters used in this study.

2.5 Coating adhesion testing and failure analysis

The coated samples were subjected to tensile adhesion testing, where the tensile pressure required to debond the coatings was measured. This was done following the ASTM C633 standard using an Instron C633 mechanical analyzer. As shown in Fig. 2, the cylindrical sample was glued between two cylindrical rods. The load was applied in the direction perpendicular to the interface between the coating and the substrate. The tensile load was gradually increased until the coating was ruptured or detached from the substrate. The glue used in the process was Polyamide-epoxy FM 1000 Adhesive Film. The adhesion strength was calculated from the load at sample failure divided by the coating area [23].

Table 4 Deposition parameters for a thermal spray for Amdry 9951 and 995C powders

APS parameters	Amdry 9951	Amdry 995C
Carrier gas	Argon	Argon
Carrier gas flow rate (nlpm)	4.5	3.5
Powder feeding rate (g/min)	60.5	60.1
Spray distance (mm)	120	120
Number of passes	10	10
Surface speed (mm/s)	1250	1250
Plasma temperature (°C)	2922	2612
Particle velocity (m/s)	210	166
Gun current (A)	600	600
Primary gas type	Argon	Argon
Primary gas flow rate (nlpm)	56.8	56.9
Secondary gas type	Hydrogen	Hydrogen
Secondary gas flow rate (nlpm)	8.5	57
Injector standoff distance (mm)	6	6
Water flow rate (lpm)	15.6	15.7

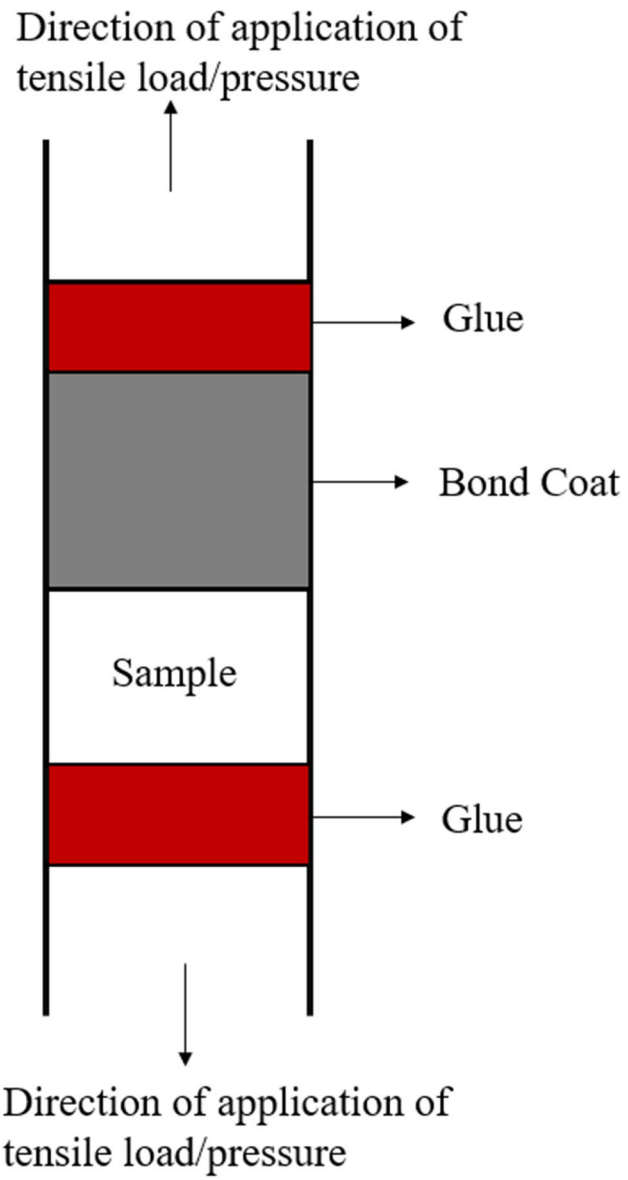

Fig. 2 Sample assembled for tensile adhesion testing; bond coat — coating layer that is attached to the sample; top coat — coating layer that is attached to the glue

2.6 Surface morphology and chemical composition characterization

The surface morphology and elemental analysis were done using FEI Quanta 650 Field Emission SEM. 3D optical profile measurements were done using an Olympus LEXT OLS4000 3D Laser Microscope to understand the variation in the microtexture heights, the peak-to-valley spacing, and the density and uniformity of the features. After the

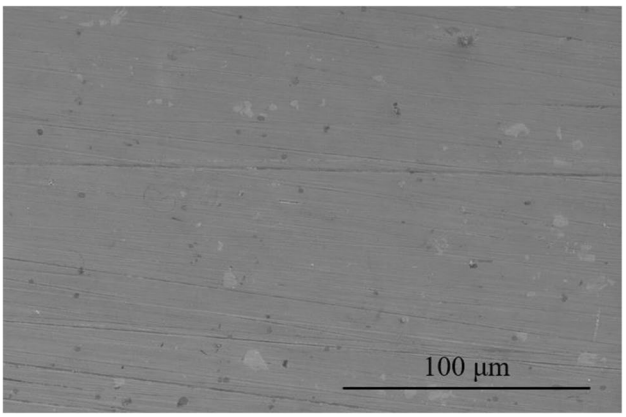

Fig. 3 SEM image of untextured Al 7075 surface

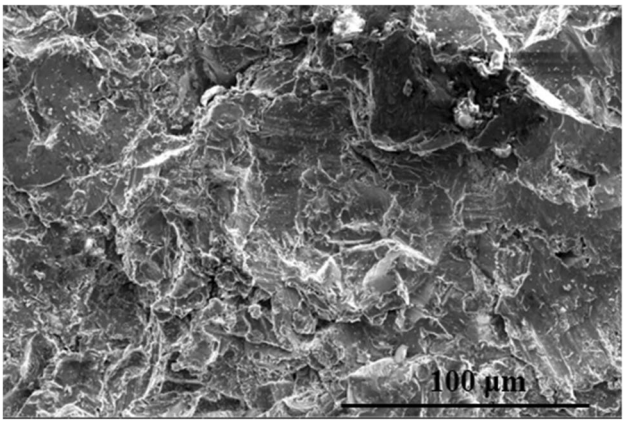

Fig. 4 SEM image of the surface of a grit-blasted sample

deposition of the coating, the cross-sectional morphology characterization and EDS analysis were also performed using the FEI Quanta 650 Field Emission SEM.

3 Results

3.1 Surface morphology

As a reference, Fig. 3 shows the surface of a plane untextured aluminum sample, while the surface of a grit-blasted sample is shown in Fig. 4. In grit-blasting, alumina particles hit the aluminum surface at a very high velocity, causing plastic deformation. The deformation is dependent on the velocity, shape, size, and hardness of the alumina particles [24].

Figure 5 shows the variation of the surface morphology with changing laser fluences. It can be seen that at higher laser fluences, the ablation is much more significant than at lower ones. The fluence at which the laser starts to mark features on the surface is between 0.38 J/cm^2 and 0.45 J/cm^2.

Figure 6 shows the variation of the surface morphology with changing laser repetition rate (frequency). Keeping the fluence constant, the number of laser pulses hitting the surface per second at a lower frequency is significantly less than that at a higher frequency. This provides less time for the molten surface material to cool down, resulting in higher temperatures and, subsequently, more ablation. Hence, the laser rearranges the molten material differently at higher frequencies compared to lower ones. As can be seen, the surface seems much more ablated and roughened at higher frequencies.

Figure 7 shows the different laser surface microtextured patterns. It can be seen that pillar-like structures have been formed on the surface with periodic grooves due to the thermomechanical process of melting and resolidification combined with some ablation. The thermally sprayed molten powders enter into the grooves and thus provide interlocking. The surface shown in Fig. 7(c) was obtained with the highest number of pulses per unit area, compared to the other two surfaces. The three laser microtextured patterns were chosen in such a way that it provides a range of variations in feature height and spacing between the peaks. Looking at the morphology, some resolidified droplet formation appears to occur, which further reinforces the process of melting, ablation, and resolidification of the material. On the other hand, the surface features reported by Kromer et al. [6, 7, 18] consist of a series of uniform holes drilled on the aluminum surface by laser ablation. Since the spacing between these holes was greater than 100 µm, the increase in the surface area was much less than that obtained by the full-area microtexturing method reported in this paper.

Figure 8 quantifies the micropillar height variations. The average height for the laser microtextured features was around 5 µm which is less than the average surface feature height of 6.5 µm for grit-blasted surfaces. There are considerable height variations on the laser microtextured and grit-blasted samples, with maximum heights reaching up to 27 µm, 28.2 µm, 41.6 µm, and 61.48 µm for line #1, line #2, line #3, and line #4 respectively. The average distance between the peaks in all the laser microtextured patterns was 5 µm. Compared to this, the depth of the laser-ablated holes on the aluminum surface reported by Kromer et al. [6, 7, 18] is 25–80 µm. Even though a larger hole depth results in a larger increase in surface area, it takes more time and does not always necessarily imply full infiltration by the thermally sprayed coating.

Figure 9 shows the surface morphology variation of a grit-blasted aluminum sample. It can be observed that there is no periodicity in the features formed on the surface as the grits impact the surface in a randomized manner.

Figures 10, 11, and 12 provide a detailed surface profile for the three laser microtexture patterns shown in Fig. 7. The 2D map shows the differences in height and density of the

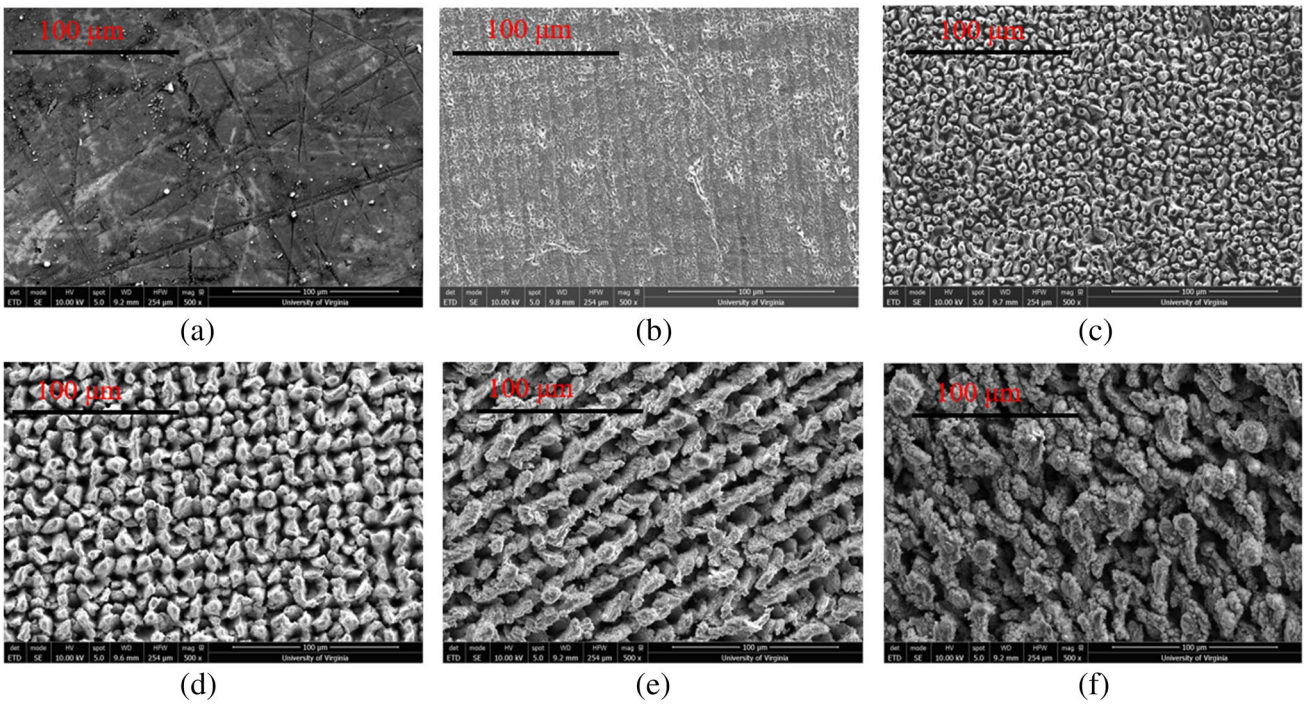

Fig. 5 **a** SEM image of untextured aluminum surface; SEM image of laser microtextured aluminum surface at a fluence of **b** 0.38 J/cm^2, **c** 0.45 J/cm^2, **d** 0.61 J/cm^2, **e** 0.76 J/cm^2, and **f** 0.91 J/cm^2. The frequency and the scanning speed were kept constant at 400 kHz and 60 mm/s, respectively

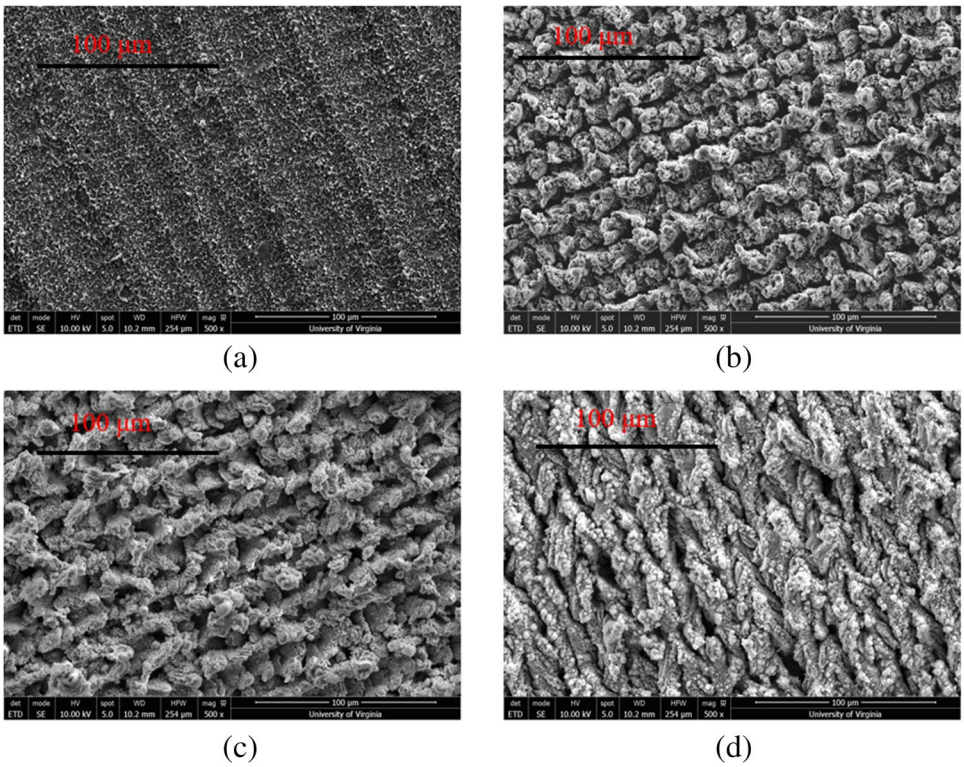

Fig. 6 SEM image of laser microtextured aluminum surface at **a** 20 kHz, **b** 200 kHz, **c** 300 kHz, and **d** 600 kHz. The laser fluence and the scanning speed were kept constant at 0.916 J/cm^2 and 60 mm/s, respectively

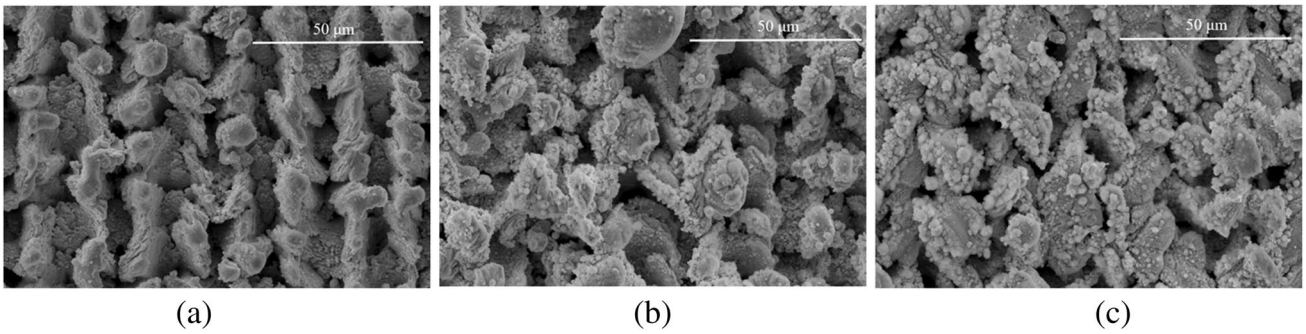

Fig. 7 **a** SEM image of laser microtextured (0.763 J/cm^2, 60 mm/s, and 400 kHz) aluminum sample; **b** SEM image of laser textured (0.916 J/cm^2, 60 mm/s, and 400 kHz) aluminum sample; **c** SEM image of laser microtextured (0.803 J/cm^2, 60 mm/s, and 600 kHz) aluminum sample

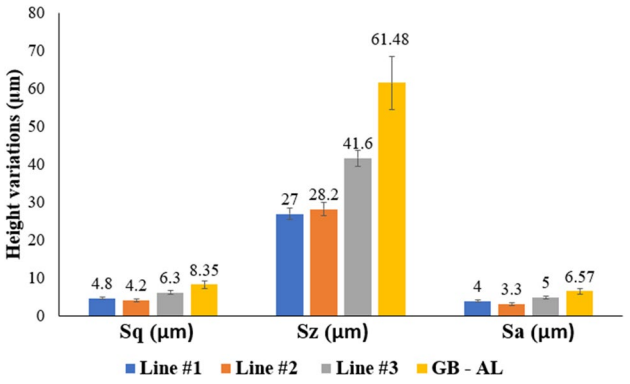

Fig. 8 Feature height variations on aluminum substrate. Line #1 — 0.763 J/cm^2, 60 mm/s, and 400 kHz; line #2 — 0.916 J/cm^2, 60 mm/s, and 400 kHz; and line #3 — 0.803 J/cm^2, 60 mm/s, and 600 kHz; GB — grit-blasted. Sq, RMS roughness; Sz, max peak to max valley distance; Sa, average roughness; The line # denotes the different laser parameters used

features across the surface, while the 3D map gives a more thorough visualization of the distribution of the features. It can also be observed that line #2 has higher peaks than those of line #1, and line #3 has higher peaks than those of line #1 and line #2. This can be attributed to the fact that line #3 had the highest number of laser pulses per unit area, and line #2 had more laser fluence than line #1. Since the scan speed was kept constant, the laser frequency and fluence are the two main factors controlling the height of the peaks on the surface. These two parameters are closely associated with each other in controlling the height of the micropillars.

The cross-sectional interface morphology of the laser microtextured samples (line #2) and the thermally sprayed coating are shown in Figs. 13 and 14. The EDS spectra in Figs. 13 and 14 show the oxygen concentration at the sample — Amdry 995C interface and sample-9951 interface. Even though nitrogen gas was constantly blown on the samples during the laser microtexturing process to displace the oxygen in the air, the samples still showed some oxidation. The oxidation could be further reduced by increasing the gas

Fig. 9 3D surface profile of a grit-blasted sample

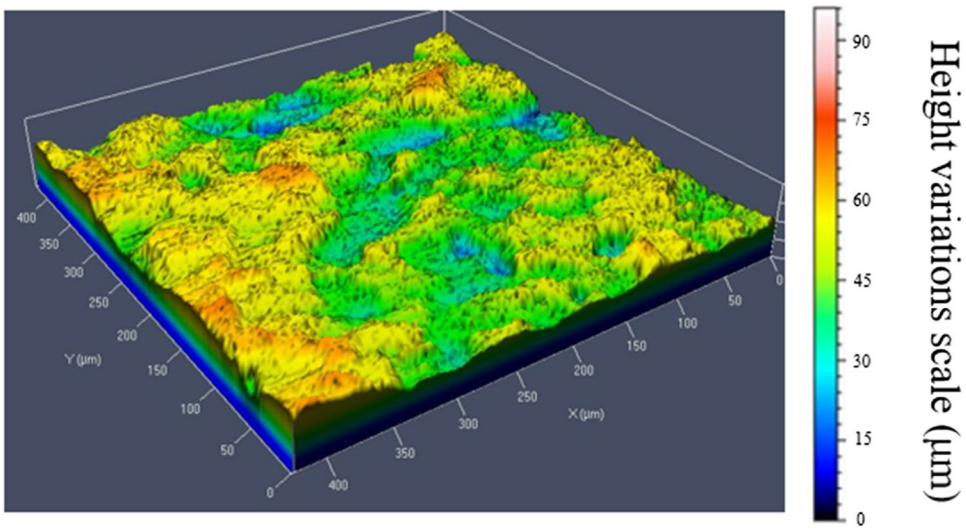

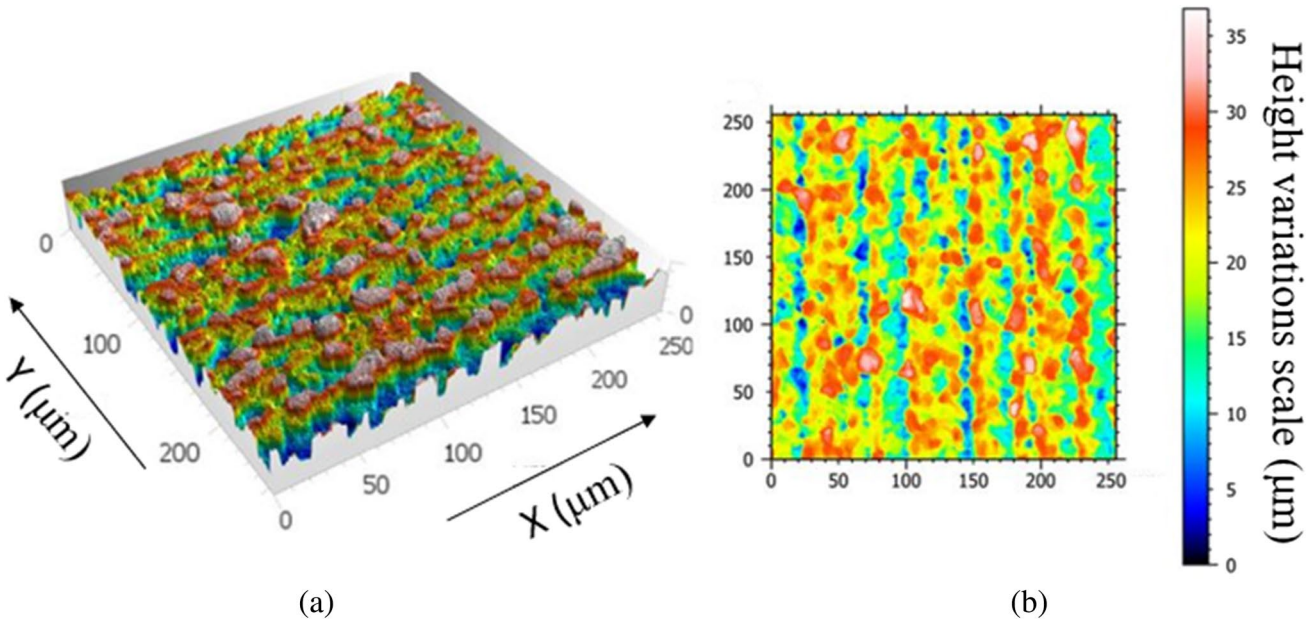

Fig. 10 **a** 3D surface profile of line #1 and **b** 2D surface profile of line #1; axis scales are in microns

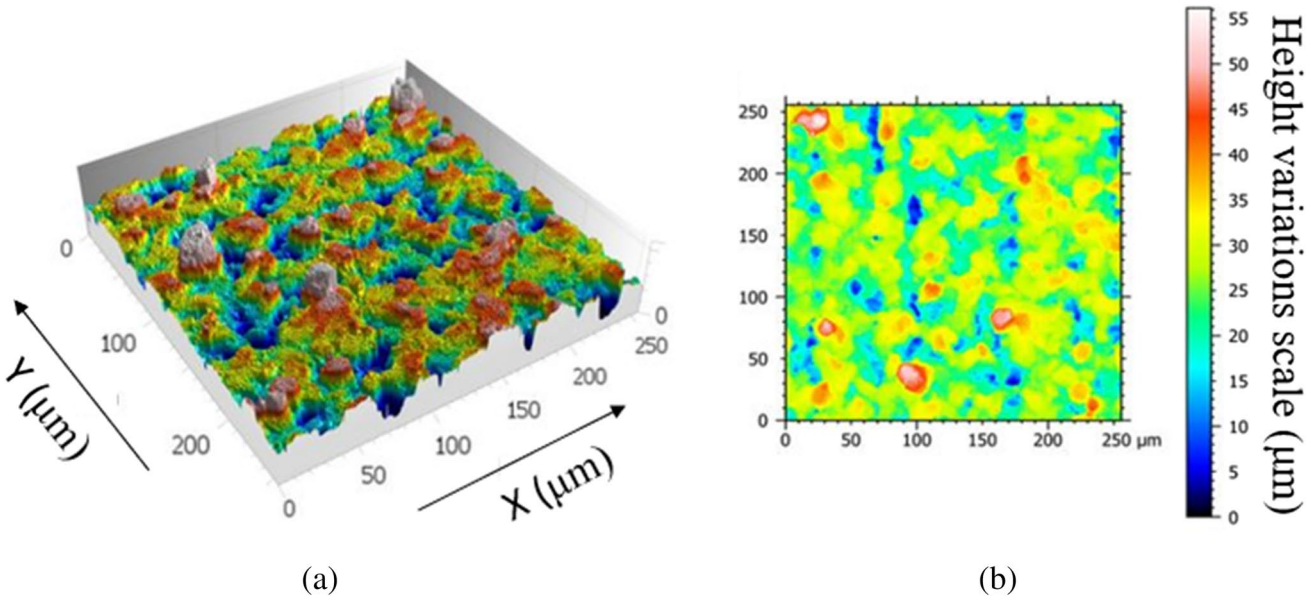

Fig. 11 **a** 3D surface profile of line #2 and **b** 2D surface profile of line #2; axis scales are in microns

flow rate on the surface of the sample. However, the samples would need to be in a vacuum to prevent oxidation entirely. Oxidation can also happen during the thermal spray process, depending on the thermal spray parameters and the kind of coating powder used.

Figure 15 shows the cross-sectional interface morphology of the grit-blasted sample and for thermal sprayed Amdry 995C particles. It can be seen that the coating on the grit-blasted sample has much less infiltration than that on the laser microtextured surfaces. This is because of the absence of dense periodic grooves on the surface of the grit-blasted samples. Hence, even though the grit-blasted surface has the maximum peak-to-valley distance, its surface features are non-periodic and more spaced out, compared to those of the laser microtextured surfaces. The average thickness of the coating was found to be around 275 μm.

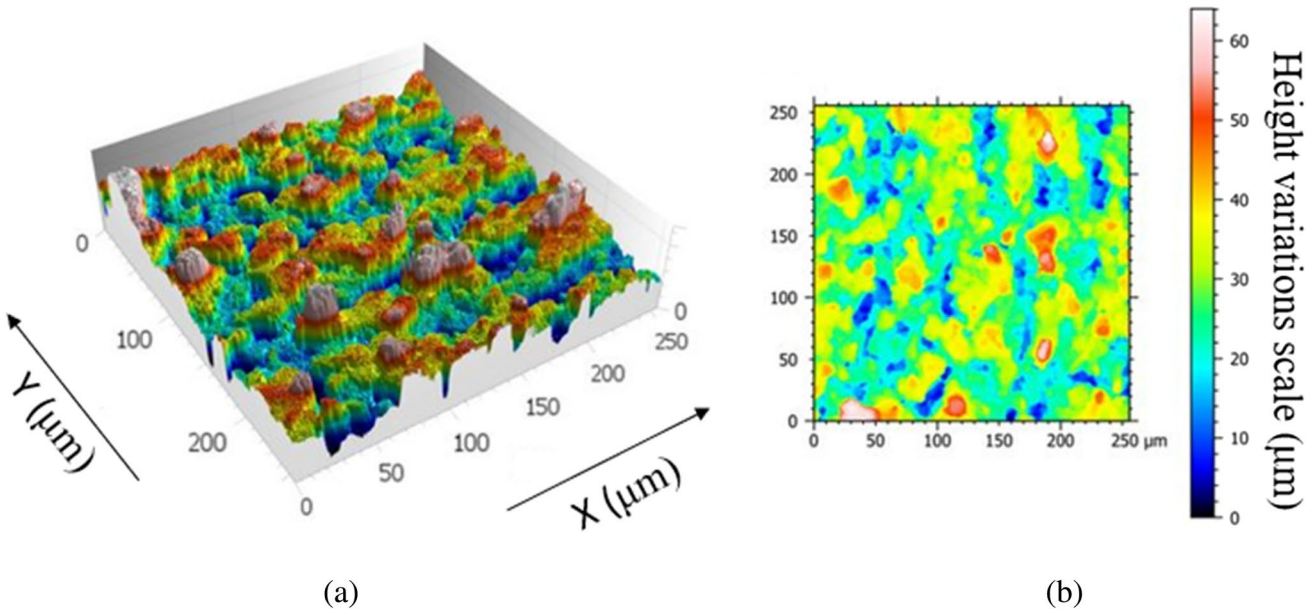

Fig. 12 **a** 3D surface profile of line #3 and **b** 2D surface profile of line #3; axis scales are in microns

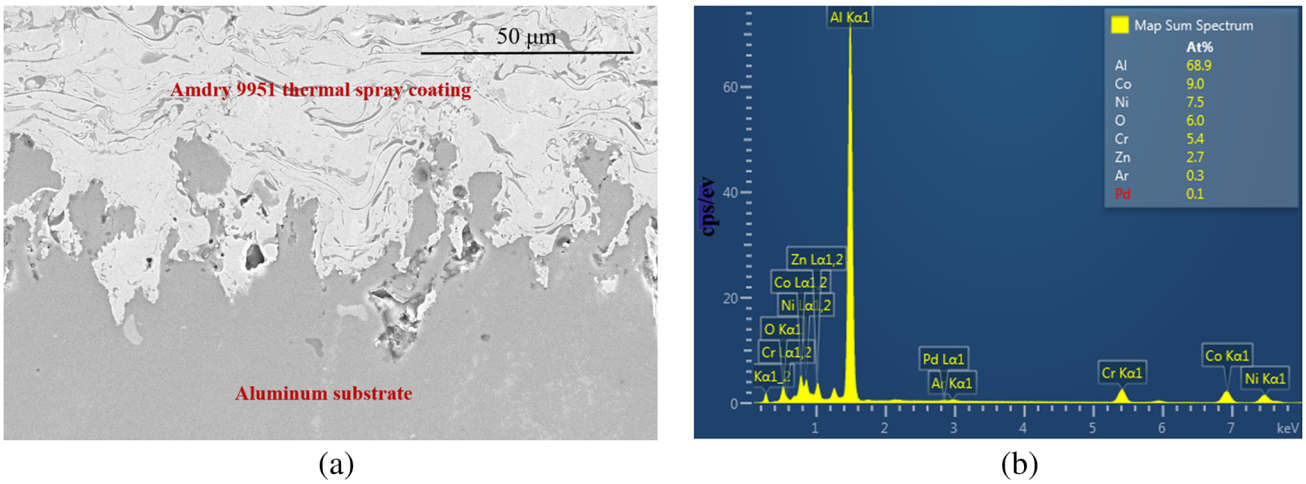

Fig. 13 **a** SEM cross-section image of the interface of line #3 and Amdry 9951; **b** EDS spectra showing the elemental composition of the interface of line #3 and Amdry 9951; and line #3 — 0.803 J/cm^2, 60 mm/s, and 600 kHz

3.2 Wettability and surface energy study

The water wettability and the surface energy of the laser microtextured surfaces were investigated using contact angle measurements. The measurements were done using a Ramè-hart Goniometer model 250. The surface energy of the aluminum was measured to be 852.46 ± 0.95 mN/m. The untextured aluminum surface was found to be mildly hydrophilic with water contact angles (CA) of 81° ± 6°. On the other hand, the laser microtextured aluminum surfaces were found to be highly hydrophilic, exhibiting water contact angles of 25° ± 8°. This behavior can be explained by the fact that the water contact angle on a flat hydrophilic surface decreases with an increase in surface area, as expressed by Wenzel's equation [25, 26]:

$$\cos\Theta_r = r\cos\Theta_f \quad (1)$$

where Θ_f is the contact angle of water on an ideally smooth flat surface; Θ_r is the contact angle of water on a rough surface with r as the roughness parameter ($r = 1$ for smooth surfaces and $r > 1$ for rough surfaces).

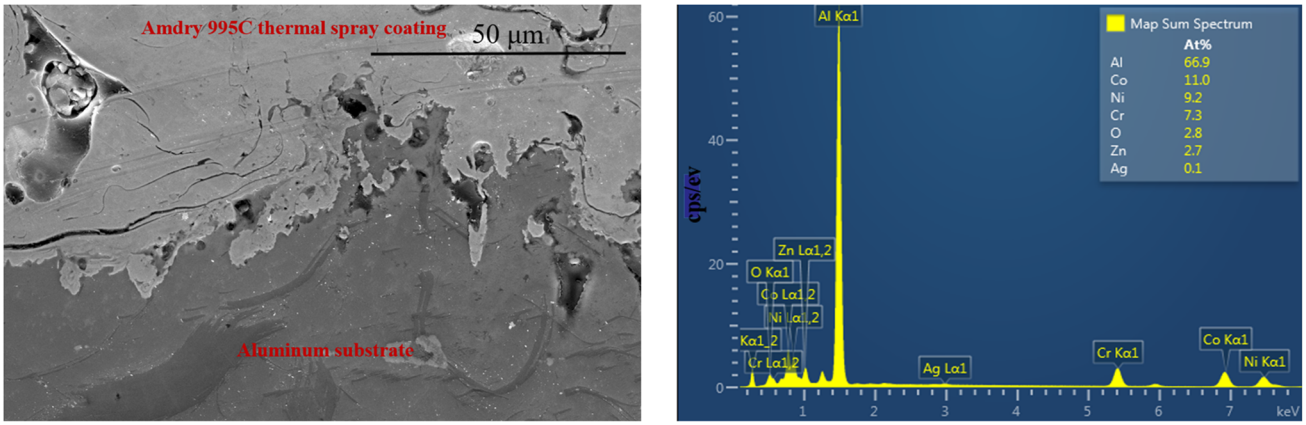

Fig. 14 **a** SEM cross-section image of the interface of line #3 and Amdry 995C; **b** EDS spectra showing the elemental composition of the interface of line #3 and Amdry 995C; and line #3 — 0.803 J/cm^2, 60 mm/s, and 600 kHz

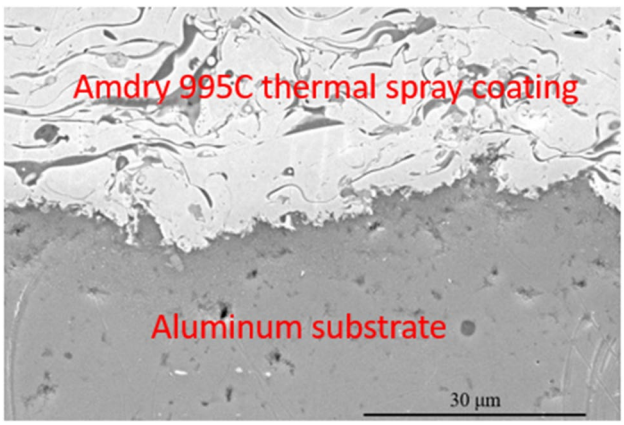

Fig. 15 SEM cross-section image of the interface of grit-blasted (GB) surface and Amdry 995C

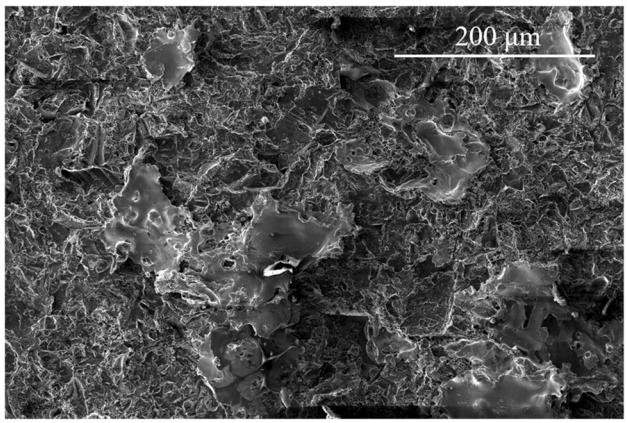

Fig. 16 Surface showing thermally sprayed coating on grit-blasted aluminum sample after tensile adhesion measurement test has been performed. Coating failure shows delamination of the thermally sprayed coating on a grit-blasted aluminum sample after the adhesion testing

3.3 Failure analysis

Figure 16 shows the thermally sprayed surface coating on the grit-blasted aluminum sample after the tensile adhesion test has been performed. Delamination can be observed across the surface of the coating in the case of the grit-blasted sample. The grit-blasted sample displayed cohesive failure at the epoxy-coating interface as well as adhesive failure, while the laser microtextured sample displayed only adhesive failure at the epoxy-thermal spray coating interface at the sample pull-off pressure.

3.4 Adhesion strength measurement results

We obtained significantly higher tensile adhesive strength for laser microtextured surfaces, compared to those reported in previous laser microtexturing research studies [6, 7, 17–19]. Our results are shown in Fig. 17. Four samples were tested for each of the laser microtexturing and grit-blasting methods to obtain the adhesion data and the associated error bars. The laser microtextured patterns in our study were significantly denser than those reported in previous literature, as the laser was used to scan the surface area of the samples in its entirety. Thus, it can be proven that densely packed features are beneficial in increasing bonding strength.

4 Discussion

The features on the surface that are formed by melting, ablation, and resolidification of the materials are affected by the different laser parameters like fluence, pulse width, speed,

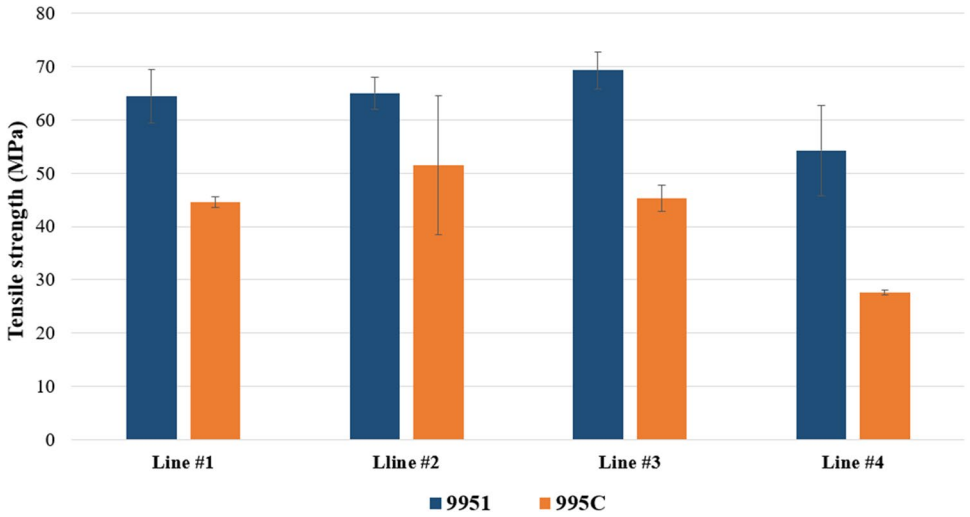

Fig. 17 Adhesion strength for grit-blasted and laser micro-textured samples. Line #1 — 0.763 J/cm^2, 60 mm/s, and 400 kHz; line #2 — 0.916 J/cm^2, 60 mm/s, and 400 kHz; line #3 — 0.803 J/cm^2, 60 mm/s, and 600 kHz; and line #4 — grit-blasted. Lines #1, #2, and #3 denote the different laser parameters used

and frequency. The increase in laser frequency leads to an increased number of pulses per unit of surface area. This gives rise to deeper surface features, increased surface area, and hence, increased adhesion of the coating. The depth and density of the features can be controlled by changing the fluence and frequency of the laser. Moreover, higher laser power results in the ablation of more surface materials which leads to the formation of more particles. These particles can settle down and resolidify on top of the surface "pillars," providing nanoscale roughness which can further increase the adhesion of the coating. Feature height needs to be chosen so that the microtexture is stable under atmospheric plasma spray (APS) processing conditions.

The mechanism behind the formation of the pulsed laser-induced micropillars can be explained by ripple-like structures formed during the early stages of the microstructure evolution. Interference between the incident and the scattered laser light at the surface, heat-mass transfer, and hydrodynamic and plasmonic effects are the possible reasons behind the creation of the ripples. These ripples are broken down gradually as the microstructure develops, giving rise to the micropillars. The breaking down of the ripples can be attributed to molten material expansion and sputtering caused by the recoil pressure of the laser-matter interaction [27, 28]. The expelled molten material drops cool down drastically as soon as it leaves the laser-irradiated area. The effect of the recoil pressure on the molten material ceases to exist as the surface temperature drops below the vaporization point at the end of the laser pulse. Finally, gravitational forces and surface tension make the molten material settle back down on the surface [10].

The influence of the laser power density on the melt depth can be obtained by solving a one-dimensional heat conduction problem in the liquid and solid regions of the laser-irradiated area [29]. The penetration depth $X(t)$ can be expressed as a function of the laser power density I and irradiation time t as follows [29]:

$$X(t) = \left[-\frac{b_0}{2} + \left(\frac{b_0^2}{4} + \frac{a_0^3}{27}\right)^{1/2}\right]^{1/3} + \left[-\frac{b_0}{2} - \left(\frac{b_0^2}{4} + \frac{a_0^3}{27}\right)^{1/2}\right]^{1/3} - \frac{\alpha_l m_s}{16AI} \tag{2}$$

where

$$a_0 = \frac{3\alpha_l^2 m_s^2}{256(AI)^2}\left(\frac{192(AI)^2 t}{\alpha_l m_s^2} + 31\right) \tag{3}$$

$$b_0 = -\frac{\alpha_l}{8AI}\left[\frac{\alpha_l^2 m_s^2}{256(AI)^2}\left(\frac{288(AI)^2 t}{\alpha_l m_s^2} + 47\right) + \frac{t\left(18(AI)^2 t + 3\alpha_l m_s^2\right)}{m_s}\right] \tag{4}$$

$$m_s = \rho\left[c_p\left(T_m - T_0\right) + L\right] \tag{5}$$

Here α_l is the thermal diffusivity in the liquid phase; T_m is the melting point; ρ is the density; c_p is the specific heat of materials in a solid phase; A is the absorptivity of materials; L is the latent heat of fusion; and T_0 is the initial temperature.

Furthermore, the temperature profile $T_s\,(x,t)$ in the solid metal region and the temperature distribution $T_l\,(x,t)$ in the liquid region is given as follows:

$$T_s(x,t) = T_m - \left(T_m - T_0\right)\left\{1 - \exp\left[-\frac{1}{\alpha_s}\frac{\mathrm{d}X(t)}{\mathrm{d}t}(x - X(t))\right]\right\}, X(t) \le x < \infty \tag{6}$$

$$T_l(x,t) = T_m - \frac{AI}{k_l}[x - X(t)] + \frac{AI}{2\alpha_l k_l\left[1 + \frac{X(t)}{\alpha_l}\frac{\mathrm{d}X(t)}{\mathrm{d}t}\right]} \times \frac{\mathrm{d}X(t)}{\mathrm{d}t}\left[x^2 - X^2(t)\right], 0 \le x \le X(t) \tag{7}$$

where x is the distance from the surface of the substrate; k_l is the thermal conductivity in the liquid phase; α_s is the thermal diffusivity in the solid phase; and AI is the absorbed laser power density.

The influence of the laser power density on the melt depth can be obtained by solving a one-dimensional heat conduction problem in the liquid and solid regions of the laser-irradiated area [29].

It should be noted that for all the laser microtextured and even the grit-blasted surfaces, the adhesion strength of Amdry 9951 powder is more than that of Amdry 995C powder. This is because the mean particle size of Amdry 9951 powder is much smaller, compared to Amdry 995C powder. This allows for increased infiltration of the molten particles into the laser-generated microtexture, thereby providing more tensile adhesive strength, as shown in Fig. 18. Optimizing coating-substrate adhesion requires adaptation of the powder size to the surface topography to achieve a superior surface filling ratio [9]. The average laser-formed feature height in this work was around 5 µm, compared to feature depths of 80–180 µm reported in previous laser studies [6, 7]. Hence, the throughput of the full-area laser microtexturing method is higher, and the associated cost will be much lower.

Compared to grit-blasting, which only provides macroscale roughness, the fully microtextured laser method provides superior control and micro-scale roughness. The maximum adhesion strength reported in the scientific literature for thermally sprayed Amdry 9951 (CoNiCrAlY) bond coat to laser microtextured surface is around 52 MPa [18]. This value is comparable to that of the measured grit-blasted samples, which is around 55 MPa. In this paper, we have demonstrated the adhesion strength of bond coat to laser microtextured samples of 65 MPa, which is an increase of around 17%.

Some of the other potential applications of improved adhesion strength thermal spray coatings include oxidation and hot corrosion resistance of airfoils, turbine buckets, ceramic clearance control coatings, exhaust manifolds, flue gas, and fly ash systems. So, the method of surface mictrotexturing presented in this paper could have a wide range of varied applications in improving the adhesion strength of thermally sprayed coatings on other metals and alloys.

5 Conclusion

The key points presented in this paper are as follows:

(i) This paper demonstrates a novel method for laser microtexturing through a thermomechanical process of creating dense, uniform pillar-like features for the improvement of coating adhesion strength. The entirety of the area of the surface was laser microtextured by forming densely populated micropillars, and this led to an increase of around 65% in the total surface area. The micro "pillar"-like shape of the microtexture significantly increases the contact area ratio, and this led to a substantial increase in the adhesion strength of atmospheric plasma sprayed metallic coatings.

(ii) The control of laser power and frequency allowed the variation of micropillar height to over 40 µm. The micropillars contributed to a substantial increase in the atmospheric plasma sprayed coating adhesion strength, compared to untextured, grit-blasted, and

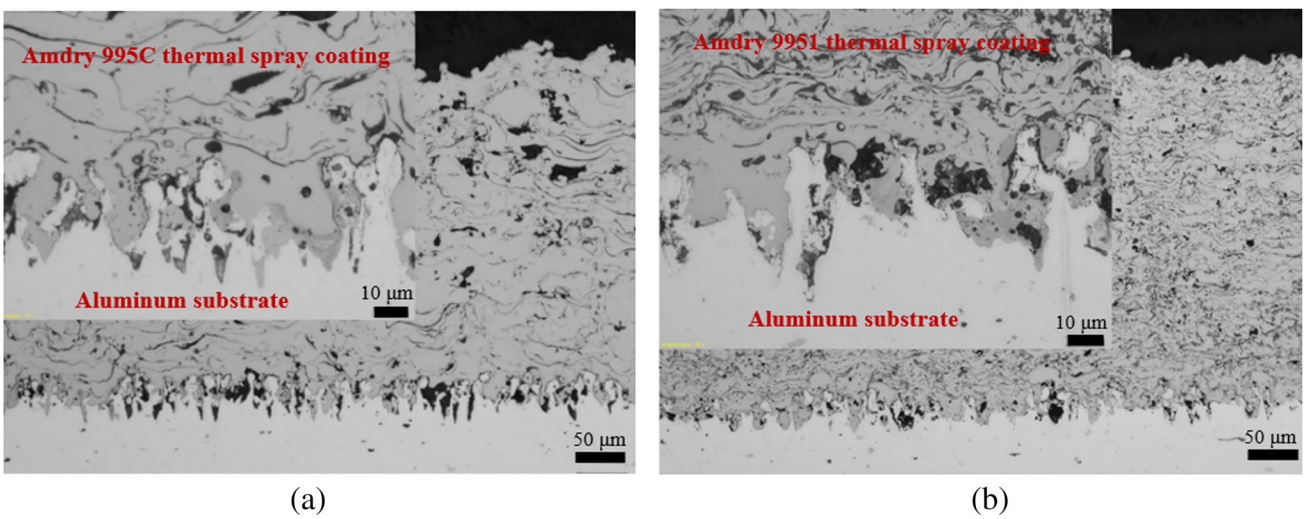

Fig. 18 Interface showing **a** infiltration of Amdry 995C powder on laser microtextured surface and **b** infiltration of Amdry 9951 on laser microtextured surface. Infiltration of Amdry 9951 into the grooves is much more than that of 995C due to the smaller mean particle size

other laser microtextured surfaces, as reported in the literature.

(iii) The increase in bond strength was measured and explained due to thermally sprayed particles filling the gap between the pillars. The results of the laser microtexturing process parameter's effect on surface morphology are reported. The cross-section of the thermally sprayed coating of laser microtextured surfaces was studied to provide an understanding of adhesion strength improvements.

Funding This work was supported by the 2020 CCAM Innovation award, NSF IUCRC, and the Langley Professor award.

Declarations

Competing interests The authors declare no competing interests.

References

1. Lamraoui A, Costil S, Langlade C, Coddet C (2010) Laser surface texturing (LST) treatment before thermal spraying: a new process to improve the substrate-coating adherence. Surf Coat Technol 205:164–167. https://doi.org/10.1016/j.surfcoat.2010.07.044
2. Bagade VU, Duraiselvam M, Sarangi N (2022) Effect of laser surface texturing on coating adherence and tribological properties of CuNiIn and MoS_2 coating. Trans Indian Inst Met 75:239–250. https://doi.org/10.1007/s12666-021-02417-0
3. Kromer R, Danlos Y, Aubignat E, Verdy C, Costil S (2017) Coating deposition and adhesion enhancements by laser surface texturing – metallic particles on different classes of substrates in cold spraying process. Mater Manuf Process 32:1642–1652. https://doi.org/10.1080/10426914.2017.1364750
4. Mulroney AT, Gupta MC (2017) Optically transparent superhydrophobic polydimethylsiloxane by periodic surface microtexture. Surf Coat Technol 325:308–317. https://doi.org/10.1016/j.surfcoat.2017.06.066
5. Garcia-Alonso D, Serres N, Demian C, Costil S, Langlade C, Coddet C (2011) Pre-/during-/post-laser processes to enhance the adhesion and mechanical properties of thermal-sprayed coatings with a reduced environmental impact. J Therm Spray Technol 20:719–735. https://doi.org/10.1007/s11666-011-9629-x
6. Kromer R, Costil S, Cormier J, Courapied D, Berthe L, Peyre P, Boustie M (2015) Laser surface patterning to enhance adhesion of plasma sprayed coatings. Surf Coat Technol 278:171–182. https://doi.org/10.1016/j.surfcoat.2015.07.022
7. Kromer R, Costil S, Verdy C, Gojon S, Liao H (2018) Laser surface texturing to enhance adhesion bond strength of spray coatings – cold spraying, wire-arc spraying, and atmospheric plasma spraying. Surf Coat Technol 352:642–653. https://doi.org/10.1016/j.surfcoat.2017.05.007
8. Long J, Cuo Z, Lin C, Zhou C, He Z, Xie X (2019) Formation mechanism of hierarchical micro- and nanostructures on copper induced by low-cost nanosecond lasers. Appl Surf Sci 464:412–421. https://doi.org/10.1016/j.apsusc.2018.09.055
9. Kromer R, Cormier J, Costil S (2016) Role of powder granulometry and substrate topography in adhesion strength of thermal spray coatings. J Therm Spray Technol 25:933–945. https://doi.org/10.1007/s11666-016-0411-y
10. Tan N, Xing Z, Wang X, Wang H, Jin G, Xu B (2017) Effects of texturing patterns on the adhesion strength of atmosphere plasma sprayed coatings. J Mater Res 32:1682–1692. https://doi.org/10.1557/jmr.2017.164
11. Kromer R, Danlos Y, Costil S (2018) Cold gas-sprayed deposition of metallic coatings onto ceramic substrates using laser surface texturing pre-treatment. J Therm Spray Technol 27:809–817. https://doi.org/10.1007/s11666-018-0718-y
12. Zhan X, Liu Y, Yi P (2021) Effect of substrate surface texture shapes on the adhesion of plasma-sprayed Ni-based coatings. J Therm Spray Technol 30:270–284. https://doi.org/10.1007/s11666-020-01126-2
13. Lyphout C, Nylén P, Östergren LG (2011) Relationships between process parameters, microstructure, and adhesion strength of HVOF sprayed IN718 coatings. J Therm Technol 20:76–82. https://doi.org/10.1007/s11666-010-9543-7
14. Spadaro C, Sunseri C, Dispenza C (2007) Laser surface treatments for adhesion improvement of aluminum alloys structural joints. Radiat Phys Chem 76:1441–1446. https://doi.org/10.1016/j.radphyschem.2007.02.047
15. Kadleckova M, Minarik A, Smolka P, Mracek A, Wrzecionko E, Novak L, Musilova L, Gajdosik R (2018) Preparation of textured surface on aluminium-alloy substrates. Materials (Basel) 12:109–120. https://doi.org/10.3390/ma12010109
16. Wong RCP, Houk AP, Kim JK, Yu TX (1997) Improvement of adhesive bonding in aluminum alloys using a laser surface texturing process. J Mater Process Technol 63:579–584. https://doi.org/10.1016/S0924-0136(96)02687-8
17. Sharma MM, Eden TJ, Golesich BT (2015) Effect of surface preparation on the microstructure, adhesion, and tensile properties of cold-sprayed aluminum coatings on AA2024 substrates. J Therm Spray Technol 24:410–422. https://doi.org/10.1007/s11666-014-0175-1
18. Kromer R, Costil S, Cormier J, Berthe L, Peyre P, Courapied D (2016) Laser patterning pretreatment before thermal spraying: a technique to adapt and control the surface topography to thermomechanical loading and materials. J Therm Spray Technol 25:401–410. https://doi.org/10.1007/s11666-015-0352-x
19. Zhang C, Zhang D, Luo C, Peng W, Zang X (2021) Nanosecond pulse laser assisted cold spraying of Al–Cu aluminum alloy. Coatings 11:267–272. https://doi.org/10.3390/coatings11030267
20. Lima CRC, Guilemany JM (2007) Adhesion improvements of thermal barrier coatings with HVOF thermally sprayed bond coats. Surf Coat Technol 201:4694–5470. https://doi.org/10.1016/j.surfcoat.2006.10.005
21. Crespo V, Cano IG, Dosta S, Guilemany JM (2015) The influence of feedstock powders on the CGS deposition efficiency of bond coats for TBCs. J Alloys Compd 622:394–401. https://doi.org/10.1016/j.jallcom.2014.09.216
22. Karaoglanli AC, Dikici H, Kucuk Y (2013) Effects of heat treatment on adhesion strength of thermal barrier coating systems. Eng Fail Anal 32:16–22. https://doi.org/10.1016/j.engfailanal.2013.02.029
23. ASM Thermal Spray Society (TSS), Accepted practice to test bond strength of thermal spray coatings. https://www.asminternational.org/documents/17679604/17683439/AcceptedPracticeBondStrengthApprovedformatted_Intro.pdf/4bcf5903-414d-413f-ab69-7cf0cc9123bd. Accessed 24 Aug 2021
24. Lambiase F, Liu F (2022) Recent advances in metal-polymer joining processes. In Rakesh P, Davim P (ed) Mechanical engineering series, joining processes for dissimilar and advanced materials, 3rd edn. Woodhead Publishing Reviews: Mechanical Engineering Series, pp 123–151

25 Wenzel RN (1936) Resistance of solid surfaces to wetting by water. Ind Eng Chem 28:988–994. https://doi.org/10.1021/ie50320a024
26. Madry K, Nowicki W (2021) Wetting between Cassie-Baxter and Wenzel regimes: a cellular model approach. Eur Phys J E 44: 138–149. https://link.springer.com/article/10.1140/epje/s10189-021-00140-8
27. Nayak BK, Gupta MC (2010) Self-organized micro/nano structures in metal surfaces by ultrafast laser irradiation. Opt Lasers Eng 48:940–949. https://doi.org/10.1016/j.optlaseng.2010.04.010
28. Zhang J, Zhang S, Chen G, Jia Z, Qu Y, Guo Z (2022) Laser micro-texture formation mechanism based on modified heat-mass transfers and hydrodynamic models. Int J Mech Sci 230:107528–107538. https://doi.org/10.1016/j.ijmecsci.2022.107528
29. Xie J, Kar A (1997) Mathematical modeling of melting during laser materials processing. J Appl Phys 81:3015–3022. https://doi.org/10.1063/1.364336

LANGMUIR

pubs.acs.org/Langmuir Article

Superhydrophobic Surface by Laser Ablation of PDMS

Anustup Chakraborty, Narayana R. Gottumukkala, and Mool C. Gupta*

Cite This: *Langmuir* 2023, 39, 11259–11267 Read Online

ACCESS | Metrics & More | Article Recommendations | Supporting Information

ABSTRACT: Superhydrophobic surfaces have important applications in generating anti-icing properties, preventing corrosion, producing anti-biofouling characteristics, and microfluidic devices. One of the most commonly used materials to make superhydrophobic surfaces is poly(dimethylsiloxane) (PDMS). Various techniques, including spin-coating, dip-coating, spray coating, surface etching, and laser-textured mold methods, have been used to make superhydrophobic surfaces. However, all these methods require several steps, the usage of multiple chemicals, and/or surface modifications. In this paper, a one-step, low-cost method to induce superhydrophobicity is described. This was done by the pulsed laser deposition of laser-ablated PDMS micro/nanoparticles, and the method applies to a variety of surfaces. This technique has been demonstrated on three important classes of material—glass, poly(methyl methacrylate) (PMMA), and aluminum. Water contact angles of greater than 150° and roll-off angles of less than 3° were obtained. Optical transmission value of as high as 90% was obtained on glass or PMMA coated with laser-ablated PDMS micro/nanoparticles. Furthermore, this method can also be used to make micron-scale patterned superhydrophobic PDMS surfaces. This would have potential applications in microfluidic microchannels and other optical devices.

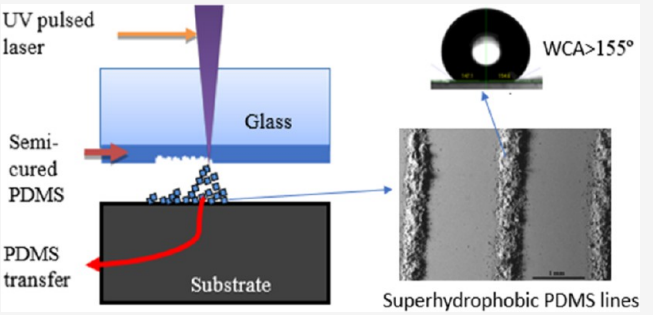

1. INTRODUCTION

A superhydrophobic surface is characterized by a water droplet having a contact angle (CA) of greater than 150°, a contact angle hysteresis of less than 5°, and a roll-off angle of less than 5°.[1] Superhydrophobic surfaces are of great interest due to their applications in the areas of anti-icing,[2] corrosion resistance,[3] anti-biofouling,[4] fluid flow drag reduction,[5] solar panel cleaning,[6] wind blades ice protection,[7] batteries for energy storage,[8] textiles,[9] and microfluidics.[10]

Some of the commonly used methods to fabricate superhydrophobic surfaces are spin-coating, surface etching,[1] vapor-liquid sol−gel,[11] electroless replacement deposition,[12] chemical etching, solution-immersion process, spray coating,[13] and the laser-textured mold method.[14−16] Su et al.[11] developed a simple and highly efficient vapor-liquid sol−gel method of fabricating a robust superhydrophobic surface on polyester textiles with tetraethyl orthosilicates and dihydroxyl-terminated poly(dimethylsiloxane) as reactants in the presence of hydrochloric acid as catalyst. Su et al.[12] also put forward a method in which steel plates were deposited in $CuSO_4$ solution, followed by immersion in V-poly(dimethylsiloxane) (V-PDMS) solution. The steel plates were then treated with ultraviolet (UV) light, thereby making the steel surface superhydrophobic. Esmaeilirad et al.[17] developed physically and thermally stable superhydrophobic aluminum alloy surfaces using chemical etching. Micro-nano structures were formed on the Al alloy surface by treating it with a solution of HCl and CH_3COOH, followed by immersing the alloy in a solution of silanes to lower the surface energy. The maximum water contact angle obtained was 165°. A similar process was used by Chu and Wu[18] to obtain superhydrophobic Al and Cu surfaces. Xu et al.[19] developed a method for creating superhydrophobic surfaces using a solution-immersion process in which copper foams were immersed in the ethanolic stearic acid solution for varying periods. As the immersion time increased, the clusters formed on the copper foams became denser and covered more surface area. The water contact angle (WCA) increased with immersion time, reaching 156° after 4 days, and the sliding angle (SA) decreased to a minimum of 4°. Similarly, Zhao et al.[20] developed a chemical approach for fabricating superhydrophobic surfaces by immersing SiO_2-coated SiC nanowires in an ethanol solution of fluoro alkylsilane for a day. Gong et al.[21] presented a spray coating method in which SiO_2 nanoparticles blended with PDMS could be sprayed onto a surface to make it superhydrophobic. Wu et al.[22] demonstrated a method in which macro/nanoscale binary aluminum structures were replicated into PDMS to make a superhydrophobic surface. A similar method was used by Mulroney et al.,[23] where aluminum was microtextured by a

Received: March 27, 2023
Revised: June 25, 2023
Published: August 2, 2023

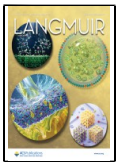

https://doi.org/10.1021/acs.langmuir.3c00818
Langmuir 2023, 39, 11259−11267

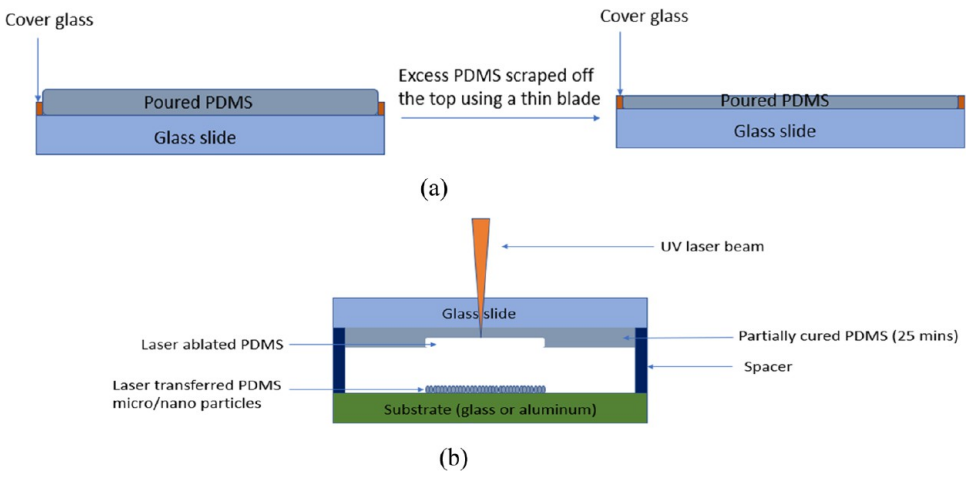

Figure 1. (a) Schematic representation of the cross-section view of the PDMS deposition process on the glass; (b) schematic representation of the pulsed laser-ablated transferring process of PDMS onto different substrates.

nanosecond laser followed by replication of the surface features on polycarbonate through hot embossing. Thereafter, PDMS was thermally cured on the microtextured polycarbonate sheet and pulled off, thereby yielding a superhydrophobic surface with CA above 150° and a roll-off angle (ROA) of below 2°. However, all the aforementioned methods of fabricating superhydrophobic surfaces involve multiple steps, several chemicals, including acids, and/or surface modifications.

This paper reports a one-step, fast, acid-free, lower-cost method of producing superhydrophobic surfaces. This is done by pulsed laser deposition of laser-ablated PDMS micro/nanoparticles. The substrate on which the PDMS micro/nanoparticles are deposited does not need to be textured, which is a major advantage, and it makes this method conducive for large-scale preparation with high throughput. Moreover, the deposited film of PDMS micro/nanoparticles is only a few micrometers in thickness, and the thickness can be controlled.

This method can be applied to a wide variety of materials and has a broad range of applications. The deposition of ablated PDMS micro/nanoparticles has been demonstrated on three important materials—glass, poly(methyl methacrylate) (PMMA), and aluminum. High optical transmission values were obtained on glass coated with PDMS using the laser-ablated PDMS micro/nanoparticles method. Since high transparency is required for many practical applications involving superhydrophobic surfaces,[21] this method can be used to produce superhydrophobic surfaces on solar panels, greenhouses, and other applications involving water-resistant glasses or plastics. Further, micron-scale patterned PDMS can be deposited by this method. These lines can be varied in width and can be used to make superhydrophobic channel walls in microfluidic devices to increase the fluid flow rate.[10,17]

2. EXPERIMENTAL SECTION

2.1. Materials. The Poly(dimethylsiloxane) (PDMS) SYLGARD 184 Silicon Elastomer was used for laser ablation studies. The substrates used were microscope glass slides of length = 3 in., width = 1 in., and thickness = 0.04 in. purchased from Amscope. The aluminum alloy (McMaster-Carr Al 7075) samples of 1 in. length, 1 in. width, and 0.07 in. thickness were polished down to a roughness of less than 1 μm. The PMMA samples of 4 mm thickness, 1 in. width, and 1 in. length were purchased from Ding&ng. The chemical composition of Al 7075 by weight was Al = 89.77%, Zn = 5.4%, Cu = 1.42%, Mn = 0.12%, Mg = 2.42%, Fe = 0.42%, Cr = 0.21%, Ti = 0.11%, and Si = 0.13%.

2.2. Sample Preparation. The PDMS that was used in this experiment was a two-part solution mixture. Ten parts of the polymer and 1 part of the curing agent were mixed thoroughly and placed in a vacuum desiccator for 30 min. to eliminate air pockets introduced during the mixing process. After eliminating the air bubbles, the PDMS solution was carefully poured and spread onto a microscope glass slide, as shown in Figure 1a. The thickness of the PDMS layer was roughly 100−120 μm. As shown in the Figure 1a, this thickness was attained by placing cover glasses of 100−120 μm thickness around the edges of the top face of the glass slide and ensuring that the poured PDMS forms a smooth coverage by scraping off any excess PDMS off the top using a thin blade. Keeping a relatively low PDMS thickness makes it easier for the laser light to be able to focus on the surface of the cured PDMS without undergoing significant absorption or scattering in the bulk of the PDMS layer. It also provides better control of the laser spot over the selected scan area. The poured PDMS on the glass slide was subjected to a temperature of 100 °C for 25 min on a hot plate to partially cure the PDMS. Two other glass slides with poured PDMS were prepared using the same process, and they were cured for 15 and 20 min., respectively. This was done to study the effect of different curing times on the laser ablation process. The thickness of the poured PDMS on these glass slides was also maintained at 100−120 μm. The glass slides and the aluminum on which the ablated PDMS micro/nanoparticles are to be deposited were treated with plasma (Jelight Company UVO-Cleaner Model 18) for 10 min.

2.3. Laser Ablation Procedure. A 355 nm wavelength nanosecond pulsed laser was used to ablate the PDMS coating made on a glass slide. The 355 nm wavelength 20 ns pulsed width laser from Coherent Matrix 355-8-50, operated at 50 kHz pulse repetition rate, at 8 W average power, was used in this study as shown in Figure S1. High Dynamics PIMag linear *XY* stages were used for mounting the samples, and the laser beam was scanned using the Sino-Galvo SG7210 system.

The 355 nm wavelength laser was chosen because the absorption of light by PDMS is higher in the UV spectrum. The UV nanosecond pulsed laser was used to ablate the deposited PDMS on glass, and the ablated material was transferred onto the target substrate through evaporation of the ablated PDMS fragments. The experimental setup of this experiment is shown in Figure 1b. Aluminum and glass were used as substrates. After the formation of the ablated PDMS micro/nanoparticles coating on the substrate, the substrates were heated for an additional 10 min at 100 °C to ensure good bonding and to fully cure the PDMS.[24]

2.4. Abrasion Testing Procedure. A shear (abrasion) test was performed using a micro tribometer (CETR Inc., CA). Figure S2

https://doi.org/10.1021/acs.langmuir.3c00818
Langmuir 2023, 39, 11259−11267

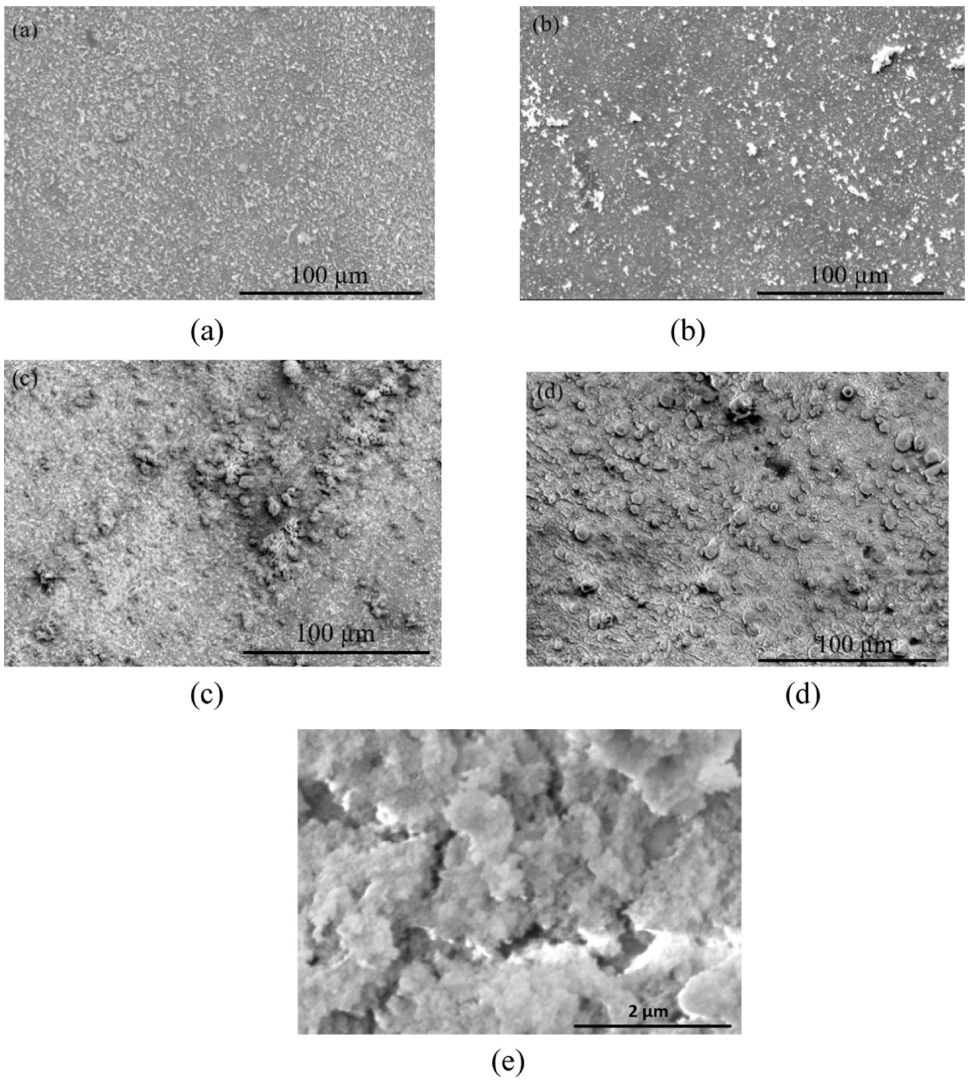

Figure 2. Deposited PDMS micro/nanoparticles on glass at different UV laser fluences. The laser beam scan speed, frequency, and the line spacing were kept constant at 200 mm/s, 50 kHz, and 20 μm, respectively. The laser energy density values used were (a) 1.12 J/cm^2; (b) 1.68 J/cm^2; (c) 1.98 J/cm^2; (d) 2.28 J/cm^2; (e) magnified scanning electron microscopy (SEM) image of PDMS micro/nanoparticles coating.

shows a schematic of the shear test setup. A tool steel blade with a dimension of 3 × 2.4 × 7 mm^3 was attached to a 1000 N load cell. The cell can record both normal and lateral forces. During the shear test, the glass substrate with the laser-ablated PDMS micro/nanoparticles coating was first glued onto the sample stage of the micro tribometer. Then, the steel blade was brought into contact with the substrate under a 2 N normal force F_n, which keeps the blade in good contact with the substrate surface. The sample was moved laterally at a speed of 0.5 mm/s toward the steel blade. Once the steel blade came in contact with the coating, a shear force (F_s) was applied to the coating. The variation of the lateral shear force was recorded as a function of time until the coating was completely scraped off. The nominal ultimate shear strength τ_{Max} can be defined by eq 1

$$\tau_{max} = \frac{F_{S,max}}{A_{int}} \quad (1)$$

where $F_{S,max}$ is the maximum shear force during the shear test, and A_{int} is the interfacial contact area of the coating. An acoustic emission (AE) signal was also collected by the AE sensor attached to the substrate to monitor the process of scraping the coating off of the surface.

2.5. Surface Characterization. The surface morphology analysis of the laser-ablated PDMS micro/nanoparticles was done by using a FEI Quanta 650 Field Emission Microscope, and chemical composition was done by X-ray photoelectron spectroscopy (XPS) (PHI Versaprobe III). The abrasion resistance of the surface was determined by using the CETR micro tribometer. The water contact angle measurements were done using the Ramé-Hart Model 250 Goniometer.

2.6. Optical Characterization. Optical transmission measurements were obtained using a UV−visible-near-infrared (UV−VIS−NIR) spectrophotometer (Agilent CARY 5000) with a tungsten halogen visible and deuterium arc UV light source and a silicon photodiode receiver. The wavelength range for the scan was from 200 to 1100 nm to ensure complete coverage of the UV and visible spectrum and some of the near-infrared (IR) spectrum as well. The measurements were done on different areas of a UV fused silica window (Thorlabs WG41010R), poured, and partially cured PDMS on silica and PDMS micro/nanoparticles deposited silica surface to ensure repeatability and minimize variability.

3. RESULTS AND DISCUSSION

3.1. Laser Ablation Process Optimization. Different laser parameters were tested for the laser ablation process to determine the optimal condition to achieve superhydrophobic surfaces. It was found that scan speeds above 200 mm/s made the laser beam move too fast and did not ablate enough PDMS

https://doi.org/10.1021/acs.langmuir.3c00818
Langmuir 2023, 39, 11259−11267

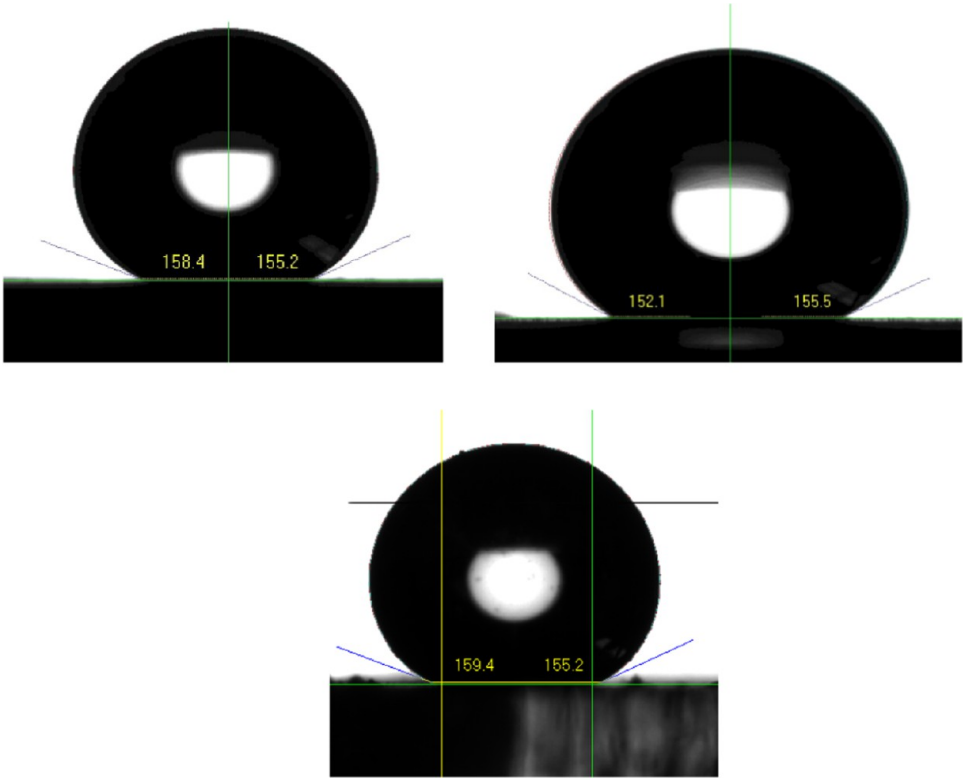

Figure 3. Contact angle of water on PDMS micro/nanoparticles deposited film on aluminum (left), PMMA (bottom), and glass (right) surfaces.

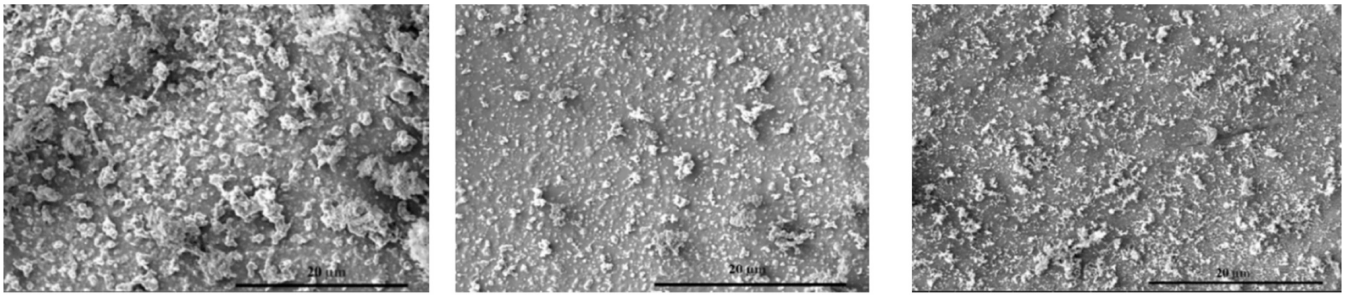

Figure 4. PDMS micro/nanoparticles distribution at spacer thickness of (a) 1 mm, (b) 5 mm, and (c) 8 mm.

per unit area to create a superhydrophobic surface on the substrate. Hence, the laser scan speed was chosen to be 200 mm/s. The laser fluences were varied across a range of 1.1−2.3 J/cm^2, keeping the scan speed constant at 200 mm/s. Figure 2 shows the effect of varying laser fluence on the deposited PDMS micro/nanoparticles on the glass substrate. It was observed that at higher fluences, more PDMS particles get ablated and deposited on the substrate. It is necessary to have a certain number of PDMS micro/nanoparticles on the substrate to achieve superhydrophobicity. The substrate surface starts to show superhydrophobicity above 2 J/cm^2. The side-to-side line spacing and the frequency of the laser were kept constant at 20 μm, and the laser was operated at 50 kHz, respectively. Nitrogen gas was blown on the PDMS during the laser ablation process to reduce oxidation. This enabled multiple uses of the same PDMS material for the laser ablation process. The contact angle of water on PDMS micro/nanoparticle-deposited glass, PMMA, and aluminum substrate surfaces were 153.8 ± 1.7, 157.3 ± 2.1, and 156.8 ± 1.6° respectively, as shown in Figure 3. The corresponding roll-off angles were 4.2, 3.1, and 3.8°, respectively. The separation between the PDMS-coated top glass and the substrate on which the laser-ablated PDMS micro/nanoparticles were deposited was 1 mm.

3.2. Plasma-Treated Glass Slides and Aluminum. The water contact angle (WCA) on a plane glass slide was found to be 43.4 ± 3.8°, and the WCA on a plasma-treated glass slide was found to be 23.3 ± 4.2°. Meanwhile, the aluminum surface was found to be mildly hydrophilic with water contact angles of 81.4 ± 5.8°, and the WCA on the plasma-treated aluminum sample was found to be 19.3 ± 3.6°. The decrease in the WCA can be attributed to an increase in the surface free energy due to the plasma treatment.[25] The plasma treatment of glass also allows for achieving an increased bond between the PDMS and glass.[24−26]

3.3. Variation of the PDMS Micro/Nanoparticles Coating Thickness. As shown in Figure 1b, there are two spacers, which are pieces of solid plastic separating the top glass coated with PDMS and the bottom substrate. Varying the

https://doi.org/10.1021/acs.langmuir.3c00818
Langmuir 2023, 39, 11259−11267

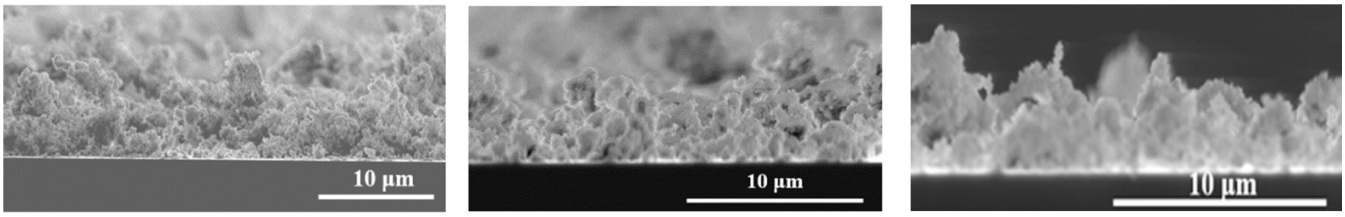

Figure 5. SEM image of the cross-section of the laser-ablated PDMS micro/nanoparticles coating with spacer thicknesses of (a) 1 mm, (b) 5 mm, and (c) 8 mm.

thickness of the spacer varied the distance between the PDMS-coated top glass and the bottom substrate. This, in turn, affects the morphology of the laser-ablated PDMS micro/nanoparticles coating and its thickness.

Figure 4 shows the different morphologies of the PDMS micro/nanoparticles-coated surface at different spacer thicknesses. The laser fluence used was 2 J/cm^2. It can be seen that at a smaller spacer thickness, more particles are present on the surface. The sizes of the particles also vary, ranging from a few nanometers to a few microns. The surface stopped being superhydrophobic with a spacer thickness of more than 8 mm as the film was not continuous and very thin.

Figure 5 shows the thickness variation of the PDMS micro/nanoparticles-coated surface at different spacer thicknesses. The average coating thickness gradually decreases with an increase in the spacer thickness. This is because, with increasing spacer thickness, a lesser number of laser-ablated PDMS micro/nanoparticles reach the substrate. It can be seen that the laser-ablated PDMS micro/nanoparticles deposited at a spacer thickness of 1 mm had the highest average thickness of around 8 μm, while that deposited at spacer thicknesses of 5 and 8 mm had average thicknesses of around 4 and 2 μm, respectively. The coating is non-uniform with a lot of thickness variations, as can be seen in Figure 7a–c.

3.4. Elemental Analysis of the Surface. Figure 6 shows the XPS spectrum of the different PDMS samples using a monochromatic X-ray source (1486.6 eV). Plane PDMS on glass refers to the poured and partially cured (25 min). PDMS on glass and then laser treated refers to the poured and cured (25 min) PDMS on glass that has been ablated by the laser to deposit the PDMS micro/nanoparticles on the substrate. There is no noticeable change in the position of the peaks, which indicates that there is no significant degradation of the PDMS.[27]

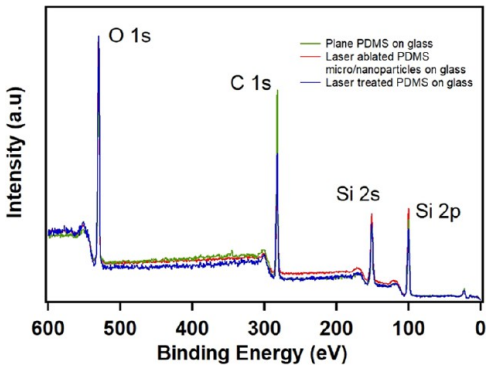

Figure 6. XPS spectrum showing the peaks for the different elements (C, Si, and O). Spectra are shown only from 0 to 600 eV so that different colors can be seen easily.

The atomic percentage composition of the different elements is shown in Table 1. The carbon content of all the samples under consideration was found to remain fairly constant. The silicon content of the laser-treated PDMS on glass increased by around 5%, while the oxygen content of both the laser-ablated PDMS micro/nanoparticles and the laser-treated PDMS on glass reduced considerably. This can be attributed to the breaking and forming of bonds between elements due to laser–matter interaction.

Table 1. Elemental Composition (atom %) of the Different Samples of PDMS

sample under consideration	elemental composition (atom %)		
	O 1s	C 1s	Si 2p
plane PDMS on glass	45.2	32.3	20.5
laser-ablated PDMS micro/nanoparticles	39.7	33.2	21.4
laser-treated PDMS on glass	33.4	33	26.6

3.5. Optical Transmission Measurement. The optical transmission measurements are shown in Figure 7. On average, the optical transmission value of the cured PDMS on fused silica is less than that of plane fused silica by about 6–7%. On the other hand, the optical transmission value of the laser-ablated PDMS micro/nanoparticles-coated fused silica is less than that of plane glass by around 15% on average. The optical transmission value of the laser-ablated PDMS micro/nanoparticles-coated PMMA is less than that of uncoated PMMA by around 10% on average. The lower transmission of the laser-ablated PDMS micro/nanoparticles-coated glass is mainly caused by the scattering of light by the PDMS particles. The ablated PDMS micro/nanoparticles coating was deposited at a spacer length of 8 mm and a laser fluence of 2 J/cm^2. Coatings deposited at shorter spacer lengths have more PDMS micro/nanoparticles on the surface and greater coating thickness; subsequently, they will have a lesser optical transmission value compared to the coating deposited at an 8 mm spacer length due to increased optical scattering. The optical transmission values reduce significantly in the shorter wavelength range due to increased light scattering at shorter wavelengths.[28]

The laser-ablated PDMS micro/nanoparticles-coated glass was placed on top of a solar cell, and the change in efficiency was measured. This was done to simulate a solar panel with a laser-ablated PDMS micro/nanoparticles-coated glass. The solar cell gave an efficiency of 4.45% with clear glass; meanwhile, the same solar cell gave an efficiency of 3.98% with the laser-ablated PDMS micro/nanoparticles-coated glass. One sun illumination was used for the experiment. The solar

https://doi.org/10.1021/acs.langmuir.3c00818
Langmuir 2023, 39, 11259–11267

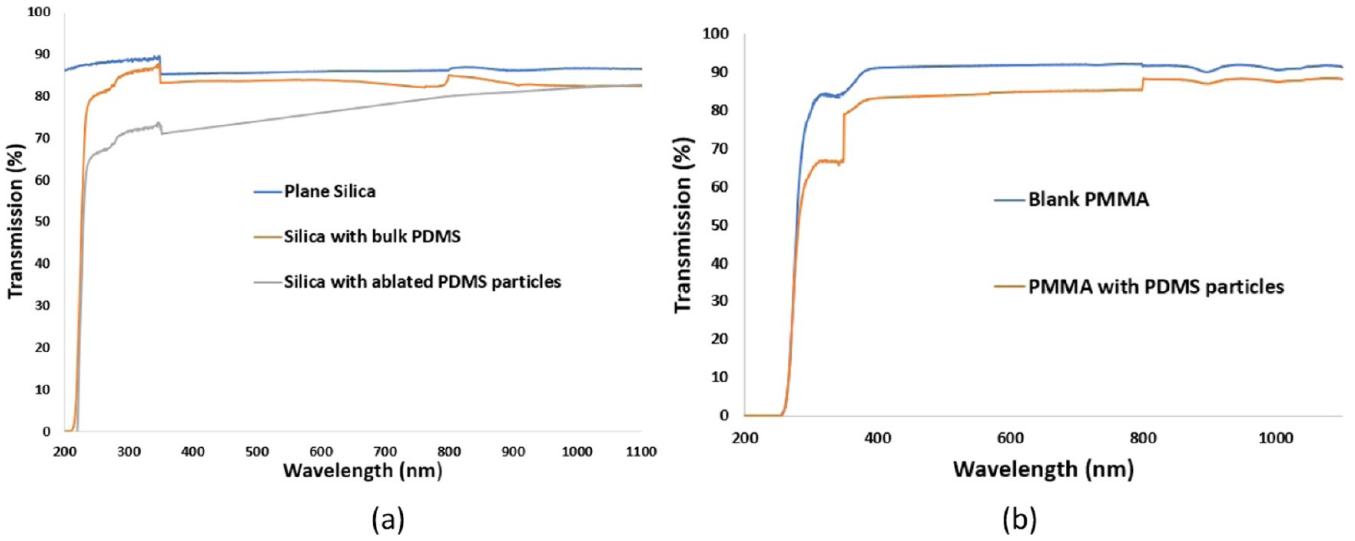

Figure 7. Optical transmission measurements on (a) silica and (b) PMMA.

cell used was a reference solar cell supplied by NREL with a rated efficiency of 4.49% under 1 sun illumination.

3.6. Shear Strength of the PDMS Micro/Nanoparticles Coating at Different Coating Thicknesses. Figure 8 shows

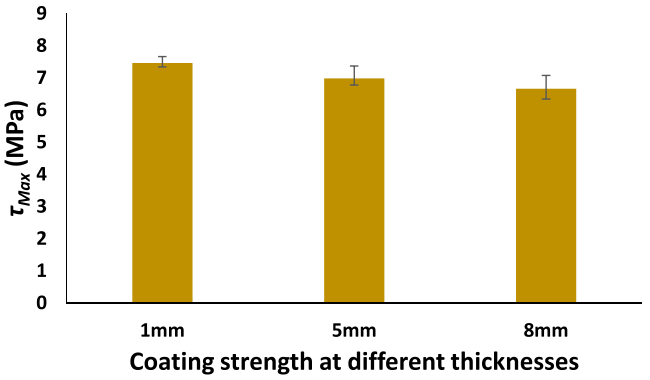

Figure 8. Nominal ultimate shear strength (τ_{Max}) of different coating thicknesses.

the shear strength of the laser-ablated PDMS micro/nanoparticles coating at different spacer thicknesses. There is a slight variation in the coating shear strength with changing spacer thicknesses. The shear strength obtained at a spacer thickness of 5 mm is slightly lower than that at 1 mm by around 0.56 MPa, and the shear strength obtained at a spacer thickness of 8 mm is slightly lower than that at 5 mm by around 0.32 MPa. This can be attributed to the coating thickness variations with different spacer thicknesses. The coating deposited at 1 mm spacer thickness requires more force to be scraped off than the coating deposited at 5 mm spacer thickness. This is because the coating deposited at 1 mm spacer thickness is thicker than the coating deposited at 5 mm spacer thickness. The same reasoning can be applied to the coating deposited at 8 mm spacer thickness to account for the decreased shear strength.

3.7. Patterning of PDMS Lines. The laser-ablated PDMS micro/nanoparticles deposition technique can also be used for patterned PDMS lines on different substrates, as shown in Figure 9. A laser fluence of 2 J/cm^2 was used for the laser ablation process. The spacer thickness was 1 mm. These PDMS lines are composed of laser-ablated PDMS micro/nanoparticles that bond to the substrate and form a continuous film, and their width and spacing can be varied. This technique can be used to coat microchannels in microfluidic devices and make them superhydrophobic.

To make the PDMS line patterns on the substrate, two metal masks were used. The masks had openings in the shape of fingers. The length of these fingers was 2 mm, and the width of these fingers was 500 and 200 μm, respectively. The separation between the openings was 1.4 mm. Accordingly, the width of the PDMS lines was 500 and 200 μm, respectively, and the spacing between the deposited PDMS lines was roughly around 1.4 mm. The metal masks were placed on the surface of

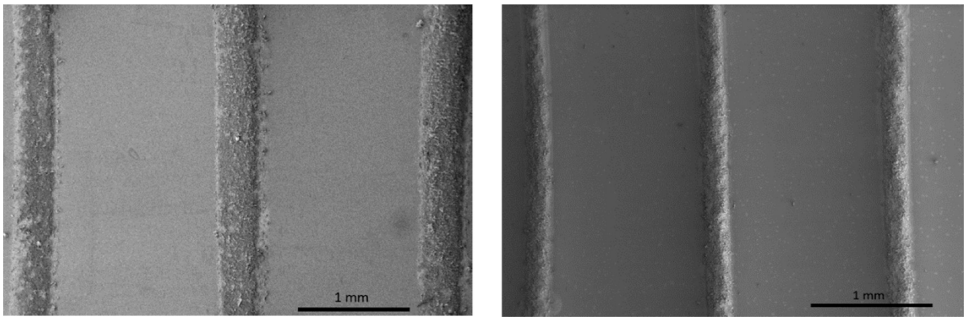

Figure 9. SEM image of deposited PDMS lines on glass with a line width of 500 μm (left) and 200 μm (right).

https://doi.org/10.1021/acs.langmuir.3c00818
Langmuir 2023, 39, 11259−11267

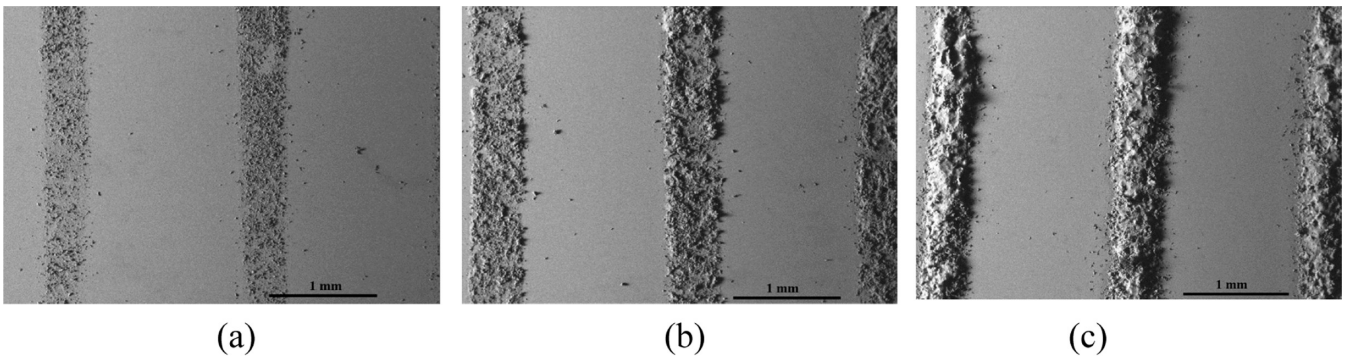

Figure 10. SEM images showing the effect of the curing time of the poured PDMS on the laser-deposited PDMS micro/nanoparticles. The PDMS lines were deposited after curing the poured PDMS on glass for (a) 15 min, (b) 20 min, and (c) 25 min.

the glass substrates during the laser ablation process. Hence, the ablated PDMS micro/nanoparticles were deposited through the open areas of the mask. In the absence of the mask, the vaporized PDMS fragments generated from the laser ablation process would spread and settle across the entire surface of the substrate without forming any patterns of lines.

3.8. Effect of Initial Curing Time of PDMS on the PDMS Lines. Figure 10 shows how the ablated PDMS micro/nanoparticles coating is affected by different curing times of the poured PDMS on the glass. With lower curing times of the poured PDMS, the deposited PDMS lines become "broken" in certain places due to inhomogeneous particle distribution. It can be seen that a curing time of 25 min leads to a more consistent and uniform coating compared to curing times of 15 and 20 min. No significant difference in the deposited PDMS lines was observed with curing times of more than 25 min. If it is cured too long, it may not deposit and just decomposes. The spacer thickness used for the deposition of the PDMS lines was 1 mm. The substrate used was glass.

4. DISCUSSION

Laser processing is used in various industrial sectors such as aerospace, automobile, electronics, photovoltaics, biomedical, and general manufacturing. High-power lasers are available at a relatively lower cost. Using our laboratory laser, it took 3 s to deposit PDMS on one square inch area. This could be reduced significantly by using higher-power commercial lasers. So, the method can be used for large-area preparation.

One of the factors that affect the laser-ablated PDMS micro/nanoparticles-coating method is the curing of PDMS. The curing condition for the pristine PDMS is roughly two days at room temperature, 45 min at 100 °C, 20 min at 125 °C, or 10 min at 150 °C.[29] Uncured or semi-cured PDMS is viscous and is liquid compared to its cured counterpart. Hence, when semi-cured PDMS is subjected to laser irradiation, fewer particles are ablated and ejected in comparison with cured PDMS. This results in inconsistencies in the ablated PDMS micro/nanoparticles coating. The superhydrophobicity of the laser-ablated PDMS micro/nanoparticles-coated surface is due to the hierarchical scale roughness of the surface combined with the low surface free energy of PDMS.[30−32]

The laser ablation of the PDMS occurs through thermal, thermo-oxidative, and mechanical reactions, resulting in the evaporation of macromolecular fragments.[33,34] After these fragments are released, they come in contact with the substrate and settle on the surface, forming a thin coating of PDMS micro/nanoparticles. The farther the substrate from the laser-ablated PDMS, the lesser the fragments that reach the substrate due to the spreading of the vapor. The efficiency of the PDMS laser ablation process depends on the amount of absorbed light energy.[34] Laser radiation absorption is described by Bouguer−Lambert law

$$I(z) = I_0\eta \exp(-\chi z) \tag{2}$$

where I_0—is the incident laser intensity on the surface; χ—is an absorption coefficient of PDMS at the laser wavelength; z—is the coordinate measured into the depth of the material; η—is the coefficient determining the absorbed energy share.

Energy absorbed in the sample layer during time t

$$E = S\int_0^t I(z)\mathrm{d}t = S\eta I_0 \exp(-\chi z)t \tag{3}$$

where S—is the cross-sectional area of the laser beam on the sample surface. The intensity lost in a layer of thickness z[31]

$$\Delta I = I_0 - I(z) = I_0(1-\eta)\exp(-\chi z) \tag{4}$$

Using eq 3 and the PDMS absorption coefficient value of 7.38 at 355 nm,[35] the energy absorbed by the PDMS layer at a fluence of 2 J/cm^2 was found to be 7.41 J. The robustness/adhesion of the laser-ablated PDMS particles to the substrate is a critical consideration. The mechanical robustness of the laser-ablated PDMS micro/nanoparticle coating can be improved by modifying the uncured PDMS solution by adding epoxy or reinforcing it with nanosilica hybrid nanofillers or both.[36] The uncured PDMS solution can also be blended with polymers like polyurethane (PU) to enhance the mechanical properties of the laser-ablated PDMS micro/nanoparticles coating.[37] Shear strength values of over 40 MPa[36] can be potentially achieved by these improved methods. Generally, PDMS coatings display low adhesion strength in comparison to metals due to their non-polar nature and low surface free energy.[38,39] However, the bonding of the PDMS micro/nanoparticle coating to the aluminum and glass surface can be attributed to micromechanical adhesion. When the laser-ablated PDMS micro/nanoparticles land on the substrate surface, they fill the microvoids, rugosity, and pores on the surface, forming mechanically interlocked bonds. Other factors, like attractive electrostatic forces, may also enhance the bonding.[40]

The scattering of the PDMS particles on the substrate surface could be a concern during the laser ablation process. It can be seen in Figure 10c that there are a few scattered stray PDMS particles in between the PDMS lines. This can be avoided by firmly placing the metal mask on the substrate and

https://doi.org/10.1021/acs.langmuir.3c00818
Langmuir 2023, 39, 11259−11267

minimizing the spreading of the laser-ablated PDMS macromolecular fragments underneath the mask.

The laser-ablated PDMS micro/nanoparticles technique offers a versatile approach for creating superhydrophobic surfaces, which find extensive applications in various fields such as aerospace, defense, automotive, biomedical, engineering, sensors, apparel,[41] anti-freeze surfaces, anti-fog coating, antibacterial surfaces,[42] and more. This method allows for the generation of patterns or localized superhydrophobic regions, enabling the fabrication of superhydrophobic patches. Additionally, it holds significant potential to enhance the efficiency of fluid flow and reduce resistance in microfluidic systems.[42]

5. CONCLUSIONS

The key points presented in this paper are as follows:

(i) This paper demonstrates a laser process of creating superhydrophobic surfaces in which pulsed laser-ablated PDMS nano/microparticles are deposited on various surfaces producing superhydrophobic thin films. We demonstrated the superhydrophobic properties of glass, PMMA, and aluminum surfaces, and the method is applicable to a variety of materials. The PDMS micro/nanoparticles are generated by laser ablation of partially cured PDMS followed by subsequent deposition on a substrate, thereby making the substrate superhydrophobic.

(ii) The surface morphology and the optical transmission properties of the laser-ablated PDMS micro/nanoparticles deposited film were studied, and the science behind the formation of the thin films was explained. Various factors, such as laser ablation parameters, the effect of the curing time of the PDMS, and spacer distance (distance between the substrate and the initial PDMS-coated substrate), were considered.

(iii) Furthermore, it was shown that this method could be used to make patterned superhydrophobic PDMS by placing a metal mask on the substrate. It can potentially be used to make superhydrophobic microchannels in microfluidic devices and other applications.

ASSOCIATED CONTENT

Supporting Information

The Supporting Information is available free of charge at https://pubs.acs.org/doi/10.1021/acs.langmuir.3c00818.

Setup of an UV nanosecond laser (Figure S1) and schematic of an abrasion test setup (Figure S2) (PDF)

AUTHOR INFORMATION

Corresponding Author

Mool C. Gupta − *Charles L. Brown Department of Electrical and Computer Engineering, University of Virginia, Charlottesville, Virginia 22904, United States;* orcid.org/0000-0002-1782-5354; Email: mgupta@virginia.edu

Authors

Anustup Chakraborty − *Charles L. Brown Department of Electrical and Computer Engineering, University of Virginia, Charlottesville, Virginia 22904, United States*

Narayana R. Gottumukkala − *Charles L. Brown Department of Electrical and Computer Engineering, University of Virginia, Charlottesville, Virginia 22904, United States;* orcid.org/0000-0002-1546-2713

Complete contact information is available at: https://pubs.acs.org/10.1021/acs.langmuir.3c00818

Notes

The authors declare no competing financial interest.

ACKNOWLEDGMENTS

The authors thank John Tyler Daspit (Mechanical and Aerospace Engineering, UVA) for his help in obtaining the PDMS coating shear strength measurements. The authors would also like to thank the NSF IUCRC award and the Langley Professor award for their financial support. Last, we would like to extend our gratitude to UVA NMCF for the XPS and SEM facilities.

REFERENCES

(1) Park, S.; Huo, J.; Shin, J.; Heo, K. J.; Kalmoni, J. J.; Sathasivam, S.; Hwang, G. B.; Carmalt, C. J. Production of an EP/PDMS/SA/AlZnO Coated Superhydrophobic Surface through an Aerosol-Assisted Chemical Vapor Deposition Process. *Langmuir* **2022**, *38*, 7825−7832.

(2) Gupta, M. C.; Mulroney, A. Ice adhesion and anti-icing using microtextured surfaces. In *Ice Adhesion: Mechanism, Measurement, and Mitigation*; Wiley: New York, 2020; pp 389−417.

(3) Vazirinasab, E.; Jafari, R.; Momen, G. Application of superhydrophobic coatings as a corrosion barrier: A review. *Surf. Coat. Technol.* **2018**, *341*, 40−56.

(4) Agbe, H.; Sarkar, D. K.; Chen, X. G. Tunable superhydrophobic aluminum surfaces with anti-biofouling and antibacterial properties. *Coatings* **2020**, *10*, 982−992.

(5) Kouser, T.; Xiong, Y.; Yang, D. Contribution of superhydrophobic surfaces and polymer additives to drag reduction. *ChemBioEng Rev.* **2021**, *8*, 337−356.

(6) Sarkın, A. S.; Ekren, N.; Sağlam, Ş. A review of anti-reflection and self-cleaning coatings on photovoltaic panels. *Sol. Energy* **2020**, *199*, 63−73.

(7) Qin, C. C.; Mulroney, A. T.; Gupta, M. C. Anti-icing epoxy resin surface modified by spray coating of PTFE Teflon particles for wind turbine blades. *Mater. Today Commun.* **2020**, *22*, No. 100770.

(8) Li, C.; Wei, J.; Qiu, K.; Wang, Y. Li-air battery with a superhydrophobic Li-protective layer. *ACS Appl. Mater.* **2020**, *12*, 23010−23016.

(9) Ahmad, I.; Kan, C. W. A review on development and applications of bio-inspired superhydrophobic textiles. *Materials* **2016**, *9*, 892−926.

(10) Tropmann, A.; Tanguy, L.; Koltay, P.; Zengerle, R.; Riegger, L. Completely superhydrophobic PDMS surfaces for microfluidics. *Langmuir* **2012**, *28*, 8292−8295.

(11) Su, X.; Li, H.; Lai, X.; Zhang, L.; Wang, J.; Liao, X.; Zeng, X. Vapor-liquid sol-gel approach to fabricating highly durable and robust superhydrophobic polydimethylsiloxane@silica surface on polyester textile for oil-water separation. *ACS Appl. Mater. Interfaces* **2017**, *9*, 28089−28099.

(12) Su, X.; Li, H.; Lai, X.; Zhang, L.; Liang, T.; Feng, Y.; Zeng, X. Polydimethylsiloxane-based superhydrophobic surfaces on steel substrate: fabrication, reversibly extreme wettability and oil-water separation. *ACS Appl. Mater. Interfaces* **2017**, *9*, 3131−3141.

(13) Ali, H. M.; Qasim, M. A.; Malik, S.; Murtaza, G. Techniques for the Fabrication of Superhydrophobic Surfaces and Their Heat Transfer Applications. In *Heat Transfer - Models, Methods and Applications*; Intechopen, 2018.

(14) Liu, B.; Wang, W.; Jiang, G.; Mei, X.; Wang, Z.; Wang, K.; Cui, J. Study on hierarchical structured PDMS for surface superhydrophobicity using imprinting with ultrafast laser structured models. *Appl. Surf. Sci.* **2016**, *364*, 528−538.

(15) Jiang, T.; Koch, J.; Unger, C.; Fadeeva, E.; Koroleva, A.; Zhao, Q.; Chichkov, B. N. Ultrashort picosecond laser processing of micromols for fabricating plastic parts with superhydrophobic surfaces. *Appl. Phys. A* **2012**, *108*, 863−869.
(16) Sarbada, S.; Shin, Y. C. Superhydrophobic contoured surfaces created on metal and polymer using a femtosecond laser. *Appl. Surf. Sci.* **2017**, *405*, 465−475.
(17) Esmaeilirad, A.; Rukosuyev, M. V.; Jun, M. B. G.; van Veggel, F. C. J. M. A cost-effective method to create physically and thermally stable and storable superhydrophobic aluminum alloy surfaces. *Surf. Coat. Technol.* **2016**, *285*, 227−234.
(18) Chu, F.; Wu, X. Fabrication and condensation characteristics of metallic superhydrophobic surface with hierarchical micro-nano structures. *Appl. Surf. Sci.* **2016**, *371*, 322−328.
(19) Xu, J.; Jinliang, X.; Cao, Y.; Ji, X.; Yan, Y. Fabrication of non-flaking, superhydrophobic surfaces using a one-step solution-immersion process on copper foams. *Appl. Surf. Sci.* **2013**, *286*, 220−227.
(20) Zhao, J.; Li, Z.; Zhang, M.; Meng, A. Superhydrophobic surfaces of SiO_2-coated SiC nanowires: Fabrication, mechanism and ultraviolet-durable superhydrophobicity. *J. Colloid Interface Sci.* **2015**, *444*, 33−37.
(21) Gong, X.; He, S. Highly Durable Superhydrophobic Polydimethylsiloxane/Silica Nanocomposite Surfaces with Good Self-Cleaning Ability. *ACS Omega* **2020**, *5*, 4100−4108.
(22) Wu, Y.; Wang, J.; Zhang, D.; Li, L.; Zhu, Y. Preparation and characterization of superhydrophobic surface based on polydimethylsiloxane (PDMS). *J. Adhes. Sci. Technol.* **2019**, *33*, 1870−1881.
(23) Mulroney, A. T.; Gupta, M. C. Optically transparent superhydrophobic polydimethylsiloxane by periodic surface microtexture. *Surf. Coat. Technol.* **2017**, *325*, 308−317.
(24) Xiong, L.; Chen, P.; Zhou, Q. Adhesion promotion between PDMS and glass by oxygen plasma pre-treatment. *J. Ades. Sci. Tech.* **2014**, *28*, 1046−1054.
(25) Chau, K.; Millare, B.; Lin, A.; Upadhyayula, S.; Nunez, V.; Xu, H.; Vullev, V. I. Dependence of the quality of adhesion between poly(dimethylsiloxane) and glass surfaces on the composition of the oxidizing plasma. *Microfluid. Nanofluid.* **2011**, *10*, 907−917.
(26) Lundevall, Å.; Sundberg, P.; Mattsson, L. Improved glass bonding with plasma treatment. *Appl. Adhes. Sci.* **2018**, *6*, 4959−4970.
(27) Greczynski, G.; Hultman, L. X-ray photoelectron spectroscopy: Towards reliable binding energy referencing. *Prog. Mat. Sci.* **2020**, *107*, 100591−100637.
(28) Lockwood, D. J. Rayleigh, and Mie Scattering. In *Encyclopedia of Color Science and Technology*; Luo, M. R., Ed.; Springer: New York, 2016; pp 1097−1107.
(29) Al-Harbi, L. M.; Darwish, M. S. A.; Khowdiary, M. M.; Stibor, I. Controlled Preparation of Thermally Stable Fe-Poly-(dimethylsiloxane) Composite by Magnetic Induction Heating. *Polymers* **2018**, *10*, 507−515.
(30) Cortese, B.; D'Amone, S.; Manca, M.; Viola, I.; Cingolani, R.; Gigli, G. Superhydrophobicity Due to the Hierarchical Scale Roughness of PDMS Surfaces. *Langmuir* **2008**, *24*, 2712−2718.
(31) Vudayagiri, S.; Junker, M.; Skov, A. Factors affecting the surface and release properties of thin polydimethylsiloxane films. *Polym. J.* **2013**, *45*, 871−878.
(32) Chakraborty, A.; Mulroney, A.; Gupta, M. C. Superhydrophobic surfaces by microtexturing: A critical review. *Prog. Adhes. Adhes.* **2021**, *6*, 621−649.
(33) Kunizhev, B. I.; Torshkhoeva, Z. S.; Zhelikhazhev, R. N.; Starov, A. V. Destruction of polymers under the action of laser radiation. *IOP Conf. Ser.: Mater. Sci. Eng.* **2021**, *1083*, 1083−1089.
(34) Arnold, N.; Bityurin, N. Model for laser-induced thermal degradation and ablation of polymers. *Appl. Phys. A: Mater. Sci. Process.* **1999**, *68*, 615−625.
(35) Stankova, N. E.; Atanasov, P. A.; Nikov, Ru. G.; Nikov, R. G.; Nedyalkov, N. N.; Stoyanchov, T. R.; Fukata, N.; Kolev, K. N.; Valova, E. I.; Georgieva, J. S.; Armyanov, A., St. Optical properties of polydimethylsiloxane (PDMS) during nanosecond laser processing. *Appl. Surf. Sci.* **2016**, *374*, 96−103.
(36) Wang, X.; Lin, Z. Robust, hydrophobic anti-corrosion coating prepared by PDMS modified epoxy composite with graphite nanoplatelets/nano-silica hybrid nanofillers. *Surf. Coat. Technol.* **2021**, *421*, No. 127440.
(37) Muharrem, T.; Senaslan, F.; Celik, A. Investigation of corrosion and thermal behavior of PU−PDMS-coated AISI 316L. *e-Polym.* **2021**, *21*, 355−365.
(38) Hamdi, M.; Saleh, M. N.; Poulis, J. A. Improving the adhesion strength of polymers: effect of surface treatments. *J. Adhes. Sci. Technol.* **2020**, *34*, 1853−1870.
(39) Bao, L.; Fan, H.; Chen, Y.; Yan, J.; Yang, T.; Guo, Y. Effect of surface free energy and wettability on the adhesion property of waterborne polyurethane adhesive. *RSC Adv.* **2016**, *6*, 99346−99352.
(40) von Fraunhofer, J. A. Adhesion and cohesion. *Int. J. Dent.* **2012**, *2012*, 1−8.
(41) Manoharan, K.; Bhattacharya, S. Superhydrophobic surfaces review: Functional application, fabrication techniques and limitations. *J. Micromanuf.* **2019**, *2*, 59−78.
(42) Barati Darband, G. H.; M Aliofkhazraei, M.; Khorsand, S.; Sokhanvar, S.; Kaboli, A. Science and Engineering of Superhydrophobic Surfaces: Review of Corrosion Resistance, Chemical and Mechanical Stability. *Arabian J. Chem.* **2020**, *13*, 1763−1802.

https://doi.org/10.1021/acs.langmuir.3c00818
Langmuir 2023, 39, 11259−11267

14

Superhydrophobic Surfaces by Microtexturing: A Critical Review

Anustup Chakraborty, Alan T. Mulroney and Mool C. Gupta*

Charles L. Brown Department of Electrical and Computer Engineering, University of Virginia, Charlottesville, Virginia, USA

Abstract Superhydrophobicity is a property of surfaces characterized by extreme water repellence and it is observed in highly textured low surface energy materials. The surface roughness can be varied widely. There are several ways by which superhydrophobicity can be achieved on various kinds of surfaces. Polymer surfaces have a wide range of applications and are a good candidate for making superhydrophobic surfaces. Superhydrophobic surfaces are well known for their self-cleaning and anti-icing properties so that water droplets roll off the surface taking away all the external contaminant particles that are present on the surface along with it. Surfaces that have a static water drop contact angle of greater than 150° and a roll-off angle of less than 10° can be termed as superhydrophobic surfaces. The various methods for making superhydrophobic surfaces that have been developed are templating, lithography, plasma treatment, electrochemical deposition, layer-by-layer self-assembly, sol-gel deposition, wet chemical reaction, hydrothermal reaction, chemical vapor deposition, and electrospinning. Many physical and chemical methods have been used to design and fabricate superhydrophobic surfaces. However, surfaces are prone to damage by scratches, abrasion, or even brief contact with fingers, and, therefore, surfaces might lose their superhydrophobicity. Hence, improving mechanical robustness and self-replenishment of superhydrophobic surfaces upon damage is an active area of research. Potential applications of superhydrophobic surfaces include biomaterials, microelectronics, microfluidics, coatings, textiles, and so on. Various superhydrophobic surfaces have been discussed in this paper, namely poly(dimethylsiloxane), polytetrafluoroethylene, etc., and their applications.

Keywords Surface microtexture, superhydrophobic, wetting, polymer

Corresponding author: mgupta@virginia.edu

K.L. Mittal (ed.) Progress in Adhesion and Adhesives, Volume 6, (621–650) © 2021 Scrivener Publishing LLC

14.1 Introduction

14.1.1 Background

The hydrophobicity of a smooth surface is enhanced by roughness and it modifies the interaction of the surface with a liquid [1]. Superhydrophobic materials have a lot of potential applications [2]. For durability and protection, larger-scale sacrificial micropillars can protect fragile fine-scale surface topographies against degradation resulting in a loss of superhydrophobic properties [3]. A great deal of interest has been shown in the fabrication of superhydrophobic surfaces [4]. Preparation of polymeric materials with controlled surface wettability can be done by spin-coating a silica mixture dispersed in an organic solvent mixture onto the polymer surface [5]. The combination of a low surface free energy solid, and a low interfacial contact area between water and solid, is needed to produce water-repellent or superhydrophobic surfaces. Slight tilting of the surface should make the water easily roll off the surface while cleaning the surface by carrying all the contaminant particles away without leaving any residue [6]. In addition to the self-cleaning characteristics, water-repellent surfaces can also prevent or reduce corrosion [7] and may prevent the buildup of ice [8].

When considering the methods to produce a superhydrophobic surface, two major techniques are investigated in research and used in industry: chemical coatings and surface microtexture. Chemical coatings demonstrate the ease of fabrication, low-cost application, and high scalability [9, 10]. However, chemical coatings face durability challenges [10] and can be application limited [7]. Meanwhile, surface microtexture is often more difficult to fabricate [11] and does not easily scale to large area applications [12, 13]. The advantages of surface microtexture include superior durability [14], longevity [15], and fine control over the resultant wetting properties [16, 17]. It is worthwhile to mention that controlled and reversible conversion between superhydrophobic and superhydrophilic wetting states can be used for targeted drug delivery, water-harvesting, and antireflective, waterproofing, and liquid self-transportation coatings [18].

To produce a superhydrophobic surface, the presence of microtexture alone is not sufficient. This is due to the interactions between water and the surface. These interactions can be manipulated by the presence of surface microtexture [19]. However, the surface free energy of the material is an integral aspect of the wetting dynamics. Table 14.1 lists the highest reported water contact angles (CAs) for a few surfaces with their corresponding surface free energy. It is interesting to note that surfaces like polypropylene (PP) or poly(methyl methacrylate) (PMMA) need to be microtextured and then coated with something with a lower surface free energy, like poly(dimethylsiloxane) (PDMS). The reported roll-off angles (ROAs) for PTFE Teflon, FEP Teflon, PDMS, and PS are 2°, 4°, 2° and 8° respectively [16, 17, 20–24].

The surface free energy of a solid refers to the capability of the surface to bond with other surfaces. It can easily be realized that a high surface free energy material

Table 14.1 Water contact angles (CAs) on different surfaces with their corresponding surface free energy [16, 17, 20–24].

Surface	Surface free energy (mJ/m^2)	CA (°)
Polytetrafluoroethylene (PTFE Teflon)	18	168
Fluorinated ethylene propylene (FEP Teflon)	19	160
Poly(dimethylsiloxane) (PDMS)	21	163
Polypropylene (PP)	29	160
Poly(vinylidene fluoride) (PDVF)	30	171
Polyethylene (PE)	31	173
Polystyrene (PS)	36	158

will interact with a liquid atop the surface more readily than a comparable low surface free energy material. These interactions manifest primarily in the form of van der Waals forces and electrostatic attraction. Conversely, the surface tension of a liquid refers to the force directed inward from the surface of the liquid and is caused by the imbalance of forces at the surface. Thus, the force balance between the surface tension of the liquid and surface free energy determines the shape of the liquid when sitting atop a solid surface, and this behavior is known as wetting. Specifically, a low surface free energy solid and high surface tension liquid will have a comparatively low interfacial contact area. It is the interfacial contact area that is of particular interest when attempting to manipulate wetting [25].

Because of this force balance, a drop of water will take a consistent shape when resting atop a surface. The equilibrium contact angle (θ_E) (hereafter referred to as the static CA) is the angle measured between the solid surface and the tangent of the curve of the droplet at the point where the droplet contacts the surface, as depicted in Figure 14.1. The static CA can be calculated using Young's equation [26], as seen in equation 14.1, where θ_E is the static CA (*degrees*), γ_{LV} is the surface tension of the liquid-vapor interface (*mN/m*), γ_{LS} is the interfacial tension of the liquid-solid interface (*mN/m*), and γ_{SV} is the surface tension of the solid-vapor interface (*mN/m*).

$$\cos\theta_E = \frac{(\gamma_{SV} - \gamma_{LS})}{\gamma_{LV}} \tag{14.1}$$

A surface is said to be hydrophilic when the static CA of a 10 μL drop of deionized water is less than 90°. When the static CA is 90° or greater, the surface is said to be hydrophobic. When the static CA is 150° or greater, the surface is said to be superhydrophobic [27]. A combination of low surface free energy materials and surface texture can be used to make superhydrophobic surfaces. An example of a

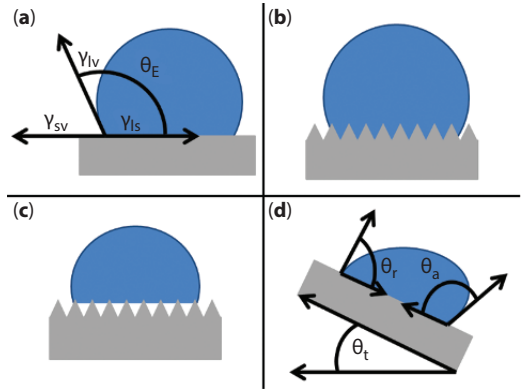

Figure 14.1 The various parameters and wetting modes for a droplet of liquid on a surface: (a) Static contact angle (θ_E), (b) Wenzel wetting, (c) Cassie-Baxter wetting, (d) Advancing contact angle (θ_a) and receding contact angle (θ_r), with roll-off angle (θ_t) of the surface. The different surface and interfacial tensions (mN/m) are liquid-vapor γ_{LV}, liquid-solid γ_{LS}, and solid-vapor γ_{SV} [19]. This figure is reprinted from "Anti-ice and Condensation Properties of Microtextured Superhydrophobic Surfaces", Ph.D. thesis, with permission from the author.

naturally occurring superhydrophobic surface is the surface of a lotus leaf. When a raindrop falls on a lotus leaf, it may bounce off after impact or roll off the lotus leaf dragging along dirt particles [28].

The presence of surface microtexture alters the interfacial interaction between a liquid and a solid. When in the Wenzel wetting state [27], water penetrates between and around surface microtexture features, as seen in Figure 14.1b. Wenzel's equation, equation 14.2, includes a roughness factor correction (r, *unitless*) to calculate the Wenzel CA (θ_W, *degrees*) from the static CA.

$$\cos \theta_W = r \cos \theta_E \tag{14.2}$$

As can be seen in equation 14.2, the introduction of surface roughness will make a hydrophobic surface more hydrophobic, while a hydrophilic surface will become more hydrophilic.

There also exists a wetting state disparate from Wenzel wetting, in which the liquid sits atop surface microtexture features, with air between microtexture features. This wetting state, as seen in Figure 14.1c, is known as Cassie-Baxter wetting [29]. The Cassie-Baxter equation can be simplified to the form included as equation 14.3. In the simplified Cassie-Baxter equation, the Cassie-Baxter CA (θ_{CB}, *degrees*) is calculated from the static CA using the same roughness factor correction as used to calculate the Wenzel CA, but also includes a fractional contact area (f_s,

unitless) correction factor. As can be seen, if $f_s = 1$, being the Wenzel wetting state, equation 14.3 can be simplified, resulting in equation 14.2.

$$\cos \theta_{CB} = r f_s \cos \theta_E - (1 - f_s) \tag{14.3}$$

A derivation and discussion of Young's, Wenzel's, and Cassie-Baxter's equations has been given by Mulroney [19], with a full derivation by Whyman, Bormashenko, and Stein [26].

Though the CA is the most common quantity reported when discussing a superhydrophobic surface, there are several other quantities measured and analyzed. The roll-off angle (ROA) is the angle of tilt from the horizontal of the surface, at which a 10 μL drop of deionized water sitting atop the surface begins to move, as depicted in Figure 14.1. The ROA is also often called the sliding angle (SA) because it is at this angle when the drop of water begins sliding down the surface. During a surface tilt measurement, and before motion begins, some deformation of the water drop will occur, and this causes the static CA measurements to change. The drop will lean towards the lower side of the tilted surface, and this is the direction in which the drop will slide when the movement begins. The static CA measurement taken on the side of the drop on the lower side of the tilted surface will be greater than the static CA measured on a flat and level surface and is known as the advancing contact angle (ACA). The static CA measurement taken on the opposite side of the drop from the ACA measurement will be less than the static CA measured on a flat and level surface and is known as the receding contact angle (RCA). The difference between the ACA and RCA is known as the contact angle hysteresis (CAH). Figure 14.1 also depicts the ACA and RCA of a drop of water experiencing deformation due to surface tilt.

Two examples demonstrate the role of surface microtexture in reducing the wettability of a low surface free energy material. Yeong and Gupta demonstrated that microtexturing a Fluorinated ethylene propylene (FEP) Teflon sheet increased the CA from 112° to 160°; while the ROA was decreased from 45° to 4° [21]. Similarly, Chun *et al.* demonstrated that microtexturing polystyrene increased the CA from 103° to 158° [17].

Liquids other than water are also of interest in analyzing wetting properties. The CAs of a number of liquids on microtextured PDMS were measured by Caffrey [30]. As expected and can be seen in Table 14.2, liquids with a surface tension lower than that of water demonstrated a lower CA.

Surfaces that have both superhydrophobic and superoleophobic properties are of great interest. ZnO and SiO_2 nanoparticles can be used to induce these properties and also create surface roughness for maintaining robustness. The contact angles and sliding angles were measured for the surfaces using water, ethylene glycol, and hexadecane, as shown in Figure 14.2. The surface tensions for ethylene glycol and hexadecane are 45 mN/m and 27.6 mN/m, respectively [31].

Table 14.2 Contact angles and sliding angles of different liquids on textured PDMS [30]. This figure is reprinted from "Superhydrophobic Properties of Replicated Laser Microtextured Surfaces", PhD Thesis, with permission from the author.

Sample	Advancing CA (°)	Receding CA (°)	Sliding angle (°)
Water (distilled)	161.3	157	4
Kerosene	wets	wets	–
Gasoline	wets	wets	–
Ethyl Alcohol	84.5	68.9	25
Isopropyl Alcohol	wets	wets	–
Oil (10W30)	81.4	50	25
Naphtha	wets	wets	–
Ethylene Glycol 50%	144.2	134.3	25

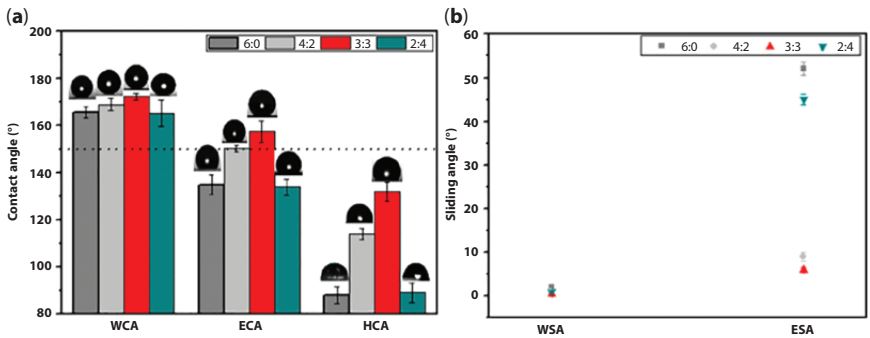

Figure 14.2 (a) WCA (water contact angle), ECA (ethylene glycol contact angle), and HCA (hexadecane contact angle) of the coatings fabricated by four different ZnO/SiO_2 nanoparticle mass ratios; (b) WSA (water sliding angle) and ESA (ethylene glycol sliding angle) of the coatings fabricated by four different ZnO/SiO_2 nanoparticle mass ratios [31]. This figure is reprinted from *Langmuir* 35, J. Peng, X. Zhao, W. Wang, and X. Gong, Durable Self-cleaning Surfaces with Superhydrophobic and Highly Oleophobic Properties, 8404-8412, copyright 2019, with permission from ACS.

14.1.2 State-of-the-Art

Advances in the study of microtextured superhydrophobic surfaces are actively occurring in various areas. One of the most active areas is the study of modifications to microtexture geometry and the resultant changes in wetting properties. Another very active area is the study of low ice adhesion surfaces. Related to the study of microtexture geometry is the goal of achieving optical transparency while

retaining superhydrophobic properties. The behavior of condensation on a microtextured surface and the effects of surface condensation on wetting are areas that present many challenges and have a growing body of research.

14.1.2.1 Microtexture Geometry

Factors like the height of nanopillars, the spacing between pillars, the intrinsic contact angle, and the impinging velocity of water nanodroplets heavily impact the transition of the water droplet from the Wenzel to Cassie-Baxter wetting state. There is a critical pillar height that determines whether the water drop sitting on the pillared surface is in the Wenzel or Cassie-Baxter wetting state. The free energy barrier between Wenzel and Cassie-Baxter states can be calculated using statistical mechanics and a simulation of rain impacting the surface. The barrier varies from a few tenths of $k_B T_0$ (where k_B is the Boltzmann constant, and T_0 is the ambient temperature) for a rough surface at the critical pillar height to near 8 $k_B T_0$ for the surface with pillar height greater than the length scale of water droplets. The barrier for the Wenzel to Cassie-Baxter state is much greater than from the Cassie-Baxter to Wenzel state for a very rough surface [32].

A study by Ambrosia analyzed the effects of surface fraction and the heights of pillars on the static CA of a water droplet on a graphite surface [33]. It was observed that the static CA increased with pillar height to a certain point, after which the static CA was no longer affected significantly by the pillar height. The increase in pillar height and the corresponding change in static CA were more noticeable when the pillar height was smaller or had a smaller pillar surface fraction. As the pillar surface fraction was decreased below 36%, simulations showed that the static CA fell short of the Cassie-Baxter model predictions. The reason for this is the sagging of part of the water droplet between the tops of the pillars [33].

14.1.2.2 Ice Adhesion

Microtextured surfaces that exhibit superhydrophobic wetting may or may not also exhibit low ice adhesion properties. The presence of surface microtexture has been shown to increase ice adhesion strength in some cases [34] and to decrease ice adhesion strength in others [21]. Barthwal, and coworkers [35] were able to reduce the ice adhesion strength of microtextured aluminum from 1200 kPa to 50 kPa using a combination of chemical etching and anodizing, plus a coating of PDMS infused with silicone oil. There are several common techniques for measuring ice adhesion strength. The two most common techniques are: pushing a probe against ice and measuring the force required for the ice to break away from the surface, and freezing a probe tip inside the ice, and then measuring the normal force required to pull the ice off the surface [36].

Brassard *et al.* [8] noted that water might be present between microtexture features and then join the main body of surface ice, thereby acting as an anchor for the ice and so increasing the ice adhesion strength. This was supported by Meuler *et al.*

[37] and Wang *et al.* [38], who each identified that water vapor inside the air pockets of the Cassie-Baxter wetting state would condense and freeze, again acting as an anchor for the main body of ice. It has also been suggested by Yeong and Gupta [21] that because water expands as it freezes, the ice will penetrate between microtexture features, again acting as an anchor and increasing the ice adhesion strength.

14.1.2.3 Optical Transparency

The presence of surface microtexture is known to introduce light scattering, causing a transparent smooth surface to appear opaque [11, 16, 19, 21]. However, certain microtexture pattern designs may allow light to pass through the surface. Mulroney and Gupta [16], and separately Chun *et al.* [17] investigated periodic microtexture patterns whereby a prescribed smooth surface area was left untextured, allowing light to pass through with minimal interference. Chun *et al.* [17] demonstrated the relationship between the distance between lines of microtexture and the changes to the static CA of microtextured polystyrene substrate. Mulroney and Gupta [16] demonstrated the same for a PDMS surface, while also analyzing the change in ROA, the effect of the space between microtexture lines on optical transmission percent, and the effect of the number of replication steps used to produce the microtexture pattern. It was found that an even number of replication steps caused an inverted microtexture profile where the water was strongly pinned to the microtextured PDMS, rather than easily rolling off the surface.

14.1.2.4 Anti-Condensation Surfaces

The presence of condensation has been shown to increase the water wettability of the surface while also altering the wetting state of the surface. Wu and Zhang [39] found that the presence of condensation on a surface caused the wetting state to transition from superhydrophobic to hydrophobic. This was attributed to the condensation droplets condensing onto the surface and then merge into the larger drop being studied, causing the interfacial contact area between the drop and the surface to increase. Yin *et al.* [40] found that the wetting state of the surface transitioned from Cassie-Baxter to Wenzel due to the presence of condensation.

To manipulate the condensation behavior, Yan *et al.* [41] applied an AC field across a superhydrophobic surface and demonstrated that the AC field reduced the growth of condensation on the surface.

14.2 Fabrication of Microtextured Surfaces

14.2.1 Surface Materials

Some of the material systems considered for making superhydrophobic surfaces are of low surface free energy such as fluorocarbons and compounds made out of polysiloxane; organic and inorganic compounds are also used in some cases. Microroughness and nano-roughness can be achieved for most surfaces. Polymers and

minerals are also good candidates for superhydrophobic surfaces. However, they sometimes have hydrophilic components in them. Therefore, they cannot be used in industries like printing and packaging that require highly superhydrophobic surfaces. Environmentally-friendly non-renewable materials are currently being replaced with bio-based materials, derived from wood, plant fibers, and agricultural residues [42]. Lignocellulose is one of the examples. Recent developments have been made in the cardboard and cotton industries by producing superhydrophilic materials where cellulose was used as the base material. Amongst environmentally-friendly materials, cellulose nano-crystals and composites have been cited [42]. The surface free energy of cellulose is lowered through a roughening process. The durability of the applied rugose layer allows required improvements. Many recent experiments have been done on the durability and robustness of lignin-coated cellulose nanocrystal (L-CNC) particles. Commercial biodegradable L-CNC particles were made to stick to the substrate and made the surface rough. The resulted coatings displayed attributes like self-cleaning properties, water repellency, durability against sandpaper abrasion, finger-wipe, knife scratches, water jet, UV radiation, high-temperature exposure, and exposure to acid and alkali solutions. Similarly, in the field of textile materials, superhydrophobic flame-retardant cotton was developed by a research group using layer-by-layer assembly of branched polyethylenimine (bPEI), ammonium polyphosphate (APP), and fluorinated polyhedral oligomeric silsesquioxanes (F-POSS). This discovery is an important one in the field of flame-proof materials. An effective method to use lignocellulose (LC) as base-support to fabricate superhydrophobic surfaces with flame retardant properties was discovered in 2018 [42]. PDMS-stearic acid-modified kaolin-coated LC attained a water static CA of 156°. The kaolin particles also displayed good flame-retardant properties [42].

There are many examples of both naturally occurring and artificially made superhydrophobic surfaces. The natural surfaces include both plant and insect surfaces. The most naturally distinguishable superhydrophobic surface is that of the lotus leaf. Lotus leaf is extremely repellent to water and this very property inspired scientists to do further research on superhydrophobic surfaces. The term 'lotus effect' is associated with superhydrophobic behavior. Various research institutions have fabricated superhydrophobic surfaces using photolithography. These have been mainly done with the use of silicon rods and glass fibers. Water static CAs of over 160° have been achieved on these surfaces [43].

Silicones are one of the most widely used materials for fabricating superhydrophobic surfaces. A major advantage of silicones is their chemical inertness, which has led to their widespread and common use. The coating and its properties do not seem to be significantly influenced by organic solvents. Figure 14.3 shows the progression of static CA and sliding angles as a function of immersion time in the polar solvents acetone and ethanol and the non-polar solvent toluene [44]. Static CA values remain virtually unchanged for all samples. Sliding angles show a small increase in polar solvents and a small decrease in toluene. The annealed samples are less affected than the non-annealed samples.

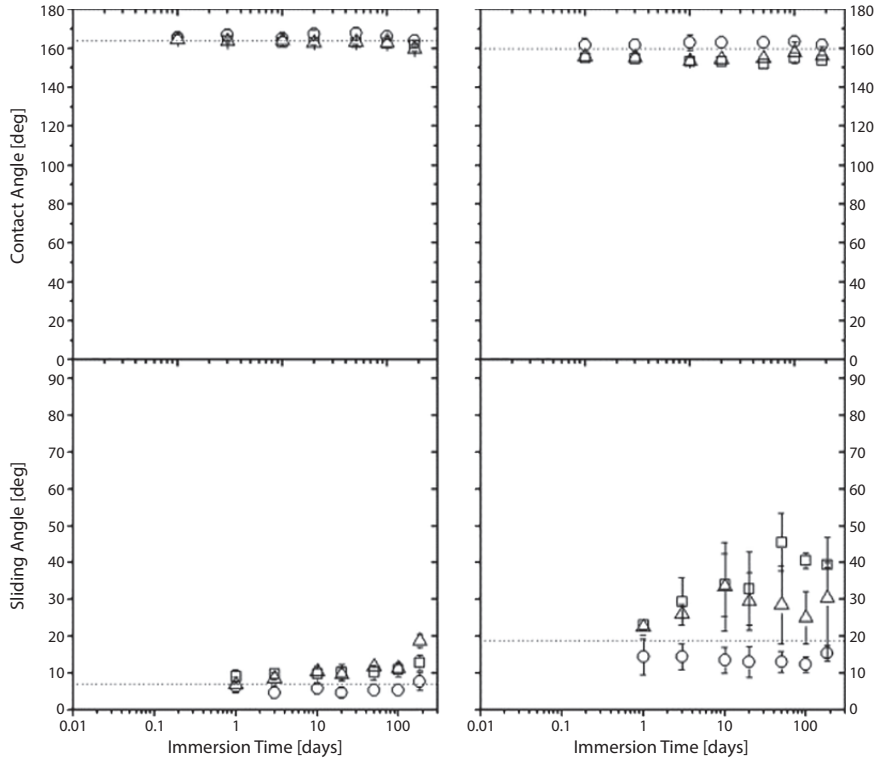

Figure 14.3 Contact and sliding angles of annealed (left) and non-annealed (right) samples immersed in organic solvents (□ ethanol, Δ acetone, ○ toluene). The dotted lines indicate initial values [44]. This figure is reprinted from *Applied Surface Science* 253, J. Zimmermann, G. Artus, S. Seeger, Long term studies on the chemical stability of a superhydrophobic silicone nanofilament coating, 5972-5975, copyright 2007, with permission from Elsevier.

The adhesion behavior of superhydrophobic surfaces has become an emerging topic to researchers in various fields. Controlling the chemical compositions and topological structures via various methods or technologies is crucial to fabricate and modulate different adhesion properties, like low-adhesion, high-adhesion, and anisotropic adhesion on superhydrophobic surfaces [45].

14.2.2 Methods of Fabrication of Superhydrophobic Surfaces

14.2.2.1 Plasma Treatment

Plasma treatment can be used to deposit low surface free energy materials and to etch a surface; by etching the surface roughness is enhanced, as seen in Figure 14.4. Plasma deposition modifies a surface with low surface free energy materials deposited from fluorinated gas or hydrophobic monomers. There are different types of

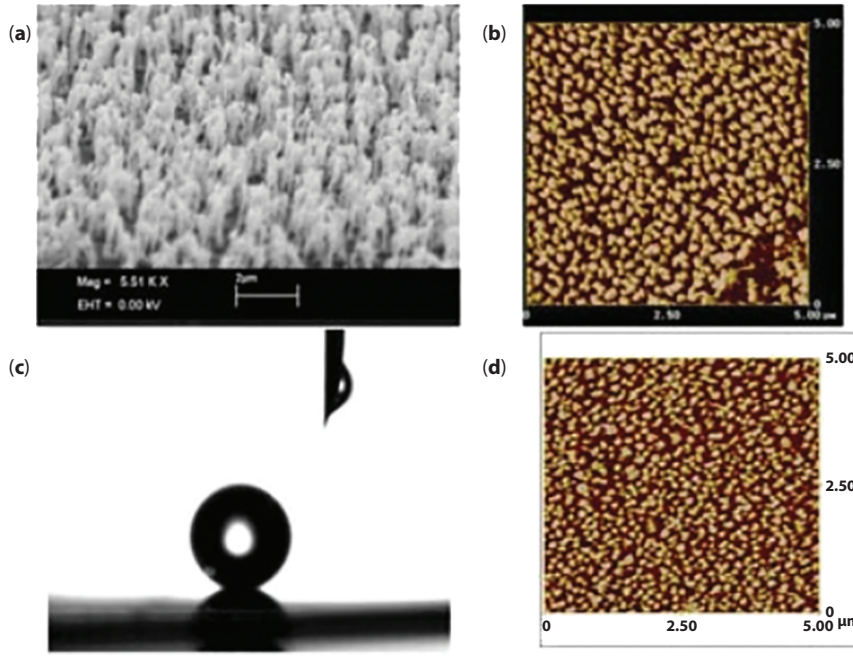

Figure 14.4 (a) SEM image of a PDMS elastomer (Sylgard 184) surface after a 6 min SF_6 plasma treatment. 1.45 μm-high nano-columns are shown. (b) AFM top-view image of the same elastomer surface after a 2 min treatment in SF_6 plasma (roughness rms~133 nm and periodicity~240 nm). (c) Image of a water droplet while rolling off the plasma treated PDMS elastomer surface after being conformally coated with a 20 nm-thick fluorocarbon (FC) film. (d) AFM top-view image of photosensitive elastomer PS264 surface after a 2 min treatment in SF_6 plasma (roughness rms~76 nm) [2, 97]. This figure is reprinted from *Encyclopedia of Polymer Science and Technology, 4th edition*, M. Wolfs, T. Darmanin, and F. Guittard (Eds.), Superhydrophobic Polymers, copyright 2013, with permission from John Wiley & Sons, Inc.

plasma treatments to make superhydrophobic polymeric surfaces: etching fluorinated polymers, fluorinated gas plasma treatment, plasma polymerization, and more complex superhydrophobic polymeric surface fabrication using plasma etching or deposition [2].

14.2.2.2 Laser Ablation

Chemical methods of microtexturing the surface of solids sometimes utilize toxic chemicals. Hence, a great alternative is to use laser-based physical microtexturing to achieve the desired wettability behavior. Modification of the surface can be done with lasers of different pulse widths (nano, pico, and femtosecond laser) [46]. Fabrication of micro/nano patterned surfaces using femtosecond laser micromachining techniques are scalable, one-step processes and can be applied to virtually all kinds of

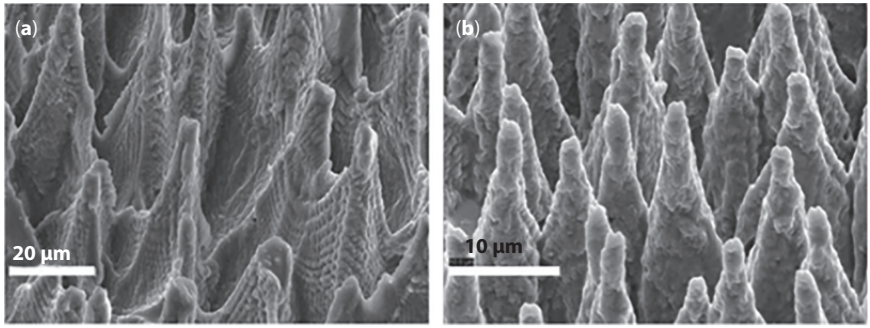

Figure 14.5 SEM image of replicated micro/nanostructures on PDMS surfaces from ultrafast laser textured masters: (a) Ti (b) Si [48]. This figure is reprinted from *Applied Surface Science* 266, B. K. Nayak, P. O. Caffrey, C. R. Speck, M. C. Gupta, Superhydrophobic surfaces by replication of micro/nano-structures fabricated by ultrafast-laser-microtexturing, 27-32, copyright 2013, with permission from Elsevier.

materials [47]. The resultant morphology and the roughness of polymer substrates microtextured by laser ablation are dependent on the laser parameters (energy, number of pulses, etc.). Appropriate laser parameters can make hydrophobic surfaces superhydrophobic [48]. Organic substrates that are intrinsically hydrophobic can sometimes be laser ablated and made superhydrophobic. Poly(dimethylsiloxane) (PDMS) and polytetrafluoroethylene (PTFE) are organic materials that are of great interest [49]. Laser pulses causing ablation can lead to the formation of hierarchical morphology on the PDMS. Since the laser technique is an etching method, fragments can be detached from the substrate and redeposited and this leads to additional surface roughness, as seen in Figure 14.5. A simple, cost-effective method of producing superhydrophobic surfaces is by direct replication of micro/nano-structures onto PDMS from a replication master. The master is usually microtextured by an ultrafast laser. Reported water contact angles of 154º have been achieved. The contact angle can be controlled by varying the height of the microtexture features [48]. Polymeric materials tend to be cheaper and easier to manipulate compared to metals. Hence, polymeric materials are a better choice for surface-engineered applications [50].

A high water repellent poly(ethylene terephthalate) (PET) surface was produced with a laser-assisted magnetron sputtering method. The laser was responsible for the overall morphology of the polymer while the magnetron sputtering deposited a thin fluorocarbon layer quasi-simultaneously. Superhydrophobic properties (static CA 160.8º and CAH of 10.2º) were obtained and this can be attributed to the synergetic effects of laser ablation of PET and the fluorocarbon deposition [2].

14.2.2.3 Chemical Etching

A surface roughening methodology by chemical etching was developed for the fabrication of superhydrophobic surfaces on three crystalline metals, namely,

aluminum, copper, and zinc [51]. The key to the etching technique was the utilization of a dislocation etchant that preferentially dissolves the dislocation sites within the grains. The surfaces, once hydrophobized with fluoroalkylsilane, exhibited superhydrophobic properties with water contact angles of larger than 150°. Furthermore, they showed roll-off angles of less than 10° for 8-μL water drops. Aluminum samples were etched by immersing in Beck's dislocation etchant in a polyethylene bottle at a temperature of 14°C. The etchant was a 40 mL mixture of 37 wt % HCl, 12.5 mL of H_2O, and 2.5 mL of 40 wt% HF. The etching time was varied from 5 s to 15 s. Copper samples were washed with 13 wt % HNO_3 for 15 min. Then, they were etched with Livingston's dislocation etchant in a closed glass bottle at ambient temperature. The etchant was made by mixing 0.06 mL of 7 wt % HCl, 0.02 mL of CH_3COOH, and 53.92 mL of H_2O. The etching time was varied from 8 h to 24 h. Zn samples were etched with 50 mL of 4.0 mol L^{-1} HCl solution in a glass beaker at room temperature. The etching time was varied from 30 s to 40 s. After etching, all the specimens were ultrasonically rinsed with water and dried at 80°C in air. At room temperature, a 3-fold molar excess of water was added to a methanol solution of fluoroalkylsilane (tridecafluorooctyltriethoxysilane, $C_8F_{13}H_4Si(OCH_2CH_3)_3$. The etched metallic specimens were immersed in the hydrolyzed silane solution for 1 h at room temperature. Then, they were heat-treated at 130 °C for 1 h [51]. The results of the wetting analysis of the various materials and etching parameters are presented in Table 14.3.

Table 14.3 Water contact angle data for the etched surfaces after fluorination for various etching times [51]. This figure is reprinted from Langmuir 21, B. Qian, Z. Shen, Fabrication of Superhydrophobic Surfaces by Dislocation-Selective Chemical Etching on Aluminum, Copper, and Zinc Substrates, 9007-9009, copyright 2005, with permission from ACS.

Sample		Equilibrium contact angle (deg)	Advancing contact angle (deg)	Receding contact angle (deg)	Contact angle hysteresis (deg)
Metal	Etching time				
Al	5 s	124	133	107	26
Al	10 s	148	154	137	17
Al	15 s	156	158	153	5
Cu	8 h	138	143	119	24
Cu	16 h	146	154	133	21
Cu	24 h	153	155	145	10
Zn	30 s	137	143	116	27
Zn	60 s	152	154	141	13
Zn	90 s	155	156	149	7

14.3 Properties of Microtextured Surfaces

Superhydrophobic surfaces have a wide range of properties that are useful for industrial and household applications. Some of the properties are discussed below.

14.3.1 Antifogging

Fog is commonly formed when vapor condenses because of a change in temperature, humidity, or convection. The presence of fog on a surface could scatter light, reducing the optical properties of transparent surfaces. Thus, antifogging is crucial for the surfaces utilized in windshields, safety glasses, eyeglasses, etc. When the contact angle is below 40 degrees, moisture is condensed into a thin film, and no fog is visible on the surface. However, a large number of small condensed water droplets are also formed on the surface. On the other hand, when moisture condenses, fog is developed on superhydrophobic surfaces. Interestingly, the superhydrophobic surfaces reduce the fog formation by increasing the evaporation rate, as per Chen *et al.* [52]. The fog formed on a normal glass condensed to create a water film on the surface in a couple of minutes, whereas the fog formed on a superhydrophobic glass disappeared in 10 s and no water film was created thanks to the increased area. Chen *et al.* [52] fabricated a superhydrophobic surface using silica capsule particles with an apparent static CA of 152° and a ROA of less than 8° by the dip-coating method. This highly transparent surface could increase the evaporation rate of the fog and therefore caused the fog to disappear [53].

14.3.2 Antibacterial

Antibacterial properties are fundamental in biosensors, mechanical and marine hardware, and for the prevention of microorganisms that contaminate implants used for surgeries. In an attempt to solve this issue, antibacterial coatings that diminish the bacterial attachment to the surface are utilized. In this regard, one of the investigators [54] created silver nanoparticles on cotton filaments and then adjusted these particles using hexadecyltrimethoxysilane to induce superhydrophobicity. The sample's antibacterial activity is shown in Figure 14.6. The results showed that the typical cotton showed no antibacterial action, though the silver doped cotton surfaces killed all the microscopic organisms beneath and around them. This shows a noticeable inhibition zone with an average of 8.78 mm around the samples [54].

14.3.3 Antireflection

Antireflection is vital in optical devices like solar cells, light-emitting diodes, and laser optics. A high transmission rate is required for reducing light reflection.

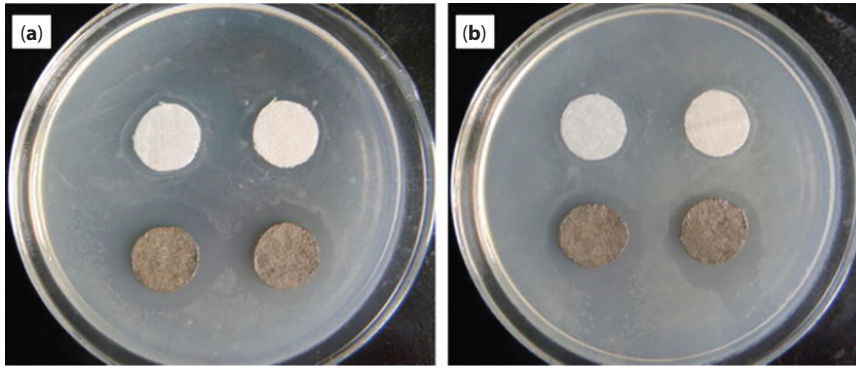

Figure 14.6 Antibacterial activity of (a) normal cotton (the upper two) and Ag NP modified cotton (the lower two) textiles. Normal cotton samples did not show any antibacterial activity. The silver modified cotton textiles placed on the bacteria-inoculated surfaces killed all the bacteria under and around them and a distinct inhibition zone with an average width of 8.78 mm around the cotton samples was observed. (b) normal cotton (the upper two) and hydrophobized Ag NP modified cotton (the lower two) textiles. After hydrophobization, the average width of the inhibition zone of the silver modified samples was reduced to 6.84 mm. This may be attributed to the prohibition of the diffusion of Ag+ from the silver particles by hydrophobization [54]. Reprinted with permission from IntechOpen, M. Khodaei, X. Chen and H. Li, Superhydrophobic surfaces - fabrications to practical applications, in: *Superhydrophobic Surfaces – Introduction and Applications*, 1-11, (2020).

According to the effective medium theory, if 100% transmission is required, the microstructure height, h, must satisfy the following condition:

$$h = \frac{\lambda}{\sqrt{n_1 \times n_2}} \tag{14.4}$$

where λ is the propagating wavelength, n_1 is the refractive index of air, and n_2 is the refractive index of the optical surface. Alternatively, to make the surface anti-reflective, roughness is required. Surfaces with considerable roughness exhibit antireflection properties. Metal-assisted (Au, Pt, or Pt/Pd) etching is employed to create superhydrophobic nanostructures on silicon surfaces. This sort of etching process is employed for producing low reflective surfaces. If the nanostructures are formed appropriately, the reflectivity of these surfaces may be reduced to almost zero. Due to low reflection, the surface can absorb most of the incident light, being a desired property of high-efficiency solar cells [53].

14.3.4 Self-Cleaning

Non-wettable surfaces attract a lot of attention due to their ability to repel liquid drops and remain unwetted [55]. The extreme repellence of water by superhydrophobic surfaces helps in washing away the dirt when the water drops roll over the surfaces. This is particularly useful in solar panels where a transparent self-cleaning surface is needed. Park *et al.* [56] fabricated a microshell array of PDMS. The layer had a static CA of 151° and the CAH was 19° [53].

14.3.5 Effect of Temperature on Surface Properties

The variation of superhydrophobicity with temperature is a very interesting phenomenon. For example, Al, Cu, and Ti show hydrophilic properties just after laser ablation processing. But, after they are treated in the oven, they show increased static CA values, as shown in Figure 14.7 [57]. Maximum and minimum static CAs are indicated by the error bars. The error bars indicate the maximum and minimum static CAs and sliding angles (SAs) for each of five different samples of Al, Cu, and Ti.

Different kinds of heat treatments at different temperatures affect differently the wettability of the samples in different ways. As the heat treatment temperature is increased, the wettability transition time for Al and Ti decreased. The wettability transition time for Cu was only reduced when the temperature was increased from 100 °C to 150 °C. Subsequently, at a higher temperature (200 °C), Cu showed a longer wettability transition time compared to the wettability observed at 150 °C. Among the heat treatment temperatures discussed, Al and Ti showed fast wettability transition times (90 min and 30 min, respectively) at 200 °C. Cu showed a wettability transition of 120 min at 150 °C. Apart from showing static CAs greater than 150 °, Al, Cu, and Ti surfaces showed high adhesion to water (petal effect). As heat treatment time was prolonged, the superhydrophobic surfaces changed from petal effect to lotus effect. This transition is marked by the appearance of low SAs (SA < 10°) with a tilting speed of $1.6° s^{-1}$. In the case of all metals except Cu, when the heat treatment temperature was increased, the sliding angle appeared after a shorter time and became smaller with a gradual increment of time. In addition, changing the petal effect to the lotus effect required different times for each metal. As an example, the SA for Al appeared after 6 h with heat treatment at 200 °C and after 12 h with heat treatment at 150 °C. In the case of Ti, the SA appeared after 2 h with heat treatment at 200 °C and after 12 h with heat treatment at 150 °C. In the case of Cu, the SA appeared after 12 h with heat treatment at 150 °C and 200 °C. The SA at 150 °C was smaller than that at 200 °C. With prolonged heat treatment time, the SA value for each material decreased. A low SA might indicate a high-quality superhydrophobic surface that demonstrates the lotus effect. Al and Cu samples treated at 100 °C did not show SAs within 24 h even though the static CA was greater than 150°. Hence, heat treatment time should be increased to change the superhydrophobic surface from the petal effect to the lotus effect on Al and Cu samples treated at 100 °C. This is also affirmed by the results from Al, Cu, and Ti

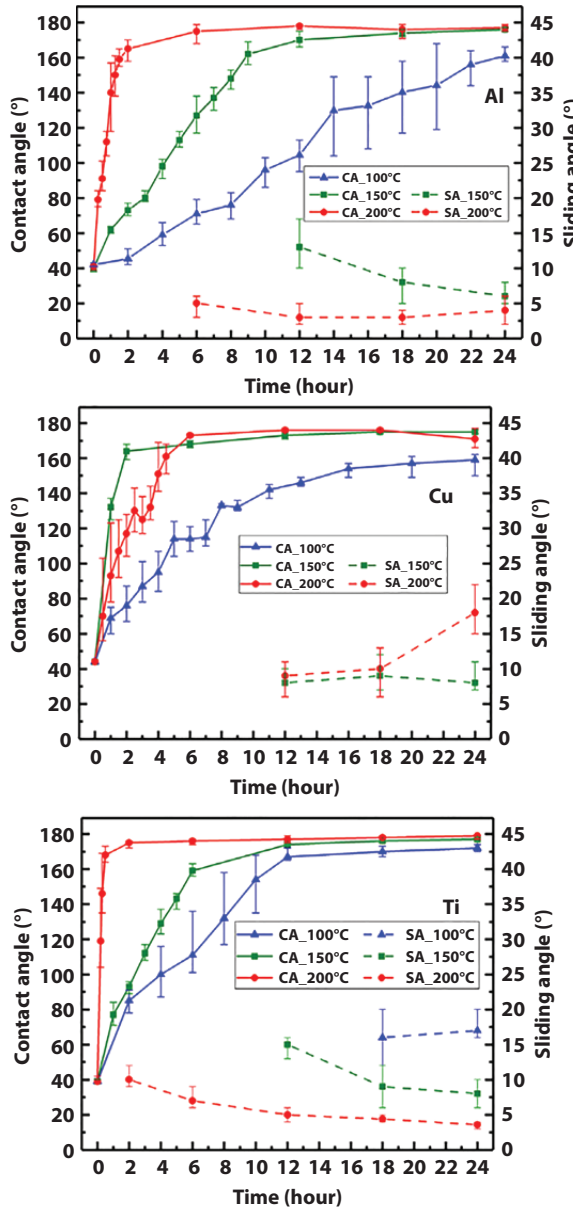

Figure 14.7 Contact angles and sliding angles of Al, Cu, and Ti samples measured at various times after heat treatment (100, 150, and 200 °C) [57]. This figure is reprinted from *Advanced Engineering Materials* 20, Chi-Vinh Ngo, Doo-Man Chun, Effect of Heat Treatment Temperature on the Wettability Transition from Hydrophilic to Superhydrophobic on Laser-Ablated Metallic Surfaces, 1701086, copyright 2018, with permission from Wiley-VCH.

samples treated at 150 °C and 200 °C and Ti samples treated at 100 °C. Treating the Cu samples at 200 °C with longer treatment times reduced superhydrophobicity (decrease in static CA and increase in SA) [57].

A study has been done on the superhydrophobicity of polyurethane/organoclay nanocomposites as they go through a cycle of temperature at high and low humidity, as shown in Figure 14.8. The initial temperature of the experiment was

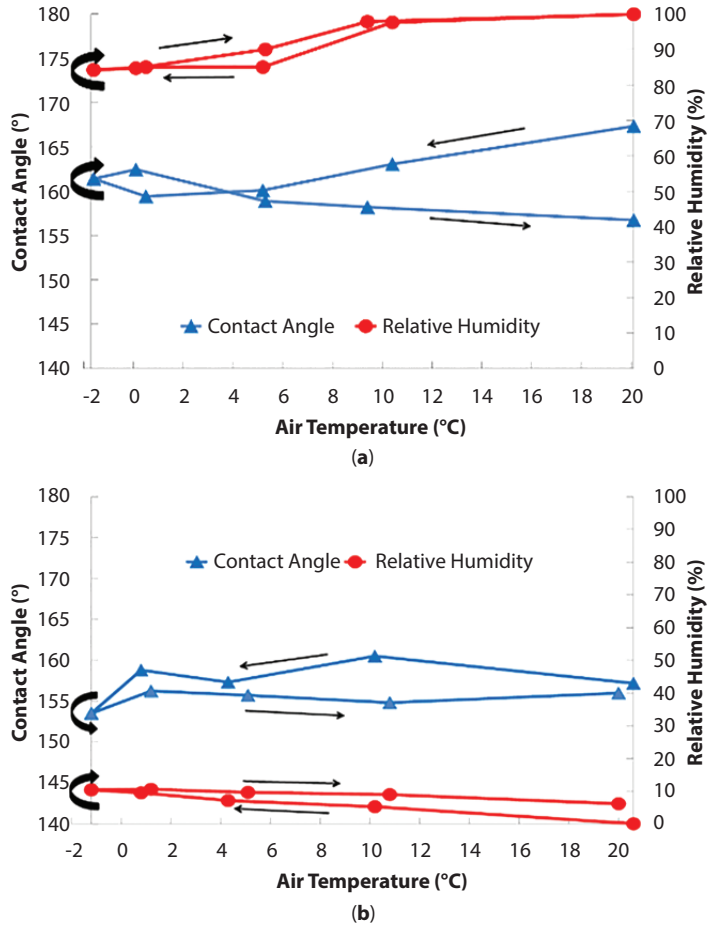

Figure 14.8 (a) Water contact angle measurements for a complete temperature cycle at high relative humidity (over 85%); (b) Water contact angle measurements for a complete temperature cycle at low relative humidity (less than 10%) [58]. This figure is reprinted from *Nanotech TechConnect Briefs* 1, Y. Yeong, A. Steele, I. Bayer, G. DeCombarieu, C. Lakeman, E. Loth, Impact of Temperature and Humidity on Superhydrophobicity of Polyurethane/Organoclay Nanocomposites, 383-386, copyright 2011, with permission from TechConnect.

20 °C and the direction of the temperature cycle is shown by arrows. The saturated air condenses at lower temperatures on the nanocomposites. This results in a decrease in static CA and an increase in the wettability of the surface. The level of condensation depends on the humidity in the air. The ROA was lower (around 3°) during the first half of the temperature cycle and gradually increased to around 8° during the second half of the cycle [58]. Nanostructured surfaces that were coated with hydrophobic diamond-like carbon (DLC) maintained superhydrophobicity with a static CA greater than 150° for annealing temperatures between 25 and 300°C. The DLC was deposited via plasma polymerization of hexamethyldisiloxane (HMDSO). It has been noted that nanostructured surfaces that have an aspect ratio higher than 5.2 may maintain superhydrophobicity at very high annealing temperatures (~350°C). But, the hydrophobicity on surfaces with lower aspect ratio nanostructures gradually degraded at temperatures higher than 350°C. All superhydrophobic surfaces became superhydrophilic after annealing at temperatures higher than 500°C, irrespective of the aspect ratio [59].

14.4 Applications

14.4.1 Anti-Icing

Each year ice storms adversely impact electrical transmission lines, communication frameworks, aviation infrastructure, roads, etc. In an attempt to decrease this kind of harm, distinctive strategies have been created, such as local warming by chemical means, which have a few restrictions in viable applications. However, superhydrophobic surfaces can be used to reduce ice adhesion strength, as noted in Section 14.1.2. Further, because water on a superhydrophobic surface does not spend a significant amount of time on the surface before rolling off, the water is removed before solidifying into ice.

The accumulation of ice on the wings of aircraft is a critical safety concern, the presence of which can lead to structural damage and loss of aerodynamic properties [60]. These effects lead to the use of complex anti-icing systems, additional preparation costs for aircraft, and the delay or cancellation of some flights. Similarly, ice may accumulate on the edges of wind turbine blades. This ice can cause an imbalance of the turbine blade, reducing power generation efficiency, increasing maintenances costs, and can cause personal or property damage [61, 62]. Both aircraft wings and wind turbines are difficult to access during use, and so prevention or remediation systems must be incorporated into the design. Auxiliary heating systems are often incorporated into the leading edge of the aircraft wing or turbine blade; however, these consume energy, introduce complexity, and create additional risk of system failure [63–67]. The implementation of a surface that passively prevents or reduces ice buildup would mitigate many of these concerns, and the fabrication for these surfaces is being investigated [68, 69].

14.4.2 *Drag Reduction*

Drag force is one of the main problems facing a solid moving in water like a ship or a submarine. Several superhydrophobic coatings have been fabricated, inspired from shark skin, to minimize drag. The presence of air pockets between microtexture features, as described in the Cassie-Baxter wetting model, can diminish the contact between solid and liquid so that the drag will be lessened [54]. Drag diminishment by superhydrophobic surfaces was explored in different works such as the study by Dong and co-workers [70], where they created a superhydrophobic coating on the curved surface of a model ship by electroless deposition of gold aggregates. The average velocities of the model ship before and after the coating were measured in a sink with a size of 6 m × 0.6 m × 0.3 m. To calculate the average velocity, two identical iron wires were set across the sink and they were connected to the model ship by nylon wires, as shown in Figure 14.9a. The model ship was powered through an open circuit and the moving velocity of the ship was tuned by connecting a series resistance in the circuit. The value of the resistance ranged from 0.1 to 1.3 Ohm, corresponding to different sailing velocities. The velocity difference between the

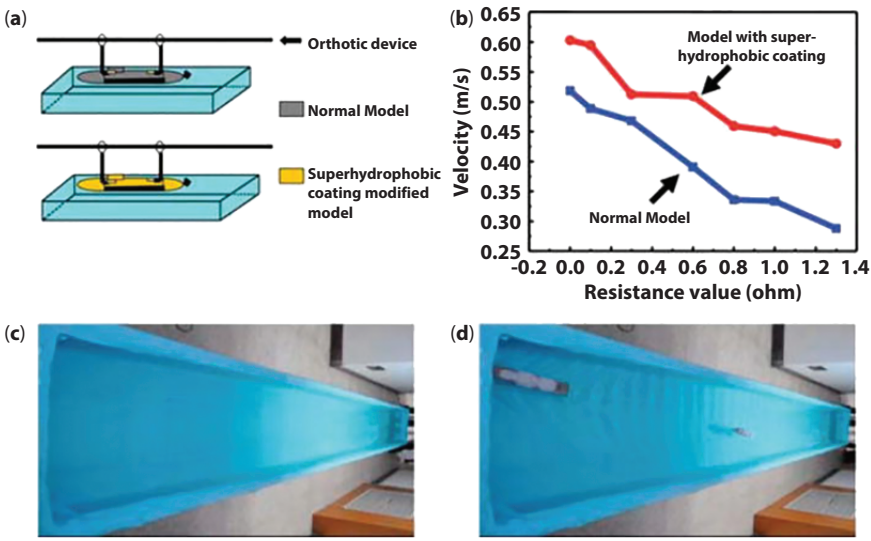

Figure 14.9 (a) Illustration of the device for the drag-reducing test; (b) velocity of the model ships with and without a superhydrophobic coating versus the values of the resistance in the circuit powering the ship; (c) snapshots at the beginning and (d) at the end of the drag-reducing test [54, 70]. Reprinted with permission from IntechOpen , M. Khodaei, X. Chen and H. Li, Superhydrophobic surfaces - fabrications to practical applications, in: *Superhydrophobic Surfaces – Introduction and Applications*, 1-11, (2020).

model ships with and without a superhydrophobic coating increased with increasing resistance in the circuit, indicating an increase in the drag-reducing effects, as shown in Figure 14.9b. The superhydrophobic model ship displayed a surprising drag decrease of 38.5%. On the uncoated surface, the drag occurs between solid and water, but on the superhydrophobic surface, the drag occurred between solid and water in some locations and between air and water in others, known as the plastron effect, which resulted in a greatly reduced overall drag of the ship. Entrapped air in surface asperities causes drag reduction of superhydrophobic surfaces. Drag reduction is affected by the wettability of the surface, Reynolds number, direction and size of features on the surface, and shear rate [71].

14.4.3 Anti-Corrosion

Due to the shedding of water and self-cleaning properties, all superhydrophobic surfaces are to a certain extent capable of withstanding chemical attacks in aqueous acid, i.e., alkaline, or salt solutions. However, these surfaces often exhibit low mechanical durability and can, depending on the material composition, be chemically reactive [72]. When damaged, the surfaces may become more hydrophilic. To this end, improving mechanical robustness has become one of the key issues in the development of superhydrophobic surfaces with long-lasting corrosion resistance. Xiu *et al.* [73] demonstrated that the superhydrophobicity of a silica surface with micro and nanoscale hierarchical structures withstood mechanical abrasion better than a nanostructured superhydrophobic surface, as seen in Figure 14.10. After abrasion, only the nanostructures on the peaks of the microstructures were removed. The nanostructures at the bottom were largely preserved, which was critical for retaining the surface superhydrophobicity [74].

14.4.4 Solar Cells

The self-cleaning nature of superhydrophobic surfaces is advantageous to solar power generation. The presence of contaminants, such as dust, dirt, or other organics, prevents sunlight from reaching the solar cells. Also, the presence of surface water and ice increases the reflectivity of the surface [63, 75]. Chemical or mechanical removal of water, ice, and contaminants requires auxiliary systems or physical access to the solar cells, which may not be possible in every application. Microtextured superhydrophobic surfaces have been demonstrated to remove these contaminants and prevent the accumulation of surface water and ice [76–78]. Furthermore, the microtexture pattern may introduce a secondary benefit as an anti-reflection coating [79], thereby aiding in the capture of more solar energy.

14.4.5 Water-Repellent Textiles

Superhydrophobic coatings are most often applied on rigid substrates. But, in applications like textile fabrics, the substrate (fabric) is not rigid. In the work of

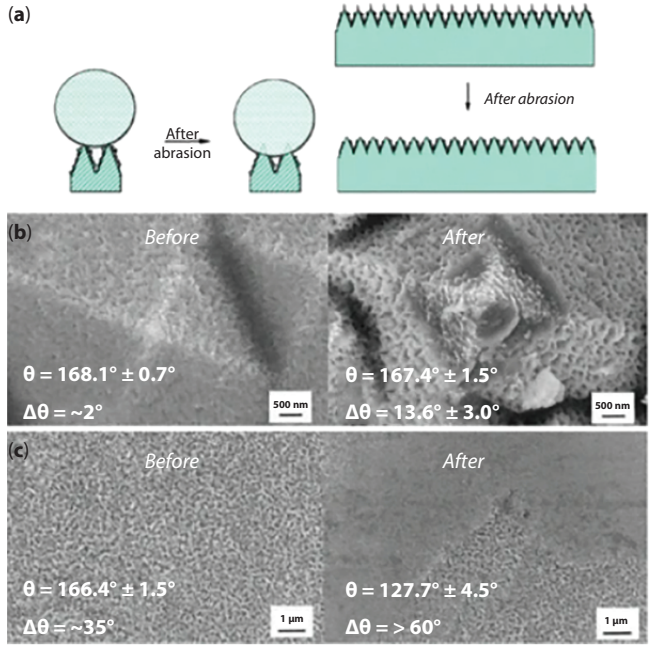

Figure 14.10 (a) Illustration of water droplet on Si with two-scale structures before and after abrasion; (b) SEM morphology, static contact angle (θ), and contact angle hysteresis (Δθ) of Si with two-scale structures before and after abrasion; (c) SEM morphology, static contact angle and contact angle hysteresis of Si with nanostructures before and after abrasion [74]. This figure is reprinted from the *Journal of Coatings Technology and Research* 13, D. Zhang, L. Wang, H. Qian, Superhydrophobic surfaces for corrosion protection: a review of recent progresses and future directions, 11-29, copyright 2016, with permission from Springer Nature.

Wang *et al.* [80], superhydrophobic surfaces were created by modifying cotton substrates with n-dodecanethiol and gold micro/nanostructures. All surfaces showed an apparent static CA greater than 150° and retained the superhydrophobicity after folding the surfaces several times [42]. Superhydrophobic textile fabrics were prepared by Zimmermann *et al.* [44], with polymethylsilsesquioxane nanofilaments. Since the normal contact angle is unsuitable for superhydrophobic textile properties, a parameter, named the water-shedding angle, was used for determining the wettability of the fabrics. When a water drop is allowed to fall onto the inclined substrate, the drop completely rolls-off the surface. The authors called this minimum angle the water-shedding angle. Wang *et al.* [81] prepared fabrics modified with a fluorinated-decyl polyhedral oligomeric silsesquioxane and a fluorinated alkyl silane. The prepared fabric showed both self-healable superhydrophobicity, superoleophobicity, and exhibited durability to acids, ultraviolet

rays, machine wash, and abrasion resistance. Due to the anticipated applications of superhydrophobic fabrics, durability against scratching, abrasion, and general wear is necessary. Highly specialized technical textiles are used in automotive and aerospace industries, filtration, construction, medicine, etc. Elementary grafting processes or thin-layer deposition can be used to induce chemical modifications of the fiber surface that affect (super-)repellent behavior with regard to water or oils, coating or fiber-matrix adhesion, surface conductivity in the context of antistatic behavior, and proteins and cell adsorption and adhesion, which influence biofilm growth [82].

14.5 Future Outlook

Continued research into the primary and secondary effects of microtextured superhydrophobic surfaces reveals opportunities to improve the current designs and fabrication techniques. In addition, research efforts focus on how these surfaces can affect application areas more broadly, such as wind power generation and refrigeration. Further, new and novel consequences of the behavior of water on these surfaces are being discovered. And so, concurrent research occurs today on design, applications, and novel consequences of these surfaces.

Plasma treatment and laser ablation suffer from scalability concerns [16, 22, 83], while chemical etching suffers from application and materials limitations [8, 84]. Meanwhile, the use of nanoparticles shows promise in overcoming these limitations. The coating of metallic nanoparticles shows potential for increased durability [67], simple fabrication techniques [85], and large area coverage [86]. Without these achievements, the viability is in doubt for these surfaces in corrosive [87] or extreme temperature [8, 60] environments.

In many applications, such as anti-icing surfaces or solar cells discussed earlier in Sections 14.4.1 and 14.4.4, respectively, the applications are the centerpiece of the research. The addition of a microtextured surface may reduce the ice adhesion strength on a wind turbine [88], and the combination of native low surface free energy materials and surface microtexture can prevent ice buildup [7]. In addition, the natural anti-reflection properties of microtextured surfaces [29, 89] couples well with solar power generation applications [90, 91]. However, opaque materials are not viable in solar power generation applications [16, 63, 69, 75]. Nevertheless, a commercialization opportunity exists for cold storage applications, solar power generation, and wind power generation.

Novel consequences of microtextured superhydrophobic surfaces involve the kinetics of condensation coalescence into a droplet [92, 93]. From this, new research areas such as the possibility of manipulating wetting properties [94, 95] and condensation behavior [41, 96], are being pursued. It is interesting to note that fully-controllable wetting properties can also be induced on the surface of synthetic materials, such as PDMS, by using plasma treatment under appropriate conditions in SF_6 gas [97].

Acknowledgments

The authors would like to thank the NASA Langley Professor Program, National Science Foundation (NSF) I/UCRC award: IIP-1338917, and NSF award: IIP-1343450 for their support of this research.

References

[1] N. Shirtcliffe, G. McHale and M. Newton, The superhydrophobicity of polymer surfaces: Recent developments, *J. Polym. Sci. B: Polym. Phys.* **49**, 1203-1217 (2011).
[2] M. Wolfs, T. Darmanin, and F. Guittard, Superhydrophobic polymers, *in Encyclopedia of Polymer Science and Technology*, 4th edition, John Wiley & Sons (2013).
[3] E. Huovinen, L. Takkunen, T. Korpela, M. Suvanto, T. T. Pakkanen, and T. A. Pakkanen, Mechanically robust superhydrophobic polymer surfaces based on protective micropillars, *Langmuir* **30**, 1435-1443 (2014).
[4] Y. Shen, Y. Wu, Z. Shen, and H. Chen, Fabrication of self-healing superhydrophobic surfaces from water-soluble polymer suspensions free of inorganic particles through polymer thermal reconstruction, *Coatings* **8**, 144-157 (2018).
[5] I. Yilgor, S. Bilgin, M. Isik, and E. Yilgor, Tunable wetting of polymer surfaces, *Langmuir* **28**, 14808-14814 (2012).
[6] P. F. Rios, H. Dodiuk, S. Kenig, S. McCarthy, and A. Dotan, Durable ultra-hydrophobic surfaces for self-cleaning applications, *Polym. Adv. Technol.* **19**, 1684-1691 (2008).
[7] A. Mulroney, E. Kessler, S. Combs, and M. C. Gupta, Low ice adhesion surfaces using microtextured hydrophobic tapes and their applications in refrigeration systems, *Surf. Coat. Technol.* **351**, 108-114 (2018).
[8] J. Brassard, J. Laforte, C. Blackburn, J. Perron, and D.K. Sarkar, Silicone based superhydrophobic coating efficient to reduce ice adhesion and accumulation on aluminum under offshore arctic conditions, *Ocean Eng.* **144**, 135-141 (2017).
[9] M. Kreder, J. Alvarenga, P. Kim, and J. Aizenberg, Design of anti-icing surfaces: Smooth, textured or slippery?, *Nat. Rev. Mater.* **1**, 15003 (2016).
[10] Y. Wang and T. McCarthy, Dip-coating deposition on chemically patterned surfaces: A mechanistic analysis and comparison with topographically patterned surfaces, *Langmuir* **30**, 2419-2428 (2014).
[11] S.D. Bhagat and M. C. Gupta, Superhydrophobic microtextured polycarbonate surfaces, *Surf. Coat. Technol.* **270**, 117-122 (2015).
[12] B. K. Nayak and M. C. Gupta, Self-organized micro/nano structures in metal surfaces by ultrafast laser irradiation, *Opt. Laser Eng.* **48**, 940-949 (2010).
[13] B.K. Nayak, M.C. Gupta, and P.O. Caffrey, Ultrafast laser-induced microstructure/nanostructure replication and optical properties, *Appl. Opt.* **51**, 604–609 (2012).
[14] S. Park, E. Cho, J. Sohn, P. Theilmann, K. Chu, S. Lee, Y. Sohn, D. Kim, and B. Kim, Design of multi-functional dual hole patterned carbon nanotube composites with superhydrophobicity and durability, *Nano Research* **6,** 389-398 (2013).
[15] Y. Yeong, C. Wang, K. J. Wynne, and M. C. Gupta, Oil-infused superhydrophobic silicone material for low ice adhesion with long-term infusion stability, *ACS Appl. Mater. Interfaces* **8**, 32050-32059 (2016).

[16] A. Mulroney and M. C. Gupta, Optically transparent superhydrophobic polydimethylsiloxane by periodic surface microtexture, *Surf. Coat. Technol*. **325**, 308-317 (2017).
[17] D. Chun, G. Davaasuren, C. Ngo, C. Kim, G. Lee, and S. Ahn, Fabrication of transparent superhydrophobic surface on thermoplastic polymer using laser beam machining and compression molding for mass production, *CIRP-Annals Manuf. Technol.* **63**, 525-528 (2014).
[18] J. Zhang and S. Severtson, Fabrication and application of reversibly switchable surfaces: Super-non-wetting to super-wetting: A critical review, *Rev. Adhesion Adhesives* **1**, 248-270 (2013).
[19] A. Mulroney, Anti-ice and condensation properties of microtextured superhydrophobic surfaces, Ph.D. thesis, University of Virginia, Charlottesville, Virginia, United States (2019).
[20] Z. Qin, J. Ai, Q. Du, J. Liu, and X. Zeng, Superhydrophobic polytetrafluoroethylene surfaces with accurately and continuously tunable water adhesion fabricated by picosecond laser direct ablation, *Materials and Design* **173**, 107782 (2019).
[21] Y. Yeong and M. C. Gupta, Hot embossed micro-textured thin superhydrophobic Teflon FEP sheets for low ice adhesion, *Surf. Coat. Technol.* **313**, 17-23 (2017).
[22] W. Cui and T. Pakkanen, Fabrication of transparent icephobic surfaces with self-reparability: Effect of structuring and thickness of the lubricant-elastomer layer, *Appl. Surf. Sci.* **504**, 144061 (2020).
[23] Z. Liu, H. Wang, E. Wang, X. Zhang, R. Yuan, and Y. Zhu, Superhydrophobic poly(vinylidene fluoride) membranes with controllable structure and tunable wettability prepared by one-step electrospinning, *Polymer* **82**, 105-113 (2016).
[24] X. Lu, C. Zhang, and Y. Han, Low-density polyethylene superhydrophobic surface by control of its crystallization behavior, *Macromolecular Rapid* Commun. **25,** 1606-1610 (2004).
[25] H. Ensikat, A. Schulte, K. Koch, and W. Barthlott, Droplets on superhydrophobic surfaces: visualization of the contact area by cryo-scanning electron microscopy, *Langmuir* **25**, 13077-13083 (2009).
[26] G. Whyman, E. Bormashenko, and T. Stein, The rigorous derivation of Young, Cassie–Baxter and Wenzel equations and the analysis of the contact angle hysteresis phenomenon, *Chem. Phys. Letters* **450**, 355-359 (2008).
[27] R.N. Wenzel, Resistance of solid surfaces to wetting by water, *Ind. Eng. Chem.* **28**, 988-994 (1936).
[28] A.Carré and K.L. Mittal (Eds.), *Superhydrophobic Surfaces*, CRC Press, Boca Raton, FL (2009).
[29] A. Cassie and S. Baxter, Wettability of porous surfaces, *Trans. Faraday Soc.* **40,** 546-551 (1944).
[30] P. Caffrey, Superhydrophobic properties of replicated laser microtextured surfaces, Ph.D. thesis, University of Virginia, Charlottesville, Virginia, United States (2015).
[31] J. Peng, X. Zhao, W. Wang, and X. Gong, Durable self-cleaning surfaces with superhydrophobic and highly oleophobic properties, *Langmuir* **35**, 8404-8412 (2019).
[32] T. Koishi, K. Yasouka, S. Fujikawa, T. Ebisuzaki, and X. Zeng, Coexistence and transition between Cassie and Wenzel state on pillared hydrophobic surface, *Proc. Natl. Acad. Sci. USA* **106**, 8435-8440 (2009).

[33] M. Ambrosia, M. Y. Ha, and S. Balachandar, The effect of pillar surface fraction and pillar height on contact angles using molecular dynamics, *Appl. Surf. Sci*. **282**, 211-216 (2013).
[34] P. Kim, T. Wong, J. Alvarenga, M. Kreder, W. Adorno-Martinez, and J. Aizenberg, Liquid-infused nanostructured surfaces with extreme anti-ice and anti-frost performance, *ACS Nano* **6**, 6569-6577 (2012).
[35] S. Barthwal, B. Lee, and S. Lim, Fabrication of robust and durable slippery anti-icing coating on textured superhydrophobic aluminum surfaces with infused silicone oil, *Appl. Surf. Sci.* **496**, 143677 (2019).
[36] K.L. Mittal and C.-H. Choi (Eds.), *Ice Adhesion: Mechanism, Measurement and Mitigation*, Wiley-Scrivener, Beverly, MA (2020).
[37] A. J. Meuler, J. D. Smith, K. Varanasi, J. Mabry, G. McKinley, and R. Cohen, Relationships between water wettability and ice adhesion, *ACS Appl. Mater. Interfaces* **2**, 3100-3110 (2010).
[38] Y. Wang, J. Liu, M. Li, Q. Wang, and Q. Chen, The icephobicity comparison of polysiloxane modified hydrophobic and superhydrophobic surfaces under condensing environments, *Appl. Surf. Sci.* **385**, 472-480 (2016).
[39] Y. Wu and C. Zhang, Analysis of anti-condensation mechanism on superhydrophobic anodic aluminum oxide surface, *Appl. Thermal Eng.* **58**, 664-669 (2013).
[40] L. Yin, Y. Wang, J. Ding, Q. Wang, and Q. Chen, Water condensation on superhydrophobic aluminum surfaces with different low-surface-energy coatings, *Appl. Surf. Sci.* **258**, 4063-4068 (2012).
[41] X. Yan, J. Li, L. Li, Z. Huang, F. Wang, and Y. Wei, Droplet condensation on superhydrophobic surfaces with enhanced dewetting under a tangential AC electric field, *Appl. Phys. Lett.* **109**, 161601 (2016).
[42] R. Avramescu, M. V. Ghica, C. Dinu-Pirvu, R. Prisada, and L. Popa, Superhydrophobic natural and artificial surfaces-A structural approach, *Materials (Basel)* **11**, 866-889 (2018).
[43] J. T. Simpson, S. R. Hunter, and T. Aytug, Superhydrophobic materials and coatings: a review, *Reports Prog. Phys.* **78**, 086501 (2015).
[44] J. Zimmermann, G. Artus, and S. Seeger, Long term studies on the chemical stability of a superhydrophobic silicone nanofilament coating, *Appl. Surf. Sci*. **253** 5972-5975 (2007).
[45] H. Zhu, Z. Guo, and W. Liu, Adhesion behaviors on superhydrophobic surfaces, *Chem. Commun.*, **30**, 3900-3913 (2014).
[46] A. Peethan, V.K. Unnikrishnan, S. Chidangil, and S.D. George, Laser-assisted tailoring of surface wettability- Fundamentals and Applications: A critical review, *Rev. Adhesion Adhesives* **7**, 331-366 (2019).
[47] S.F. Toosi, S. Moradi and S.G. Hatzikiriakos, Fabrication of micro/nano patterns on polymeric substrates using laser ablation methods to control wettability behavior: A critical review, *Rev. Adhesion Adhesives* **5**, 55-38 (2017).
[48] B. K. Nayak, P.O. Caffrey, C.R. Speck, and M.C. Gupta, Superhydrophobic surfaces by replication of micro/nano-structures fabricated by ultrafast-laser-microtexturing, *Appl. Surf. Sci.* **266**, 27-32 (2013).
[49] F.L. Palmieri and C.J. Wohl, Topographical modifications of polymers and metals by laser ablation to create superhydrophobic surfaces, in: *Laser Technology: Applications in Adhesion and Related Areas*, K.L. Mittal and W.-S.Lei (Eds.) pp. 3-68, Wiley-Scrivener, Beverly, MA (2018).

[50] D.G. Waugh and J. Lawrence, Wettability characterization of laser surface engineered polymers, in: *Laser Technology: Applications in Adhesion and Related Areas*, K.L. Mittal and W.-S. Lei (Eds.) pp. 99-122, Wiley-Scrivener, Beverly, MA (2018).

[51] B. Qian and Z. Shen, Fabrication of superhydrophobic surfaces by dislocation-selective chemical etching on aluminum, copper, and zinc substrates, *Langmuir* **21**, 9007-9009 (2005).

[52] Y. Chen, Y. Zhang, L. Shi, J. Li, Y. Xin, T. Yang, and Z. Guo, Transparent superhydrophobic/superhydrophilic coatings for self-cleaning and anti-fogging, *Appl. Phys. Lett.* **101,** 033701 (2012).

[53] J. Jeevahan, M. Chandrasekaran, G. B. Joseph, R.B. Durairaj, and G. Mageshwaran, Superhydrophobic surfaces: a review on fundamentals, applications, and challenges, *J. Coat. Technol. Res.*, **15**, 231-250 (2018).

[54] M. Khodaei, X. Chen, and H. Li, **Superhydrophobic surfaces - fabrications to practical applications,** in: *Superhydrophobic Surfaces – Introduction and Applications, Vol. 1*, pp. 1-11, IntechOpen (2020).

[55] A.T. Tyowua, M. Targema, and E.E. Ubuo, Non-wettable surfaces – from natural to artificial and applications: A critical review, *Rev. Adhesion Adhesives* **7**, 195-232 (2019).

[56] Y.B. Park, H. Im, M. Im, and Y.K. Choi, Self-cleaning effect of highly water-repellent microshell structures for solar cell applications, *J. Mater. Chem.* **21,** 633–636 (2011).

[57] C.V. Ngo and D.M. Chun, Effect of heat treatment temperature on the wettability transition from hydrophilic to superhydrophobic on laser-ablated metallic surfaces, *Advanced Eng. Mater.* **20**, 1701086 (2018).

[58] Y. Yeong, A. Steele, I. Bayer, G. DeCombarieu, C. Lakeman, and E. Loth, Impact of temperature and humidity on superhydrophobicity of polyurethane/organoclay nanocomposites, *NSTI-Nanotech. TechConnect Briefs* **1**, 383-386 (2011).

[59] S. Cha, E. K. Her, T. Ko, S. Kim, H. Roh, K. Lee, K. Oh, and M. Moon, Thermal stability of superhydrophobic, nanostructured surfaces, *J. Colloid Interface* Sci **391**, 152-157 (2013).

[60] Y. Liu, L. Ma, W. Wang, A. K. Kota, and H. Hu, An experimental study on soft PDMS materials for aircraft icing mitigation, *Appl. Surf. Sci.* **447**, 599-609 (2018).

[61] O. Parent and A. Ilinca, Anti-icing and de-icing techniques for wind turbines: critical review, *Cold Regions Sci. Technol.* **65**, 88-96 (2011).

[62] N. Dalili, A. Edrisy, and R. Carriveau, A review of surface engineering issues critical to wind turbine performance, *Renew. Sustain. Energy Rev.* **13**, 428-438 (2009).

[63] R. Carriveau, A. Edrisy, and P. Cadieux, Ice adhesion issues in renewable energy infrastructure, *J. Adhesion. Sci. Technol.* **26**, 37–41 (2012).

[64] O. Fakorede, Z. Feger, H. Ibrahim, A. Ilinca, J. Perron, and C. Masson, Ice protection systems for wind turbines in cold climate: characteristics, comparisons and analysis, *Renew. Sustain. Energy Rev.* **65**, 662–675 (2016).

[65] M. Nosonovsky and B. Bhushan, Superhydrophobic surfaces and emerging applications: non-adhesion, energy, green engineering, *Curr. Opin. Colloid Interface Sci.* **14**, 270-280 (2009).

[66] Y. Shen, X. Wu, J. Tao, C. Zhu, Y. Lai, and Z. Chen, Icephobic materials: Fundamentals, performance evaluation, and applications, *Prog. Mater. Sci.* **103**, 509-557 (2019).

[67] X. Huang, N. Tepylo, V. Pommier-Budinger, M. Budinger, E. Bonaccurso, P. Villedieu, and L. Bennani, A survey of icephobic coatings and their potential use in a hybrid coating/active ice protection system for aerospace applications, *Prog. Aerospace. Sci.* **105**, 74-79 (2019).

[68] D. G. Waugh, D. Avdic, K. J. Woodham, and J. Lawrence, Laser surface engineering of polymeric materials and the effects on wettability characteristics, in: *Laser Surface Modification and Adhesion*, K. L. Mittal and Thomas Bahners (Eds.) pp. 337-375, Wiley-Scrivener, Beverly, MA (2014).
[69] C. Qin, A. Mulroney, and M. C. Gupta, Anti-icing epoxy resin surface modified by spray coating of PTFE Teflon particles for wind turbine blades, *Mater. Today Comm.* **22**, 100770 (2020).
[70] H. Dong, M. Cheng, Y. Zhang, H. Wei, and F. Shi, Extraordinary drag-reducing effect of a superhydrophobic coating on a macroscopic model ship at high speed, *J. Mater. Chem. A* **1,** 5886-5891 (2013).
[71] A. Shahsavari, A. Nejat, and S.F. Chini, The potential of surface nano-engineering and superhydrophobic surfaces in drag reduction, in: *Advances in Contact Angle, Wettability and Adhesion*, Volume 4, K.L. Mittal (Ed.) pp. 239-266, Wiley-Scrivener, Beverly, MA (2020).
[72] S. Khorsand, K. Raeissi, and F. Ashrafizadeh, Corrosion resistance and long-term durability of super-hydrophobic nickel film prepared by electrodeposition process, *Appl. Surf. Sci.* **305**, 498-505 (2014).
[73] Y. Xiu, Y. Liu, D.W. Hess, and C. Wong, Mechanically Robust Superhydrophobicity on hierarchically structured Si Surfaces, *Nanotechnology* **21**, 155705 (2010).
[74] D. Zhang, L. Wang, and H. Qian, Superhydrophobic surfaces for corrosion protection: a review of recent progresses and future directions, *J. Coat. Technol. Res.* **13**, 11-29 (2016).
[75] F. Cucchiella and I. Dadamo, Estimation of the energetic and environmental impacts of a roof mounted building-integrated photovoltaic systems, *Renew. Sust. Energy Rev.* **16**, 5245-5259 (2012).
[76] S. Farhadi, M. Farzaneh, and S.A. Kulinich, Anti-icing performance of superhydrophobic surfaces, *Appl. Surf. Sci.* **257**, 6264-6269 (2011).
[77] N. Shirtcliffe, G. McHale, S. Atherton, and M. Newton, An introduction to superhydrophobicity, *Adv. Colloid Interface Sci.* **161**, 124-138 (2010).
[78] Y. Yeong, A. Milionis, E. Loth, J. Sokhey, and A. Lambourne, Atmospheric ice adhesion on water-repellent coatings: wetting and surface topology effects, *Langmuir* **31**, 13107-13116 (2015).
[79] D. Kronlund, M. Lindén, and J. Smått, A polydimethylsiloxane coating to minimize weathering effects on granite, *Const. Bldg. Mater.* **124**, 1051-1058 (2016).
[80] T. Wang, X. Hu, and S.Dong, A general route to transform normal hydrophilic cloths into superhydrophobic surfaces, *Chem. Commun.18*, 1849-1851 (2017).
[81] H. Wang, Y.Xue, J. Ding, L. Feng, X. Wang, and T.Li, Durable self healing superhydrophobic and superoleophobic surfaces from fluorinated decyl polyhedral oligomeric silsesquioxane and hydrolyzed fluorinated alkyl silane, *Angewandte Chemie* **50**, 11433-11436 (2011).
[82] T. Bahners and J.S. Gutmann, Procedures for the characterization of wettability and surface free energy of textiles – use, abuse, misuse and proper use: A critical review, *Rev. Adhesion Adhesives* **7**, 259-294 (2019).
[83] L. Xie, Z. Tang, L. Jiang, V. Breedveld, and D.W. Hess, Creation of superhydrophobic wood surfaces by plasma etching and thin-film deposition, *Surf. Coat. Technol.* **281**, 125-132 (2015).
[84] K. Li, X. Zeng, H. Li, and X. Lai, A study on the fabrication of superhydrophobic iron surfaces by chemical etching and galvanic replacement methods and their anti-icing properties, *Appl. Surf. Sci.* **346**, 458-463 (2015).

[85] J. Liu, Z. Janjua, M. Roe, F. Xu, B. Turnbull, K. Choi, and X. Hou, Super-hydrophobic/icephobic coatings based on silica nanoparticles modified by self-assembled monolayers, *Nanomaterials* **6**, 232-241 (2016).
[86] R. Karmouch, and G. Ross, Superhydrophobic wind turbine blade surfaces obtained by a simple deposition of silica nanoparticles embedded in epoxy, *Appl. Surf. Sci.* **257**, 665-669 (2010).
[87] W. Zhao, R. Zhu, J. Jiang, and Z. Wang, Environmentally-friendly superhydrophobic surface based on Al2O3@KH560@SiO2 electrokinetic nanoparticle for long-term anti-corrosion in sea water, *Appl. Surf. Sci.* **484**, 307-316 (2019).
[88] H. Sojoudi, M. Wang, N.D. Boscher, G. McKinley, and K.K. Gleason, Durable and scalable icephobic surfaces: similarities and distinctions from superhydrophobic surfaces, *Soft Matter* **12**, 1938-1963 (2016).
[89] B. K. Nayak, V. Iyengar, and M. C. Gupta, Efficient light trapping in silicon solar cells by ultrafast-laser-induced self-assembled micro/nano structures, *Prog. Photovolt: Res. Appl.* **19**, 631-639 (2011).
[90] Y. Gao, I. Gereige, A. Labban, D. Cha, T. Isimjan, and P. Beaujuge, Highly transparent and UV-resistant superhydrophobic SiO2 coated ZnO nanorod arrays, *ACS Appl. Mater. Interfaces* **6**, 2219–2223 (2014).
[91] Z. Geng and J. He, Superamphiphobic coatings with high transmittance: Structure, fabrication, and perspective, *Adv. Mater. Interfaces* **2**, 1500196 (2015).
[92] F. Chu and X. Wu, Fabrication and condensation characteristics of metallic superhydrophobic surface with hierarchical micro-nano structures, *Appl. Surf. Sci* **371**, 322-328 (2016).
[93] K. Wisdom, J. Watson, X. Qu, F. Liu, G. Watson, and C. Chen, Self-cleaning of superhydrophobic surfaces by self-propelled jumping condensate, *Proc. Natl. Acad. Sci. (USA)* **110**, 7992-7997 (2013).
[94] J. M. Oh, G. Manukyan, D. van den Ende, and F. Mugele, Electric-field–driven instabilities on superhydrophobic surfaces, *European Phys. Letters* **93**, 56001 (2011).
[95] A. Cavalli, D.J. Preston, E. Tio, D.W. Martin, N. Miljkovic, E.N. Wang, F. Blanchette, and J. W. M. Bush, Electrically induced drop detachment and ejection, *Phys. Fluids* **28**, 022101 (2016).
[96] N. Miljkovic, D. Preston, R. Enright, and E. Wang, Electric-field-enhanced condensation on superhydrophobic nanostructured surfaces, *ACS Nano* **7**,11043 11054 (2013).
[97] A. D. Tserepi, M.-E. Vlachopoulou, and E.Gogolides, Nanotexturing of poly(dimethylsiloxane) in plasmas for creating robust super-hydrophobic surfaces, *Nanotechnology* **17**, 3977-3983 (2006).